ADDIS ABABA UNIVERSITY

SCHOOL OF GRADUATE STUDIES

CONDUCTING POLYMER BASED COMPOSITES FOR ELECTROCATALYTIC REDUCTION OF OXYGEN AND FLEXIBLE SUPERCAPATTERY

BY

TEKLEWOLD GETACHEW WAMI

DECEMBER, 2020

ADDIS ABABA, ETHIOPIA

ADDIS ABABA UNIVERSITY

SCHOOL OF GRADUATE STUDIES

CONDUCTING POLYMER BASED COMPOSITES FOR ELECTROCATALYTIC REDUCTION OF OXYGEN AND FLEXIBLE SUPERCAPATTERY

BY

TEKLEWOLD GETACHEW

SUPERVISOR: PROF. SHIMELIS ADMASSIE

DECEMBER, 2020

ADDIS ABABA, ETHIOPIA

CONDUCTING POLYMER BASED COMPOSITES FOR ELECTROCATALYTIC REDUCTION OF OXYGEN AND FLEXIBLE SUPERCAPATTERY

By

Teklewold Getachew

A thesis submitted to the Department of Chemistry, College of Natural and Computational Sciences, Addis Ababa University, in partial fulfillment of the requirements for the degree of Doctor of Philosophy in Chemistry (Physical)

December, 2020

ADDIS ABABA, ETHIOPIA

ADDIS ABABA UNIVERSITY

SCHOOL OF GRADUATE STUDIES

This is to certify that the thesis prepared by Teklewold Getachew Wami entitled: *Conducting Polymer Based Composites for Electrocatalytic Reduction of Oxygen and Flexible Supercapattery* and submitted in partially fulfillment of the requirements for the degree of Doctor of Philosophy (Physical Chemistry) complies with the regulation of the university and meets the accepted standards with respect to originality and quality.

Signed by the examining committee

Name	Signature	Date
Prof. Shimelis Admassie (Advisor)	_____	_____
Prof. Tewodros Asefa (External Examiner)	_____	_____
Prof. Teketel Yohannes (Internal Examiner)	_____	_____
Dr. Weldegebriel Yohannes (Internal Examiner)	_____	_____
Dr. Negash Getachew (Chairman)	_____	_____

_____

Chairman, College Academic Commission

Declaration

I, the under signed, declare that this thesis submitted for the Degree of Doctor of Philosophy (Physical Chemistry) to the Addis Ababa University, Addis Ababa, Ethiopia is my original work, has not been presented before for any degree or examination in this or any other university and all the resources used for the thesis have been fully acknowledged.

Name: Teklewold Getachew Wami

Signature: _____

Place and date of submission

Addis Ababa University
Department of Chemistry
Addis Ababa, Ethiopia
December, 2020

Acknowledgements

First and foremost, I would like to thank the almighty God who gave me the strength and health to carry out this research work.

I am greatly indebted to my research advisor Prof. Shimelis Admassie for his valuable guidance, support and encouragement throughout my PhD study. It was a privilege to have a supervisor who cared so much about my work, and who responded to my questions and queries so promptly. I also want to thank Dr. Solomon Mehretie who gave me many useful advices during my research and paper writing.

Special thanks go to Prof. Shimelis Admassie and Prof. Ruidong Xia for facilitating to stay in South China University of Technology (SCUT) for one year. I also would like to thank Prof. Hin-Lap Yip for allowing me to work in his research laboratory with great freedom covering all the financial costs related to the research work.

I would like to thank Prof. Theodros Solomon, Prof. Wendimagegn Mamo, Prof. Teketel Yohannes, Dr. Ahmed Mustefa, Dr. Taye Beyene, Dr. Weldegebriel Yohannes, Dr. Girum Ayaleneh, Dr. Yonas Chebude, Dr. Negash Getachew and Fitsum Addis for their contribution in one way or another in this PhD work. I am very much grateful to AAU chemistry department and Kotebe Metropolitan University for the permission of this study and providing necessary resources. I must also thank all of my past and present colleagues in the Prof. Shimelis's research group for their help and friendship particularly Alemayehu Yifru, Dr. Fekadu Chekol, Dr. Belete Tesfaw and Dr. Asfaw Negash.

I want to thank Dr. Qifan Xue, Dr. H. Zhang, J. Tien and Bohan for their help in facilitating my work in School of Materials Science and Engineering (International School of Advanced Materials, SCUT). I would like to express my deepest appreciation to Liu Yang, Chunxian Huang, Li Siqi (Mickey), Ivy (Moi) and Garry Histand for all their administrative help, understanding and encouragement specially during Covid-19 pandemic.

I cannot forget the encouragement and support from all friends from Keladamba (Harar), Tollay and Sheger. Many thanks to my sisters, brother, parents and other family for their long time encouragement and support to push on to the end. Many thanks to Birhane G/Kidane (Etaba) and Emebet Mohammed (Metu) for caring my son during my study.

Finally, my special thanks goes to my wife Mekdes Mohammed and my kids Noah Teklewold and Maya Teklewold for their unconditional love and source of happiness.

List of Symbols and Abbreviations

AFM	Atomic force microscopy
2-ANSA	2-Amino-1-naphthalene sulfonic acid
4-ANSA	4-Amino-1-naphthalene sulfonic acid
5-ANSA	5-Amino-1-naphthalene sulfonic acid
8-ANSA	8-Amino-2-naphthalene sulfonic acid
b	Tafel slope
C_0	Bulk concentration of oxygen
CCCD	Constant Current Charge/Discharge
CPs	Conducting polymers
CV	Cyclic voltammetry
D_0	Diffusion coefficient of oxygen
DFT	Density functional theory
E	Potential
E^o	Equilibrium open-circuit potential
$E_{1/2}$	Half-wave potential
E_{onset}	Onset potential
E_D	Disk potential
E_R	Ring potential
ECSA	Electrochemically active surface area
ECs	Electrochemical capacitors
EDLCs	Electrical double-layer capacitors
EDX or EDS	Energy dispersive X-ray spectroscopy

EG	Ethylene glycol
ESR	Equivalent series resistance
F	Faraday constant
FSCs	Flexible supercapacitors
FCs	Fuel cells
GC	Glassy carbon
GO	Graphene oxide
FESEM	Field-emission scanning electron microscopy
i_L	Diffusion limiting current
I_D	Disk current
I_R	Ring current
ITO/PET	Indium tin oxide on polyethylene terephthalate
J_d	Diffusion-limiting current density
J_k	Kinetic current density
J_o	Exchange current density
k_f	Heterogeneous rate constant
k_{O_2}	Electron transfer rate constant
K-L	Koutecky-Levich
LG	Lignosulfonate/Lignin
LSV	Linear sweep voltammetry
MA	Mass activity
MWCNT	Multi-walled carbon nanotube
MSE	Mercury sulfate electrode

n	Number of electrons transferred
N	Collection efficiency
ORR	Oxygen reduction reaction
PEDOT	Poly(3,4-ethylenedioxythiophene)
PEDOT:PSS	Poly(3,4-ethylenedioxythiophene):(styrenesulfonate)
Pt/C	Carbon-supported platinum nanoparticles
Pt-NPs	Platinum nanoparticles
R	Universal gas constant
RDE	Rotating disk electrode
rGO	Reduced graphene oxide
RHE	Reversible hydrogen electrode
RRDE	Rotating ring- disk electrode
SA	Specific area activity
SCs	Supercapacitors
SEM	Scanning electron microscopy
Γ	Surface coverage of the catalyst
ν	Kinematic viscosity of the electrolyte
ω	Rotational rate
XRD	X-ray diffraction
XPS	X-ray photoelectron spectroscopy

Abstract

The rapid depletion of fossil fuels and the growing environmental impact of traditional energy resources have created the need to develop more efficient, low cost and environmentally friendly energy conversion and storage devices like solar cells, fuel cells, batteries and supercapacitors. In this PhD work, the application of conducting polymer based composites for electrocatalytic reduction of oxygen in fuel cell and supercapattery have been investigated.

To reduce the amount of expensive and scarce platinum metal that is used in the electrocatalytic reduction of oxygen, composites of graphene oxide (GO) and poly(3,4-ethylenedioxythiophene):poly(styrenesulfonate) (PEDOT:PSS) were investigated as a conductive support for Pt nanoparticles. The surface characteristics of the materials were examined using atomic force microscopy (AFM), X-ray diffraction (XRD), field-emission scanning electron microscopy (FESEM), and energy-dispersive X-ray spectroscopy (EDS). Cyclic voltammetry (CV) and linear sweep voltammetry (LSV) at rotating disk electrode (RDE) and rotating ring-disk electrode (RRDE) were used to characterize the electrocatalytic activities of the composite materials. The structural and electrochemical studies reveal that the addition of ethylene glycol (EG) favors the homogeneous distribution of Pt particles with reduced particle size and improves the electrocatalytic properties. A 30% and 16% increase in electrochemically active surface area (ECSA), a 1.2 and 1.1 fold in specific area activity (SA), and a 1.5 and 1.2 fold in mass activity (MA) were observed for 30% and 40% Pt loading, respectively, on PEDOT:PSS. A composite of reduced graphene oxide (rGO) and PEDOT:PSS (EG) was investigated for different (w/w) ratio of PEDOT:PSS and rGO. The 1:2 w/w ratio showed an enhanced catalytic activity with high limiting current, more positive onset potential, higher SA and MA with lower H_2O_2 yield compared to PEDOT:PSS (EG) and rGO. Furthermore, composites of rGO and conducting

polymers synthesized from 8-amino-2-naphthalene sulfonic acid (8-ANSA), 5-amino-1-naphthalene sulfonic acid (5-ANSA), 2-amino-1-naphthalene sulfonic acid (2-ANSA), and 4-amino-1-naphthalene sulfonic acid (4-ANSA) were prepared for use as metal-free electrocatalyst in oxygen reduction reaction (ORR). The best performing polymer composite was found to be GC/poly(8-ANSA)/rGO, with an enhanced electrocatalytic activity over the rGO and poly(8-ANSA) only films. More than 100 mV positive shift in the onset potential and 1.6 times increase in current density were observed. Density functional theory (DFT) calculations also confirmed the experimentally observed catalytic activities of 2-ANSA, 4-ANSA, 5-ANSA and 8-ANSA.

The application of roll-to-roll printed PEDOT:PSS, Lg/PEDOT:PSS, Mo/PEDOT:PSS, and Lg/Mo/PEDOT:PSS on flexible indium tin oxide/polyethylene terephthalate (ITO/PET) were investigated for supercapattery in neutral aqueous and gel electrolyte. The PEDOT:PSS/ITO/PET electrode achieved 2.2 mAh cm^{-2} (46.5 mAh g^{-1}) in 0.1 M NaCl and 10 mAh cm^{-2} (216.8 mAh g^{-1}) in 2 mM Pb^{2+}/0.1 M NaCl at a current density of 0.2 mA cm^{-2} (4.34 A g^{-1}). A device operating at a high voltage of 1.8 V was built using PEDOT:PSS/ITO/PET in aqueous electrolyte. The energy density of the symmetric PEDOT:PSS/ITO/PET device was found to be 6.2 Wh kg^{-1} in 0.1 M NaCl and improved to 11 Wh kg^{-1} in 3 mM Pb^{2+}/0.1 M NaCl. The PEDOT:PSS/ITO/PET electrode delivers a specific capacity of 20.88 mAh g^{-1} (75.2 C g^{-1}) and increased to 90.6 mAh g^{-1} (326.1 C g^{-1}), to 103.1 mAh g^{-1} (371 C g^{-1}), and 303.1 mAh g^{-1} (1091 C g^{-1}) at 1 A g^{-1} for Mo/PEDOT:PSS/ITO/PET, Lg/PEDOT:PSS/ITO/PET and Mo/Lg/PEDOT:PSS/ITO/PET, respectively in 0.1 M $HClO_4$. Mo/Lg/PEDOT:PSS/ITO/PET electrode exhibits an energy density of 1.9 mWh cm^{-3} as a sandwich-type symmetric gel-based device at a power density of 22 mW cm^{-3}.

List of publications

1. **Teklewold Getachew**, Fitsum Addis, Solomon Mehretie, Hin-Lap Yip, Ruidong Xi and Shimelis Admassie, Electrocatalytic reduction of oxygen at platinum nanoparticles dispersed on electrochemically reduced graphene oxide/PEDOT:PSS composites, *RSC Adv.*, **2020**, 10, 30519.

2. **Teklewold Getachew**, Fitsum Addis, Taye Beyene, Solomon Mehretie, and Shimelis Admassie, Amino-substituted naphthalene sulfonic acid/graphene composite as metal-free catalysts for oxygen reduction reactions, *Bull. Chem. Soc. Ethiop.* **2019**, 33(2), 359-372.

3. **Teklewold Getachew,** Solomon Mehretie, Hin-Lap Yip, Ruidong Xia and Shimelis Admassie, Roll-to-roll printed high voltage supercapattery in lead-contaminated aqueous electrolyte, *Phys. Chem. Chem. Phys.*, **2020**, 22, 5597.

4. **Teklewold Getachew,** Solomon Mehretie, Hin-Lap Yip, Ruidong Xia and Shimelis Admassie, Roll-to-roll printed phosphomolybdic acid/Lignin/PEDOT:PSS composite for supercapattery. Manuscript under preparation.

Table of contents

Acknowledgements ..... **i**

List of Symbols and Abbreviations ..... **iii**

Abstract ..... **vi**

List of publications ..... **vii**

Table of contents ..... **ix**

List of figures ..... **xiv**

List of tables ..... **xxiv**

1. Introduction **1**

1.1 Background 1

1.2 Objectives of the study 7

1.2.1 General objective 7

1.2.2 Specific objectives 7

2. Literature review **8**

2.1 Conducting polymers and their composites 8

2.2 Graphene and its family 12

2.3 Biopolymer-Lignin 15

2.4 Oxygen reduction reaction 16

2.4.1 Reaction pathways for ORR 19
2.4.2 Theoretical studies on the ORR in fuel cells 22
2.4.2.1 Understanding the electrocatalysis of oxygen reduction on metal catalyzed reaction 24
2.4.2.2 Origin of the electrocatalytic oxygen reduction activity of graphene-based catalysts 26
2.4.2.3 Theoretical study on the catalytic activity of conducting polymers toward oxygen reduction 27
2.4.3 Practical study on electrocatalytic oxygen reduction reaction 28
2.4.3.1 Cyclic voltammetry in oxygen reduction reaction 28
2.4.3.2 Linear sweep voltammetry (LSV) in oxygen reduction reaction 35
2.4.4 Requirements for oxygen reduction reaction electrocatalyst 43
2.4.5 Oxygen reduction reaction on platinum-based electrocatalysts 45
2.4.5.1 Graphene support material for platinum for oxygen reduction reaction 45
2.4.5.2 Electronically conducting polymer as platinum support for oxygen reduction reaction 48
2.4.6 Graphene and conducting polymer as a metal-free catalyst for oxygen reduction reaction 50
2.5 Supercapacitors 53
2.5.1 Types of supercapacitors (SCs) 55
2.5.1.1 The electric double-layer capacitor (EDLC) 56
2.5.1.2 Pseudocapacitors 58
2.5.1.3 Hybrid capacitors 59
2.5.2 Performance characterization of supercapacitors 62
2.5.2.1 Cyclic voltammetry (CV) in supercapacitors 63
2.5.2.2 Constant current charge/discharge (CCCD) test 64
2.5.2.3 Electrochemical impedance spectroscopy (EIS) 67

2.5.3 Conducting polymers in supercapacitor application 68
2.5.3.1 PEDOT:PSS in supercapacitors 70
2.5.3.2 PEDOT:PSS for flexible supercapacitors 73
2.5.4 Electrolytes for supercapacitors 73

3. Experimental 76

3.1 Reagents and materials 76
3.2 Instruments and apparatus 77
3.3 Electrode preparation and electrochemical characterization 81
3.3.1 Preparation of platinum nanoparticles dispersed on electrochemically reduced graphene oxide/PEDOT:PSS composites glassy carbon electrode (GCE) 81
3.3.1.1 Preparation of the modified glassy carbon electrode (GCE) 81
3.3.1.2 Determination of electrochemically active surface area (ECSA) 82
3.3.1.3 Determination of kinetic current (i_k), mass activity (MA) and specific area activity (SA) 83
3.3.1.4 Determination of collection efficiency (N), number of electrons transferred (n) and percentage of H_2O_2 (% H_2O_2) 83
3.3.1.5 Stability and electrochemical crossover test 84
3.3.2 Preparation of graphene/amino substituted naphathalene composite for metal-free catalyst .. 85
3.3.2.1 Synthesis of GO 85
3.3.2.2 Electrochemical reduction of GO 85
3.3.2.3 Electropolymerization 86
3.3.2.4 Electrochemical measurements 86
3.3.3 Roll-to-roll printed electrodes 87

3.3.3.1 Electrode coating procedure 87

3.3.3.2 Preparation of gel and liquid electrolyte for SCs devices 88

3.3.3.3 Electrochemical measurements 89

3.4 Physical characterization of electrodes 90

3.5 Computational Details 90

4. Results and discussion 92

4.1 Electrocatalytic reduction of oxygen at platinum nanoparticles dispersed on electrochemically reduced graphene oxide/PEDOT:PSS composites 92

4.1.1 Background 92

4.1.2 Galvanostatic deposited platinum on PEDOT:PSS 94

4.1.3 Potentiostatic deposited platinum on PEDOT:PSS 96

4.1.4 Surface characterization 99

4.1.5 Electrochemical characterization 105

4.1.5.1 Cyclic voltammetric studies 105

4.1.5.2 Linear sweep voltammetric studies at RDE 107

4.1.5.3 Linear sweep voltammetric studies at RRDE 111

4.2 Amino-substituted naphthalene sulfonic acid/graphene composite as metal-free catalysts for oxygen reduction reactions 122

4.2.1 Background 122

4.2.2 Surface characterization 123

4.2.3 Modification of glassy carbon electrode 125

4.2.4 Computational study of ORR on poly(2-ANSA), poly(4-ANSA), poly(5-ANSA)

and poly(8-ANSA) 129

4.2.5 Oxygen reduction study using cyclic and linear sweep voltammetry 133

4.3 Roll-to-roll printed high voltage supercapattery in lead-contaminated aqueous electrolyte 145

4.3.1 Background..... 145

4.3.2 Electrochemical deposition of $PbCl_2$ on PEDOT:PSS/ITO/PET film..... 147

4.3.3 XPS study of PEDOT:PSS/ITO 148

4.3.4 Cyclic voltammetry studies on PEDOT:PSS/ITO/PET films 150

4.3.5 Galvanostatic charge-discharge studies on PEDOT:PSS/ITO/PET films..... 152

4.3.6 Cyclic stability study of PEDOT:PSS/ITO/PET films..... 156

4.3.7 Electrochemical studies of symmetric devices..... 157

4.4 Roll-to-roll printed Phosphomolybdic acid/Lignin/PEDOT:PSS composite for supercapattery.. 161

4.4.1 Background..... 161

4.4.2 Structural and compositional studies..... 163

4.4.3 Cyclic voltammetric studies on PEDOT:PSS/ITO/PET films 165

4.4.4 Galvanostatic charge-discharge studies on binary and ternary composites of PEDOT:PSS/ITO/PET films 170

4.4.5 Electrochemical studies of symmetric devices..... 174

5. Conclusions..... 179

6. References..... 181

List of figures

Figure 1. The Ragone plots of various electrochemical and internal combustion power devices. 3

Figure 2. Conducting polymers and their composite materials. 9

Figure 3. A simplified schematic of a chain containing alternating single and double bonds. 10

Figure 4. The structure of (a) graphene, (b) buckyballs, (c) carbon nanotubes and (d) graphite. 12

Figure 5. A simple route for the preparation of graphene sheets from graphite. 14

Figure 6. The structural transformation between hydroquinone/benzoquinone state in LS. 15

Figure 7. Simplified reaction scheme for the oxygen reduction reaction. 19

Figure 8. Schematic representation of the qualitative Sabatier principle. 21

Figure 9. Trends in oxygen reduction activity. 25

Figure 10. (a) Potential-time excitation signal in cyclic voltammetric experiment and (b) cyclic voltammogram for a reversible $O + ne \rightleftharpoons R$ redox process. 29

Figure 11. Cyclic voltammograms for irreversible (curve A) and quasi-reversible (curve B) redox processes. 30

Figure 12. Cyclic voltammogram for a platinum electrode in 0.5 M H_2SO_4 solution (V *vs* MSE). The inset shows the different charge contributions in the hydrogen region. 31

Figure 13. Cyclic voltammogram on Pt/Vulcan electrode in 0.5 M H_2SO_4, scan rate: 20 mV s^{-1} 32

Figure 14. CO stripping voltammogram (thick line, 1^{st} cycle) and the second potential cycle (thin line) for Pt/C catalysts (40 wt.% Pt), (scan rate: 100 mV s^{-1} in de-aerated 0.1 M $HClO_4$). 34

Figure 15. LSV curve recorded in quiescent solution and LSV of the same electrochemical reaction using a rotating disk electrode set-up (RDE). 35

Figure 16. Configuration of RDE (a) and RRDE (c). Linear sweep voltammogram (LSV) curves of electrocatalysts in oxygen-saturated electrolytes with different rotating speeds (b) typical oxygen reduction curves on the disc and ring electrodes, respectively (d). 37

Figure 17. Extraction of kinetic current density (J_k) from measured ORR polarization curve in RDE setup. 38

Figure 18. Typical ORR polarization curve and the parameters used to quantitatively determine the activity 44

Figure 19. Schematic representation of a conventional capacitor (a) and a electrical double layer supercapacitor (b) 54

Figure 20. Models of the electrical double layer at a positively charged surface (a) the Helmholtz model, (b) the Gouy–Chapman model, and (c) the Stern model, showing the inner Helmholtz plane (IHP) and outer Helmholtz plane (OHP). 57

Figure 21. Schematic representation of the electrochemical energy storage system in a pseudocapacitor 59

Figure 22. Schematic representations of different possible hybridization approach between supercapacitor and battery electrodes and materials. 60

Figure 23. A hybrid lithium ion-capacitor. 61

Figure 24. Schematic correlation between EDL capacitor, pseudocapacitor, battery, and supercapattery (hybrid of supercapacitor and battery) in terms of capacitive and faradaic charge storage processes. 62

Figure 25. (a) 3-substituted polythiophene, (b) poly(3,4-ethylenedioxythiophene) (PEDOT), (c) poly(3- (4-fluorophenyl) thiophene) (PFPT). 70

Figure 26. (a) Chemical structures of PEDOT:PSS and (b) Schematic diagram of the morphology model 72

Figure 27. Classification of electrolytes for electrochemical supercapacitors 74

Figure 28. Electrochemical set up in (a) Autolab potentiostat/galvanostat (b) Pine bipotentiostat and (c) Pine rotation speed controller. 77

Figure 29. (a) AFM instrument set up and (b) Rigaku Smart Lab SE X-ray diffractometer. 78

Figure 30. (a) Thermo ESCALAB 250Xi and (b*)* Hitachi, S-4800 for FESEM imaging. 79

Figure 31. (a) PerkinElmer Spectrum 65 FT-IR Spectrometer (b) A picture of the desktop roll-to-roll printing machine and (c) Bruker Dektak XT profilometer. 80

Figure 32. A picture of samples of the printed plastic films. 88

Figure 33. Electrochemical setup for (a) 3-electrode and (b) 2-electrode system. 89

Figure 34. Typical chronopotentiograms for the electrodeposition of Pt particles onto PEDOT:PSS from the electrolyte solution of 5 mM H_2PtCl_6, 1 M H_2SO_4 with applied current and time of ■ (- 4.5 mA, 10 s), ●(- 3 mA, 15 s), ▲(- 2.25 mA, 20 s), ▼(- 1.5 mA, 30 s) and ♦(- 1.125 mA, 40 s), respectively. 95

Figure 35. Cyclic voltammograms of galvanostatically deposited Pt (40%) on PEDOT:PSS at a deposition time of 10 s (■), 15 s (●), 20 s (▲), 30 s (▼) and 40 s (♦) in N_2-saturated 0.1 M $HClO_4$ at scan rate of 20 mV s^{-1}. 96

Figure 36. Current against time response for a potentiostatic deposition of platinum on PEDOT:PSS at -0.15 V *vs* Ag/AgCl.....97

Figure 37. Cyclic voltammograms of galvanostatically (for 30 s) (▼) and potentiostatically (●) deposited Pt (40%) on PEDOT:PSS catalyst in N_2-saturated 0.1 M $HClO_4$ at a scan rate of 20 mV s^{-1}.....98

Figure 38. Background corrected oxygen polarization LSV curves for galvanostatically (for 30 s) (▼) and potentiostatically (●) deposited Pt (40%) on PEDOT:PSS in O_2-saturated 0.1 M $HClO_4$ at a scan rate of 20 mV s^{-1} rotating at 1600 rpm.....99

Figure 39. XRD patterns of (a) PEDOT:PSS/Pt (30%), PEDOT:PSS(EG)/Pt (30%), and rGO/PEDOT:PSS(EG)/Pt (30%) (b) over a narrow range of 2θ (35-44 degrees) for PEDOT:PSS/Pt (30%) and PEDOT:PSS(EG)/Pt (30%).....100

Figure 40. The 2D AFM images of (a) PEDOT:PSS (b) PEDOT:PSS/Pt and (c) PEDOT:PSS(EG)/Pt.101

Figure 41. SEM images (a, c, e) used for EDS (x 50 k), EDS (b, d, f) spectrum, SEM images (g, i, k) and elemental color maps for carbon (h (i), j (i), l (i)), oxygen (h (ii), j (ii), l (ii)), sulfur (h (iii), j (iii), l (iii)) and platinum (h (iv), j(iv), l(iv)) for PEDOT:PSS/Pt (30%), PEDOT:PSS(EG)/Pt (30%) and rGO/PEDOT:PSS(EG)/Pt (30%), respectively.....104

Figure 42. Cyclic voltammograms of (a) different wt% Pt catalyst on PEDOT:PSS (b)

rGO:PEDOT:PSS(EG)/Pt (30%) catalyst in N_2-saturated 0.1 M $HClO_4$ at scan rate of 20 mV s^{-1}. 106

Figure 43. Background corrected oxygen polarization curves for (a) PEDOT:PSS/Pt, (b) PEDOT:PSS(EG), 30% and 40% platinum on PEDOT:PSS(EG) and PEDOT:PSS (c) rGO and rGO/PEDOT:PSS/Pt (30%) in O_2-saturated 0.1 M $HClO_4$ at a scan rate of 20 mV s^{-1} rotating at 1600 rpm. 108

Figure 44. Mass transport corrected Tafel plots for (a) PEDOT:PSS/Pt, PEDOT:PSS(EG)/Pt and (b) rGO/PEDOT:PSS(EG)/Pt obtained from disk current in the cathodic sweep at 1600 rpm. Scan rate: 20 mV s^{-1}.....111

Figure 45. Ring ($Fe(CN)_6^{4-} \rightarrow Fe(CN)_6^{3-} + e^-$) and (disk $Fe(CN)_6^{3-} + e^- \rightarrow Fe(CN)_6^{4-}$) currents for the determination of the collection efficiency on 1:0 in 1 M KNO_3 supporting electrolyte with 10 mM $K_3Fe(CN)_6$. Negative sweeps at 20 mV s^{-1}; E_{Ring} = 1.3 V. 112

Figure 46. Variation of the collection efficiency with potential and catalyst loading for the different catalysts (a) PEDOT:PSS(EG)/Pt, and (b) rGO/PEDOT:PSS(EG)/Pt (30%). 113

Figure 47. (a) RRDE voltammograms disk current density, (b) ring current density, (c) the number of electron transferred, and (d) % H_2O_2 formation as a function of the disk potential for various rGO/PEDOT:PSS composite at 1600 rpm in 0.1 M $HClO_4$ solution. 115

Figure 48. (a) RRDE volatmmograms, (b) % H_2O_2 formation and (c) electron transfer number (n) as a function of the disk potential for various platinum loadings on PEDOT:PSS(EG) at 1600 rpm in 0.1 M $HClO_4$ solution.....117

Figure 49. (a) % H_2O_2 and (b) n as a function of the disk potential for PEDOT:PSS(EG)/Pt (30%), rGO/PEDOT:PSS(EG)(1:0)/Pt (30%) and rGO/PEDOT:PSS(EG)(1:2)/Pt (30%) at 1600 rpm in 0.1 M $HClO_4$ solution. 118

Figure 50. Comparative study of methanol tolerance ability of rGO/PEDOT:PSS(EG)(1:2)/Pt (30%) and Pt/C (Etek, 20%) by chronoamperometry at 0.8 V in O_2-saturated 0.1 M $HClO_4$ with a rotational speed of 1600 rpm. 120

Figure 51. Chronoamperometric responses of rGO/PEDOT:PSS(EG)(1:2)/Pt (30%) and Pt/C (Etek, 20%) by chronoamperometry at 0.8 V in O_2-saturated 0.1 M $HClO_4$ with a rotational speed of 1600 rpm. 121

Figure 52. XRD patterns of (a) graphite and (b) GO. 124

Figure 53. FT-IR spectra of (a) graphite and (b) GO. 125

Figure 54. Cyclic voltammograms obtained for the electropolymerization of (a) 8-ANSA on GC and (b) 8-ANSA on GC/rGO from a solution containing 2 mM 8-ANSA monomer in 0.1 M HNO_3 at a scan rate of 100 mV s^{-1} for 16 scans between -0.8 V to 2.0 V *vs* Ag/AgCl. 126

Figure 55. Electrochemical reduction of GO on (a) bare glassy carbon and (b) 8-ANSA in 0.1 M Na_2SO_4 solution for 20 cycles at a scan rate of 50 mV s^{-1}. 128

Figure 56. Dimers of (a) 2-ANSA, (b) 4-ANSA, (c) 5-ANSA, and (d) 8-ANSA molecular cluster. Hydrogen atoms were omitted for clarity. 130

Figure 57. CVs of oxygen reduction at (a) GO and (b) rGO modified glassy carbon electrode in an O_2

saturated 0.1 M KOH solution at a scan rate of 20 mV s^{-1}. 134

Figure 58. Comparison of the background corrected (a) cyclic voltammograms and (b) linear sweep voltammograms of (♦) GC/rGO, (▲) GC/poly(5-ANSA)/rGO, (●) GC/poly(4-ANSA)/rGO, (□)GC/poly(2-ANSA)/rGO, and (∇) GC/poly(8-ANSA)/rGO (c) linear sweep voltammograms of (♦) GC/rGO, (+) GC/poly(8-ANSA), (∇) GC/poly(8-ANSA)/rGO, and (●) GC/rGO/poly(8-ANSA) electrodes in 0.1 M KOH at a scan rate of 20 mV s^{-1} rotating at 1600 rpm. 135

Figure 59. Linear sweep voltammograms of GC/poly(8-ANSA)/rGO at different rotation speeds (400, 900, 1600 and 2500 rpm) and a scan rate of 20 mV s^{-1} 137

Figure 60. K-L plots (J^{-1} *vs* $\omega^{-1/2}$) at different electrode potentials in 0.1 M KOH..... 138

Figure 61. Electron transfer number as a function of potential of GC/rGO, GC/poly(8-ANSA), and GC/poly(8-ANSA)/rGO..... 139

Figure 62. RRDE voltammograms of GC/rGO, GC/poly(8-ANSA), and GC/poly(8-ANSA)/rGO at 1600 rpm. The ring current was polarized at + 1.0 V. 140

Figure 63. Tafel plots for the ORR at GC/poly(8 ANSA)/rGO (▲), GC/poly(8-ANSA) (●), and GC/rGO (■) at an electrode rotation rate of 1600 rpm. 141

Figure 64. Reaction order plot for oxygen reduction reaction on GC/rGO, GC/poly(8-ANSA), and GC/poly(8-ANSA)/rGO (the slope stands for the reaction order number)..... 142

Figure 65. CV curves of 10 cycles for (a) PEDOT:PSS/PET, (b) PEDOT:PSS/ITO/PET (c) ITO/PET in 1 mM Pb^{2+}/0.1 M NaCl at a scan rate of 50 mV s^{-1}. 148

Figure 66. (a) Full range survey X-ray photoelectron spectra of the PEDOT:PSS/ITO/PET film (a') before and (b') after deposition of Pb (b) Pb 4f spectra for adsorbed lead ions on PEDOT:PSS/ITO/PET and (c) Cl 2p spectra on PEDOT: PSS/ITO/PET. 149

Figure 67. CV curves (a) PEDOT:PSS/PET film in 0.1 M NaCl, (b) PEDOT:PSS/PET in 1 mM Pb^{2+}/0.1 M NaCl, (c) PEDOT:PSS/ITO/PET in 1 mM Pb^{2+}/0.1 M NaCl and (d) ITO/PET in 1 mM Pb^{2+}/0.1 M NaCl at a scan rate of 50 mV s^{-1}. 151

Figure 68. CV curves of PEDOT:PSS/ITO/PET (a) 0.5 mM Pb^{2+}/0.1 M NaCl, (b) 1 mM Pb^{2+}/0.1 M NaCl, (c) 1.5 mM Pb^{2+}/0.1 M NaCl, (d) 2 mM Pb^{2+}/ 0.1 M NaCl, at a scan rate of 50 mV s^{-1}. 152

Figure 69. GCD curves of PEDOT:PSS/ITO/PET in (a) 0.1 M NaCl, (b) 0.5 mM Pb^{2+}/0.1 M NaCl, (c) 1 mM Pb^{2+}/0.1 M NaCl, (d) 1.5 mM Pb^{2+}/0.1 M NaCl, and (e) 2 mM Pb^{2+}/0.1 M NaCl at 0.2 mA cm^{-2} 153

Figure 70. (a) GCD curves of PEDOT:PSS/ITO/PET in 1 mM Pb^{2+}/0.1 M NaCl at (a') 0.2 mA cm^{-2}, (b') 0.4 mA cm^{-2}, (c') 0.6 mA cm^{-2} and (d') 0.8 mA cm^{-2}. (b) Areal capacity of PEDOT:PSS/ITO/PET in 1 mM Pb^{2+}/0.1 M NaCl at different current density. 154

Figure 71. Normalized capacity against number of cycles for PEDOT:PSS/ITO/PET in 1 mM Pb^{2+}/0.1 M NaCl at a current density of 0.4 mA cm^{-2} 156

Figure 72. (a) CV curves and (b) GCD curves (0.1 mA cm^{-2} or 1 A g^{-1}) PEDOT:PSS/ITO/PET symmetric devices with (a') 0.1 M NaCl, (b') 1 mM Pb^{2+}/0.1 M NaCl, (c') 2 mM Pb^{2+}/0.1 M NaCl, and (d') 3 mM Pb^{2+}/0.1 M NaCl 158

Figure 73. Ragone plots for PEDOT:PSS/ITO/PET symmetric devices with (a) 0.1 M NaCl, (b) 1 mM Pb^{2+}/0.1 M NaCl, (c) 2 mM Pb^{2+}/0.1 M NaCl, and (d) 3 mM Pb^{2+}/0.1 M NaCl. 159

Figure 74. XPS survey spectra of (a) PEDOT:PSS/ITO/PET, (b) Lg/PEDOT:PSS/ITO/PET, (c) Mo/PEDOT:PSS/ITO/PET and (d) Mo/Lg/PEDOT:PSS/ITO/PET. 163

Figure 75. Deconvoluted core level spectra of (a) C1s, (b) O1s, (c) S2p and (d) Mo3d of a Mo/Lg/PEDOT:PSS/ITO/PET film. 164

Figure 76. Cyclic voltammograms of (a) PEDOT:PSS/ITO/PET, (b) Lg/PEDOT:PSS/ITO/PET and (c) Mo/PEDOT:PSS/ITO/PET at different scan rate in 0.1 M $HClO_4$.....166

Figure 77. Plots of peak currents *versus* square root of scan rates (a) Lg/PEDOT:PSS/ITO/PET.....167

Figure 78. CV curves of (a) Mo/Lg/PEDOT:PSS/ITO/PET at different scan rate in 0.1 M $HClO_4$, (b) Lg, Mo, Lg/Mo composited with PEDOT:PSS on ITO/PET and pristine PEDOT:PSS/ITO/PET at 20 mV s^{-1} in 0.1 M $HClO_4$.....169

Figure 79. GCD curves (a) PEDOT:PSS/ITO/PET, (b) Lg/PEDOT:PSS/ITO/PET (c) Mo/PEDOT:PSS/ITO/PET and (d) Mo/Lg/PEDOT:PSS/ITO/PET at different current density in 0.1 M $HClO_4$. 171

Figure 80. (a) A plot of potential *versus* time of Mo/PEDOT:PSS, Lg/PEDOT:PSS and Mo/Lg/PEDOT:PSS at 1.0 A g^{-1} (b) the specific capacity of electrodes at different current density. 173

Figure 81. (a) CV curves at a scan rate of 20 mV s^{-1}, (b) GCD curves at a current density of 0.5 A g^{-1} and (c) columbic efficiency of PEDOT:PSS, Lg/PEDOT:PSS, Mo/PEDOT:PSS and

Mo/Lg/PEDOT:PSS on ITO/PET.....175

Figure 82. Cycle life of all devices and the inset is the GCD curves of the first five cycles and the last five cycles for Lg/Mo/PEDOT:PSS/ITO/PET. 177

Figure 83. The Ragone plots of this work and values for previously reported supercapacitor devices. .178

List of tables

Table 1. Fuel cell type. 17

Table 2. Kinetic parameters for oxygen reduction on PEDOT:PSS/Pt, PEDOT:PSS(EG)/Pt, and rGO/PEDOT:PSS(EG)/Pt (30%) in 0.1 M $HClO_4$ at 1600 rpm. 110

Table 3. Comparison of the kinetic parameters of the electrocatalyst materials for ORR. 119

Table 4. Natural charges obtained from the natural bond orbital (NBO) analysis in the dimers and dimer O_2 complexes (where the binding site in all dimers is C_8-C_9), calculated using B3LYP/6-311++G(d,p)/PCM/water calculations. Other possible binding sites are also shown in *bold-italic* fonts 131

Table 5. Change in Gibbs free energy of formation, ΔG_f (kcal mol^{-1}), equilibrium interatomic Distances (Å) between the oxygen atoms, r(O=O), and the carbon atoms, r(O-C), in the dimers and dimer-O_2 complexes 133

Table 6. Tafel slopes and exchange current densities for the ORR at GC/rGO, GC/8-ANSA, and GC/8-ANSA/rGO. 143

Table 7. Comparison of materials and specific performance of the catalyst in 0.1 M KOH. 144

Table 8. Comparison of our result with some reported values of PEDOT based electrodes. 155

Table 9. Comparison of values in our work with reported symmetric supercapacitor devices. 160

1. Introduction

1.1 Background

Energy is one of the most important issue in the modern world. The cost and availability of energy have a significant impact on our quality of life, the health of national economies, relationships between nations, and the stability of our environment. Access to energy and its consumption per inhabitant could be used as a comparative tool for nations' prosperity and technological developments[1, 2].

A fast-growing world population (8.8 billion around 2035), rapid change of living standard in many countries like China and India (one-third of the world population), and the hunger for fuel that has developed as a consequence have led to a rapid rise in the need for energy. Such ever-increasing demand could place a significant strain on the current energy infrastructure[1, 3, 4] and has also an economic impact. Historical and current energy systems are heavily dependent on fossil fuels (coal, oil, and gas) which are millions of years of solar energy stored in the form of chemical energy generated through the photosynthetic process in nature[1]. However, eight countries have 81% of all world crude oil reserves, six countries have 70% of all-natural gas reserves and eight countries have 89% of all coal reserves[4]. The massive use of traditional fossil fuels by modern society resulted in global warming, climate change, emission of pollutants (e.g. CO, NOx), and rapid depletion of precious resources[5, 6]. Therefore, clean, efficient and environmental-friendly alternative energy resources should be integrated with the current energy

system to address energy insecurity in the future, reduce environmental damage, minimize inequality and safeguard damage on global economic growth[4].

Systems for electrochemical energy storage and conversion (batteries, fuel cells, and electrochemical capacitors (ECs)) are promising alternative energy/power source to minimize the problem faced today as long as these energy devices are designed to be more sustainable and more environmentally friendly[7].

The Ragon plot (Figure 1) compare the current status of different electrochemical devices in terms of their energy and power performance. It is found that batteries and fuel cells have a low power density and high energy density whereas conventional capacitors have a high power density with a low energy density. Supercapacitors are located between batteries and traditional capacitors. Each of these stand-alone technologies by themselves lack the requisite qualities to meet the commercial needs that have been shaped by the consumption of fossil fuels. Consequently, hybrid energy storage devices that strive to advance along the diagonal of a so-called Ragone plot, by combining the high power characteristics of supercapacitors with the high energy content of rechargeable batteries in the aqueous and organic electrolyte are named supercaptteries as observed in Figure 1 (I and J)[8].

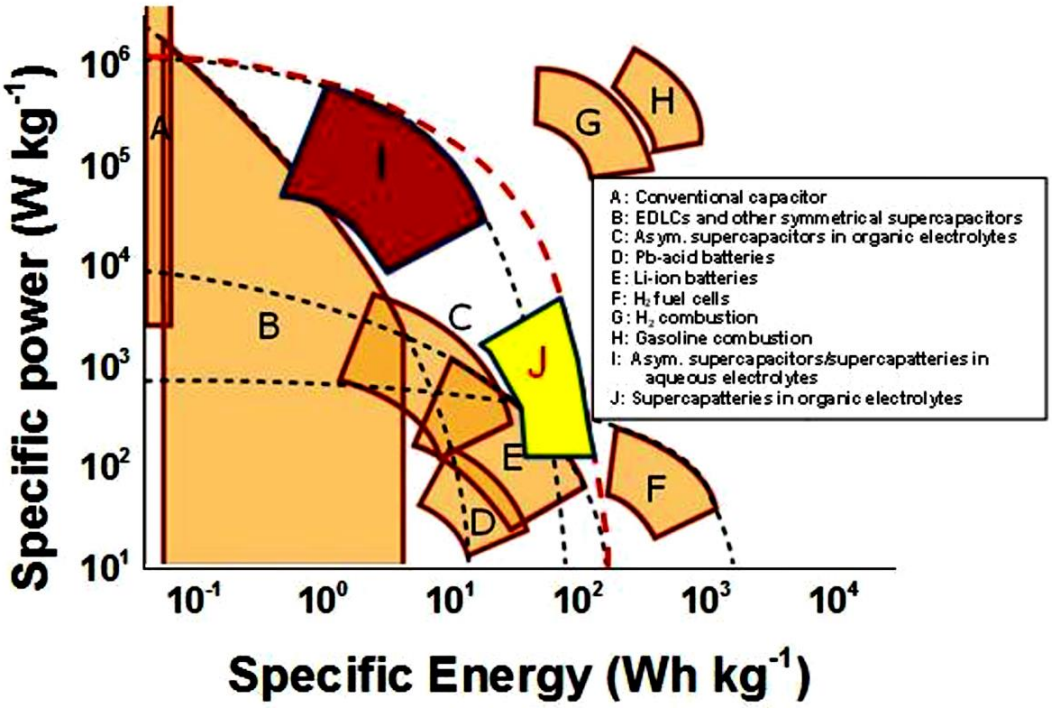

Figure 1. The Ragone plots of various electrochemical and internal combustion power devices[8].

Electrochemical devices have demonstrated the capacity to satisfy sustainable, clean, practically viable and affordable technological requirements of the modern society. However, the commercial success of these technologies have technical challenges. For example, cost reductions and durability improvements must be sufficiently achieved to make polymer electrolyte fuel cells (PEFCs) commercially competitive with conventional technologies, such as the internal combustion engine used in transportation applications. Although several functional components work in PEFCs to produce electricity, the majority of cost and durability issues arise from the cathodic electrochemical oxygen reduction reaction (ORR)[9]. As a result, the development of effective and efficient electrocatalysts at the cathode has received comparatively greater research and developmental attention as compared with the electrocatalysts at the anode.

At present, platinum is well known to exhibit the best ORR performance in both acidic and alkaline media. However, serious deficiencies resulted from poisoning of the active sites due to methanol crossover (methanol transport from anode to the cathode side), as well as catalyst ripening and dissolution practically inhibit the catalytic activity. Furthermore, the high cost and scarcity of this metal limit its broad applicability and commercialization on a mass scale. Thus, research should be focused on low platinum loading or platinum-free catalyst that are cost-effective with high performance, and excellent durability for electrocatalytic oxygen reduction[9, 10]. Metal-free carbon-based materials showed many advantages compared to metal-containing electrocatalysts, such as widely available precursors, environmentally friendly, strong resistance to the poisoning of CO and methanol crossover[11]. At the current stage of technology, carbon-supported Pt and Pt-based alloy catalysts are the most active and stable catalysts for an ORR, which have been used for fuel cell cathodes. It is widely accepted now a days that nanoparticles tend to show better catalytic performance than their bulk counterpart because of their smaller particle size, as well as the "nano-effect", originated from the small size[12, 13]. One of the most widely used techniques for maximizing the performance of Pt-based electrocatalysts is to load Pt nanoparticles (Pt-NPs) onto supporting nanomaterials to obtain supported catalysts that are less costly and have a large specific surface area, good conductivity, high catalytic activity, and high stability.

The supporting matrix, which determines the distribution and stability of catalyst Pt-NPs on the surface, plays an important role in the performance of the electrocatalyst. Therefore, the structures and properties of the catalyst support have a significant effect on both the activity and the durability of the supported catalysts[14, 15]. An ideal Pt catalyst support material needs to have

several properties including high surface areas, electronic conductivity, electrochemical stability, strong cohesion to catalyst particles, and the ability to homogeneously distribute uniformly sized nanoparticles[9, 14].

Vulcan carbon (VC) has been widely used as support for Pt-NPs, due to their high availability, high conductivity, low cost, large surface area, and pore structure. However, it suffers from thermo-chemical instability and corrosion caused by electrochemical oxidation under fuel cell operating conditions[14, 16, 17]. Hence, to mitigate for potential degradation effects and the subsequent aggregation of Pt-NPs, various alternatives have been introduced as potential alternative electrocatalyst supports. One of the possible options is to use highly graphitic carbon materials, such as carbon nanofibers, nanotubes, nanohorns, and graphenes. These carbon materials show far more resistant toward degradation, given the relatively small number of edge plane sites, which act as reactive centers for carbon oxidation[17, 18]. Conducting polymers (CPs) are also useful supports for the dispersion of platinum metal catalysts, due to their high accessible surface area, prevention of particle agglomeration, low resistance, and high stability in three-dimensional structure [17, 19].

The synthesis methods or procedures for Pt supported nanoparticles have a significant influence on the composition, structure, and other properties of the catalysts, which would, therefore, affect their catalytic activity and stability[12]. In order to achieve high ORR activity and stability of the electrocatalysts, many synthesis methods have been explored. The currently employed synthesis methods includes wet impregnation[20, 21], colloidal[13, 22], microemulsions[23], magnetic sputtering[24, 25], microwave irradiation[26-28], polyol process[29, 30] and electrochemical deposition[31, 32]. The

electrochemical deposition is an efficient method for the preparation of metal particles and it is widely used with different strategies/methodologies, such as cyclic voltammetry[33], potential step deposition[34], galvanostatic[35], potentiostatic[36] and pulsed electrodeposition[32, 35].

The recent rapid development of portable and flexible electronics in modern society requires flexible supercapacitors (FSCs), which are foldable, stretchable, and/or bendable, with large energy and power density. Consequently, future developments of supercapacitors are moving toward thinner, lighter, and cheaper solutions, as many existing supercapacitors are still too bulky and heavy for their intended applications[37, 38]. The intrinsic flexibility of conducting polymers has made them favored materials in flexible and lightweight energy storage devices, which play an important role in future portable and wearable electronic devices[39]. Among CPs, PEDOT:PSS, is a suitable material for FSCs owing to its excellent flexibility, tunable conductivity, and its high environmental stability. Furthermore, PEDOT:PSS dispersions are commercially available for roll-to-roll mass production on a flexible substrate[38, 40, 41].

1.2 Objectives of the study

1.2.1 General objective

The main objective of this work is to develop efficient, stable, and cheap materials from carbon-based, biopolymer, conducting polymer, transition metals, and their nanocomposite for use in fuel cell electrocatalysis for the oxygen reduction reaction and flexible supercapattery.

1.2.2 Specific objectives

The specific objectives of this work are to:

1. develop and investigate platinum catalyst support material from PEDOT:PSS and rGO composite with high stability and electocatalytic activity for oxygen reduction reaction.
2. develop and characterize metal-free catalysts from graphene materials and amino-substituted naphthalene sulfonic acid for oxygen reduction reaction.
3. construct homemade, flexible, cheap, and scalable PEDOT:PSS based roll-to-roll printed electrode material applicable for supercapattery.
4. modify the home-made large area electrodes with biopolymers lignin and phosphomolybdic acid for supercapattery.
5. investigate and optimize the energy storage capacity of the flexible electrodes in supercapattery using aqueous and gel electrolyte.

2. Literature review

2.1 Conducting polymers and their composites

In the 21st century, the use of polymers moves from primarily passive materials such as coatings and containers to active materials with useful optical, electronic, energy storage, and mechanical properties as a result of the discovery of electronically conducting polymers. These new class of polymers possessing high electronic conductivity in the partially oxidized (or, less frequently, in the reduced) state was discovered by three collaborating scientists, Alan J. Heeger, Alan G. MacDiarmid and Hideki Shirakawa for which they received the Nobel Prize in Chemistry in 2000[42, 43]. Since the first report of doping of polyacetylene in 1977 by these group[44], various important electronically CPs have been investigated continuously, including polypyrrole (PPy), polyaniline (PANI), polythiophene (PT), poly(3,4-ethylenedioxythiophene) (PEDOT), trans-polyacetylene, and poly(p-phenylene vinylene) (PPV)[45]. Figure 2 shows the structure of common electronically conducting polymers and their composite materials.

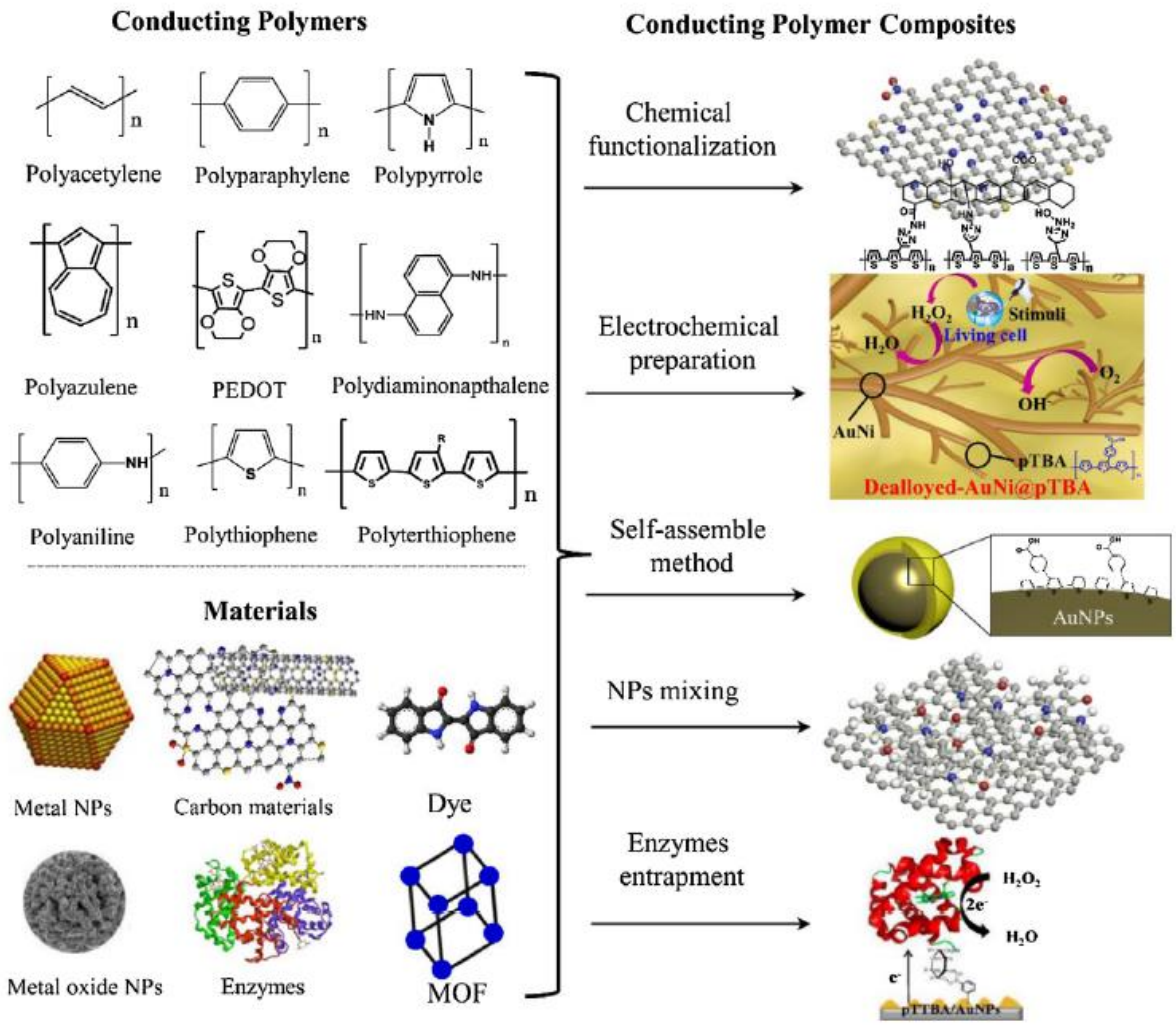

Figure 2. Conducting polymers and their composite materials[46].

The common feature of an electronically conducting polymer is the presence of alternating single and double bonds along the backbone of polymer (Figure 3). Every bond contains a strong localised "sigma" (σ) bond while every double bond contains a sigma and less strongly localised "pi" (π) bond which is weaker. The overlap among the p-orbitals in the series of π -bonds allow the electrons to be more easily delocalized and move freely between the atoms. However, conjugation is not enough to make the polymer material conductive. CPs should be doped using different methods (chemical, electrochemical and photo) in order to achieve high conductivities.

Un-doped polymers have been reported as insulators but, upon doping, their conductivity can change from insulating to metallic[43, 45, 47]. Through doping, the polymer undergo redox processes and form charge carriers. The electrical conductivity results from the existence and the ability of those charge carriers to move along the π-bonded highway[48].

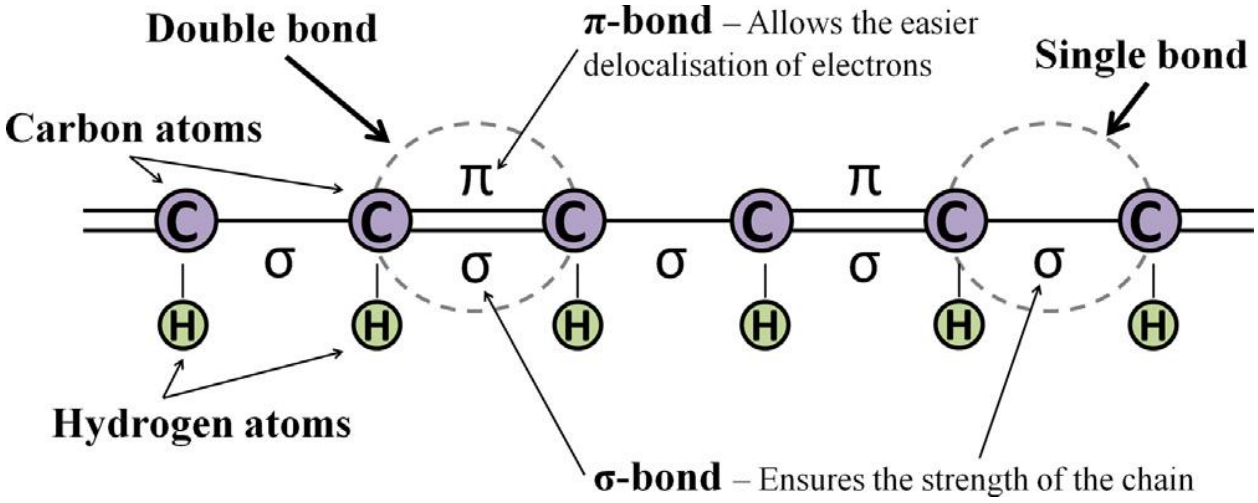

Figure 3. A simplified schematic of a chain containing alternating single and double bonds[47].

In contrast, redox conducting polymers contain electrostatically and spatially localized redox sites which can be oxidized or reduced, and the electrons are transported by an electron exchange reaction (electron hopping) between neighboring redox sites[42].

There are currently two main methods for synthesizing conductive polymers: chemical and electrochemical. During chemical synthesis the monomer solution is mixed with relatively strong chemical oxidants like ferric chloride, ammonium persulfate and hydrogen peroxide. This

process is simple and creates a powder or a thick film of the polymer, and allows its bulk production, which makes it the method of choice for commercial applications[43, 47].

Electrochemical polymerization occurs by applying an electrical current through electrodes placed into a solution containing the monomer of the polymer, the solvent and the doping agent. The synthesis of a polymer by electrochemical polymerization occur if its monomer can undergo oxidation/reduction in the presence of an electrical potential. The electrical current causes the monomer to deposit and oxidize/reduce on the positively/negatively charged working electrode, forming insoluble thin film of the polymer with a well-controlled thickness (down to 20 nm) and morphology. The electrochemical deposition can be carried out using three techniques: the galvanostatic (constant current), the potentiostatic (constant potential) and potentiodynamic methods (sweep potential)[47].

To enhance the activity and/or improve the stability of conducting polymer (CP), CP composites can be prepared from metal nanoparticles, enzymes, metal oxide nanoparticles, etc (Figure 2). Vapor polymerization, chemical functionalization, *in situ* polymerization, solution processing are among the different method used to prepare CP composite[46, 49].

Conducting polymers and their composites are attractive materials for various applications, such as electrochromic devices, light emitting diodes (LED), printed circuit boards, fuel cells, energy storage devices in batteries and supercapacitors, sensor materials, ion-exchanger membranes, corrosion protective coatings, and others[42, 50, 51].

2.2 Graphene and its family

Graphene is one atom thick single carbon layer packed into a two-dimensional (2D) honeycomb lattice and is a basic building block for graphitic materials of all other dimensionalities (Figure 4). It can be wrapped up into 0 D fullerenes, rolled into 1D nanotubes, or stacked into 3D graphite[52].

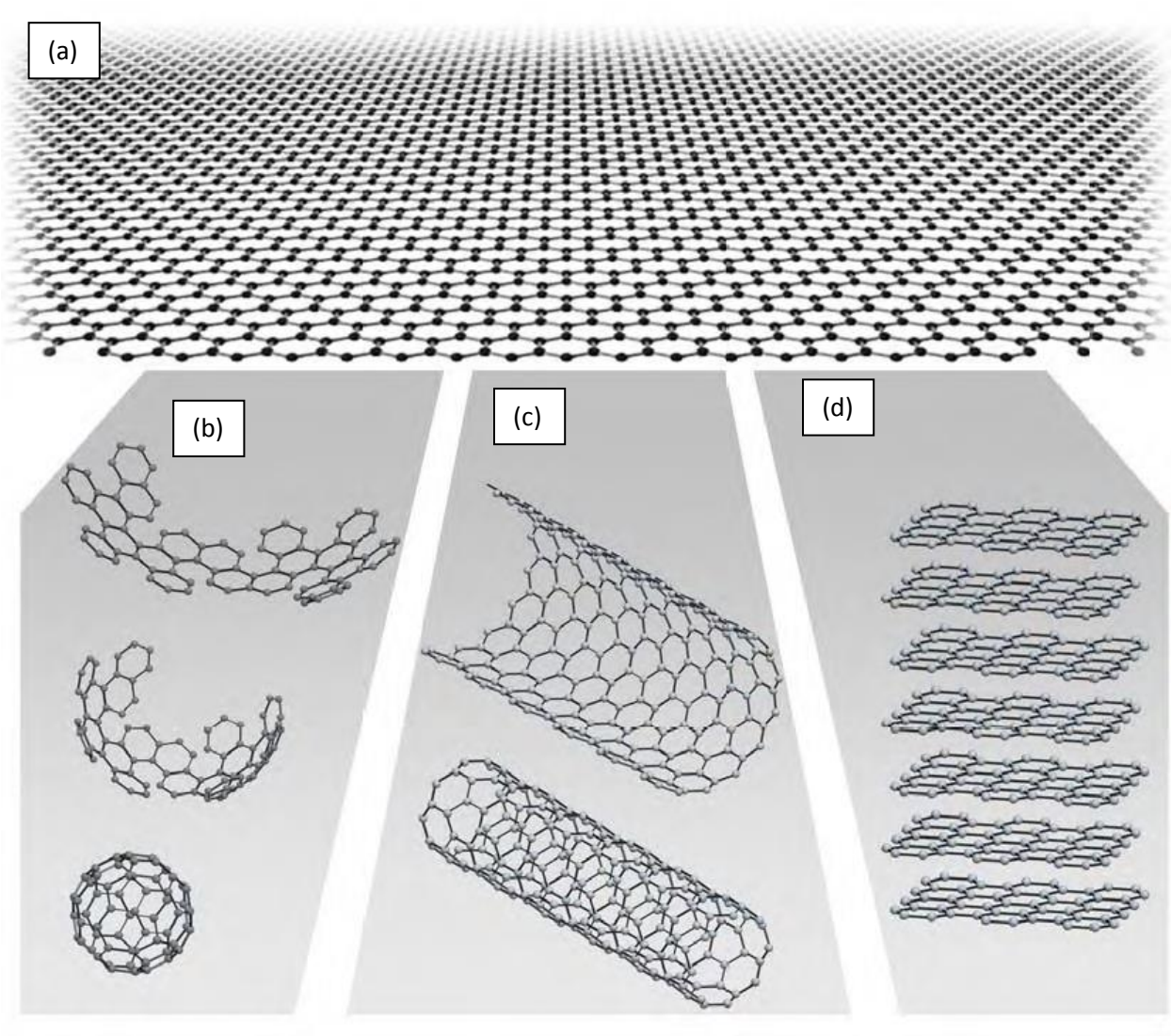

Figure 4. The structure of (a) graphene, (b) buckyballs, (c) carbon nanotubes and (d) graphite.

The theory of the building block of graphite as one atomic layer later called graphene was laid out for the first time in 1947 by P. R. Wallace[53]. The name graphene was first coined by Boehm et al. in 1986 but in 1997 IUPAC formalized and incorporated into their Compendium of Chemical Technology[54]. In 2004, two scientists who had emigrated from Russia, Andrei Geim and Kostya Novoselov, at Manchester University successfully identified single layers of graphene in a simple tabletop experiment. Previously graphene was considered to be thermodynamically unstable and could exist only as an integral part of larger 3D structures, usually grown epitaxially on top of monocrystals with matching crystal lattices[52, 55]. This single atomic layer carbon has remarkable properties, such as high surface area, good thermal conductivity, outstanding electrical conductivity, mechanical flexibility, chemical stability and optical transparency. Because of these fascinating properties, graphene and graphene-based composites have attracted increasing research interest for various application including energy conversion and storage (e.g., fuel cells and capacitors), sensors, electrocatalysis and electronic devices[56].

Mechanical exfoliation[57, 58], chemical vapor deposition[59, 60], a self-assembled template of surfactants[61], liquid-phase exfoliation of graphite[62], ball-milling synthesis[63], electrochemical exfoliation of graphite[64-67] and reduction of graphene oxide (GO) that derived from chemical exfoliation of graphite[68-72] are the most commonly used methods to synthesize graphene. Among these, mechanical exfoliation and chemical vapor deposition (CVD), have the advantage of preparing graphene with high quality and large area. However, high temperature and explosive gases of H_2 and CH_4 are usually required in the CVD method while mechanical exfoliation is a very sophisticated and time-consuming process[71, 73].

Oxidation of graphite, like modified Hummers' method, in which graphite is firstly oxidized with strong oxidant to graphene oxide (GO) flakes, followed by chemical or thermal reduction could realize low-cost, large-scale production of graphene. However, these method uses strong acids (e.g., H_2SO_4, HNO_3) and oxidants (e.g., $KMnO_4$, $K_2S_2O_8$, H_2O_2) to produce decorated plane of carbon atoms (Figure 5) by oxygen-containing groups which expand the interlayer distance and make the atomic-thick layers hydrophilic. Therefore, this layer can be exfoliated in water under moderate ultrasonication. If the exfoliated sheets contain only one or a few layers of carbon atoms like graphene, these sheets are named graphene oxide (GO). The carcinogenic reductant like hydrazine is required in these chemical methods to reduce GO to rGO. The graphene products usually retain more defects with uncontrollable geometrical shapes[67]. Graphene exfoliated using electrochemical methods is of high quality and has few defects. Besides, the method is simple, easily scalable, and cost-effective, and most importantly allowing the tuning of the level of oxidation[66, 67].

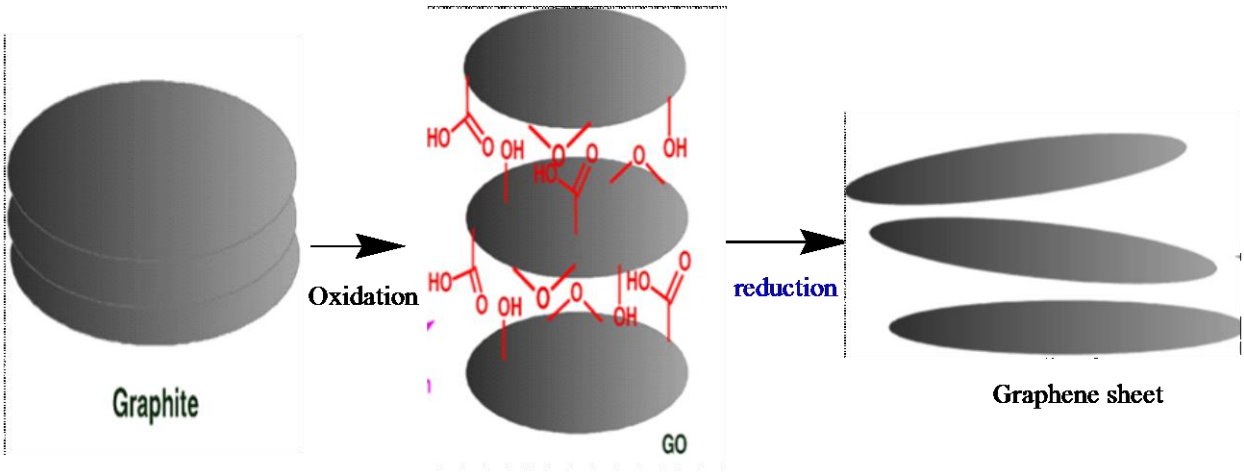

Figure 5. A simple route for the preparation of graphene sheets from graphite[55].

Reduced graphene oxide (rGO) sheet shows low dispersibility in solvents and tends to restack as a graphite-like structure as a result of the removal of most of the oxygen functionalities. This aggregation of the rGO sheets reduces the available surface area and limits electron and ion transport which reduces the performance of the sheet[55, 74-77].

2.3 Biopolymer-Lignin

Lignin is a highly branched, three-dimensional phenolic polymer with a wide variety of functional groups and the second abundant biopolymer after cellulose in wood cells. Lignosulfonate (LS) is the main derivative of lignin and a byproduct of sulfite process during paper making from wood pulp. This cheap and green material is reach in phenol group which can store electrical energy by switching between the benzoquinone and hydroquinone states (Figure 6). Since LS is stable in its hydroquinone state, the molecule can be oxidized to a benzoquinone state by applying a positive potential. However, LS is insulator and LS conducting composite material that enable charge transport should be prepared first in order to use as electrode material[78-80].

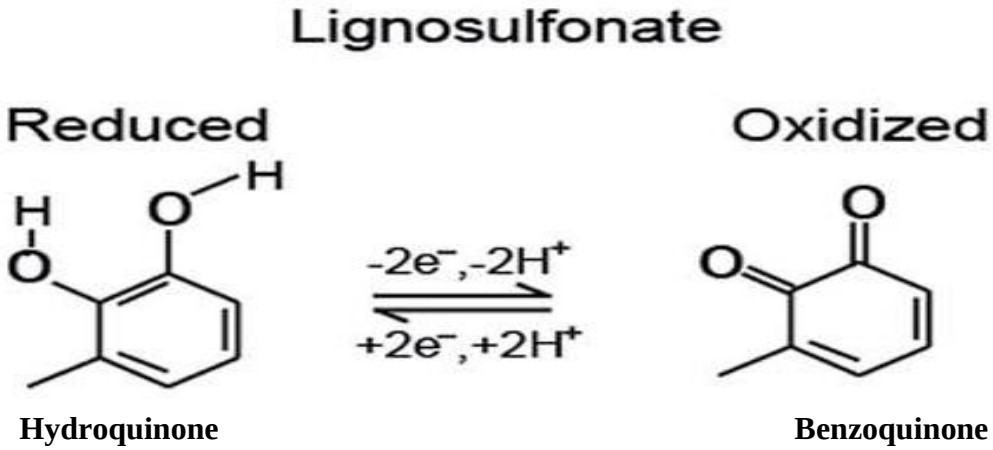

Figure 6. The structural transformation between hydroquinone/benzoquinone state in LS.

2.4 Oxygen reduction reaction

Oxygen reduction reaction (ORR) is an essential and significant electrochemical reaction in many energy-conversion devices, such as fuel cells and metal-air batteries. However, the efficiency and performance of such devices are restricted by the sluggish kinetics of this reaction that is caused by the difficulties in O_2 adsorption on the electrode surface, O–O bond activation/cleavage and oxide removal[18, 81-83].

A fuel cell (FC) converts chemical energy into electrical energy by a redox process which oxidizes a fuel at the anode and reduces oxygen gas (oxidant) at the cathode cleanly and efficiently using hydrogen or hydrocarbons as the fuel and produces water as its by-product[4, 10]. They are more efficient in converting energy to electricity (work) than internal combustion engines and most combustion systems. The 19th century and the 20th century was known as the age of the Steam and Internal Combustion Engine, respectively. Similarly, some believe the 21st century will be the age of the FCs because they are much in the news since they appear to be one of the most efficient and effective solutions to environmental problems that we face today (global warming, air pollution, acid precipitation, ozone depletion, forest destruction, and emission of radioactive substances)[4].

Fuel cells are usually classified by their operating temperature and the type of electrolyte they use. Proton exchange membrane fuel cell (PEMFC), alkaline fuel cell (AFC), phosphoric acid fuel cell (PAFC), molten carbonate fuel cell (MCFC) and solid oxide fuel cell (SOFC) are classified based on the electrolyte used in the FCs. State-of-the-art fuel cell electrolytes are

listed in Table 1, along with the mobile ionic species, temperatures of operation, and fuels typically utilized. PEMFC and AFC are low-temperature fuel cells that have an operating temperature lower than 100^{o}C. The medium temperature fuel cells have an operating temperature between 100 and 300^{o}C. This type includes PAFC. High-temperature fuel cells have an operating temperature between 600 and 1000^{o}C and include the MCFC and the SOFC. A higher temperature is preferred for higher efficiency and greater fuel flexibility of FCs due to better electrode activity, but for portable (intermittent) power applications, lower temperature operation is typically favored as it enables rapid start-up and minimizes stresses due to thermal cycling. To avoid corrosive liquids used as an electrolyte, fuel cell developers preferred solid oxide and polymer electrolyte fuel cells over alkali, phosphoric acid, or molten carbonate fuel cells. Nevertheless, each of the fuel cell types listed in Table 1 has been demonstrated in complete fuel cell systems, with alkali and phosphoric being the most mature technologies, and polymer electrolyte membrane fuel cells the most recent[10, 84].

Table 1. Fuel cell type[84, 85].

Fuel cell	Electrolyte	Fuel	Temperature (^{o}C)	Mobile ion
PEMFC	Sulfonated polymers (Nafion)	H_2 or CH_3OH	70-100	H^+
AFC	KOH (aq)	H_2	60-90	OH^-
PAFC	H_3PO_4	H_2	150-220	H^+
MCFC	Molten (Li, Na, K)$_2CO_3$	Hydrocarbons, CO	600-700	CO_3^{2-}
SOFC	Yttria (Y_2O_3)-stabilized zirconia (ZrO_2)	Hydrocarbon, CO	650-1000	O_2^-

Metal-air batteries generate electrical power as a result of redox reaction between a metal negative electrode (anode) and an air-breathing positive electrode (cathode) through an aqueous or aprotic electrolyte. Like low temperature fuel cell, the cathode structure of the metal air batteries includes the current collecting layer, the gas diffusion layer and catalyst layer. The metal anode gets oxidized to produce metal ions (M^+) that move through the electrolyte to the cathode and react with O_2 to form metal oxides[86-88]. Lithium-air (Li-air) batteries, sodium-air (Na-air) batteries, aluminum-air (Al-air) batteries, magnesium-air (Mg-air) batteries, and zinc-air (Zn-air) batteries are among the various metal-air batteries[86].

Compared with the anode, the overpotential of the cathode in fuel cells and metal air batteries is high due to strong kinetic inhibition of oxygen reduction reaction. This leads to cell voltage losses. The low rate for ORR at the cathode is a limiting factor in the efficiency of these devices. Besides, oxygen reduction can also occur through an intermediate two electrons, H_2O_2 route, which can limit the efficiency of the cell[10, 89, 90]. Therefore, implementing fuel cells and metal air batteries in our daily life requires highly effective, but low-cost, electrocatalysts to efficiently reduce O_2. The term electrocatalysis is a specific form of catalyst that functions in electrochemical reactions that depend strongly on the nature of electrode material and applied to those electrochemical reactions that start from dissociative chemisorption or a reaction step in which the electrode surface is involved. The electrode potential is an important adjustable variable that can produce dramatic changes in the rate of the electrocatalytic reactions which enable for handling the selectivity of electrocatalytic processes[91].

2.4.1 Reaction pathways for ORR

ORR involves several elementary steps and various reaction intermediates. An atomic-level understanding of the ORR mechanism is still in its early stages because of the high complexity of ORR kinetics. The reaction proceeds by either four-electron pathways or by two-electron pathways depending on the electrode materials as well as on the reaction conditions such as solution pH and electrode potential[18, 92].

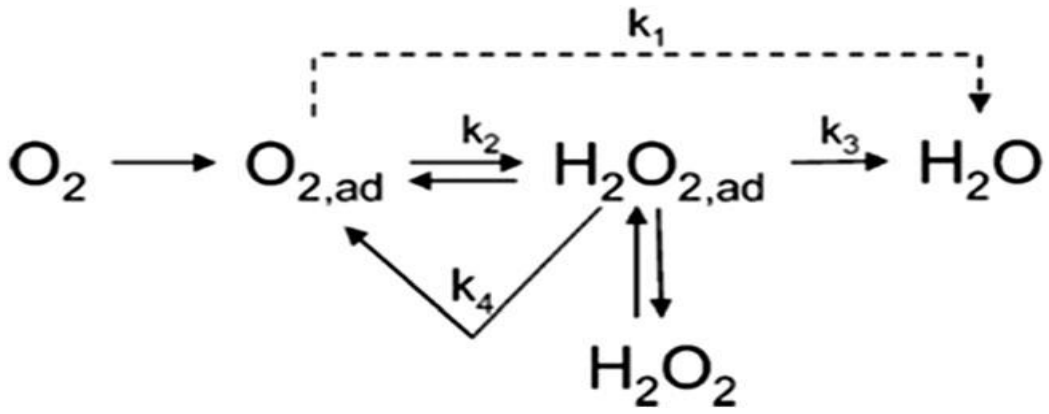

Figure 7. Simplified reaction scheme for the oxygen reduction reaction[92].

Figure 7 represents a simplified reaction scheme for the ORR in acid media. According to the mechanism above, k_1 is a 'direct' reaction pathway involving a four-electron transfer forming H_2O with no intermediates. However, k_2 describes the reaction pathway whereby O_2 is first transformed to H_2O_2 by a two-electron transfer and may be further reduced to H_2O *via* k_3; if these reactions occur consecutively, this is known as the 'series reaction pathway'. The H_2O_2 intermediate may also be desorbed or disproportionate chemically *via* k_4. If the reaction involves the combination of a 'direct' reaction pathway (*via* k_1) and series reaction pathway'(*via* k_2 and k_3) it is called a ''parallel'' pathway. In a dissociative mechanism, the chemisorbed O_2 involves

the splitting of the O–O bond and the hydrogenation of atomic O to OH and H_2O whereas an associative mechanism involves direct proton/electron transfer to it and to OOH, which breaks into O and OH as shown in Equations (1) and (2), respectively[18, 92, 93].

$$\frac{1}{2}O_2 + * \rightarrow O* \xrightarrow{e^- + H^+} HO* \xrightarrow{e^- + H^+} H_2O + * \quad (1)$$

$$O_2 + * \xrightarrow{e^- + H^+} HOO* \xrightarrow{e^- + H^+} H_2O + O* \xrightarrow{e^- + H^+} HO* \xrightarrow{e^- + H^+} H_2O + * \quad (2)$$

where * represents the catalytically active sites.

The associative mechanism (Equation 2) involves three different intermediates, namely, *OOH, *O, and *OH, while the dissociative pathway only involves *O and *OH [94]. In principle, one would want a catalyst to reduce oxygen molecules by a process that is dominated by the four-electron pathway to the water. Nevertheless, the reduction of oxygen to H_2O_2 is unavoidable during the ORR process and related to factors such as defects, active site densities, and/or interparticle distances[93].

O_2 reduction pathways were affected to a great extent by the O_2 adsorption modes on catalyst surfaces. To study the oxygen reduction mechanism, it is crucial to know the nature and coverage of adsorbed reaction intermediates. However, there is no simple adequate spectroscopic method for identifying adsorbed intermediates. The most active catalyst for the ORR is the one that exhibits intermediate binding to its intermediates as it was first proposed by a French chemist called Paul Sabatier[95]. The idea behind this principle is that a desirable catalyst should bind atoms and molecules with an intermediate strength: not too weakly to be able to

activate the reactants, and not too strongly to be able to desorbs the product[96]. The Sabatier principle is readily illustrated in a so-called volcano plot (Figure 8) which has some measure of the catalytic rate on the ordinate and the stability of the intermediate (bond strength) on the abscissa[96, 97].

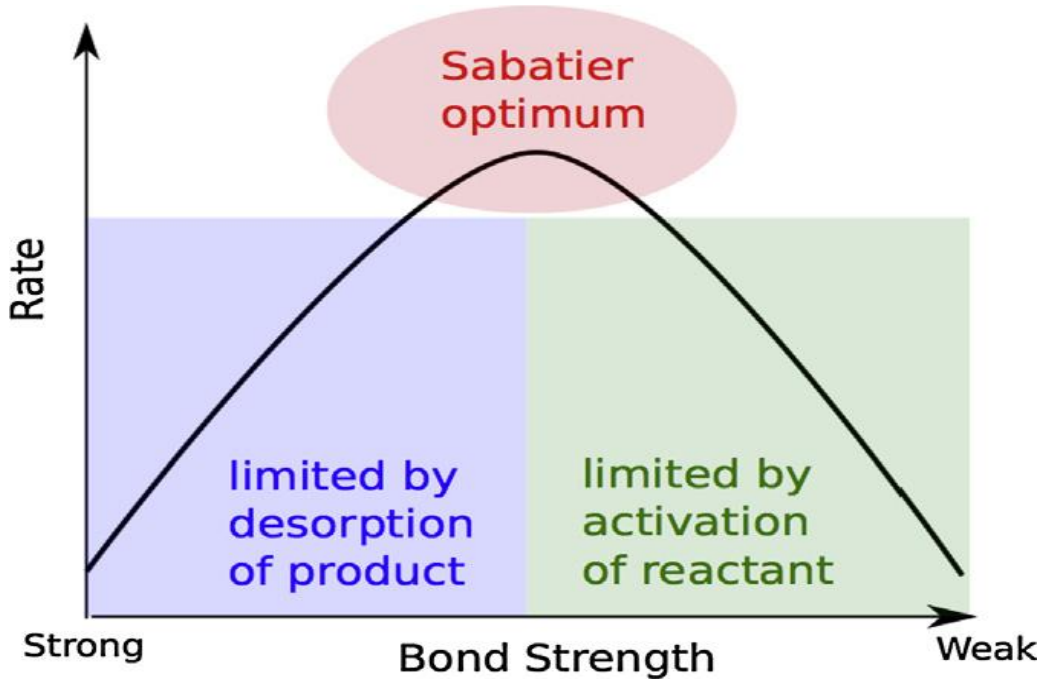

Figure 8. Schematic representation of the qualitative Sabatier principle [96].

The above picture provides a general qualitative understanding of the optimum catalyst requirement but does not specify the bond strength that corresponds to the optimum catalyst. For these reasons, the Sabatier principle cannot be used as a basis for catalyst design rules. The advent of computational electronic structure methods that are efficient enough to treat reactions on metal surfaces and accurate enough to have predictive power has significantly changed the availability of systematic data for adsorption energies and activation energies for surface chemical reactions[96].

2.4.2 Theoretical studies on the ORR in fuel cells

In order to derive the mechanism behind the ORR, screen better electrocatalysts, and improve the catalytic activity, it is important to determine the nature and the coverage of reaction intermediates using computational study, which is almost impossible with spectroscopic methods. In the past few years theoretical modeling studies in electrocatalyst materials which are enabled by better computational algorithms and fast computational facilities complement experimental study and shed light on detailed surface phenomena, the formation of intermediates, and the activation energies related to elementary reaction steps and provided a better understanding of ORR mechanisms. Methodologies that employ structure-activity relationships such as adsorption energy, activation energies, and d-band centers have shown encouraging results in identifying better electrocatalysts. The major issue with the theoretical study of ORR is how to model the interface effectively. Therefore, better models and methodologies need to be developed to study electrochemical systems[98, 99]. There are three adsorption models for molecular oxygen adsorption which are Griffiths, Pauling, and Yeager (bridge) models.

Griffiths model

In this model, O_2 interacts with two bonds with a single substrate atom. This type of bonding can be viewed as rising from two contributions: (1) σ-type bonding is formed by overlapping between π- orbitals of O_2 and empty d_z^2 orbitals on the metal surface atom, (2) π back bond from the partially filled d_{xy} or d_{yz} orbitals of the metal to the antibonding π^* orbitals of O_2.

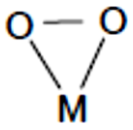

Pauling model

In this model, end on adsorption through a single σ type bond with a σ orbitals of O_2 donates electron density to an acceptor d_z^2 orbitals on the metals.

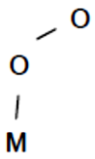

Bridge (Yeager) model

This model involves the formation of a bridge bonded structure formed by the interaction between the oxygen sp^2 orbitals and the partially filled d_{xy} or d_{yz} orbitals of the two surface atoms principally for the reaction on platinum metals.

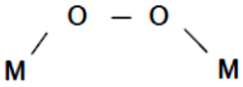

Yeager adsorption is typically followed by oxygen bond dissociation, where the oxygen reduction proceeds exclusively through the direct route. Four electron reduction reactions takes place in the case of Griffiths and Bridge models, while parallel two and four electrons reduction simultaneously take place in the Pauling model[99, 100].

The knowledge established by experimental investigations and computational studies is important for understanding the ORR activity trends on various metal or carbon-based catalysts,

so as to get guidance for the development of effective ORR electrocatalysts. Computational studies can provide insights regarding intermediates, their geometries, and energies[99].

2.4.2.1 Understanding the electrocatalysis of oxygen reduction on metal catalyzed reaction

Based on possible pathways for ORR, researchers dedicated to find the rate-determining step (RDS), and understand the sequence of electron transfer and proton transfer. Different computational studies predicted that ORR on metal catalysts are mainly hindered (rate-limiting) by three steps: (1) the first electron transfer of ORR[101]; (2) the hydration of oxygen[102, 103]; and (3) a recently wider accepted adsorption of intermediate species such as *OOH, *O, and *OH[94, 104]. Thus, it is reasonable to investigate the oxygen adsorption energy (ΔE_O) and search a catalyst surface with the optimal adsorption energy for every intermediate to achieve the best catalytic activity. The binding energies of all the intermediates in ORR are governed by a linear scaling relation (LSR) between ΔE_O and ORR activity. LSR refers to the phenomenon whereby moving toward stronger adsorption of OOH* (one intermediate) to facilitate the dissociation of O_2 molecule will result in a less favored subsequent reduction and desorption of OH* (another intermediate). On the other hand, a surface with weaker adsorption of OOH* that promotes OH* desorption will result in difficulty for O_2 adsorption. Therefore, based on an LSR, an ideal catalyst should have a surface that adsorbs all intermediates neither too weakly nor too strongly. This phenomenon yields the well-known volcano-shaped plot of catalytic activity as a function of different catalyst surfaces, as shown in Figure 9[93, 105].

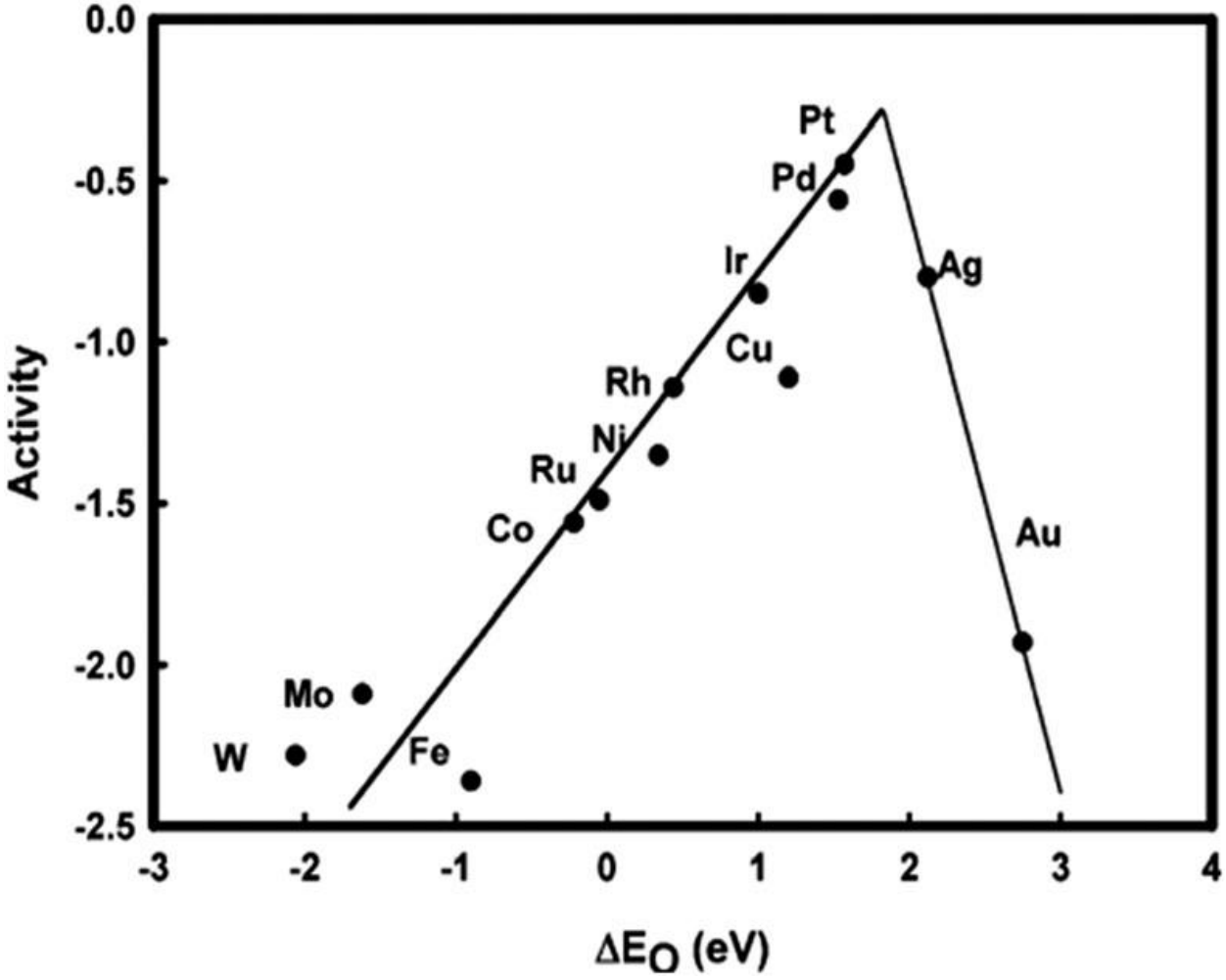

Figure 9. Trends in oxygen reduction activity[104].

The volcano plot in Figure 9 indicates that there was some room for improvement. The most active catalyst (peak of the volcano plot) should exhibit somewhat lower oxygen binding energy than platinum to its intermediates, *OOH, *O, and *OH. In principle, a number of different metal alloy surfaces satisfy this requirement and could be a candidate but almost all metals are thermodynamically unstable at the working conditions of cathodes PEM fuel cell. Consequently, the vast majority of research into ORR catalysis has been focused on Pt and its alloys, as they constitute the only class of materials that are both active and stable[95].

2.4.2.2 Origin of the electrocatalytic oxygen reduction activity of graphene-based catalysts

More insights into the chemistry of graphene and its catalytic performance in the ORR can be gained utilizing theoretical modeling of this process. Understanding the role of catalytic surfaces and the nature of intermediates involved in the ORR is very important for understanding the pathway and mechanism of ORR electrocatalysis[106, 107]. Yan Jiao et al[107] performed DFT calculations to systematically investigate the nature and origin of ORR activity of a series of heteroatom-doped graphene (N, B, S, and P) catalysts. The calculations, allow derivation of a volcano plot between the ORR activity and the adsorption free energy of intermediates on metal-free materials, similarly as in the case of metallic catalysts. For all heteroatom-doped graphene models, the calculation of the free energy shows the first electron transfer step to form OOH* is the ORR rate-determining step. This study shows that graphene-based metal-free catalysts possess the potential to surpass the ORR performance of the state-of-the-art Pt catalyst.

Zhang et al.[108] studied electrocatalytically active sites and their associated electron transfer processes for nitrogen-doped graphene (NG) using density functional theory (DFT). The energy calculated for each ORR step showed that the ORR active sites on single NG had either high positive spin density or high positive atomic charge density. N-doping could introduce an asymmetrical spin density and atomic charge density, making it possible for NG to give high electrocatalytic ORR activity. Also, quantum mechanical calculations revealed that pyridinic and/or graphitic-N in the carbon frameworks could play an essential role in enhancing electrocatalytic ORR activity.

For dual-doped B, N-graphene the energy of HO_2 adsorption (E_{ad}), which is the rate-determining step of the ORR process, on various catalyst models was used as the criterion to evaluate the ORR activity of each catalyst[109]. The authors also employed density functional theory (DFT) calculations to further understand the interactions between nitrogen and boron dopant species. They found a beneficial synergistic effect in a B–C–N in heteroring towards the ORR. The charge-transfer process induces a synergistic coupling effect between N and B dopants, in which N has the role of an electron-withdrawing group to indirectly activate B and thus make the latter an active site to enhance the ORR activity. The strength of the synergistic effect decreases gradually as the distance between the B and pyridinic N dopants increases. The study also shows that B atom at meta position to a pyridinic N atom has the highest E_{ad} value, whereas an ortho B atom directly bonded to N (both pyridinic and graphitic forms) as BN has the lowest activity owing to the lack of the C bridge[109].

2.4.2.3 Theoretical study on the catalytic activity of conducting polymers toward oxygen reduction

V.G. Khomenko et al.[110] studied the mechanism and explain the reasons of the catalytic activity for polyaniline, polypyrrole (PPy), polythiophene (PTh), and poly(3-methyl)thiophene (PMeT) using quantum-chemical calculations of the electronic structure and their adsorption complexes with molecular oxygen. They found that adsorption of molecular oxygen (electron acceptor) on all polymer (electron donor) surface is realized only when both oxygen atoms form bonds with surface carbon atoms, i.e. a bridge model of adsorption is most probably. The electron density displaced from the surface to O_2 during adsorption occupies the antibonding MO's of adsorbed

oxygen molecule which is responsible for the destabilization of the O–O bond in O_2 (ads.) during the chemisorptions of O_2 on polymer. Hence, π bonds in O_2 (ads.) and surface adsorption sites undergo rupture and forming new two donor-acceptor C–O σ-bonds which exhibit a decrease in bond orders and an increase in the bond length of O–O in chemisorbed oxygen molecules. Thus, chemisorbed O_2 molecules have a fairly high degree of activation and can be easily reduced, which accounts for the catalytic activity of electronically conducting polymers.

2.4.3 Practical study on electrocatalytic oxygen reduction reaction

Hydrodynamic methods together with voltammetric methods such as linear sweep voltammetry and cyclic voltammetry are the most commonly used techniques to assess the performance and extract fundamental data for electrocatalytic ORR.

2.4.3.1 Cyclic voltammetry in oxygen reduction reaction

Cyclic voltammetry (CV), is an electrochemical technique in which the potential of a stationary working electrode (in an unstirred solution), is scanned linearly between two values at a fixed rate using a triangular potential waveform (Figure 10a.). Depending on the information sought single or multiple cycles can be used. It is very useful for initial electrochemical studies of new systems and offers a rapid location of redox potentials of electro-active species as shown in the cyclic voltammogram in Figure 10b and Figure 11[111, 112].

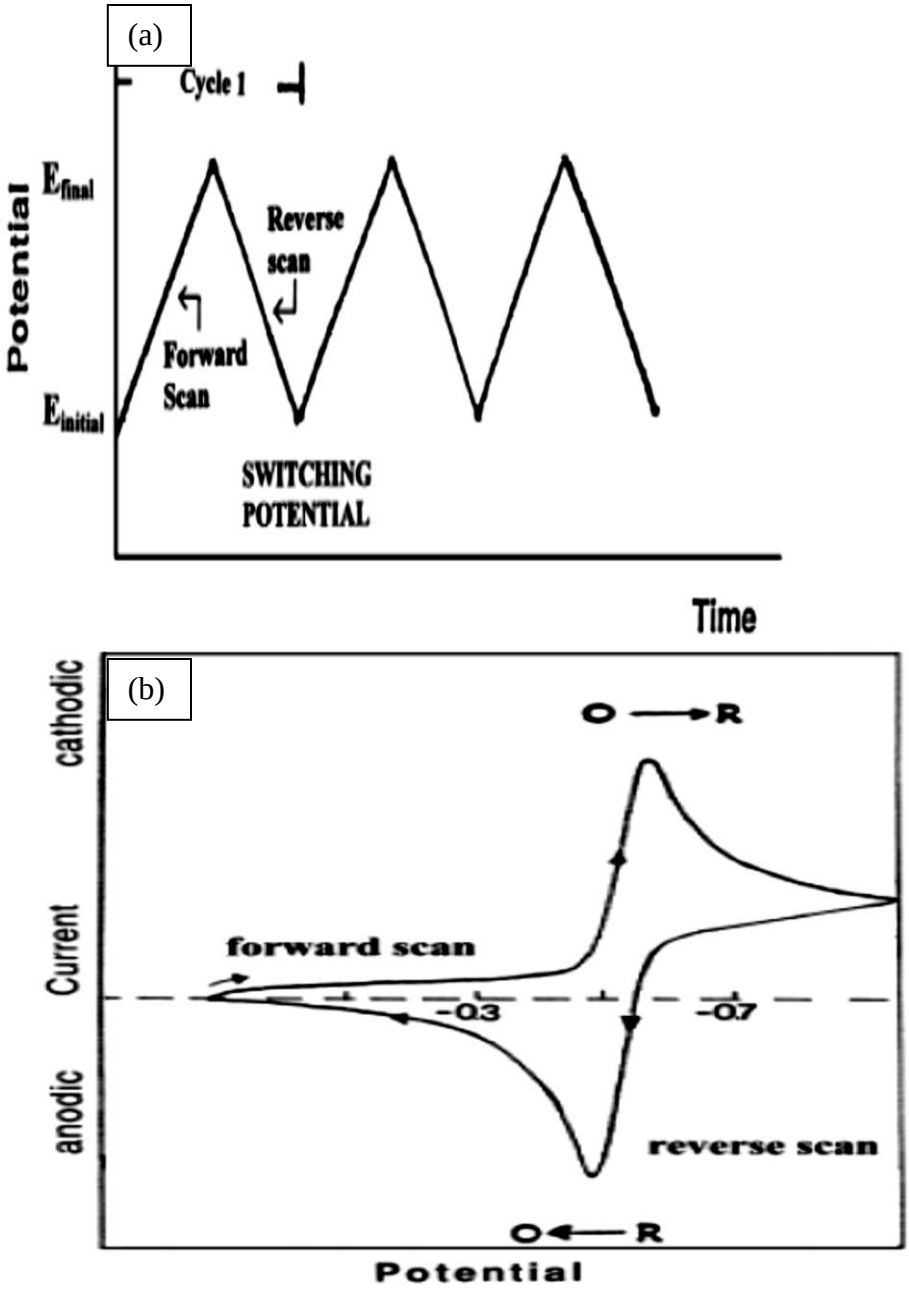

Figure 10. (a) Potential-time excitation signal in cyclic voltammetric experiment and (b) cyclic voltammogram for a reversible O + ne ⇌ *R* redox process[111].

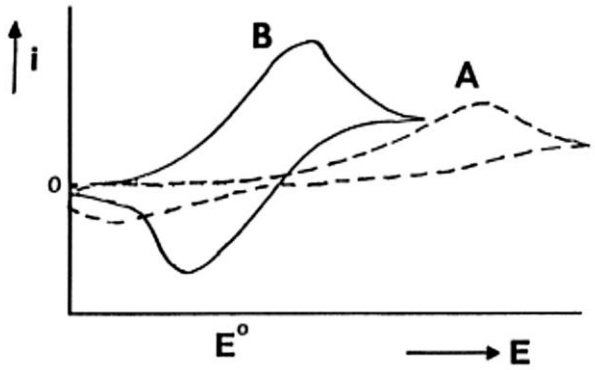

Figure 11. Cyclic voltammograms for irreversible (curve A) and quasi-reversible (curve B) redox processes[111].

The difference between anodic peak potential (Ep, a) and cathodic peak potential (Ep, c) in CV, often symbolized by ΔEp, is an indicative test for reversible processes. For electrode reactions that have rapid electron transfer kinetics which are often referred to as reversible electron transfer reactions (Figure 10b), the separation between peak potential is close to 59/n mV. Thus, the peak separation can be used to determine the number of electrons transferred. For those electrode reactions with slow electron transfer processes relative to the voltage scan rate, the individual peaks are reduced in size and widely separated. This happens because the kinetics of the reaction is 'slow' and thus the equilibria are not established rapidly or the current takes more time to respond to the applied voltage than in the reversible case. For these cases, the reactions are referred to as quasi-reversible or irreversible (Figure 11) electron transfer reactions [111-113].

Cyclic voltammetry is also used to study the state of the electrocatalyst surface by determination of the electrochemically active surface area (ECSA) and surface coverage. To design highly

efficient platinum electrocatalysts for practical application Pt dispersed with large surface areas are extremely important. ECSA of such Pt-based electrocatalysts is used to determine the specific activity for evaluation and comparison of the different catalysts from various sources.

The charge densities involved in the electro-adsorption and/or electro-desorption (stripping) of probe species such as hydrogen (H), copper (Cu), silver (Ag), carbon monoxide (CO), oxygen (O), and hydroxide (OH), are used to estimate the ECSA of various Pt electrocatalysts. The charge passed from under potential deposition (UPD) or the subsequent stripping processes of H, CO and some metal cations on Pt electrode surfaces are commonly employed method for determination of ECSA[113].

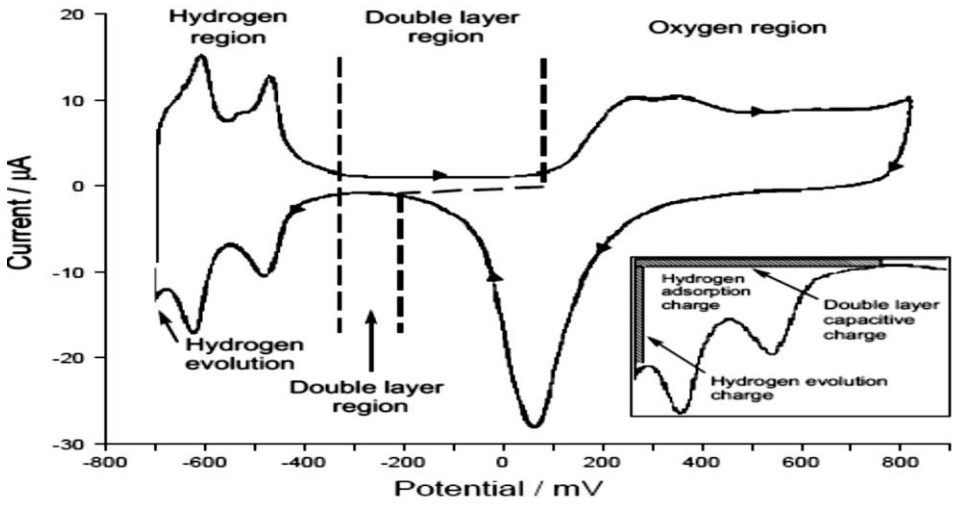

Figure 12. Cyclic voltammogram for a platinum electrode in 0.5 M H_2SO_4 solution (V *vs* MSE). The inset shows the different charge contributions in the hydrogen region[114].

By assuming hydrogen adsorbs in a form of monolayer (ratio for Pt and H is normally assumed to be 1:1), one can use charge associated with hydrogen adsorption/desorption voltammetric

peaks, corrected for double layer charging, to evaluate the amount of hydrogen adsorbed on the surface (Q_H) (Figure 12)[35]. The charge integration (Figure 13) obtained from cyclic voltammogram after the double layer correction is used to calculate ECSA.

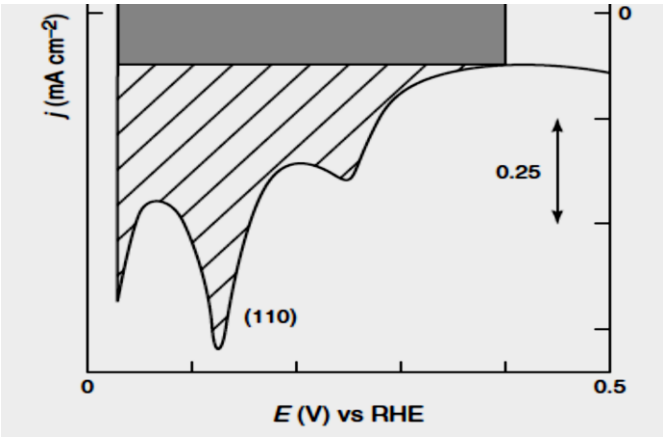

Figure 13. Cyclic voltammogram on Pt/Vulcan electrode in 0.5 M H_2SO_4, scan rate: 20 mV s^{-1}. The gray rectangle is the estimated double layer charge and the vulcane capacitance used to correct the charge due to the hydrogen adsorption [98].

The integration that can be carried out is, therefore:

$$\mathbf{Q_H} = \frac{\mathbf{1}}{\mathbf{\upsilon}} \int_{\mathbf{V_1}}^{\mathbf{V_2}} (\mathbf{j} - \mathbf{j_{dl}}) \mathbf{dV} \qquad \mathbf{(3)}$$

where *v* is the sweep rate at which the cyclic voltammetry is recorded, j is the current density, j_{dl} is the current density due to the double layer charging and dV is the change in potential.

ECSA is calculated using the following equation:

$$\mathbf{ECSA_{Pt,cat}\ (m^2 g_{pt}^{-1})} = \frac{\mathbf{Q_H}}{\mathbf{m \times 210\ \mu C\ cm^{-2}}} \qquad \mathbf{(4)}$$

where Q is the average of charges exchanged during hydrogen adsorption (μC cm^{-2}) which is obtained after double-layer correction; m is the mass of platinum loading (μg cm^{-2}) and the numerical value 210 (μC cm^{-2}) represents the charge required to oxidize a monolayer of hydrogen on Pt surface.

ECSA can also be determined by CO stripping voltammetry by forming a saturated CO adlayer on the catalyst surface which is achieved by holding electrode at a potential below CO oxidation onset potential (typically around 0.05 V *vs.* RHE) while CO is introduced into the electrolytic solution. After saturation, CO is removed from the solution by purging with an inert gas stream. In the final step, the electrode potential is swept in a positive direction so that adsorbed CO is oxidized according to:

$$\mathbf{CO_{ads} + H_2O \rightarrow CO_2 + 2H^+ + 2e^-} \qquad \textbf{(5)}$$

For the case of Pt catalysts surface area covered by CO (S_{CO}) is evaluated as:

$$\boldsymbol{S_{CO} = \frac{Q_{CO}}{420\ \mu C\ cm^{-2}}} \qquad \textbf{(6)}$$

where Q_{CO} is the total charge under CO stripping peak, while the value of 420 μC cm^{-2} corresponds to the charge required to strip CO monolayer. The ratio for Pt and CO is 0.68.

There are some uncertainties related to surface area measurement by CO stripping. The first one relates to the nature of CO bonding on the surface. The second one is related to the correction of CO charge for the contributions due to double-layer charging and metal oxide formation.

Practically, this is solved by considering that oxide layer formation is the same with and without CO adlayer formed on the surface. This means that the baseline for CO stripping experiment is the second cycle in cyclic voltammetry experiments after CO adlayer is oxidatively stripped (Figure14).

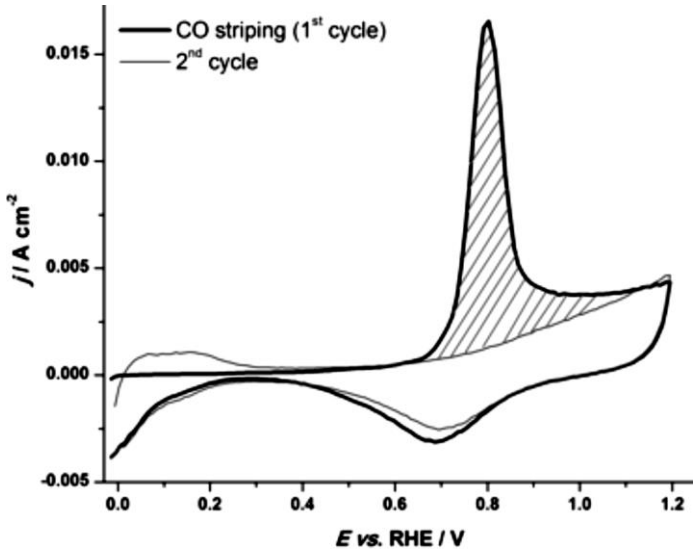

Figure 14. CO stripping voltammogram (thick line, 1st cycle) and the second potential cycle (thin line) for Pt/C catalysts (40 wt.% Pt), (scan rate: 100 mV s^{-1} in de-aerated 0.1 M $HClO_4$)[113].

CV curves at a low scan rate are also used for the determination surface coverage (*Γ)* of an electrocatalyst using Equation (7).

$$\Gamma = Q/nFA \qquad (7)$$

where *Q* is the charge obtained by integrating the cathodic peak under the background correction [115].

2.4.3.2 Linear sweep voltammetry (LSV) in oxygen reduction reaction

In linear sweep voltammetry (LSV), the current passing through the working electrode is measured, while the potential between the working electrode and the reference electrode is swept linearly in time, between two preset values. The current response is plotted as a function of voltage rather than time starting from preset potential E_1 where negligible current flows and then the voltage is swept further to more reductive values where current flow begins and finally goes through a maximum before dropping (Figure15)[113].

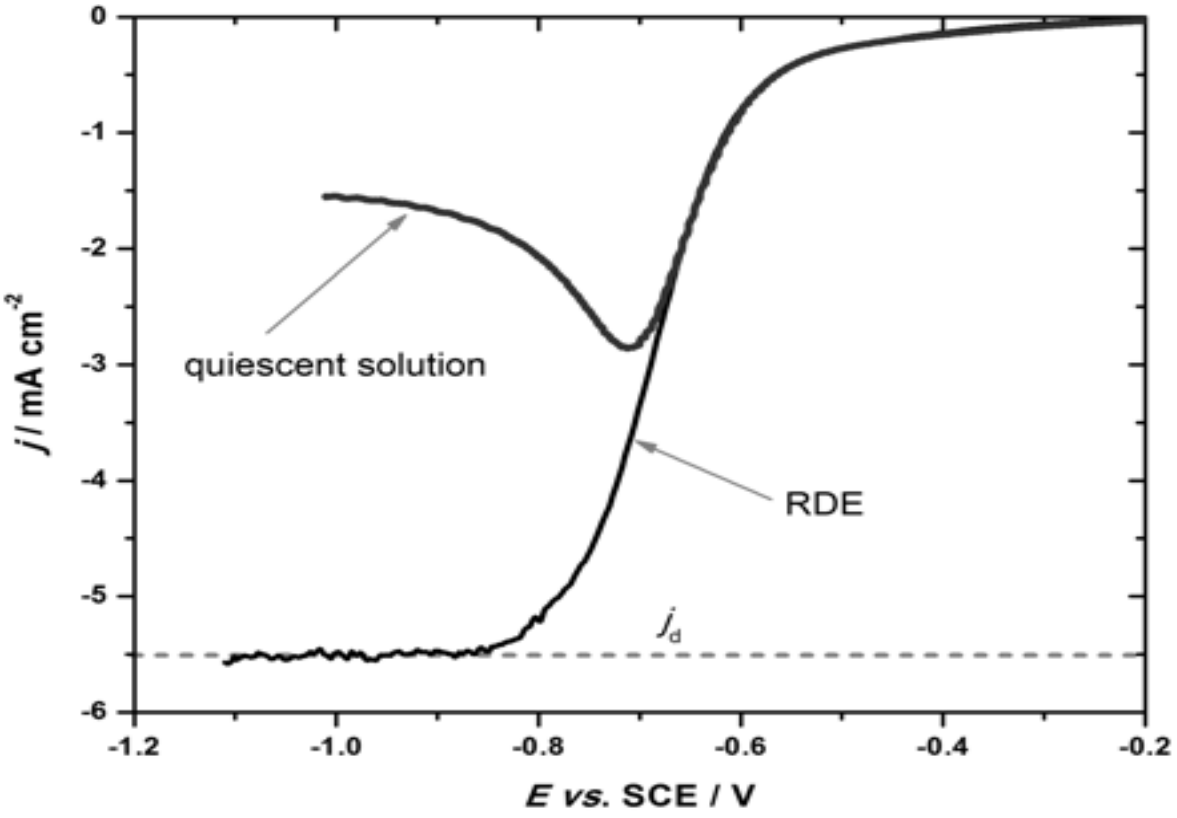

Figure 15. LSV curve recorded in quiescent solution and LSV of the same electrochemical reaction using a rotating disk electrode set-up (RDE).

If the primary focus is on the kinetics of charge transfer to investigate the mechanism and kinetics of the electrochemical reaction, the mass transfer rate can be increased so as to not represent a limiting factor of electrode kinetics. This is possible using methods of forced convection. Methods involving convective mass transport of reactants and products are sometimes called hydrodynamic methods. These involve systems where the electrode is itself in motion (e.g., rotating disks, rotating wires, streaming mercury electrodes, rotating mercury electrodes, vibrating electrodes) or ones where there is forced solution flow past a stationary electrode (conical, tubular, screen, and packed-bed electrodes in fluid streams, channel electrodes, bubbling electrodes). Mass transport of the reactant to a static electrode in a quiescent solution is diffusion-limited. However, the rates of mass transfer at the electrode surface in hydrodynamic methods are typically larger than the rates of diffusion alone, so that the relative contribution of mass transfer to electron-transfer kinetics is often smaller. The rotating disk electrode (RDE) is one of the few convective electrode systems for which the hydrodynamic equations have been solved rigorously for the steady-state[112, 113].

RDE and RRDE

Rotating disk electrode technique is one of the most extensively used techniques for investigating the mechanism and kinetics parameters of a variety of electrochemical reactions. This method enables us to separate the diffusion component of the current from its kinetic part through suitable mathematical apparatus leading to the determination of some overall kinetic parameters. In this manner, the number of electrons exchanged per molecule of reactant, the overall order of the reaction, and the overall reaction rate constants can be determined for the number of processes. This technique has also been extensively used in the determination of the

mechanism of oxygen reduction and together with the rotating ring-disk technique has led to some important conclusions about the specific steps in oxygen reduction[89, 112, 113].

Mass transport of the reactant to a static electrode in a quiescent solution can be increased by using a rotating disc electrode (RDE) (Figure 16a), an electrode attached to an electric motor that has fine control over the electrode's rotation rate. In a rotating ring-disk electrode (RRDE), RDE is surrounded by a ring electrode (Figure 16c). For RRDE, the current-potential characteristics of the disk are unaffected by the presence of the ring and the experiments involve the examination of two potentials (disk, E_D, and ring, E_R) and two currents (I_D and I_R)[113].

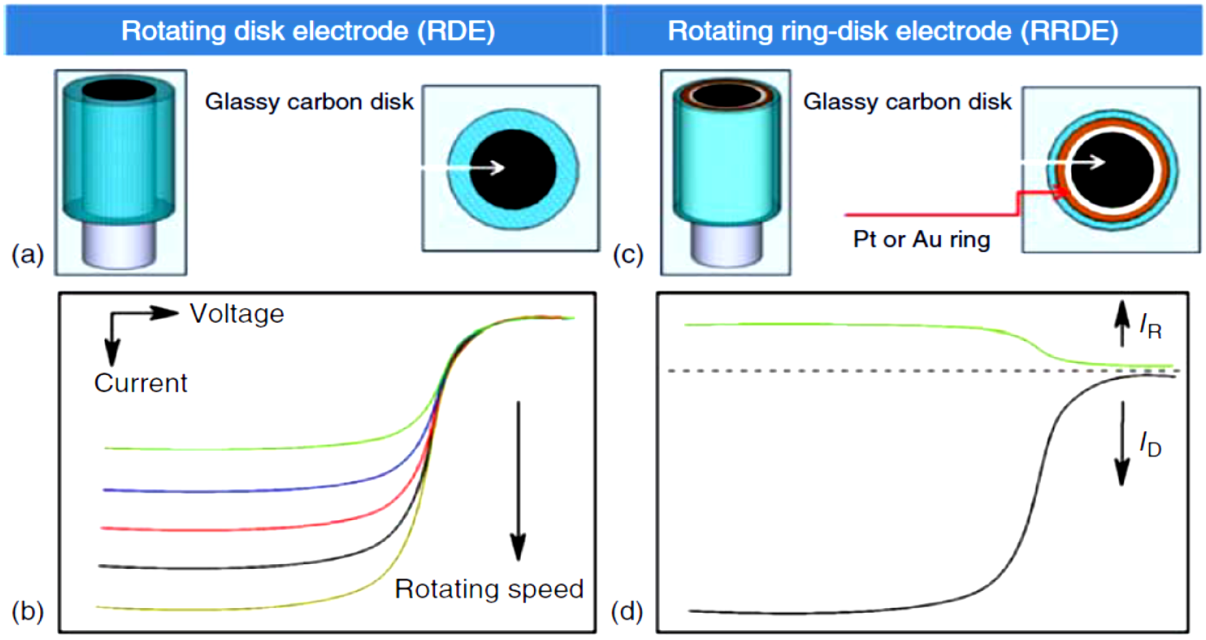

Figure 16. Configuration of RDE (a) and RRDE (c). Linear sweep voltammogram (LSV) curves of electrocatalysts in oxygen-saturated electrolytes with different rotating speeds (b) typical oxygen reduction curves on the disc and ring electrodes, respectively (d)[89].

Typical rotating disk voltammogram (Figure 17) shows three distinct regions namely: diffusion-controlled region at high overpotential which corresponds to the limiting current density (J_d) that depends only on mass transport process, mixed diffusion kinetic limitation where the rate of the reaction is controlled by charge-and-mass transfer processes and Tafel region (kinetic or activation control) where the rate of the ORR is mainly controlled by a charge transfer process[16].

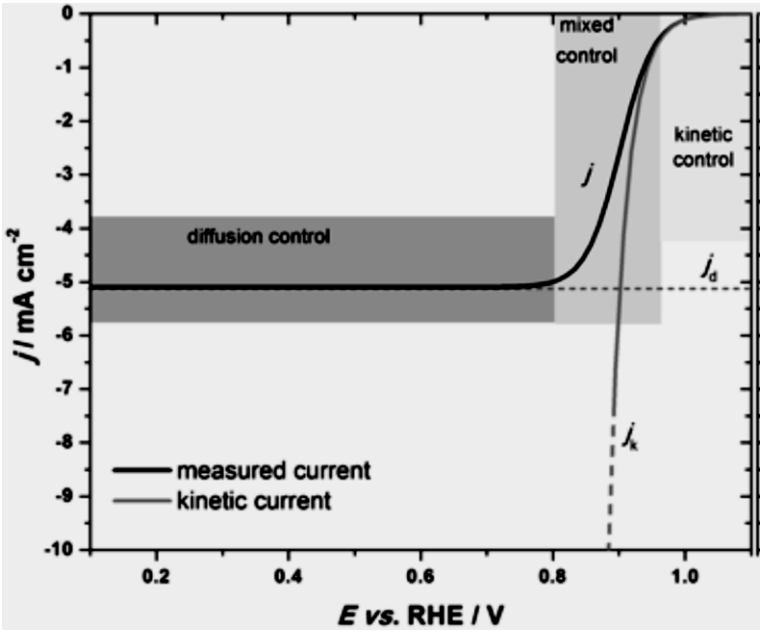

Figure 17. Extraction of kinetic current density (J_k) from measured ORR polarization curve in RDE setup[113].

The current density (current per geometric area of the electrode) of ORR in RDE is dependent on the kinetic current density (J_k) and diffusion-limiting current density (J_d). Kinetic current density (J_k) represents the current in the absence of any mass-transfer effects and is given by:

$$\mathbf{J_k = nFk_{O_2} C_{O_2}\, \Gamma = nFk_f C_{O_2}} \qquad \mathbf{(8)}$$

where J_K is the kinetic current density, n is the overall number of electrons transferred in oxygen reduction, F is the Faraday constant (F = 96485 C mol^{-1}), k_{O_2} is the electron transfer rate constant, k_f is the heterogeneous rate constant, and Γ is the surface coverage of the catalyst.

Kinetic current density is determined by the reaction kinetic process. However, the slow mass transport of the reactants (e.g., O_2) from the bulk of electrolyte solution to the electrode surface results in the formation of a concentration profile of the reactants in front of the electrode surface. If the applied overpotential is high enough, every atom/ion reaching the electrode reacts immediately, resulting in nearly zero concentration at the surface, leading to a diffusion-limiting current density, which is only determined by the rate of diffusion. Mass transport can be increased by using a rotating disc electrode (RDE) attached to an electric motor that controls over the electrodes rotation rate (ω). Levich showed the following relationship between the diffusion-controlled current density (J_d), sometimes called Levich current and the disk rotation rate (ω):

$$\mathbf{J_d = 0.2nFC_o D_o^{2/3} \upsilon^{-1/6} \omega^{1/2}} \qquad \mathbf{(9)}$$

where J_d is diffusion-limiting current density, ω is the angular velocity of the disk (in rpm), C_0 is the bulk concentration of O_2, D_0 is the diffusion coefficient of oxygen, ν is the kinematic viscosity of the electrolyte.

The overall measured current density, J, can be expressed as being dependent on the kinetic current density (J_k) and the diffusion-limiting current density (J_d), which can be expressed in terms of the Koutecky–Levich equation as follows:

$$\frac{1}{J} = \frac{1}{J_D} + \frac{1}{J_k} = \frac{1}{B\omega^{1/2}} + \frac{1}{J_k} \quad (10)$$

where ω is the electrode rotating rate. B is determined from the slope of the Koutecky–Levich plot based on the Levich equation as given below[89, 113].

$$B = 0.2nFC_o D_o^{2/3} \upsilon^{-1/6} \quad (11)$$

For estimating the kinetic current to obtain the mass transfer-corrected Tafel Equation (13), the modified Koutecky–Levich equation was used as shown in Equation (12). Tafel plots ($\log|j_k|$ *vs* E) are very useful in examining the kinetic parameter in the catalytic reaction. The exchange current density J_0 and the Tafel slope can be calculated from the intercept and slope of the Tafel plots. The higher Tafel slope leads to lower efficiency of the electrocatalyst[116, 117].

$$J_k = \frac{J \cdot J_d}{J_d - J} \quad (12)$$

where J_k is the kinetic current density and J_d is the measured limiting current density

$$\log J_k = -\frac{1}{b}(E - E^0) + \log J_0 \quad (13)$$

$$b = \frac{2.303RT}{\alpha nF} \quad (14)$$

where E is the measured potential of the working electrode, E^0 is the equilibrium open-circuit potential, b is the Tafel slope, R is gas constant (8.314 J $mol^{-1}K^{-1}$); T is the Kelvin temperature, J_k is the kinetics current density, and J_0 is the exchange current density.

Exchange current density (J_0) is a very important kinetic parameter that represents the electrochemical reaction rate at equilibrium and is considered as a measure of the intrinsic electrocatalytic activity towards ORR. A higher value of J_0 indicates a faster electrochemical reaction that is developed by the catalyst[16]. The determination of J_0 is susceptible to significant errors because of the extrapolation of the Tafel line and the linear fitting of the Tafel slope which depends on the potential range selected. Hence, a practical and conventionally accepted concept for the representation of the electrocatalytic activity is the determination of the mass activity (MA) and the specific area activity (SA) of the electrocatalysts specifically for Pt and Pt-group metals. The MA and SA can be obtained through the following equations[10, 16]:

$$\mathbf{MA\ (A\ mg^{-1}) = \frac{i_k}{m_{Pt}}} \qquad \mathbf{(15)}$$

$$\mathbf{SA\ (mA\ cm^{-2}) = \frac{i_k}{ECSA}} \qquad \mathbf{(16)}$$

where i_k is kinetic current, m_{Pt} mass of platinum and ECSA is an electrochemically active surface area.

RRDE voltammetry is designed to provide an inherent analysis of the reaction selectivity instead of relying on complex calculations and data plotting techniques such as K–L plot. RRDE

measurements were used to assess the extent of peroxide formation, the number of electrons transferred per O_2 molecule (n), and pathways for ORR. The equations used to calculate n (the apparent number of electrons transferred during ORR, the percentage of H_2O_2 released during ORR (% H_2O_2), and the collection efficiency (N) are the following[113, 118].

$$\mathbf{n} = \frac{\mathbf{4i_d}}{\mathbf{i_d} + \frac{\mathbf{i_r}}{\mathbf{N}}} \quad \textbf{(17)}$$

$$\mathbf{\%\ H_2O_2} = \frac{\mathbf{200i_r}}{\mathbf{i_d} + \frac{\mathbf{i_r}}{\mathbf{N}}} \quad \textbf{(18)}$$

$$\mathbf{N} = -\frac{\mathbf{i_r}}{\mathbf{i_d}} \quad \textbf{(19)}$$

where N is the collection efficiency of RRDE, and i_d and i_r are the disk and ring electrode currents, respectively.

The value of N for an ideal RRDE is independent of the reaction and rotational rate (ω) but dependent only on its geometrical parameters. However, when a thick catalyst layer is loaded on the disk, the geometry of the RRDE changes; therefore, it is necessary to calibrate the N value of the RRDE with the catalyst. The calibration of N is carried out using a simple one-electron transfer redox pair reaction[118].

$$Fe(CN)_6^{3-} + e^- \underset{\text{On the ring}}{\overset{\text{On the disk}}{\rightleftharpoons}} Fe(CN)_6^{4-}$$

2.4.4 Requirements for oxygen reduction reaction electrocatalyst

For electrocatalysis of an ORR, the most important criteria are high catalytic activity, good electrical conductivity, good electrochemical (not being oxidized at high electrode potentials) and chemical stability (not being oxidized by proton and oxygen and not soluble in acidic or basic aqueous solution). Moreover, favorite structure with optimum composition, favorite morphology, high specific surface area, small particle size, high porosity, and uniform distribution of catalyst particles on the support, and strong interaction between the catalyst particle and the support surface are also important[12].

The catalyst's activity measures how fast the electrochemical reaction can be speeded up by the catalyst. Electrocatalytic activity of different electrocatalyst can be compared using onset potential (E_{onset}) and half-wave potentials ($E_{1/2}$) (Figure 18). Onset potential is defined as the potential at which the catalyzed ORR current starts to appear or the potential at which the ORR current is 5% of the diffusion-limited current. The half-wave potential is the potential at which the current is half of the diffusion-limited current. The more positive is the potential (E_{onset} and $E_{1/2}$) the more active is the catalyst. The selectivity of the catalysts that reduce O_2 *via* the four-electron pathway, i.e., the lowest the yield of (H_2O_2) and the electron transfer number of ORR are also important parameters for evaluating the performances of catalysts[14].

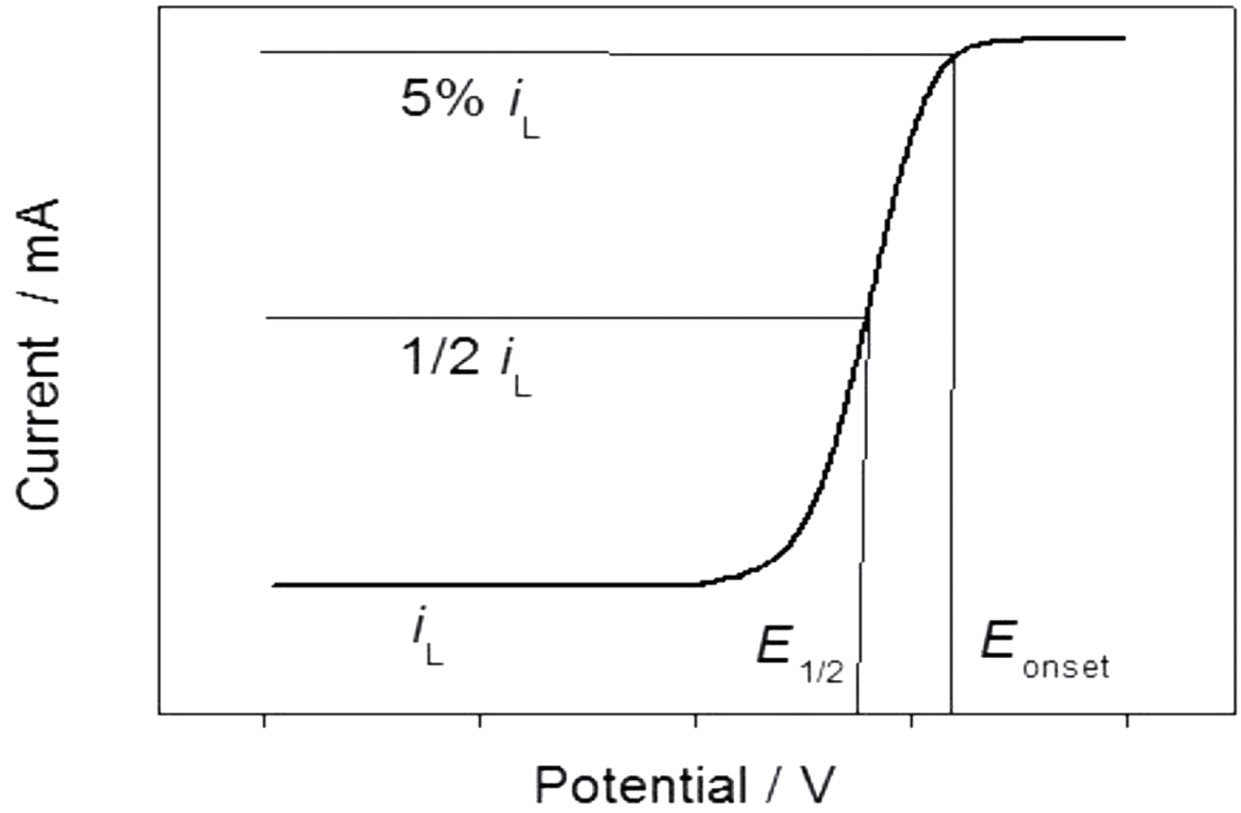

Figure 18. Typical ORR polarization curve and the parameters used to quantitatively determine the activity.

The United States Department of Energy (DOE) has set of 'benchmark' standards for research purposes, with a Pt mass activity (MA) target of 0.44 A mg_{Pt}^{-1} @ 900 mV iR free and a corresponding specific area activity (SA) target of 0.72 mA cm^{-2} @ 0.9 V for electrocatalysts for use in the portable applications market by the year 2017. The most commonly employed commercial catalyst, Pt/C (Etek), typically achieves SA of 0.2 mA cm^{-2} and MA of 0.1 A mg_{Pt}^{-1} [10].

2.4.5 Oxygen reduction reaction on platinum-based electrocatalysts

In the last two decades, enormous achievements have been made in the development of the ORR electrocatalysts. Among the different electrocatalyst for ORR, Pt is still the benchmark and most efficient element for ORR despite effort has been made to replace with less precious metal and metal-free catalysts[93].

2.4.5.1 Graphene support material for platinum for oxygen reduction reaction

Graphene is emerged as a new kind and promising platinum electrocatalyst support material in recent years due to its unique physicochemical properties, including excellent electrical and thermal conductivities, fast charge transport mobility, good transparency, great mechanical flexibility, astonishing elastic properties and huge specific surface area (theoretically 2630 m^2 g^{-1} for a single layer)[14]. Therefore, graphene-based materials are one of the feasible catalyst supports for Pt metals[14]. In the past decade, graphene-based supports displayed remarkable catalytic activity[21, 28, 70, 119], electrochemical stability[119, 120], mechanical stability[120] , high electroactive surface area[21, 120] compared to traditional carbon materials.

Scientists have aimed to improve the electrocatalytic activity and stability of catalysts towards ORR by employing different techniques for deposition of platinum nanoparticles as well as synthetic of graphene family as support or metal-free catalyst. One of the main problems associated with the use of graphene is its inevitable aggregation and restacking exhibited by unsatisfactory electrochemical performance[121]. Chao Xu et al.[122], synthesized graphene-metal

(Au, Pt, and Pd) NPs using graphene oxide sheets as a precursor in the solution approach and the metal NPs formed first and were adsorbed onto the surface of carbon sheets, which is not only beneficial for the following reduction of graphene oxide but also prevents the restacking of these reduced graphene sheets. Simultaneous reduction of platinum nanoparticles and GO using chemical treatment exhibited much better ORR catalytic performance than commercially available Pt/C catalyst[123]. The superior activities were attributed to the large ECSA of platinum on graphene (Pt/G), which could facilitate the diffusion of O_2 on the graphene surface to the Pt metal sites.

Graphene composites consisting of secondary building blocks such as carbon black, carbon nanotube, and conducting polymers have been made to inhibit the restacking of graphene nanosheets (GNS)[119]. Li et al.[124] insert carbon black particles (CB) between the Pt/rGO sheets which effectively prevent stacking of rGO and promote the diffusion of oxygen molecules through the rGO sheets. The composite structure not only enhances the catalytic activity but also dramatically improves the durability of the catalyst with the insertion of CB particles between rGO sheets. Hussain et al.[125] synthesized nitrobenzene-functionalized graphene nanosheets (NB/G) as electrocatalysts for oxygen reduction reaction in 0.1 M KOH. Comparable specific activity was observed by Pt-NB/G (0.184 mA cm^{-2}) to that of commercial 20 wt.% Pt/C catalyst (0.214 mA cm^{-2}) at 0.9 V *vs* RHE.

The underlying catalyst–support interactions can be regulated by introducing heteroatom ‘‘dopants’’ (i.e., nitrogen, sulfur) into the graphitic carbon support structures. The heteroatom species serve as nucleation sites and allow the deposition of uniformly sized and well-dispersed

platinum nanoparticles (Pt-NPs). They also modify the electronic structure of the Pt-NPs which can lead to ORR activity enhancements through weakened interactions with adsorbed surface species (i.e., OH_{ads}) and strengthened interactions between the doped carbon supports and the Pt-NPs[9]. Hoque and co-workers used graphene and sulfur-doped graphene as catalyst support for Pt-NPs for ORR in 0.1 M $HClO_4$[126]. They found that the amount of sulfur significantly affects the electrochemical activity and stability of nanowire catalysts due to the influence of the sulfur dopants present in graphene. Their experimental and computational investigations show that with increasing sulfur contents, the number of graphene layers increased, the ratio of sp^2 and sp^3 carbon decreases, indicating a less graphitic character of sulfur doped graphene (SG). Moreover, band gap increases and the electrical conductivity decreases with increasing the amount of sulfur in graphene. For the optimum amount of sulfur (1.40%) a mass activity of 182 mA mg_{Pt}^{-1} and specific activity of 662 μA cm^{-2} Pt at 0.9 V *vs* RHE were recorded for sulfur-doped graphene as catalyst support for Pt-NPs.

Compared to other heteroatoms, nitrogen doping plays a more critical role in modifying the carbon structure, due to the comparable atomic size of nitrogen and carbon, as well as the presence of five valence electrons in the nitrogen atoms available to form strong covalent bonds with carbon atoms[127]. Bai et al.[128] investigated graphene and nitrogen (N)-doped graphene synthesized by a solvothermal method as catalyst supports for oxygen reduction reactions. Pt nanoparticles supported on N-doped graphene can contribute to four-electron oxygen reductions in acidic solution, but they demonstrated much slower reaction kinetics in alkaline solution. Despite its low efficiency in catalyzing the ORR in acidic solution, nitrogen doped graphene greatly improved the electrocatalytic performance of Pt when employed as supporting material.

The enhanced performance is due to improved carbon-catalyst binding which stabilizes catalyst nanoparticles dispersed on the substrate.

The introduction of other heteroatoms, such as P, S, and B to form two or three co-doped heteroatom carbon nanomaterials can further enhance the catalytic activity. Boron and nitrogen-dual-doped graphene sheets (BNG) prepared by Zhu et al[28] for Pt support show an excellent electron-donating of BNG to Pt that facilitates the reduction of O_2 and strengthens BNG/Pt interaction. The Pt/BNG catalyst exhibits nearly three times as high mass activity as that of commercial Pt/C in O_2-saturated 0.1 M $HClO_4$ at 0.9 V *vs* RHE which is nearly three times as high as that of commercial Pt/C.

2.4.5.2 Electronically conducting polymer as platinum support for oxygen reduction reaction

Electron conductive polymers are convenient substrates for the immobilization of dispersed platinum particle at the molecular level[19, 129] and have an advantage over commonly used carbon support[130] due to prevention of particle agglomeration[131], permeability to water[132], charge transferability through their films[133], have mixed electronic and ionic conductivity and their porous structure[50]. Electrodeposition of metals is the most widely used method to prepare metal/ polymer composites. The electrodeposition of metal particles in conductive polymer layers can be employed either by a one-step method where polymer electrosynthesis is performed in the presence of metal precursors or polymer layer electrosynthesis (in the absence of metal) followed by metal electrodeposition (two-step methods)[17]. The one-step preparation methods result in a

three-dimensional homogeneous distribution of metal particles in the bulk of the CP layer whereas electrodeposition carried out in a separate step, generally results in preferential deposition on the outer polymer surface[134]. However, electrodeposited platinum microparticles into polyaniline (PA) films on glassy carbon (GC) electrodes by two-step methods were dispersed three-dimensionally in the polymer film[135].

Gajendran et al.[136] studied the electrochemical reduction of oxygen on poly(o-phenylenediamine) (PoPD) containing platinum nanoparticles incorporated into the polymer film by cyclic voltammetry in acidic solution. A platinum loading of about 175 μg cm^{-2} on the PoPD electrode results in 70 times greater in the reduction current than the bare platinum electrode. The catalytic effect is due to the synergistic effects between the dispersed platinum particles and PoPD film. The electrocatalytic activity depends on the metal loading in the catalysts. Berhanu and shimelis[36] prepared platinum loaded (17-303 μg) p-(4-amino-3-hydroxynaphtalene sulfonic acid) at constant electrode potential from a 0.5 M H_2SO_4 solution containing 2 mM $H_2PtCl_6.6H_2O$. They found that lower platinum loading on the polymer gave better electrocatalytic activity than the higher loading. The platinum loaded p-(AHNSA) was found to change the oxygen reduction reaction path from 2 in p-(AHNSA) to 4 electrons. Chemically prepared poly(3,4-ethylenedioxythiophene):poly(styrene-4-sulfonate) supported catalysts for the chemical deposition of Pt as a thin film in a Nafion matrix on carbon electrodes were found to exhibit similar oxygen reduction activities, exchange current densities and mechanisms to a commercial carbon-supported catalyst[132]. Coutanceau et al.[131] studied the electrocatalytic reduction of oxygen at platinum particles dispersed in a polyaniline conducting matrix, electropolymerized on a GC electrode, with different platinum loadings ranging from 11 to 600

μg cm^{-2}. They found that, for the smallest platinum loadings, the total number of exchanged electrons is definitely lower than four (production of water) and may reach three which is a result of as much of hydrogen peroxide as water is formed by the oxygen reduction reaction. Similarly, the Tafel slope varies from about 60 mV dec^{-1} at the lowest Pt loadings, to 120 – 130 mV dec^{-1} at the highest platinum loading. These variations with the platinum loading may be related to particle size effect, particularly for the lowest platinum loading, for which the particle diameter (d) is a few nanometers.

2.4.6 Graphene and conducting polymer as a metal-free catalyst for oxygen reduction reaction

Recently, several research groups prepared graphene-based metal-free catalysts using different techniques and precursor materials having comparable or superior electrocatalytic activity, stability, and tolerance to the crossover effect than commercially available Pt/C for ORR[66, 67, 69, 82, 137-140]. Bai et al.[128] investigated that N-doped graphene (N-G) demonstrated higher electrocatalytic activity in both acidic and alkaline solutions. Their study also showed the influence of electrolyte media on the selectivity of ORR pathways. They found that both N-G and graphene (G) displayed a direct four-electron pathway for the ORR in alkaline solution but follow the two-electron reductions reaction pathways in acidic solution. The enhancement of N-G electrocatalytic activity was attributed to (1) increased electrical conductivity by pyrrolic-liked nitrogen atoms within carbon structures, (2) increased in the absorption of oxygen on graphene surfaces by its sp^3-hybridized electronic structure, (3) the formation of pentagons and defects in N-doped graphene structure which furnishes more reaction sites for the ORR.

The electrochemical investigations at polyaniline (PANI), polypyrrole (PPy), polythiophene (PTh), and poly(3-methyl)thiophene (PMeT)[110], poly(p-aminobenzene sulfonic acid)[115], poly(3,4-ethylenedioxythiophene) (PEDOT)[141, 142] indicate the existence of electrocatalytic activity toward the oxygen reduction reaction as metal-free catalysts. The catalytic mechanism of conducting polymer (CP) has been explained from two aspects: (1) A strong interaction between an electron donor neutral CP and an electron acceptor O_2 molecules adsorbed on its surface *via* charge transfer, activating the latter by decreasing its molecular symmetry and increasing the lengths of O=O bonds (2) CPs naturally remained in a mildly oxidized form in the electrochemical cell. The O_2 molecules adsorbed on the surface of a CP catalyst can further oxidize CP chains to a higher oxidation degree, while themselves are reduced into O^{2-}anions[143].

The electrocatalytic performances of CP catalysts could be optimized by increasing the specific surface area and conductivities. A larger specific surface area provides CP catalysts with more exposed active sites for enhancing its catalytic activity. Hence, CPs were usually nanostructured by choosing different doping ions in their synthesis processes[143] and the choice of methods for synthesis[47]. Several techniques can be applied to increase the conductivities of CPs, such as modulating their doping ion[47], solvent additive or pre-treatment method[41, 144-146] and adding conductive additives[147]. The conductivity of commercially available PEDOT:PSS can be increased to about 1000 S cm^{-1} by treating it with dimethyl sulfoxide, ethylene glycol, or hexafluoroacetone and even up to 4380 S cm^{-1} by using concentrated sulfuric acid. The conductivities of CP catalysts can also be improved by blending highly conductive carbon nanomaterials such as carbon nanotubes and graphene[143]. The introduction of graphene[138, 148,

[149], antraquinonedisulphonate[150], nitrogen-doped carbon nanotube[151] can further enhance the catalytic activity of conducting polymers.

2.5 Supercapacitors

The use of capacitors for electrical energy storage goes back to the year 1745 on the discovery of the Leyden Jar by Dean Kleist at Leyden or almost simultaneously to Musschenbroek at Kamin, Pomernania[152]. A Leyden jar is an early capacitor consisting of a glass jar coated inside and outside with a thin layer of silver foil with the outer foil being grounded, the inner foil could be charged with an electrostatic generator, or a source of static electricity, and could produce a strong electrical discharge from a small and comparatively simple device[152, 153].

The use of capacitor at the beginning was in electrical and electronic products, but now they are used in fields ranging from the industrial application to automobiles, aircraft and space, medicine, computers, games, and power supply circuits[154].

A conventional capacitor (Figure 19a) is a passive component that stores energy in an electrostatic field rather than in chemical form. It consists of two parallel electrodes (plates) separated by a dielectric. When a potential difference (voltage) is applied across the electrodes, positive and negative charges migrate toward the surface of electrodes of opposite polarity. When charged, a capacitor connected in a circuit will act as a voltage source for a short time[153].

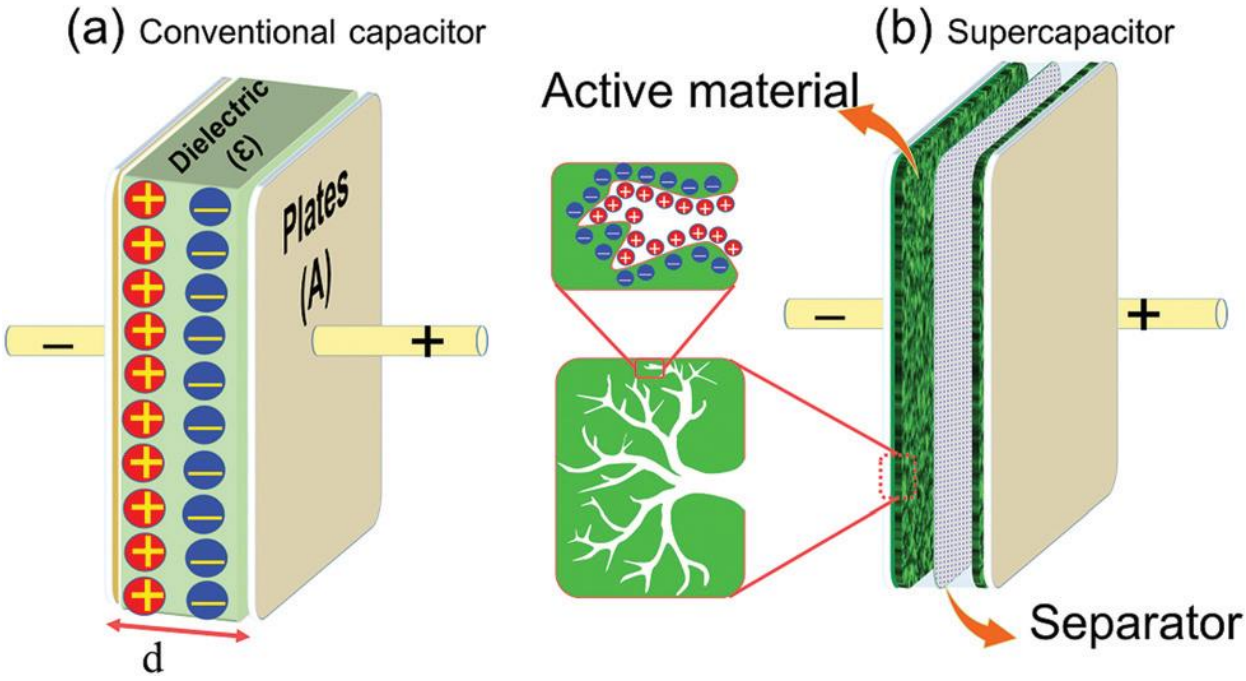

Figure 19. Schematic representation of a conventional capacitor (a) and a electrical double layer supercapacitor (b)[155].

The capacitance (C) of a capacitor measured in Farads (F) is defined as the ratio of stored charge Q to the applied voltage V.

$$\mathbf{C} = \frac{\mathbf{Q}}{\mathbf{V}} \qquad \textbf{(20)}$$

For a conventional capacitor, C is directly proportional to the surface area (A) of each electrode and the permittivity (ε) of the dielectric and inversely proportional to the distance (D) between the electrodes.

$$\mathbf{C} = \frac{\boldsymbol{\varepsilon_o \varepsilon_r A}}{\mathbf{D}} \qquad \textbf{(21)}$$

where ε_o is the permittivity of free space and ε_r is the dielectric constant (or relative permittivity) of the material between the plates[153].

Conventional capacitors are often rated in the micro- and milli-Farad ranges and those capacitors that are used in electronic circuits cannot store enough energy for applications that require significant energy in pulse form. For these applications, the development of high energy density capacitors called electrochemical capacitors (ECs) has been undertaken by various groups around the world. Electrochemical capacitors (Supercapacitors, Figure 19b) are a special kind of capacitors based on charging and discharging at the electrode-electrolyte interface of high surface area materials, such as porous carbons or some metal oxides. They are governed by the same basic principles as conventional capacitors and are ideally suited to the rapid storage and release of energy[153, 156]. They bridge the gap between batteries and conventional capacitors. Supercapacitors (also known or ultracapacitors) do not use conventional dielectrics between the plates; instead, they consist of two electrodes separated by an ion-permeable separator (such as cardboard, ceramic, glass, plastic or paper) and an electrolyte that ionically connects the two electrodes (Figure 19b)[155].

2.5.1 Types of supercapacitors (SCs)

The current research trend divide SCs into three main areas, based on the mode of energy storage and construction of SCs, the electric double-layer capacitor (EDLC*)*, the redox SCs (also referred to as pseudocapacitor), and hybrid capacitors.

2.5.1.1 The electric double-layer capacitor (EDLC*)*

The electrical double layer is the whole array of charged species and/or oriented dipoles existing at every material interface. Different models (Figure 20) of the electrical double layer are postulated to gain a structural view, predict its properties, and compare them to the known facts of real systems[112].

Models for double-layer structure

The concept of the EDL was first described and modeled by von Helmholtz in the 19th century[157]. The Helmholtz double-layer model (Figure 20a) states that two layers of opposite charge formed at the electrode/electrolyte interface and are separated by an atomic distance similar to that of two-plate conventional capacitors[153, 157]. Even though the charge on the electrode is confined to the surface according to simple Helmholtz EDL, the same is not necessarily true of the solution particularly at low concentrations of electrolyte, one has a phase with a relatively low density of charge carriers. Therefore the model should involve a diffuse layer.

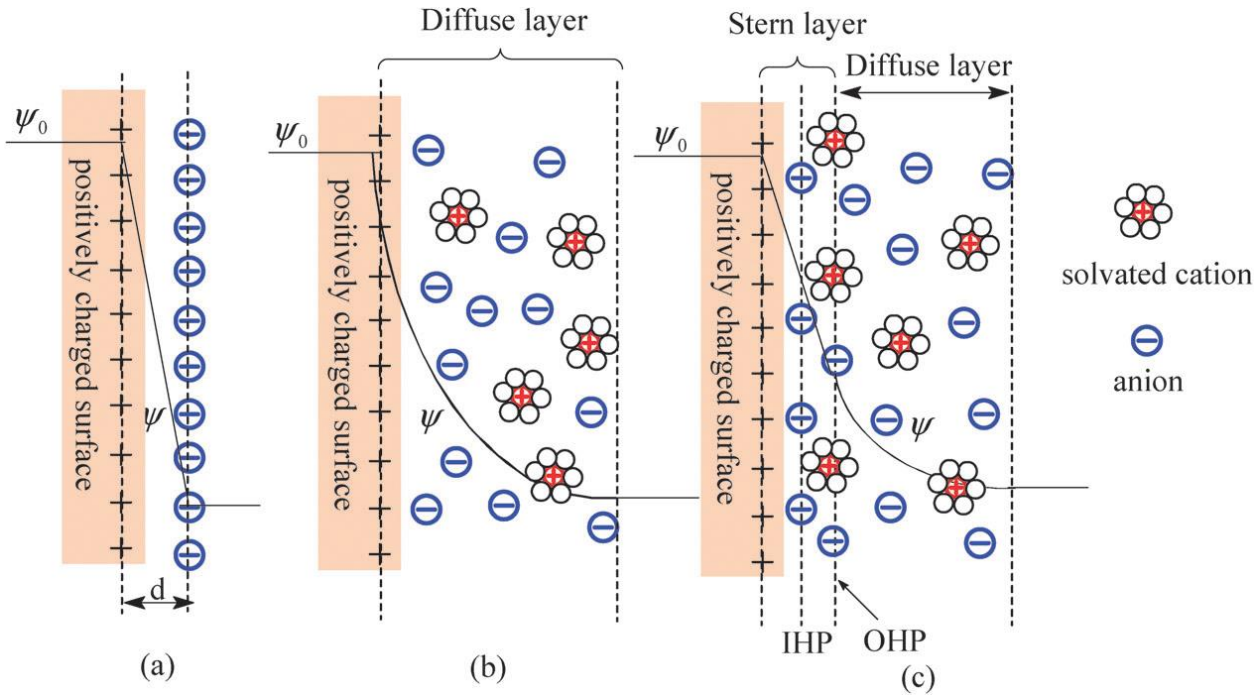

Figure 20. Models of the electrical double layer at a positively charged surface (a) the Helmholtz model, (b) the Gouy–Chapman model, and (c) the Stern model, showing the inner Helmholtz plane (IHP) and outer Helmholtz plane (OHP)[157].

Gouy and Chapman independently proposed a model based on the idea which considers a continuous distribution of electrolyte ions (both cations and anions) in the electrolyte solution, driven by thermal motion, which is referred to as the diffuse layer (Figure 20b). However, the Gouy–Chapman model leads to an over estimation of the EDL capacitance[112, 157]. Stern combined the Helmholtz model with the Gouy–Chapman model and recognized that two regions of ion distribution exist at the electrode-electrolyte interface an inner region called the compact layer (Stern layer) and the diffuse layer (Figure 20c). In the compact layer, ions (very often hydrated) are strongly adsorbed by the electrode. In addition, the compact layer consists of specifically adsorbed ions (in most cases they are anions irrespective of the charged nature of the

electrode) and non-specifically adsorbed counterions. The inner Helmholtz plane (IHP) and outer Helmholtz plane (OHP) are used to distinguish the two types of adsorbed ions. The diffuse layer region is what the Gouy–Chapman model defines[157]. Therefore, the capacitance at an electrode-electrolyte interface double layer (C_{dl}) can be regarded as consisting of two components, the compact double-layer capacitance (C_H) and the diffuse region capacitance (C_{diff}). C_H and C_{diff} are conjugate components of the overall double-layer capacitance (at a single electrode), C_{dl}, corresponding to the series relationship:

$$\frac{1}{C_{dl}} = \frac{1}{C_H} + \frac{1}{C_{diff}} \qquad (22)$$

The factors that will ultimately determine the electric double-layer capacitance include the electrode material (conducting or semiconducting), electrode area, accessibility to the electrode surface, the electric field across the electrode, and electrolyte/solvent properties[157].

2.5.1.2 Pseudocapacitors

Pseudocapacitance is a Faradaic charge storage mechanism based on fast and highly reversible surface or near-surface redox reactions that have the electrochemical signature of a capacitive electrode, i.e., a linear dependence of the charge stored with changing potential within the window of interest[5, 158].

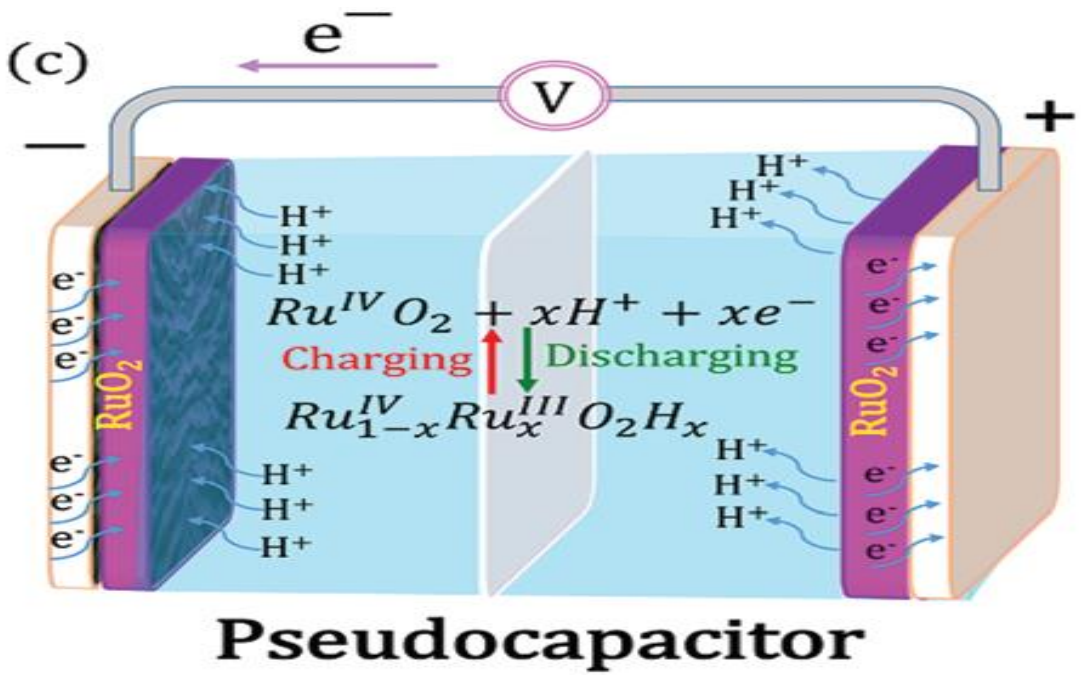

Figure 21. Schematic representation of the electrochemical energy storage system in a pseudocapacitor[155].

Different charge storage mechanisms can be distinguished in a pseudocapacitive electrode: underpotential deposition (H on Pt and Pb on Au), redox reactions of transition metal oxides (RuO_2, MnO_2) (Figure 21), intercalation pseudocapacitance (Li^+ into TiS_2) and also reversible electrochemical doping and dedoping in conducting polymers[5, 158, 159].

2.5.1.3 Hybrid capacitors

Hybrid supercapacitors (Figure 22) refer to those capacitors that use both the electrical double-layer (non-faradic capacitive) and faradaic(capacitive or non-capacitive) mechanisms to store charges. The hybrid SCs include (a) those based on composite electrodes made from both EDL

capacitive materials and pseudocapacitive materials or rechargeable battery-type electrode; (b) those of asymmetric design with one EDL electrode and the other pseudocapacitive or battery-type electrode; as well as, (c) those of the asymmetric structure with one pseudocapacitive electrode and the other rechargeable battery-type electrode[160].

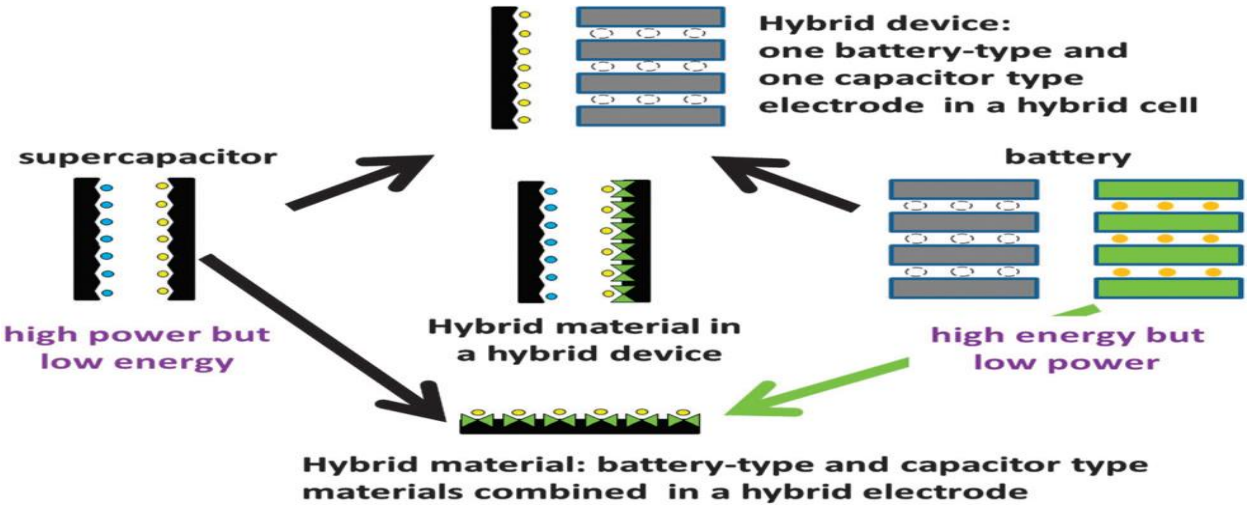

Figure 22. Schematic representations of different possible hybridization approach between supercapacitor and battery electrodes and materials[161].

For instance, a lithium-ion capacitor (Figure 23) combines a porous carbon positive electrode and a negative electrode with a battery-type redox reaction (i.e., insertion, intercalation, or conversion reaction). The cell voltage of lithium-ion capacitors is mostly controlled by the capacitive potential change at the positive electrode, while the negative battery electrode operates only within a narrow potential range. Batteries employ Faradaic reactions of the bulk electrode material which can be of the conversion or insertion/intercalation which is non-capacitive[162].

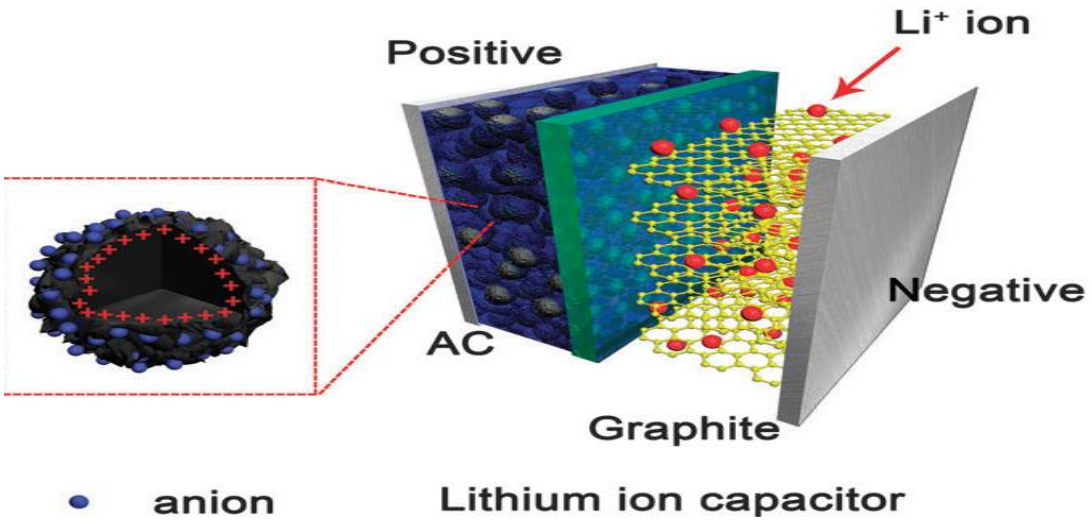

Figure 23. A hybrid lithium ion-capacitor[160].

Hybrid system (Figure 22) consisting of one electrode or a full-cell (device) containing more than a single charge storage mechanism. Hence, the term hybrid system can be applied to both a single hybrid electrode and a hybrid device[162]. Hybrid energy storage devices that combine a non-faradaically (or pseudo-faradaically) rechargeable electrochemical capacitor type of electrode with a faradaically rechargeable battery-type electrode (e.g. acid $PbO_2/PbSO_4$ or alkaline NiOOH/Ni(OH)) are named supercapatteries (Figure 24)[8, 159, 161, 163, 164].

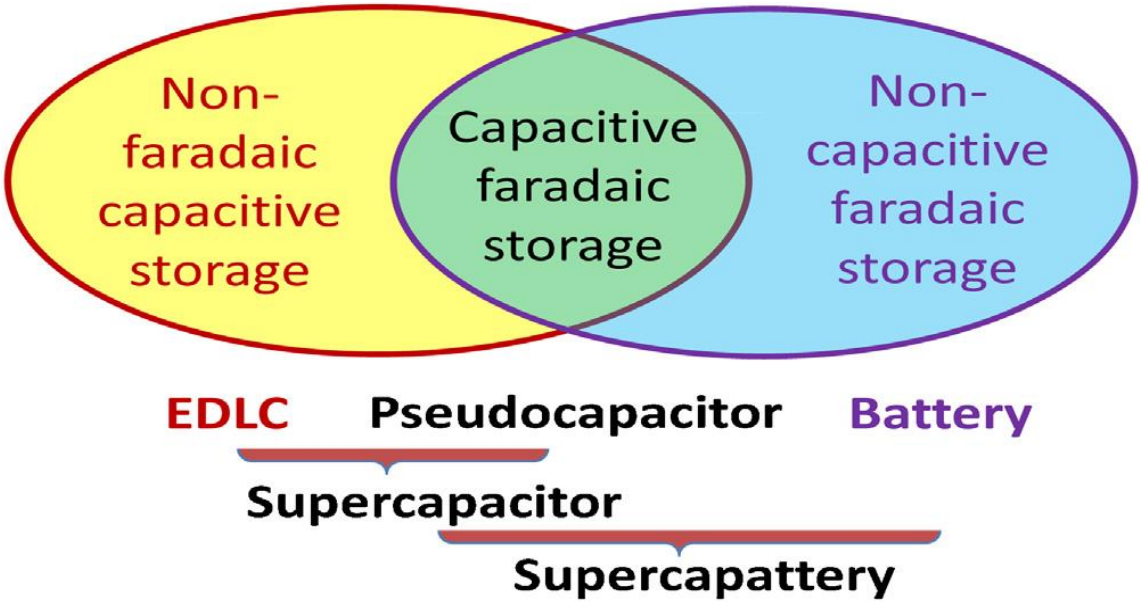

Figure 24. Schematic correlation between EDL capacitor, pseudocapacitor, battery, and supercapattery (hybrid of supercapacitor and battery) in terms of capacitive and faradaic charge storage processes[165].

2.5.2 Performance characterization of supercapacitors

Characterization is key in the supercapacitor system for the optimization and validation of all components towards its performance. The performance of a supercapacitor can be characterized by key parameters such as the cell capacitance, operating voltage, equivalent series resistance, power density, and energy density. Capacitance (F g^{-1}) and energy/power density (Wh kg^{-1} and W kg^{-1}), tested at a specific current density (A g^{-1}), are generally used to evaluate the electrochemical performance of supercapacitors. Cyclic voltammetry (CV), constant current charge/discharge (CCCD), and electrochemical impedance spectroscopy (EIS) tests are

commonly applied to characterize the electrochemical performance of supercapacitors. All such measurement fundamentally determine voltage, current, and time and other metrics, including the capacitance, equivalent series resistance, operating voltage, and, subsequently, the time constant, energy, and power performance of supercapacitor, can be derived from them[166, 167].

2.5.2.1 Cyclic voltammetry (CV) in supercapacitors

CV testing applies a linearly changed electric potential between positive and negative electrodes for two-electrode systems, or between reference and working electrodes for three-electrode configurations. The specific capacitance (Cs) at different scan rates was calculated using Equation (23):

$$\mathbf{C_s} = \frac{\mathbf{1}}{\mathbf{\nu \times m \times \Delta V}} \int_{\mathbf{V_i}}^{\mathbf{V_f}} \mathbf{I dv} \qquad \mathbf{(23)}$$

where I (A) is the response current, ν (Vs^{-1}) is the scan rate, $\Delta V = (V_f - V_i)$ is the potential window, and m (g) is the mass of the active electrode material, V_f and V_i are the final and initial potentials (V), respectively for the forward sweep[167, 168].

In addition to the capacitance and energy performance determination obtained by integrating the CV curves, CV testing by scanning a huge range of scan rates can determine the operating voltage or potential window, reversibility test, and kinetic analysis[153, 167].

2.5.2.2 Constant current charge/discharge (CCCD) test

CCCD test is the most efficient and widely used method of measurement for capacitance evaluation. It is conducted by repetitive charging and discharging of the supercapacitor device or the working electrode at a constant current level and a plot of the potential (E) *vs* time (s) is the output. This method is also called chronopotentiometry and gives access to different parameters such as capacitance, resistance, and cyclability. The specific capacitances for supercapacitors and specific capacity for hybrid materials (battery-like) can be calculated using the following equations:[153, 167, 168]

$$C_s\,(F\,g^{-1}) = \frac{I\Delta t}{m\Delta V} \qquad (24)$$

$$C_s\,(C\,g^{-1}) = \frac{I\Delta t}{m} \qquad (25)$$

$$C_A\,(F\,cm^{-2}) = \frac{I\Delta t}{A\Delta V} \qquad (26)$$

$$C_A\,(C\,cm^{-2}) = \frac{I\Delta t}{A} \qquad (27)$$

where Cs is the specific capacitance (F g^{-1}) or specific capacity (C g^{-1}); CA is the areal capacitance (mF cm^{-2}) or areal capacity (mC cm^{-2}); I is the current (mA or A); Δt is the discharging time (s), ΔV is the potential window and m is the mass of active material (g) and A is the area of the working electrode.

The efficiency of electron transfer within a device which is one of the criteria for the characterization of energy storage devices can be analyzed by calculating the columbic efficiency (η_C) using Equation (31)[155].

$$\eta_c = \frac{t_d}{t_c} \times 100\ \% \qquad (28)$$

where t_d and t_c are discharging and charging time.

Rate capability

Rate capability is one of the most important characteristics of energy storage devices and is studied by measuring the capacitance/capacity of a device at different current densities. A device with a high rate capability shows almost stable capacitance at each current density. EDLC materials often demonstrate high rate capabilities, whereas pseudocapacitive materials, which rely on Faradaic redox reactions for charge storage often result in compromises of rate capability.

Cycling stability

Cycling stability of energy storage devices can be measured by continuously repeating galvanostatic charge-discharge cycles at a given current density for a few hundred (in batteries) to several thousand (in supercapacitors) cycles. The result is often reported as the percent of the initial capacitance/capacity that the device retains after a specified number of cycles[155].

Power and energy density

Power density and energy density are the most directly relevant and widely employed metrics to evaluate the overall performance of the end applications for supercapacitor devices. Power density and energy density describe the efficiency in energy uptake/delivery and the amount of electrical energy stored or deliverable, respectively. They can be expressed either gravimetrically or volumetrically in W kg^{-1} /or W L^{-1} for power density and Wh kg^{-1} or Wh L^{-1} for energy density[166, 167]. The energy and power density of the device can be calculated using the following equations[169, 170]:

$$\mathbf{E} = \frac{\mathbf{1}}{\mathbf{2}}\,\mathbf{C}\,\mathbf{V^2} \qquad \textbf{(30)}$$

$$\mathbf{P} = \frac{\mathbf{E_{cell}}}{\mathbf{\Delta t}} \qquad \textbf{(31)}$$

where C is capacitance; V is the potential window, **E** is specific energy (Wh kg^{-1}, Wh cm^{-3}) and P is power density (W kg^{-1}, W cm^{-3}).

In the case of non-linear galvanostatic charge/discharge characteristics, the specific energy (Wh kg^{-1}) should be calculated by integrating, i.e. finding the area under the galvanostatic discharge curve using Equation (32)[171]:

$$\mathbf{E} = \frac{\mathbf{I}}{\mathbf{3.6m}} \int_{\mathbf{t(V_{max})}}^{\mathbf{t(V_{min})}} \mathbf{V(t)dt} \qquad \textbf{(32)}$$

where E specific energy (Wh kg^{-1}), m is the mass of active material (g), t (V_{max}) and t (V_{min}) is discharge time at maximum and minimum voltage, respectively.

2.5.2.3 Electrochemical impedance spectroscopy (EIS)

EIS is one of the principal methods for examining the fundamental behavior of materials. It estimates capacitance values, charge transfer, and transport-related phenomena occurring at different time scales. The EIS can be expressed as a Nyquist plot (imaginary part of the complex impedance (Im Z) *versus* real part of the complex impedance (Re Z)) on a complex plane. This is composed of three regions, a semicircle at high frequency (larger than 10^4 Hz), presenting the interface resistance, a high-to-medium frequency region (10^4 to 1 Hz), showing the pseudo charge or charge transfer resistance, and a nearly vertical line along the imaginary axis at low frequency (less than 1 Hz), indicating the capacitive behavior. The imaginary part of the impedance (Im Z) and the frequency (f) are related using the Equation (29):

$$\mathbf{C = \frac{1}{2\pi f I_m(Z)}} \qquad \textbf{(29)}$$

where f is the frequency. Normally this frequency is identified at which the phase angle reaches –45 degrees, or simply as the lowest frequency applied.

The contribution of the individual structural component to the total impedance can be determined by fitting the experimental result with suitable equivalent circuit models[166, 167, 170].

2.5.3 Conducting polymers in supercapacitor application

Supercapacitor electrodes and devices that utilize conducting polymers have the potential to bridge the gap between existing carbon-based supercapacitors and batteries to form units of intermediate specific energy. Conducting polymers are pseudo-capacitive materials, which undergo a redox reaction associated with the π-conjugated polymer chains to store charge in the bulk of the material and thereby increasing the energy stored and reducing self-discharge. In general, conducting polymers are more conductive, have high charge density and low cost compared with the relatively expensive metal oxides[153, 172].

Conducting polymers (CPs) can be p-doped with counter anions and n-doped with counter cations when oxidized and reduced, respectively with insertion/deinsertion of counterions. The simplified equations for these two charging and discharging processes are as follows[172]:

$$C_p \underset{\text{discharging}}{\overset{\text{charging}}{\rightleftharpoons}} C_p^{n+}\ (A^-)_n + ne^- \qquad (p-\text{doping})$$

$$C_p\ + ne^- \underset{\text{discharging}}{\overset{\text{charging}}{\rightleftharpoons}} (C^+)_n C_p^{n-} \qquad (n-\text{doping})$$

The insertion/deinsertion of counterions during cycling causes volumetric changes of CPs, with a progressive electrode degradation because of swelling, breaking, and shrinkage, being the origin of a conductivity loss[153].

Supercapacitor devices made solely from conducting polymers can have three configurations[172]:

- Type I (symmetric) using the same p-dopable polymer for both electrodes.
- Type II (asymmetric) using two different p-dopable polymers with a different range of electroactivity.
- Type III (symmetric) using the same polymer for both electrodes with the p-doped form used as the positive electrode and the n-doped form used as the negative electrode.

In addition, asymmetric (or hybrid) devices can be constructed using a conducting polymer and carbon, lithium, zinc, lead oxide (PbO_2), or lead sulfate electrode[172-174].

Theoretically, a Type III device based entirely on conducting polymers should be highly conductive in the charged state, release charge at higher potentials (up to at least 3 V) compared with Type I and Type II devices and in turn, result in high specific energy and power. In reality, these types of conducting polymer supercapacitor devices do not perform as expected due to the difficulty of the n-doping process. Many conducting polymers, such as polyaniline and polypyrrole, can only be p-doped due to the very negative potentials requirement for n-doping which is below the reduction potential limit of molecular solvent-based electrolytes. Therefore, n-doping requires a purified electrolyte or a room temperature ionic liquid with a wide electrochemical window[172].

Polythiophene is a promising n-dopable material but it is n-doped at very low potentials (below −2.0 V *vs* Ag|Ag+) and has low stability to oxygen and water, as well as lower conductivity than in the p-doped state. By substituting at the 3-position of the thiophene ring with phenyl, ethyl and alkoxy groups can improve stability to oxygen and water while substitution at the 3-position

with an aryl group results in more positive n-doping potentials. Some of these derivatives are shown in Figure 25[172].

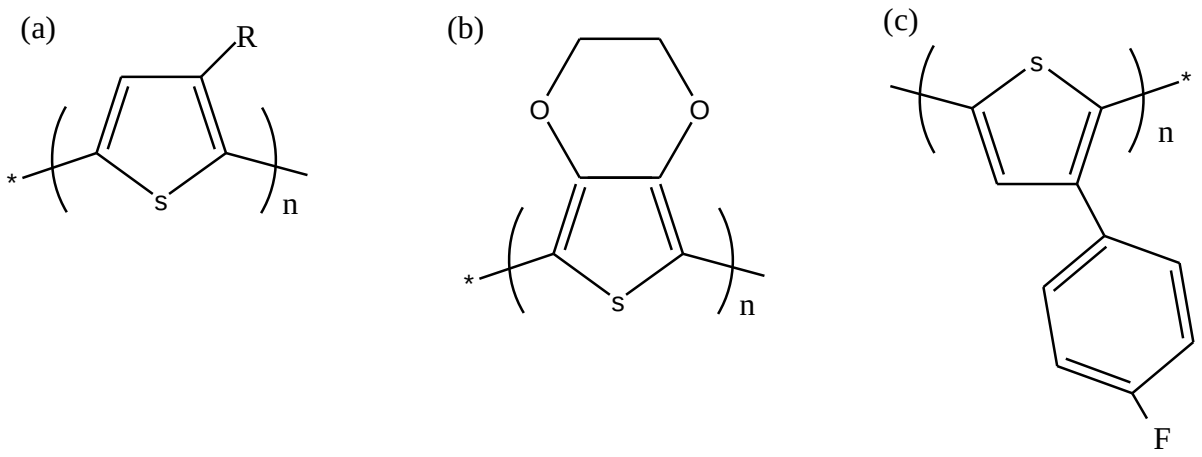

Figure 25. (a) 3-substituted polythiophene, (b) poly(3,4-ethylenedioxythiophene) (PEDOT), (c) poly(3- (4-fluorophenyl) thiophene) (PFPT).

2.5.3.1 PEDOT:PSS in supercapacitors

A popular thiophene derivative is poly(3,4-ethylenedioxythiophene) (PEDOT) which has been widely studied as electrode material in supercapacitors for its considerable capacitance, wide potential window, high conductivity, and stability. The polymer is electroactive over a particularly wide potential window (nearly 2.0 V), but the smallest specific capacitance due to a combination of the large molecular weight of the monomer unit and the low doping level. This polymer has a low band gap of 1 – 3 eV, is highly conducting in the p-doped state (300–500 S cm^{-1}), has good thermal and chemical stability and high charge mobility that results in fast electrochemical kinetics. The polymer has also been found to have good film-forming properties

and can be switched rapidly with a minimum of side reactions leading to a long cycle-life. One of the major limitations of PEDOT is that the monomer cannot be dissolved in aqueous solvents. Consequently, a volatile and toxic organic solvent, such as acetonitrile, is generally used to deposit the polymer[39, 172]. The incorporation of water-soluble insulating polystyrene sulfonate (PSS) to PEDOT leads to the enhancement of the dispersibility in an aqueous solution and some polar organic solvents due to the formation of the polyelectrolyte complex of PEDOT:PSS, resulting in better processibility and allows good device performance when using aqueous electrolytes. PSS serves as an excellent oxidizing agent, charge compensator, and a template for polymerization[41, 146].

PEDOT:PSS (Figure 26a) is the most studied and explored mixed ion-electron conducting polymer system. PEDOT:PSS is commonly included as an electroactive conductor in supercapacitors, displays, transistors, and energy-converters. Generally, charge storage in supercapacitors is due to electric double-layers formed along with electrode/electrolyte interfaces or is related to pseudocapacitance[145, 175]. It is widely accepted that charge storage in PEDOT:PSS like all other conducting polymers is related to the redox process (doping/dedoping) occurring during charging/discharging through a combination of charge injection into the polymer backbone from the current collector and ion exchange from the electrolyte to maintain charge neutrality in the film (pseudocapacitance)[172, 176]. However, experimental evidence and theoretical modeling results reported by Volkov et al.[175] significantly depart from this commonly accepted picture. It is demonstrated that the major contribution to the capacitance originates from electrical double layers formed along with the interfaces between nanoscaled PEDOT-rich and PSS-rich interconnected grains (Figure 26b) that comprises two phases of the bulk of

PEDOT:PSS. This mechanism resembles the one present in supercapacitors based on porous electrodes storing the charge by the formation of an electric double layer (a non-Faradaic phenomenon).

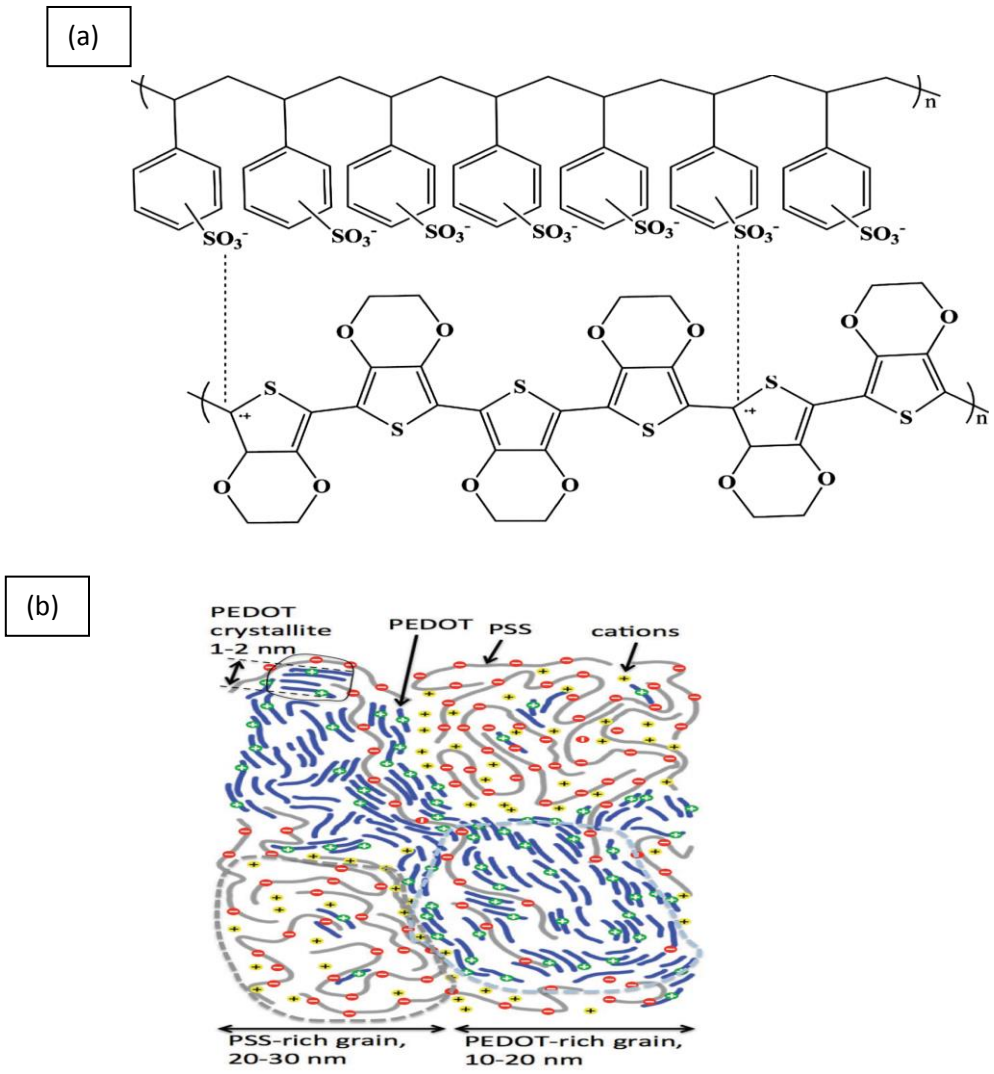

Figure 26. (a) Chemical structures of PEDOT:PSS and (b) Schematic diagram of the morphology model.

2.5.3.2 PEDOT:PSS for flexible supercapacitors

Guo et al.[39] reported PEDOT film on a flexible ITO/PET substrate prepared by electrochemical polymerization at a constant potential of 1.0 V. The PEDOT electrode shows an area capacitance of 4.3 mF cm^{-2} and specific capacitance of 108 F g^{-1} at a current density of 0.1 mA cm^{-2}. Lehtimaki et al.[74] improved the capacitance of PEDOT from 14 mF cm^{-2} to 18 mF cm^{-2} by electrochemically synthesized composite films of PEDOT in the presence of GO in the ionic liquid 1-butyl-3-methylimidazolium tetrafluoroborate ($BMIMBF_4$) onto flexible graphite-poly(ethylene terephthalate) substrates. Cheng et al.[40] successfully fabricated multilayer free-standing PEDOT:PSS electrode by spin-coating of a doped PEDOT:PSS solution. They show an improved areal specific capacitance and energy density with the increase of the PEDOT:PSS layers, suggesting larger electrochemical storage capability of the supercapacitors with more PEDOT:PSS layers. The explanation for this improvement was mainly because of an increase in the mass of the active materials, namely the PEDOT, with an increase in the layers. Several research groups studied PEDOT or PEDOT:PSS composites with rGO[177], RuO_2[178], molybdenum disulfide[179], polyaniline[180], and CNT[181] for flexible or stretchable supercapacitors.

2.5.4 Electrolytes for supercapacitors

The electrolytes are one of the vital constituents of electrochemical energy storage devices, and their physical and chemical properties play an important role in these devices' performance, including capacity, power density, rate performance, cyclability and safety[160, 182]. Electrolytes must have a high concentration of mobile ions, low resistance, low concentration of electrically

active impurities, and be chemically stable[183]. Various type of electrolyte and their classification is shown in Figure 27[182].

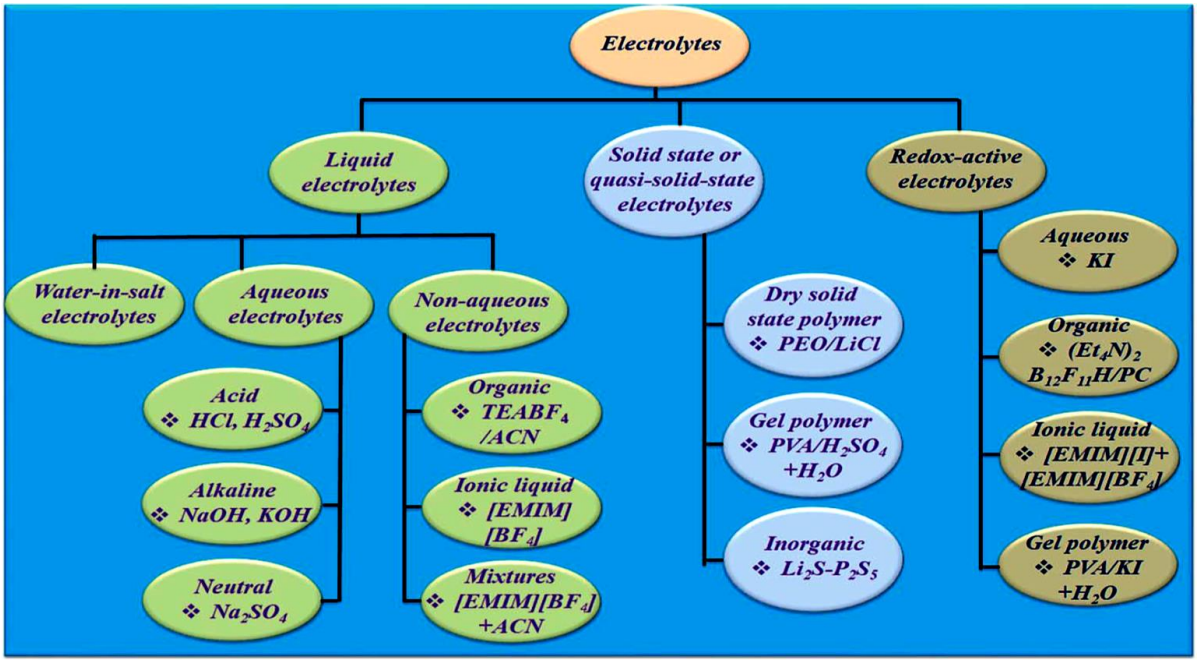

Figure 27. Classification of electrolytes for electrochemical supercapacitors.

Organic electrolytes have a wide electrochemical stability window (approximately 2.7 V) but they are, expensive, flammable, and in some cases, toxic. Although aqueous electrolytes (alkaline and acidic) have a narrower electrochemical stability window (approximately 1.23 V), they are non-flammable, inexpensive, have higher ion conductivity, and higher capacitance due to smaller ions. However, they require low-cost, electrochemically stable materials that withstand the aggressive nature of the aqueous environment. Ionic liquids (ILs) are generally defined as those salts composed solely of ions (cations and anions) with melting points below 100^0C. High thermal, chemical and electrochemical stability, negligible volatility,

and non-flammability are some advantages of IL. Low conductivity and high viscosity can significantly increase the equivalent series resistance (ESR) values which limit power performance unless it is compensated by the increase of cell voltage. Major types of solid-state electrolytes developed for ESs are polymer-based and very limited work has been focused on inorganic solid materials (e.g., ceramic electrolytes). The major advantages of such electrolytes are the simplification of packaging and fabrication processes. An electrolyte may contain redox mediators (e.g. KI) which contribute extra capacitance to the electrolyte from the reduction/oxidation of the redox mediator. Such electrolyte is redox-active electrolytes. Highly concentrated "water in salt" electrolytes are also promising electrolytes for energy storage devices. However, their high viscosity, low conductivity, and salt precipitation at low temperatures affect the performance of energy storage devices[160, 182-184].

3. Experimental

3.1 Reagents and materials

Potassium nitrate (Riedel de Haen), sodium nitrate (Sigma-Aldrich), lead nitrate (Wagtech International Ltd,UK), sodium chloride (Wagtech International Ltd,UK), 8-amino-2-naphthalene sulfonic acid (8-ANSA) (Sigma-Aldrich), 5-amino-1-naphthalene sulfonic acid (5-ANSA) (Sigma-Aldrich), 2-amino-1-naphthalene sulfonic acid (2-ANSA) (Sigma-Aldrich), 4-amino-1-naphthalene sulfonic acid (4-ANSA) (Sigma-Aldrich), potassium chloride (Sigma-Aldrich), nitric acid (Sigma-Aldrich), potassium hexacyanoferrate (III) (Riedel de Haen), hydrogen peroxide (Riedel de Haen), potassium permanganate (BDH), potassium hydroxide (BDH), graphite (Riedel de Haen), hydrochloric acid (Carlo Erba Reagents), ethylene glycol (Sigma-Aldrich), sodium sulfate (Sigma-Aldrich), 5 wt% nafion solution (Sigma-Aldrich), 4.0 mg mL^{-1} graphene oxide dispersion in water (Sigma-Aldrich), 70% perchloric acid (Fluka), 98% sulfuric acid (Carlo Erba Reagents), hexachloroplatinic acid (Research Lab Fine Chem Industries) phosphomolybdic acid, $H_3PMo_{12}O_{40}.nH_2O$ (Alfa Aesar), lignosulfonate (LC 30, Mw = 13 400, Medwestveco), and Clevios PH1000 (PEDOT:PSS) (Heraeus) were used for the preparation of electrolyte solutions and inks for electrode preparation. Indium tin oxide on polyethylene terephthalate (ITO/PET) plastic sheets (thickness of 125 mm and square resistance of 50 Ω) was purchased from FOM Technologies, Denmark. Nitrogen and oxygen gases were purchased in cylinders from Chora gas and chemical product factory. Deionized (DI) water was used throughout the experiment.

3.2 Instruments and apparatus

A potentiostat/galvanostat (Autolab PGSTAT 128N) (Figure 28a) connected to a computer with a general purpose electrochemical system (GPES v 4.9) software and Pine bipotentiostat (model AFCBP1) (Figure 28b) connected to a computer with aftermath (v 1.2.5033) software were used to characterize the electrochemical properties of different materials. Pine rotation speed controller (AFMSRCE 2957) (Figure 28c) was used during the RDE and RRDE measurements.

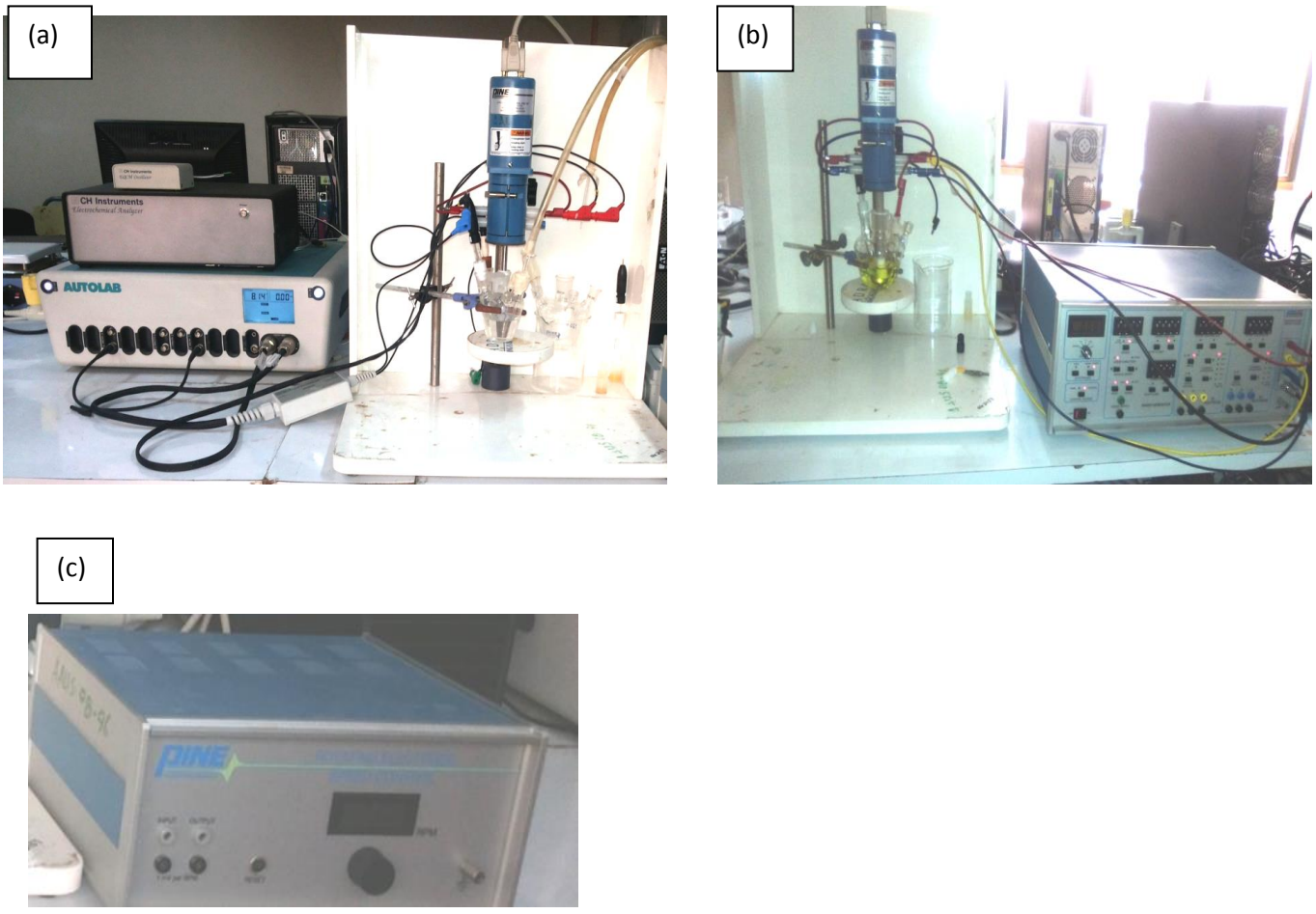

Figure 28. Electrochemical set up in (a) Autolab potentiostat/galvanostat (b) Pine bipotentiostat and (c) Pine rotation speed controller.

AFM was used to study the sample's surface morphology and dispersion of nanoparticles using a Nanotec Electronica SPM (Figure 29a). The images were processed with Ws x M software (v 3.1).

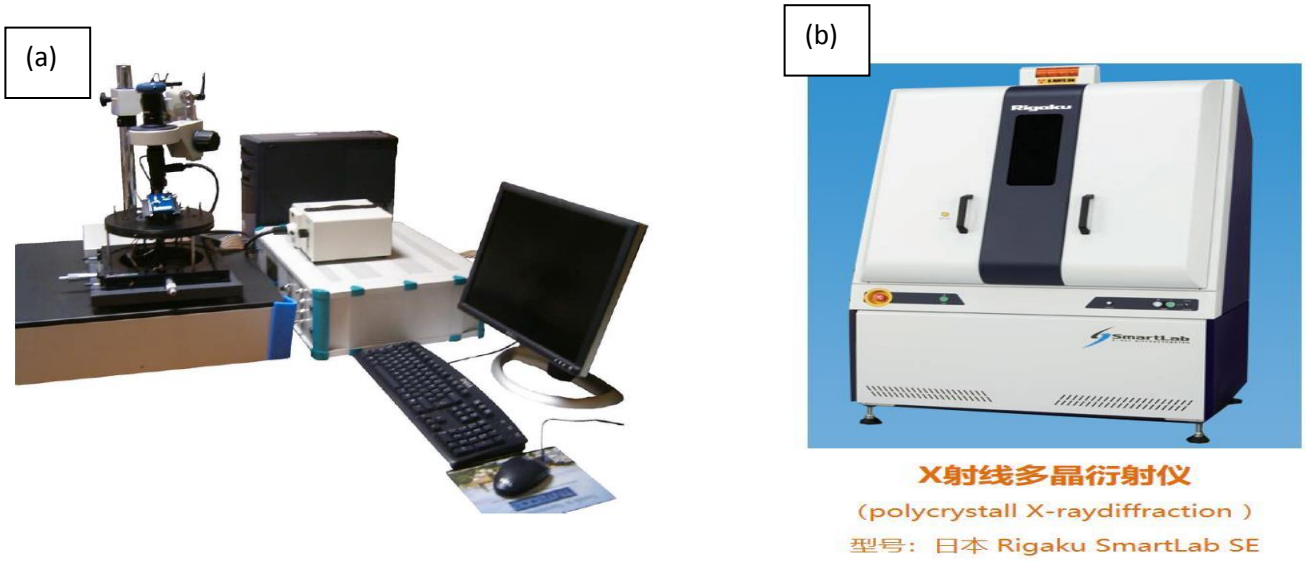

Figure 29. (a) AFM instrument set up and (b) Rigaku Smart Lab SE X-ray diffractometer.

XRD spectra were collected using Rigaku Smart Lab SE X-ray diffractometer (Cu-Kα radiation at λ = 0.15406 nm) (Figure 29b). The average crystallite size of the nanoparticles was estimated using the Debye–Scherrer Equation (33)[23, 35]:

$$\mathbf{Z = \frac{k\ \lambda}{B_{2\theta}\ \cos\theta}} \qquad \mathbf{(33)}$$

where Z is the diameter of the average crystallite size (angstrom or nm); $\boldsymbol{\lambda}$ is the X-ray wavelength (1.5406 A) for Cu Kα; θ is the Bragg angle; k is the Scherrer constant (typically from 0.9 to 1.0); B is the full width at half maximum.

X-ray photoelectron spectroscopy (XPS) measurements were performed with a Thermo ESCALAB 250Xi equipped with a monochromatic Al (Ka) X-ray excitation source operated at hν = 1486.6 eV (Figure 30a).

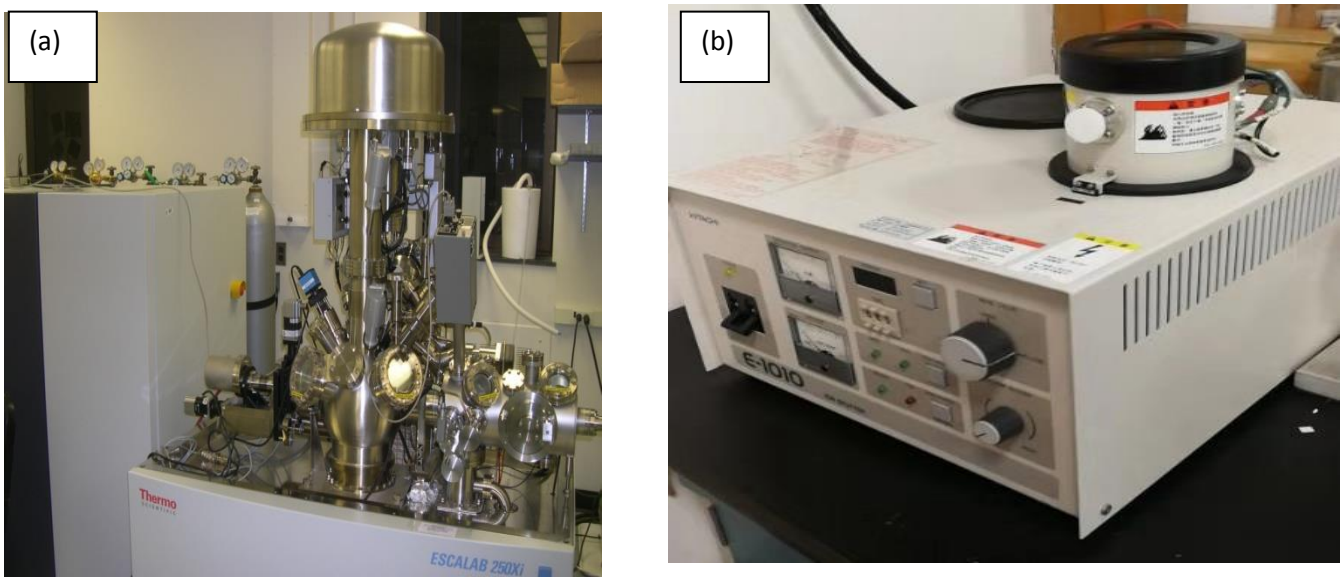

Figure 30. (a) Thermo ESCALAB 250Xi and (b*)* Hitachi, S-4800 for FESEM imaging.

FESEM measurement were performed on Hitachi, S-4800 (Figure 30b) and an EDS (HORIBA, EX-250) coupled on the FESEM was used to confirm the component in the samples.

PerkinElmer Spectrum 65 FT-IR Spectrometer (Figure 31a) was used to record the infrared spectra. Conducting plastic film electrodes were made using desk-top roll-to-roll printer from FOM Technologies, Denmark (Figure 31b). The thickness roll to roll printed were measured with Bruker Dektak XT profilometer (Figure 31c).

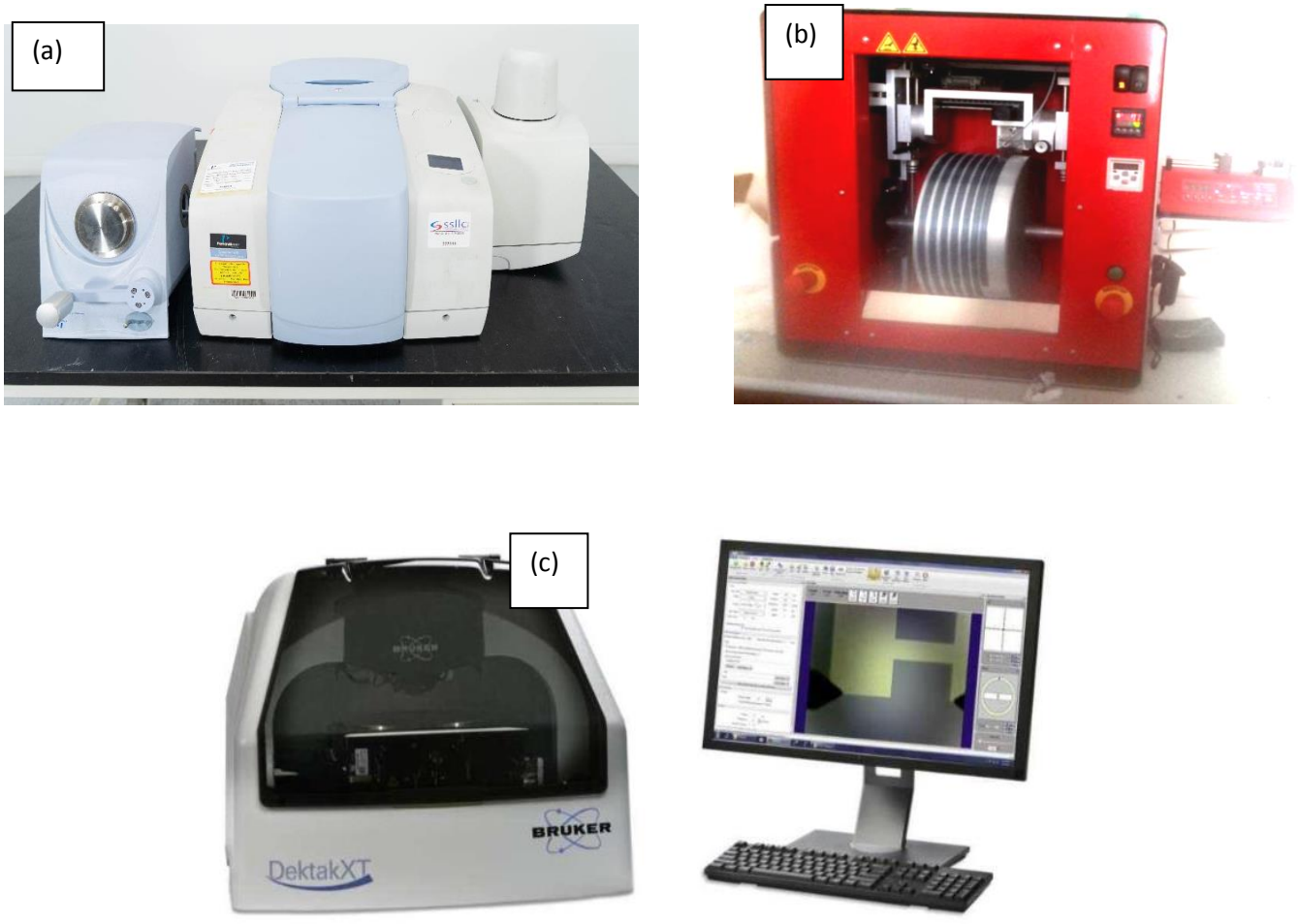

Figure 31. (a) PerkinElmer Spectrum 65 FT-IR Spectrometer (b) A picture of the desktop roll-to-roll printing machine and (c) Bruker Dektak XT profilometer.

3.3 Electrode preparation and electrochemical characterization

3.3.1 Preparation of platinum nanoparticles dispersed on electrochemically reduced graphene oxide/PEDOT:PSS composites glassy carbon electrode (GCE)

3.3.1.1 Preparation of the modified glassy carbon electrode (GCE)

The Pt support were first prepared by drop casting 3 µL of PEDOT:PSS without EG (PEDOT:PSS), PEDOT:PSS and rGO/PEDOT:PSS with EG (PEDOT:PSS (EG), rGO/PEDOT :PSS (EG)) onto a 0.196 cm^2 glassy carbon disk electrode (polished with 0.05 µm alumina powder). 6 vol % EG which is optimal concentration to improve the conductivity was added on PEDOT:PSS[185]. The addition of EG induces a conformational change in the PEDOT chain from a benzoid with a preferred coiled structure to a quinoid with a preferred linear or expanded-coil structure. This conformational change results in an increase in the intrachain and interchain charge-carrier mobility[145]. The films were then dried under room temperature overnight. The GO:PEDOT:PSS(EG) composites were prepared by mixing solution of GO and PEDOT:PSS(EG) in weight ratios of 2:1, 1:1, 1:2, 1:3 and 1:5 (GO:PEDOT:PSS(EG)).

The electrochemical reduction of GO to rGO was carried out with CV in the potential range from 0 to -1.5 V *vs* Ag/AgCl at a scan rate of 50 mV s^{-1} in N_2 saturated 0.1 M Na_2SO_4 for 20 cycles[68]. Pt particles were then electrodeposited onto PEDOT:PSS, PEDOT:PSS(EG) and rGO/PEDOT:PSS(EG) potentiostatically from a 5 mM H_2PtCl_6 in 0.5 M H_2SO_4 by applying a potential of -0.15 V (*vs* Ag/AgCl) until the amount of charge consumed to reduce Pt (IV) to Pt

(0) were 10% (m_{Pt} = 3.6 μg), 20% (m_{Pt} = 8.1 μg), 30% (m_{Pt} = 13.85 μg) and 40% (m_{Pt} = 21.6 μg) of the total mass the catalytic material assuming 100% current efficiency[34, 36]. Galvanostatic deposition of 40% platinum on PEDOT:PSS/GC for 10 s (at -4.5 mA), 15 s (at -3 mA), 20 s (at -2.25 mA), 30 s (-1.5 mA) and 40 s (-1.125 mA) were also performed. The quantity of electricity associated with double-layer charging and the reduction of surface oxide is obtained by integration in the double layer region and subtracted from the total charge for determining the mass of platinum loading[34]. 3 μL of Nafion (0.05%) was dropped on the catalyst film as a binder[186].

For comparison purposes, a thin film electrode made from a commercial Pt/C catalyst (Etek) (20 wt%) were deposited on rotating glassy carbon electrode with Pt loading of 20 mg Pt cm^{-2}.
10 mg of a 20 wt% Pt/C catalyst (Etek), 1 mL of isopropanol, 3.98 mL of deionized water and 20 mL of 5 wt% Nafion ionomer solution were mixed, ultrasonicated for 60 minutes in a water bath for the catalytic ink formation. 10 mL of the resulting suspension was dropped on glassy carbon disc electrode (0.196 cm^2) dried using solvent evaporation by covering the catalyst ink-coated electrode with a beaker to get smooth and crack free film[187].

3.3.1.2 Determination of electrochemically active surface area (ECSA)

PEDOT:PSS/Pt, PEDOT:PSS(EG)/Pt and rGO/PEDOT:PSS(EG)/Pt electrode were cycled between 0 and 1.20 V *vs* RHE for 40 cycles at 200 mV s^{-1} in 0.1 M $HClO_4$ nitrogen saturated (25 min) solution to remove residues hidden in the porous electrode and obtain stable CV curves. Then, cyclic voltammograms (3 cycles) recorded at a scan rate of 20 mV s^{-1} between 0.05 V and

1.20 V were used to determine the ECSA of the Pt catalysts. The ECSA was estimated using Equation (4) by integrating the hydrogen adsorption charge (Q) in the potential range from 0.40 to 0.075 V after correction for double-layer charging[187] .

3.3.1.3 Determination of kinetic current (i_k), mass activity (MA) and specific area activity (SA)

After the ECSA measurements, linear sweep voltammograms on RDE were recorded at 20 mV s^{-1} between 0.05 V and 1.03 V under O_2 or N_2 saturated 0.1 M $HClO_4$. The net Faradic current was obtained by subtracting the voltammogram recorded under N_2 from the one recorded under O_2[113, 187]. Then, the mass transport corrected kinetic current is extracted from the mixed activation-diffusion region of linear sweep voltammograms using Equation (12). MA and SA were calculated using Equations (15) and (16).

3.3.1.4 Determination of collection efficiency (N), number of electrons transferred (n) and percentage of H_2O_2 (% H_2O_2)

RRDE measurements were carried out at room temperature on a Pine bipotentiostat connected to a computer with aftermath (v 1.2.5033) software. Glassy carbon disk electrode (0.2472 cm^2) surrounded by a Pt ring (0.1859 cm^2) was used for RRDE measurements. Silver/silver chloride (Ag/AgCl, 3 M KCl) and a platinum wire served as reference and counter electrodes, respectively. Pine rotation speed controller (AFMSRCE 2957) was used during the RDE and

RRDE measurements. The measured potential of this reference electrode was converted to the RHE reference scale using E (*vs* RHE) = E (*vs* Ag/AgCl) + 0.21 V + 0.0591 V × pH[188]. Correction for IR drop was made after solution resistance was determined using electrochemical impedance spectra obtained for RDE catalyst layers using a frequency response analyzer (FRA, AutoLab) under N_2 or O_2 atmosphere at a rotation rate of 1600 rpm in the frequency range from 10 kHz to 0.1 Hz with a 5 mV amplitude voltage perturbation.

The disk and ring currents were recorded as a function of the disk potential scanned between 0 V and 1.2 V *vs* RHE at 10 mV s^{-1} at one rotation speed (1600 rpm). The ring electrode potential being held at +1.3 V *vs* RHE. The amount of N was determined using 1 M KNO_3 and 10 mM $K_3Fe(CN)_6$ deaerated with pure nitrogen[23, 189]. n, % H_2O_2 and the amount of N were calculated using Equations (17), (18) and (19), respectively.

3.3.1.5 Stability and electrochemical crossover test

The methanol tolerance ability of the catalyst was analyzed by chronoamperometry in O_2-saturated 0.1 M $HClO_4$ solution at a rotation speed of 1600 rpm and an applied potential of 0.8 V (*vs* RHE). The durability was performed by chronoamperometry in O_2-saturated 0.1 M $HClO_4$ at a rotation speed of 1600 rpm and an applied potential of 0.8 V (*vs* RHE) for 9,000 s.

3.3.2 Preparation of graphene/amino substituted naphathalene composite for metal-free catalyst

3.3.2.1 Synthesis of GO

Graphene oxide was synthesized from graphite powder using modified Hummer's method[190]. Specifically, graphite powder (1 g) and sodium nitrate (0.5 g) were mixed and added to concentrated sulphuric acid (23 mL) in a beaker under constant stirring at room temperature. The beaker was put in an ice bath for cooling to 0^{o}C under constant stirring for one hour and potassium permanganate (3 g) was added gradually to the mixture while keeping the temperature less than 20^{o}C. The mixture was stirred in a water bath at 35^{o}C for 6 hours to form a thick paste and the resulting solution was diluted by adding 500 mL of water under vigorous stirring. Subsequently, the suspension was further treated with 30% H_2O_2 solution (5 mL) to terminate the reaction. The resulting mixture was washed with a 1:10 HCl aqueous solution followed by filtration. The collected solid material was dried in a vacuum oven to obtain GO.

3.3.2.2 Electrochemical reduction of GO

Five mg GO was dispersed in 10 mL deionized water and ultrasonicated for 1 h. 20 μL of the graphene oxide dispersion (0.5 mg mL^{-1}) was drop-casted onto the pre-polished glassy carbon electrode (GC) or on polymer-modified GC (GC/poly(ANSA)) and was left to dry slowly in the air.

After drying, 3 μL 0.05 wt.% Nafion solution was applied to the surface of the resulting electrode to improve the adhesion of the film to the electrode surface. The electrochemical reduction of GO to rGO was carried out with cyclic voltammetry in the potential range from 0 to -1.5 V *vs* Ag/AgCl at a scan rate of 50 mV s^{-1} in N_2 saturated 0.1 M Na_2SO_4 for 20 cycles[68, 191].

3.3.2.3 Electropolymerization

Electropolymerization of 2 mM of the monomers (8-ANSA, 2-ANSA, 4-ANSA, and 5-ANSA) on bare glassy carbon electrode (GC) or on GC/rGO in 0.1 M HNO_3 was performed using cyclic voltammetry by scanning the potential between -0.8 V and 2.0 V *v*s Ag/AgCl at a scan rate of 100 mV s^{-1} for 16 cycles. Then, the modified electrode was stabilized for 24 cycles in monomer free 0.5 M H_2SO_4 until a stable cyclic voltammogram was obtained[36].

3.3.2.4 Electrochemical measurements

The oxygen reduction reaction was carried out in 0.1 M KOH solution. The oxygen reduction currents were recorded in oxygen saturated 0.1 M KOH. Cyclic and linear sweep voltammograms were recorded at a scan rate of 20 mV s^{-1}. For the RRDE measurement, the disk and ring currents were recorded as a function of the disk potential scanned between - 0.7 V and 0.1 V *vs* Ag/AgCl at 10 mV s^{-1} at one rotation speed (1600 rpm). The ring electrode potential was held at +1 V *vs* Ag/AgCl[138]. The collection efficiency (N) was determined using 1 M KNO_3 and 10 mM $K_3Fe(CN)_6$ deaerated with pure nitrogen. The measured collection efficiency was found to be 38±1.5%. The oxygen reduction currents were normalized to the geometric area of

the electrode and corrected for the background electrode current recorded in pure nitrogen saturated 0.1 M KOH solution[187].

3.3.3 Roll-to-roll printed electrodes

3.3.3.1 Electrode coating procedure

First, ITO-free PET and ITO PET-foil (1 m length) were mounted on the roller using heat-stable tape (3 M). Roll-coated PEDOT:PSS and Lg/PEDOT:PSS, Mo/PEDOT:PSS and Mo/Lg/PEDOT:PSS were fabricated on both substrate (ITO/PET or PET) using the blend of PEDOT:PSS and 6 vol % EG for pristine PEDOT:PSS and 8 mg mL^{-1} phosphomolibidic acid and 5 mg mL^{-1} lignosulfonate for Lg/PEDOT:PSS, Mo/PEDOT:PSS and Mo/Lg/PEDOT:PSS. The blend was transferred from a syringe *via* the pump to the slot-die head and roll-coated on the top of ITO-free PET and ITO PET-foil in the form of 12 mm wide stripes. The coating was performed under ambient air, with the roller kept at 70^0C and with a web speed of 0.58 m min^{-1}. The flow of the solution was set to 0.65 mL min^{-1}. After drying, the mass of active material was weighed using XPR Micro and Ultra-Microbalances (Mettler Toledo). Samples of the printed films are shown in Figure 32.

Figure 32. A picture of samples of the printed plastic films.

3.3.3.2 Preparation of gel and liquid electrolyte for SCs devices

The PVA/H_2SO_4 gel electrolyte was prepared by mixing PVA powder (1.0 g), H_2SO_4 (1.0 g), and deionized water (10.0 mL). The mixture was then heated at 85^0C under stirring until the solution becomes clear[192]. Finally, the viscous solutions were cast into polystyrene-molds and dried at room temperature. The dried gel films were peeled off the molds, cut, and put between two electrodes followed by pressing them together to assemble into a SCs.

Aqueous solution of 0.1 M NaCl or Pb^{2+}/0.1 M NaCl were used for devices with liquid electrolyte. The symmetric supercapacitors were assembled by sandwiching two roll-to-roll printed PEDOT:PSS on ITO/PET electrodes together with separator monolayer filter paper (ASTM E 832-81). The filter paper separator was soaked in aqueous solution of 0.1 M NaCl or Pb^{2+}/0.1 M NaCl.

3.3.3.3 Electrochemical measurements

The electrochemical properties of the electrode materials and symmetric devices were investigated both in 3-electrode (Figure 33a) and 2-electrode configurations (Figure 33b). The electrode materials and the devices were cycled 10 times before recording the final data. Galvanostatic charge/discharge curves were used to calculate the specific capacitance (Equation 24 or Equation 26), the specific capacity (Equation 25 or Equation 27), columbic efficiency (Equation 28), energy density (Equation 30 or Equation 32), and power density(Equation 31).

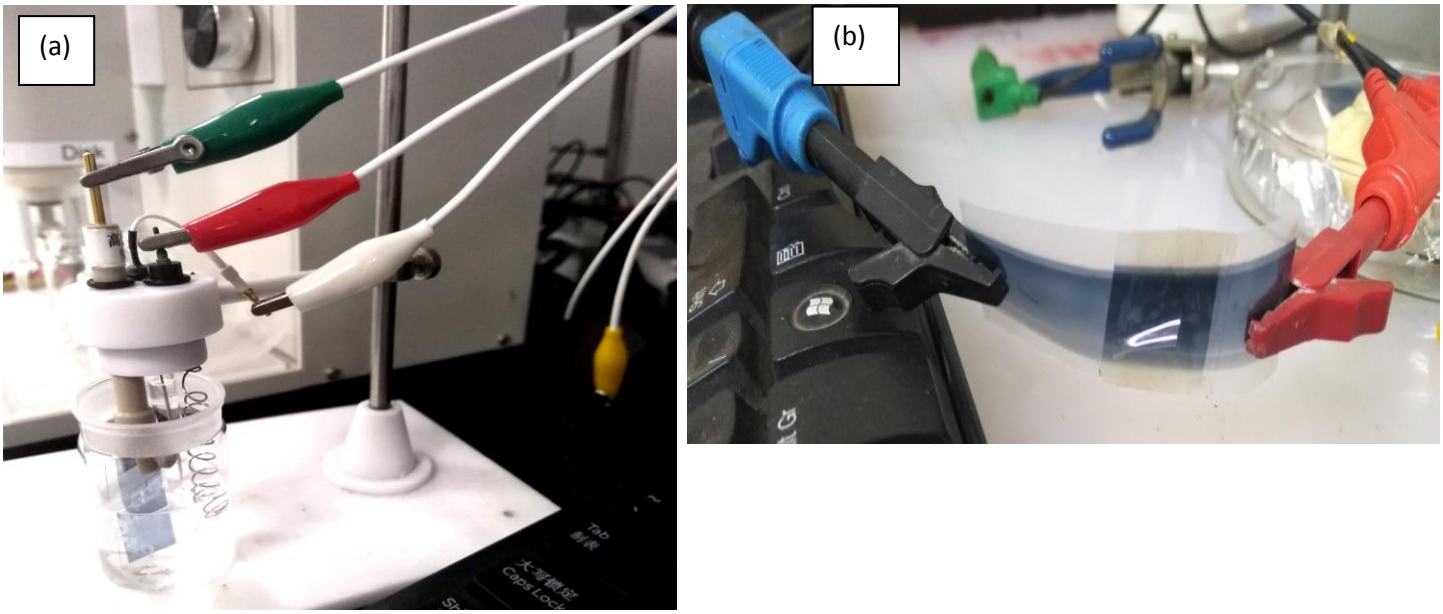

Figure 33. Electrochemical setup for (a) 3-electrode and (b) 2-electrode system.

3.4 Physical characterization of electrodes

The crystalline structure of platinum catalyst (PEDOT:PSS/Pt, PEDOT:PSS(EG)/Pt) and the structural changes occurring during the conversion of graphite to GO were investigated by using XRD.

AFM was used to study the sample's surface morphology and dispersion of Pt nanoparticles on PEDOT:PSS and PEDOT:PSS(EG).

The morphology of rGO/PEDOT:PSS(EG)/Pt was characterized by a FESEM and EDS was used to confirm the component of the rGO/PEDOT:PSS(EG)/Pt.

Samples for XPS were pristine roll to roll printed PEDOT:PSS on ITO/PET, lead deposited on PEDOT:PSS/ITO/PET, Mo/PEDOT:PSS ITO/PET, Lg/PEDOT:PSS ITO/PET, and Mo/Lg/PEDOT:PSS ITO/PET. The thickness of PEDOT:PSS, Mo/ PEDOT:PSS, Lg/PEDOT:PSS, and Mo/Lg/PEDOT:PSS on ITO/PET were 1012.75 nm, 1186.6 nm, 1552 nm, and 1357.3 nm, respectively.

3.5 Computational Details

All calculations were carried out with the Gaussian 16 program package[193]. The B3LYP[194-196] functional together with the 6-311++G(d,p) basis sets[197] were used. Solvent effects were corrected by using the polarizable continuum model (PCM) in its integral equation formalism[198] together with water as a solvent. Vibrational frequency analyses were performed to verify that the optimized structures are minima without an imaginary frequency and to obtain the free

energies of the dimers and their complexes. The Natural Bond Orbital (NBO) analysis[199, 200] was used to explore the charges on the atoms before and after the adsorption of the molecular oxygen on the dimers.

4. Results and discussion

4.1 Electrocatalytic reduction of oxygen at platinum nanoparticles dispersed on electrochemically reduced graphene oxide/PEDOT:PSS composites

4.1.1 Background

Commercialization and widespread application of fuel cells and metal-air batteries in different sectors demand the development of catalyst materials with low cost and satisfactory activity and stability[201, 202]. In all these applications, the oxygen reduction reaction (ORR) at the cathode is the major contributor to single-cell efficiency losses due to its slow kinetics. Hence, platinum (Pt) and Pt-based alloys are commonly employed catalysts to improve the kinetics of the ORR[202, 203]. However, the cost of Pt is very high and its supply is limited[32]. To circumvent this problem, several authors investigated and reported non-Pt based catalysts[204, 205] and while others used Pt-dispersed nanoparticles on different supports[201, 202] to reduce the amount of Pt-loading. The dispersion of Pt on catalyst support not only reduces the cost of the noble metals but also improves the efficiency of the electrocatalysts[131, 206]. Higher catalytic activity on a support matrix requires nanometric dimensions with a uniform distribution of Pt particles[15].

Various carbon-based materials such as carbon blacks, carbon nanotubes, carbon nanofibers, multiwall carbon nanotubes, conducting polymers, and graphene have been extensively investigated as Pt supports for ORR[15, 124, 131, 201, 207, 208]. Among these, graphene (or reduced graphene oxide, rGO) has become more attractive in recent years due to its unique physicochemical properties, like excellent conductivity, high charge-carrier mobility, good

transparency, great mechanical flexibility, and huge specific surface area [14, 121, 124, 208]. However, weak interaction of graphene with metals and restacking of graphene sheets due to pi-pi interaction are still some of the problems that are hindering its application as electrocatalyst support for Pt-NPs[9, 124]. On the other hand, conducting polymers, which are good catalysts for ORR and support materials for the dispersion of Pt metal catalysts, prevent aggregation of graphene sheets and particle agglomeration in addition to their high accessible surface area, low resistance and high stability in three-dimensional structure[17, 19, 121, 209].

Among conducting polymers, PEDOT:PSS is one of the most versatile and commercially available polymers successfully used in many different applications like organic solar cells, organic light-emitting diodes, energy storage, transistors, and sensors[210]. It can also be promising support material for Pt particle dispersion due to its chemical stability, dispersibility in water, and some organic solvents, tunable conductivity, and electrochemical performance[40, 144]. Though dependent on the method of synthesis and microstructures, PEDOT[141, 142] and PEDOT:PSS[138] also shows electrocatalytic activity for ORR. Since the electrocatalytic ORR on Pt in acidic solution is a proton-coupled electron transfer reaction[18], PEDOT:PSS, which has a polyanionic phase (PSS) will promote proton transport. The conducting polymer phase (PEDOT) further ensures electronic transport[211]. Moreover, the high boiling point polar organic compounds like ethylene glycol added into PEDOT:PSS aqueous solution to improve its conductivity [145] is known to improve the activity of Pt-supported catalyst by decreasing the average particle size, inhibition of growth of Pt particle, and evenly dispersion of Pt particle[35]. Hence, a composite of rGO and PEDOT:PSS treated with ethylene glycol combined the best features of each material. As part of numerous efforts in the search for reducing the amount of

Pt used in the electrocatalytic reduction of oxygen, this work investigates the potential application of commercially available GO and PEDOT:PSS composites with solvent additive EG as an alternative support for Pt-NPs towards ORR.

4.1.2 Galvanostatic deposited platinum on PEDOT:PSS

The typical chronopotentiometric curve for galvanostatic electrodeposition of 40% platinum on PEDOT:PSS/GC are shown in Figure 34. The curves can be divided into four-time intervals. In the beginning, the first time interval (I), Pt (IV) chlorine-complex adsorption to electrode surface occur and adsorbed ions are generated followed by the second time interval (II) where adsorbed ions discharge and transform to adsorbed atoms and then the formation of a high nuclei number. In the third time interval (III) the deposited nuclei to obtain Pt clusters. Finally, the time interval (IV), Pt macro-clusters generation developing towards a full covering of the electrode surface[31].

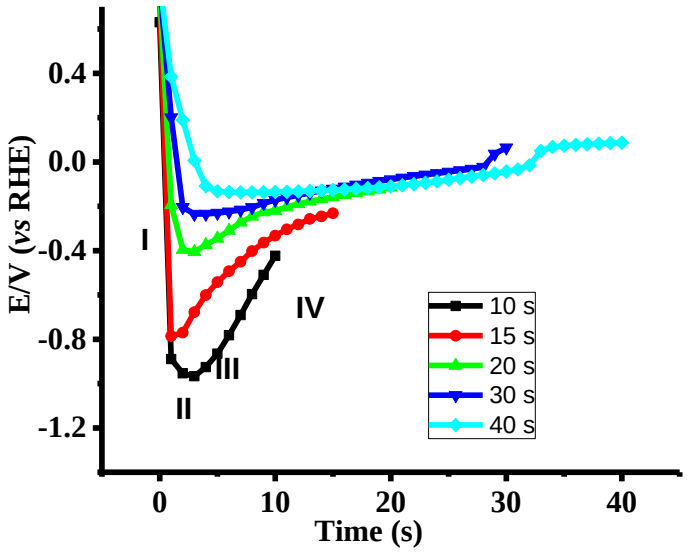

Figure 34. Typical chronopotentiograms for the electrodeposition of Pt particles onto PEDOT:PSS from the electrolyte solution of 5 mM H_2PtCl_6, 1 M H_2SO_4 with applied current and time of ■ (- 4.5 mA, 10 s), ●(- 3 mA, 15 s), ▲(- 2.25 mA, 20 s), ▼(- 1.5 mA, 30 s) and ♦(- 1.125 mA, 40 s), respectively.

As can be seen from chronopotentiometry curves in Figure 34, the larger the applied current, the more negative potential, and the earlier nucleation. The difference in the conditions (applied current and time) of nucleation and growth of the platinum nuclei at the initial stage of electrodeposition resulted in differences in the electrochemical response of the platinum particles on the surface of PEDOT:PSS.

CVs recorded at 20 mV s^{-1} for different samples with the same total platinum loading of 40% under different experimental conditions (cathodic current and time) are shown in Figure 35. The figures show the characteristics hydrogen adsorption-desorption peaks between 0.05 V and 0.3

V, a double layer region up to 0.55 V, and Pt oxide formation and reduction at a higher potential between 0.6 V - 0.95 V *vs* RHE.

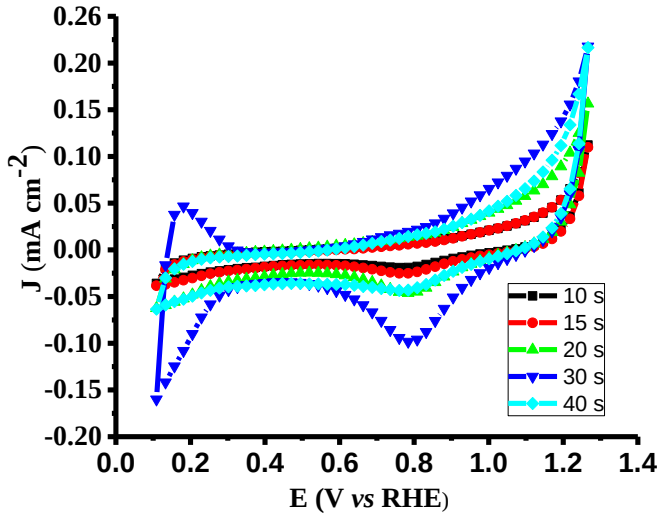

Figure 35. Cyclic voltammograms of galvanostatically deposited Pt (40%) on PEDOT:PSS at a deposition time of 10 s (■), 15 s (●), 20 s (▲), 30 s (▼) and 40 s (♦) in N_2-saturated 0.1 M $HClO_4$ at scan rate of 20 mV s^{-1}.

For electrodeposition at 10 s and 15 s, smaller hydrogen adsorption/desorption and Pt oxide peaks are observed. But, clearly observable biggest peaks are obtained for the electrode for 30 s electrodeposition which resulted, in turn, a large electrochemical surface area.

4.1.3 Potentiostatic deposited platinum on PEDOT:PSS

The current *versus* time plot in a potentiostatic step experiment (Figure 36) shows different time intervals. In the beginning (region I), a sharp increase followed by a decay of the current to its

minimum appears that corresponds to the double-layer charging current and the initial nucleation process. Then (region II), the current increases due to the free growth of independent nuclei for deposition or to the formation of new nucleation. The current increases in this zone reaching a maximum. After that (region III), the current decreases due to the overlapping of the diffusion zones of different nuclei, and the coalescence of the growth centers or the result of a decrease in the surface area of platinum particles.

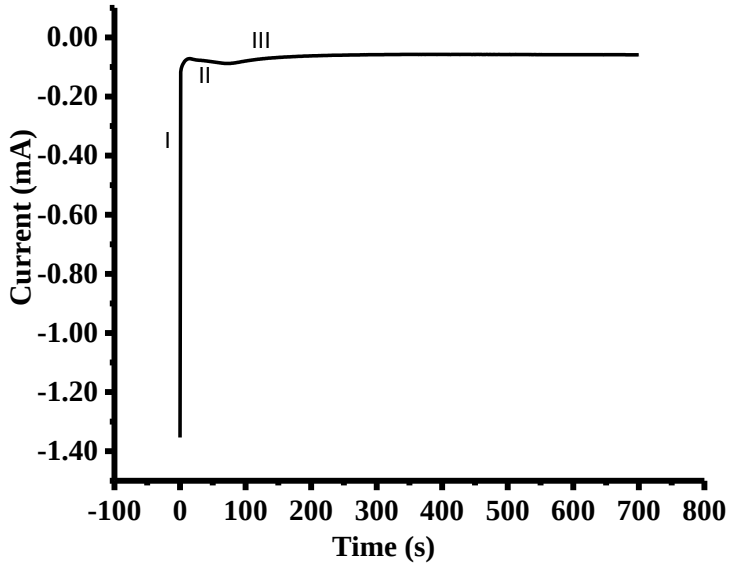

Figure 36. Current against time response for a potentiostatic deposition of platinum on PEDOT:PSS at -0.15 V *vs* Ag/AgCl.

Comparing the two CVs (Figure 37) for platinum deposited by galvanostatic and potentiostatic method, considerably higher current values in the anodic and cathodic regions are evident for Pt particles on potentiostatic method.

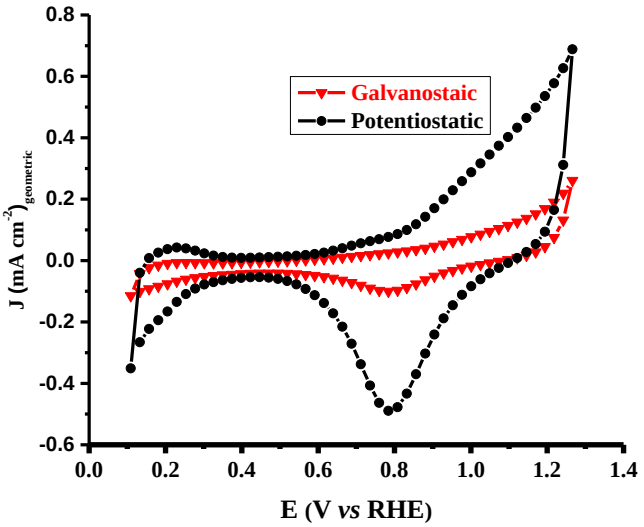

Figure 37. Cyclic voltammograms of galvanostatically (for 30 s) (▼) and potentiostatically (●) deposited Pt (40%) on PEDOT:PSS catalyst in N_2-saturated 0.1 M $HClO_4$ at a scan rate of 20 mV s^{-1}.

The ORR activity using linear sweep voltammetric method at RDE is also used to compare the two electrodeposition methods. The polarization curves of the ORR PEDOT:PSS(EG)/Pt (40%) modified rotating disc GC electrode by the two deposition methods are shown in Fig. 38. More positive onset potential and higher limiting current density were obtained for potentiostatic Pt loading on PEDOT:PSS. Hence, extensive study of PEDOT:PSS as a support for platinum particle were done by potentiostatic deposition of platinum.

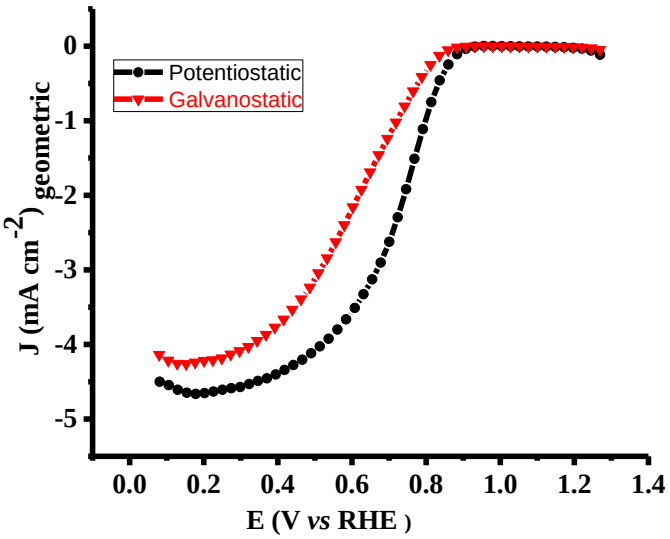

Figure 38. Background corrected oxygen polarization LSV curves for galvanostatically (for 30 s) (▼) and potentiostatically (●) deposited Pt (40%) on PEDOT:PSS in O_2-saturated 0.1 M $HClO_4$ at a scan rate of 20 mV s^{-1} rotating at 1600 rpm.

4.1.4 Surface characterization

The crystalline structure of Pt nanoparticles dispersed on to PEDOT:PSS/Pt (30%), PEDOT:PSS (EG)/Pt (30%) and rGO/PEDOT:PSS(EG)/Pt (30%) were investigated by XRD studies. Figure 39 shows the XRD patterns of PEDOT:PSS/Pt (30%), PEDOT:PSS(EG)/Pt (30%) and rGO/PEDOT:PSS(EG)/Pt (30%) films. A broad peak (Figure 39a) at $2\theta = 25^{o}$ observed in all materials correspond to the (020) plane of PEDOT:PSS[179]. The peaks at 2θ = 39.9°, 46.5°, 67.7°, and 81.9° correspond to the diffraction planes (111), (200), (220), and (311) of Pt, respectively[121].

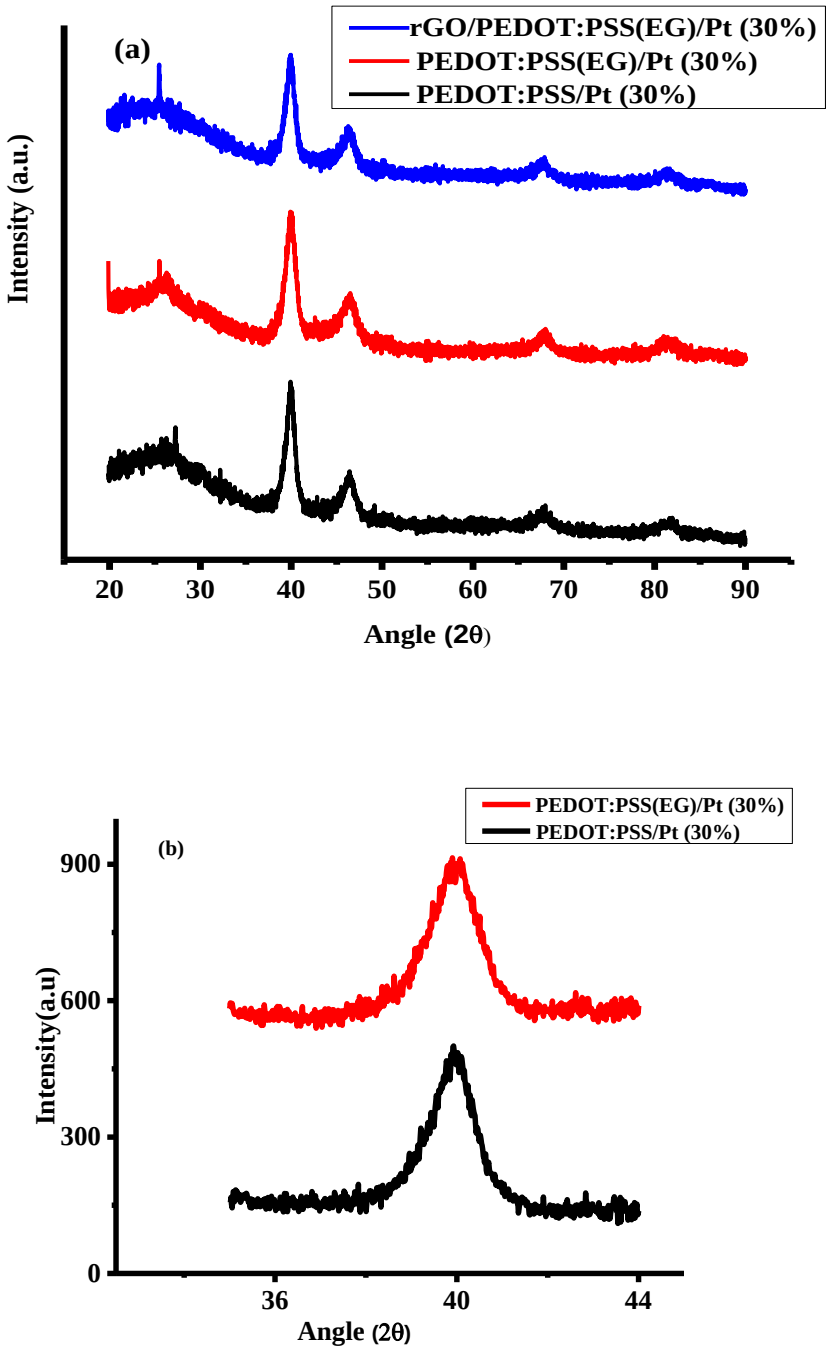

Figure 39. XRD patterns of (a) PEDOT:PSS/Pt (30%), PEDOT:PSS(EG)/Pt (30%), and rGO/PEDOT:PSS(EG)/Pt (30%) (b) over a narrow range of 2θ (35-44 degrees) for PEDOT:PSS/Pt (30%) and PEDOT:PSS(EG)/Pt (30%).

The average crystallite size of PEDOT:PSS supported Pt was calculated from the broadening of the (111) diffraction peak using Debye–Scherrer Equation (33) and Figure 39b. The average crystallite size of Pt obtained by using EG is 7.3 nm which is smaller compared to the deposition of Pt in the absence of EG (7.9 nm). But, the incorporation of rGO returned the average crystallite size of Pt supported on rGO/PEDOT:PSS(EG) to 7.9 nm. The AFM images for PEDOT:PSS/Pt (Figure 40b) and PEDOT:PSS(EG)/Pt (Figure 40c) shows a small cluster of particles not observed in PEDOT:PSS (Figure 40a) confirming the deposition of Pt particle on PEDOT:PSS films. PEDOT:PSS(EG)/Pt (Figure 40c) film shows small Pt-NPs and full coverage of the Pt particle compared to PEDOT:PSS/Pt (Figure 40b). The incorporation of EG in PEDOT:PSS not only minimizes the rate of growth of Pt clusters during electrodeposition but also improves the distribution of Pt particles[212].

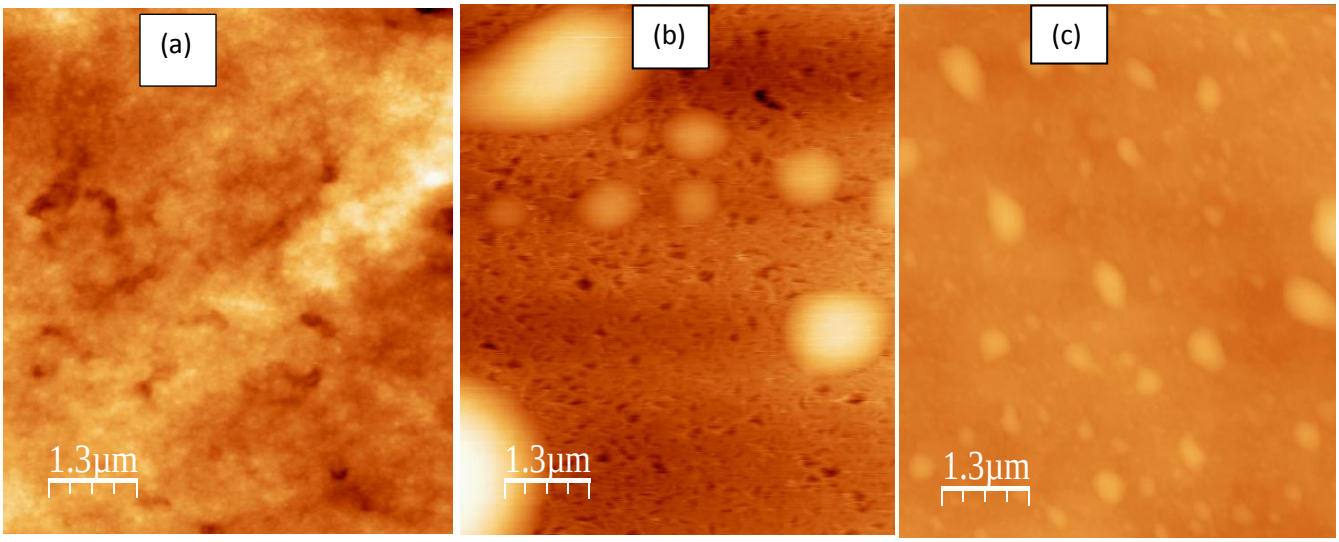

Figure 40. The 2D AFM images of (a) PEDOT:PSS (b) PEDOT:PSS/Pt and (c) PEDOT:PSS(EG)/Pt.

To further reveal the electrodeposition of the Pt particles, FESEM/EDS spectra were recorded for the PEDOT:PSS/Pt (30%), PEDOT:PSS(EG)/Pt (30%) and rGO/PEDOT:PSS(EG)/Pt (30%). A typical SEM image and the selected rectangular area used for EDS studies of Pt deposited on PEDOT:PSS (Figure 41a), PEDOT:PSS(EG) (Figure 41c) and rGO/PEDOT:PSS(EG) (Figure 41e) are shown in Figure 41.

The EDS (Figure 41 b, d, f) reveals the presence of carbon (from PEDOT or PEDOT and rGO), Sulfur (from PEDOT and PSS), oxygen (from PEDOT:PSS, rGO and EG) and Pt-NPs.

The lighter areas on PEDOT:PSS/Pt (30%) (Figure 41g), PEDOT:PSS(EG)/Pt (30%) (Figure 41i) and rGO/PEDOT:PSS(EG)/Pt (30%)(Figure 41k) are Pt particles distributed onto the surface as confirmed by EDS data (Figure 41 b, d, f). Electrochemically deposited Pt-NPs tend to agglomerate instead of dispersed nanoparticles on the surface of the substrate[15].

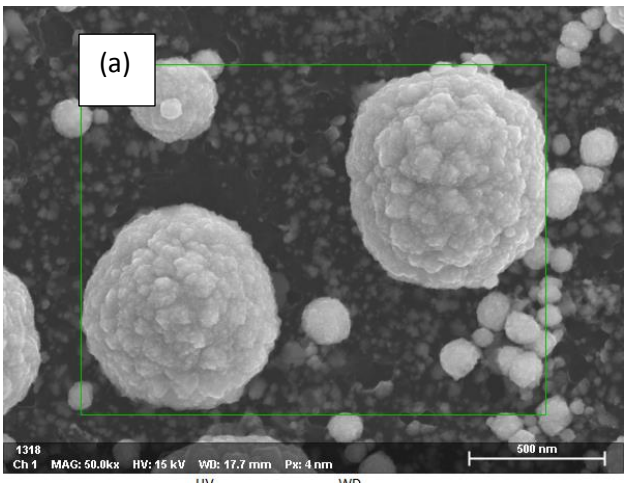
(a)
1318
Ch 1 MAG: 50.0kx HV: 15 kV WD: 17.7 mm Px: 4 nm
500 nm

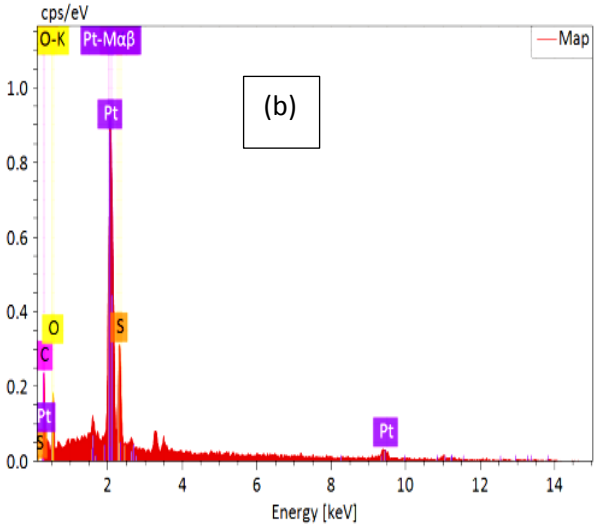
(b)
cps/eV
O-K
Pt-Mαβ
Map
Pt
O
S
C
Energy [keV]

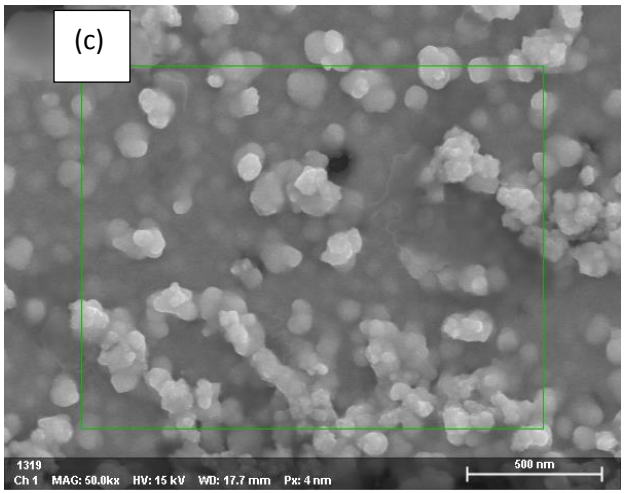
(c)
1319
Ch 1 MAG: 50.0kx HV: 15 kV WD: 17.7 mm Px: 4 nm
500 nm

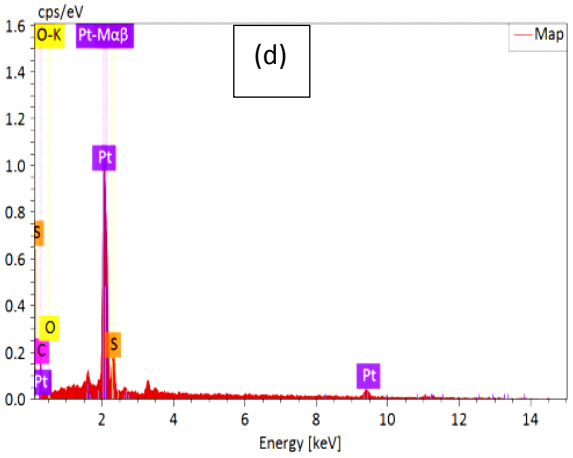
(d)
cps/eV
O-K
Pt-Mαβ
Map
Pt
S
O
C
Energy [keV]

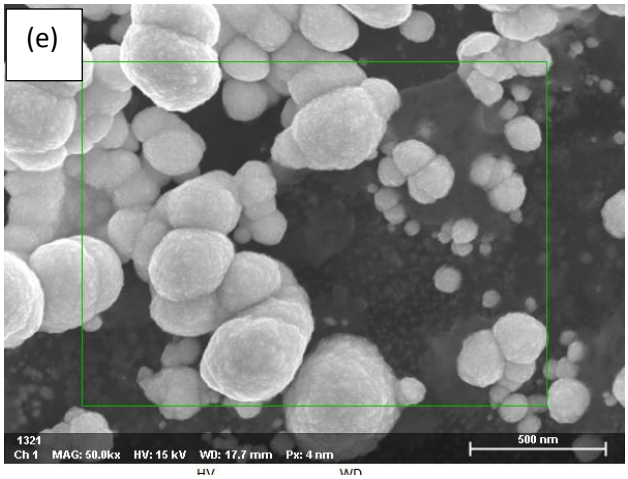
(e)
1321
Ch 1 MAG: 50.0kx HV: 15 kV WD: 17.7 mm Px: 4 nm
500 nm

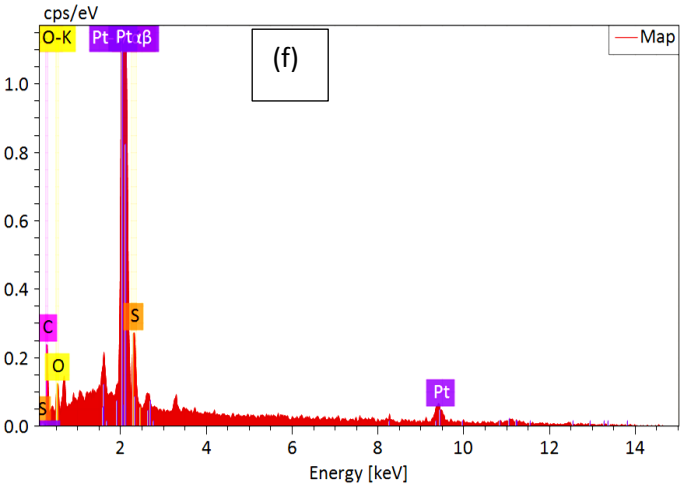
(f)
cps/eV
O-K
Pt Ptιβ
Map
C
S
O
Pt
Energy [keV]

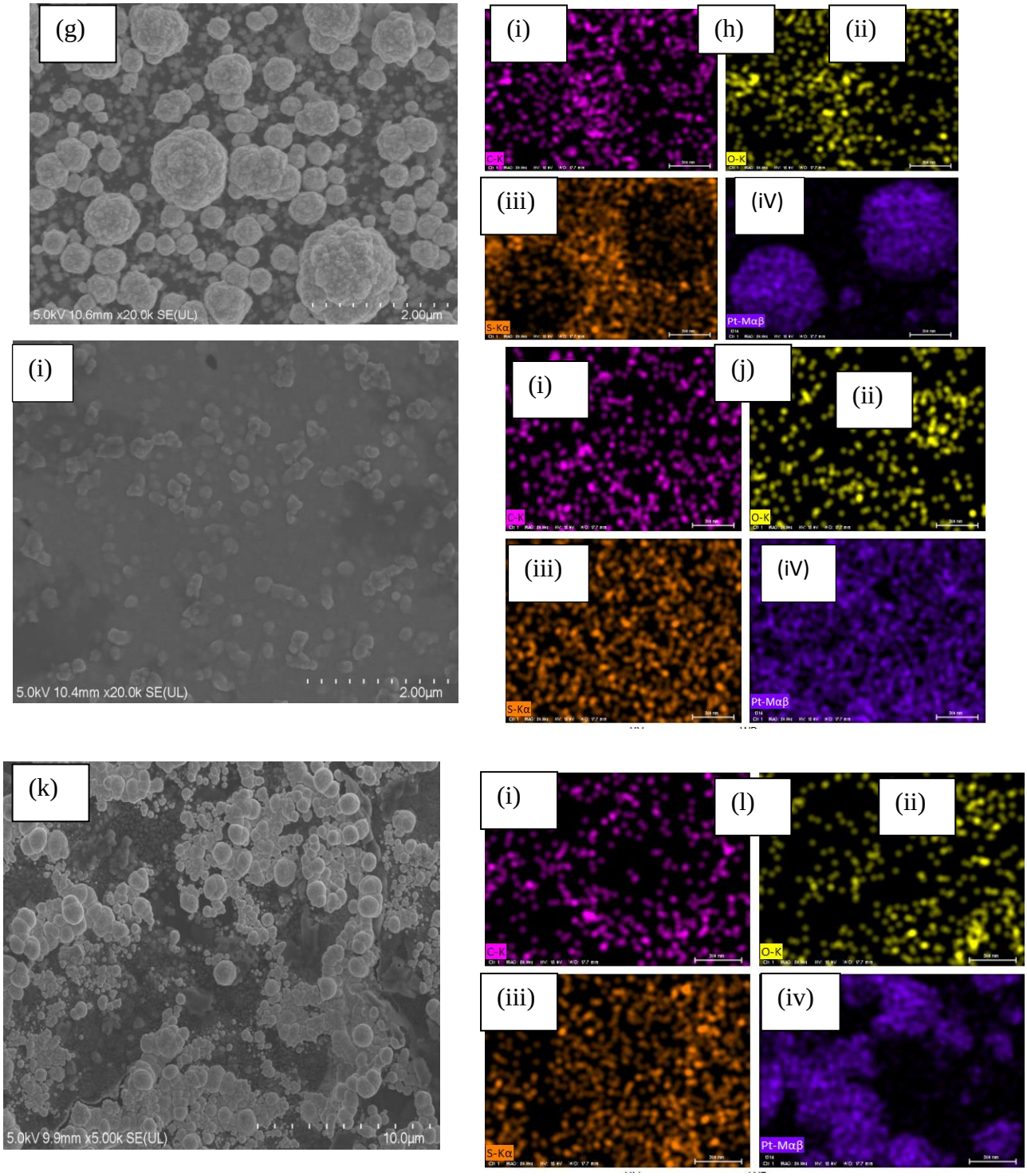

Figure 41. SEM images (a, c, e) used for EDS (x 50 k), EDS (b, d, f) spectrum, SEM images (g, i, k) and elemental color maps for carbon (h (i), j (i), l (i)), oxygen (h (ii), j (ii), l (ii)), sulfur (h (iii), j (iii), l (iii)) and platinum (h (iv), j(iv), l(iv)) for PEDOT:PSS/Pt (30%), PEDOT:PSS(EG)/Pt (30%) and rGO/PEDOT:PSS(EG)/Pt (30%), respectively.

Figure 41 (i and j (iv)) reveals that PEDOT:PSS(EG) deposite small Pt nanoparticles with full coverage compared to PEDOT:PSS (Figure 41g and h (iv)) which is in agreement with the AFM results. Figure 41k shows SEM images depicting a heterogeneous morphology for a rGO/PEDOT:PSS(EG)/Pt (30%). The composite reveals globular microstructure characteristic of PEDOT and a wrinkled morphology which is a characteristic feature of rGO. The elemental mapping images of (Figure 41 l) reveals a homogeneous distribution of C, O and S (Figure 41l (i-iii)) throughout the composite while some larger aggregated Pt within the mapped area is observed (Figure 41l (iv)).

4.1.5 Electrochemical characterization

4.1.5.1 Cyclic voltammetric studies

The cyclic voltammograms for the different Pt loading (10 - 40%) on PEDOT:PSS and 30% Pt deposited on various rGO/PEDOT:PSS composite electrodes are depicted in Figure 42a and 42b, respectively. The figures show the characteristics hydrogen adsorption-desorption peaks between 0.05 V and 0.3 V, a double layer region up to 0.55 V, and Pt oxide formation and reduction at a higher potential between 0.6 V - 0.95 V *vs* RHE except for 10% loading (Figure 42a). The exception in the cyclic voltammogram of 10% Pt on PEDOT:PSS is because the electrochemistry of the polymer support dominates the electrochemical behavior which hides the Pt fingerprint[132].

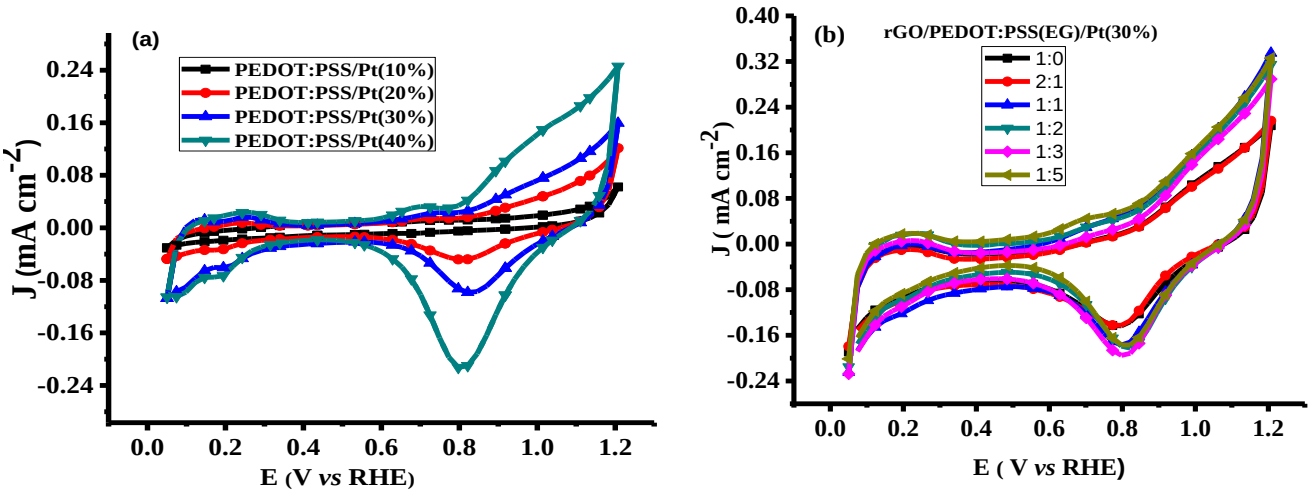

Figure 42. Cyclic voltammograms of (a) different wt% Pt catalyst on PEDOT:PSS (b) rGO:PEDOT:PSS(EG)/Pt (30%) catalyst in N_2-saturated 0.1 M $HClO_4$ at scan rate of 20 mV s^{-1}.

ECSA for PEDOT:PSS/Pt (30%) is higher than PEDOT:PSS/Pt (40%) in the presence and absence of EG. This indicates that Pt particles tend to form progressively larger agglomerates up on increase in Pt loading. In an ideal case in which the particle size is constant and no agglomerates are formed, the ECSA should be constant for different loadings[25].

The oxide reduction peak in Figure 42b increase when PEDOT:PSS(EG) was added to rGO until the w/w ratio is 1:3 and reduced on further addition of PEDOT:PSS (1:5). The reduction peak potential is also shifted to more positive value with a maximum shift of about 30 mV for 1:2 ratio. The real surface area (A_r) of platinum determined by charge integration under the hydrogen adsorption peaks increased from 0.5 cm^2 to 0.8 cm^2 as the amount of rGO/PEDOT:PSS ratio increased from 1:0 to 1:5.

4.1.5.2 Linear sweep voltammetric studies at RDE

The ORR activity was further investigated using a linear sweep voltammetric method at a RDE. The polarization curves of the ORR at PEDOT:PSS/Pt modified GC electrode for different Pt loadings are shown in Figure 43a. These polarisation curves show the characteristics of diffusion-controlled region (< 0.6 V), mixed diffusion kinetic limitation region (0.6 – 0.8 V), and Tafel region (> 0.8 V)[23]. As expected, more positive onset potential and higher limiting current density were obtained for the highest Pt loading (PEDOT:PSS/Pt) (40%).

The electrocatalytic ORR activity was also studied by adding EG to PEDOT:PSS. PEDOT:PSS(EG) modified GC electrode was also used in comparison as a reference. The onset potential and the current density are remarkably improved after platinum is deposited on PEDOT:PSS(EG). The limiting current density for ORR increased upon the addition of EG onto PEDOT:PSS ink (Figure 43b). The increase in the limiting current upon addition EG shows that the presence of EG promotes Pt particle coverage and distribution. Moreover, 30% and 16% increase in ECSA for 30% and 40% Pt loading, respectively, was observed for PEDOT:PSS(EG), showing that the increase in ECSA was more pronounced at the lower Pt loading (30%). Therefore, EG enhances the dispersion of Pt particle with large area coverage and hence increases Pt utilization[25, 35].

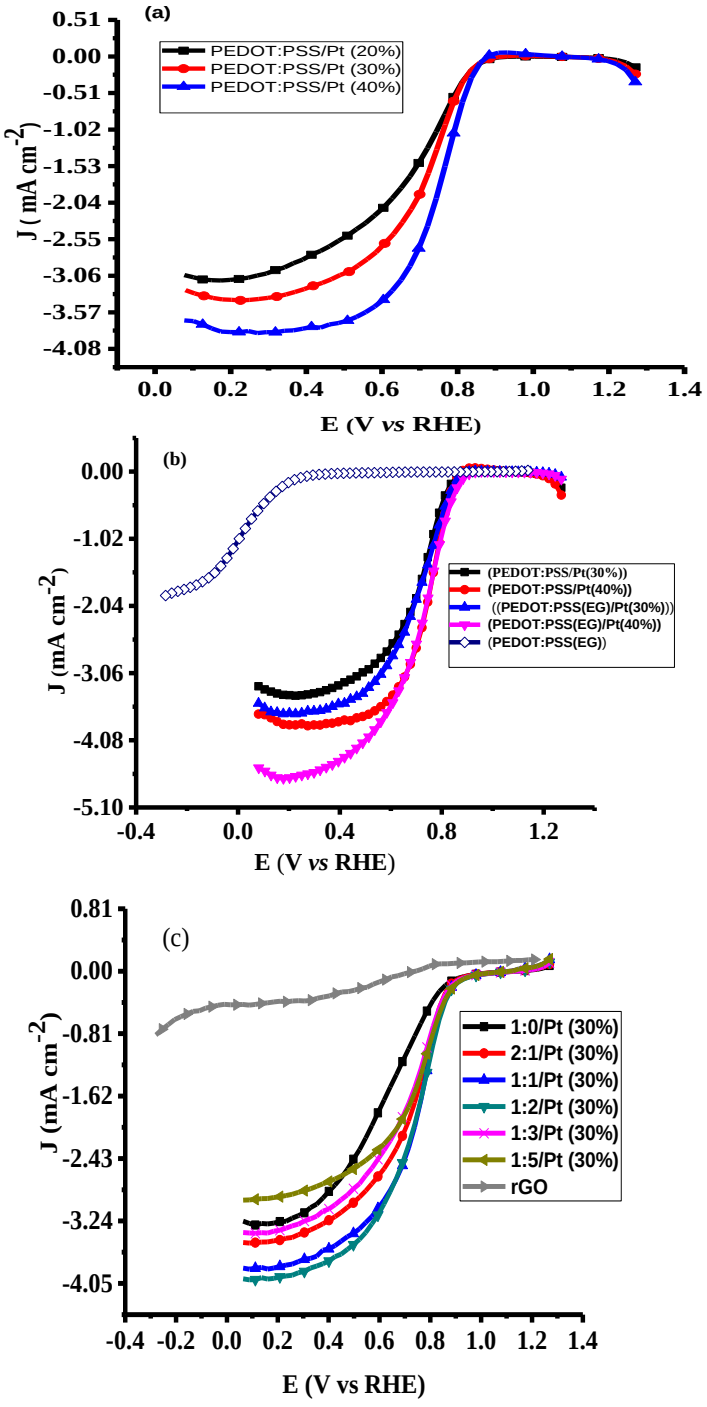

Figure 43. Background corrected oxygen polarization curves for (a) PEDOT:PSS/Pt, (b) PEDOT:PSS(EG), 30% and 40% platinum on PEDOT:PSS(EG) and PEDOT:PSS (c) rGO and rGO/PEDOT:PSS/Pt (30%) in O_2-saturated 0.1 M $HClO_4$ at a scan rate of 20 mV s^{-1} rotating at 1600 rpm.

The kinetic currents (i_k) extracted from Figure 43b were used to calculate mass activity (MA) and the specific area activity (SA) of the electrocatalyst using Equations (15) and (16). The calculated values are summarized in Table 2. An increase in SA of 1.2 and 1.1 fold and a 1.5 and 1.2 fold in MA were obtained at 0.81 V by the addition of EG on PEDOT:PSS for 30% and 40% Pt loading, respectively. These enhancements were attributed to a change in platinum morphology and inhibition of agglomeration of Pt nanoparticles during the process of electrodeposition by the addition of EG[25, 35].

Hence, using this pronounced effect of EG at 30% Pt loading different ratios of rGO and PEDOT:PSS(EG) were further investigated. Typical background-corrected polarisation curves for the rGO, rGO/Pt (30%) and rGO/PEDOT:PSS(EG)/Pt (30%) catalyst in 0.1 M $HClO_4$ at 1600 rpm are shown in Figure 43c. More positive onset potentials and higher limiting current densities were obtained as the percentage of PEDOT:PSS increased from 1:0 to 1:2. Increasing the percentage of PEDOT:PSS beyond 1:2 to 1:3 and 1:5 lowers the onset potential and limiting current density. Hence, rGO/PEDOT:PSS(EG)(1:2)/Pt (30%) which gave a 2.2 and 2.9 fold increase in the SA and MA at 0.81 V, respectively, was found to be the optimum composition.

rGO modified GC electrode (Fig. 43c) shows a clear reduction pre-wave at low overpotential, followed by a second reduction wave starting at around -0.013 V, which is indicative of a prevalent $2e^-$ reduction pathway[68]. The onset potential and the current density are remarkably improved after platinum is deposited on rGO.

Table 2. Kinetic parameters for oxygen reduction on PEDOT:PSS/Pt, PEDOT:PSS(EG)/Pt, and rGO/PEDOT:PSS(EG)/Pt (30%) in 0.1 M $HClO_4$ at 1600 rpm.

Electrocatalyst	**Pt loading** ($mg\ cm^{-2}$)	**A_r (cm^2)**	**ECSA** ($m^2\ g^{-1}$)	**SA** ($\mu A\ cm^{-2}$ Pt)		**MA** ($mA\ mgPt^{-1}$)	
				0.81 V	**0.86 V**	**0.81 V**	**0.86 V**
PEDOT:PSS/Pt (30%)	0.071	0.41	2.93	194.5	41.3	5.8	1.2
PEDOT:PSS/Pt (40%)	0.11	0.526	2.32	284.	33.4	6.6	0.7
PEDOT:PSS(EG)/Pt (30%)	0.071	0.526	3.8	228.4	49.8	8.7	1.9
PEDOT:PSS(EG)/Pt (40%)	0.11	0.61	2.68	287.3	83.7	7.71	2.24
rGO/PEDOT:PSS(EG) (1:0)/Pt (30%)	0.071	0.49	3.57	212.4	96.5	7.8	3.4
rGO/PEDOT:PSS(EG) (2:1)/Pt (30%)	0.071	0.47	3.36	514.7	158.6	17.3	5.3
rGO/PEDOT:PSS(EG) (1:1)/Pt (30%)	0.071	0.69	4.96	419	134.8	20.8	6.7
rGO/PEDOT:PSS(EG) (1:2)/Pt (30%)	0.071	0.65	4.72	472	162	22.3	7.6
rGO/PEDOT:PSS(EG) (1:3)/Pt (30%)	0.071	0.78	5.63	284.8	102.3	16.02	5.8
rGO/PEDOT:PSS(EG) (1:5)/Pt (30%)	0.071	0.77	5.58	347.5	129.7	19.4	7.2

The mass transport corrected Tafel plots ($\log|j_k|$ *vs* E) for PEDOT:PSS/Pt, PEDOT:PSS(EG)/Pt, and rGO/PEDOT:PSS(EG)/Pt are shown in Figure 44. The figures show a transition in the Tafel slope from 60 mV $decade^{-1}$ to 120 mV $decade^{-1}$ for all the catalysts. The observed Tafel slope of ~60 mV $decade^{-1}$ at low overpotential is associated to an oxygen reduction process on an oxide-covered Pt, and the 120 mV $decade^{-1}$ slope at higher overpotentials is related to reduction process taking place on oxide-free Pt surfaces [16]. The addition of EG reduces the Tafel slope for both the 30 and 40% Pt loading (Table 3) which confirms more favorable kinetics for ORR[213].

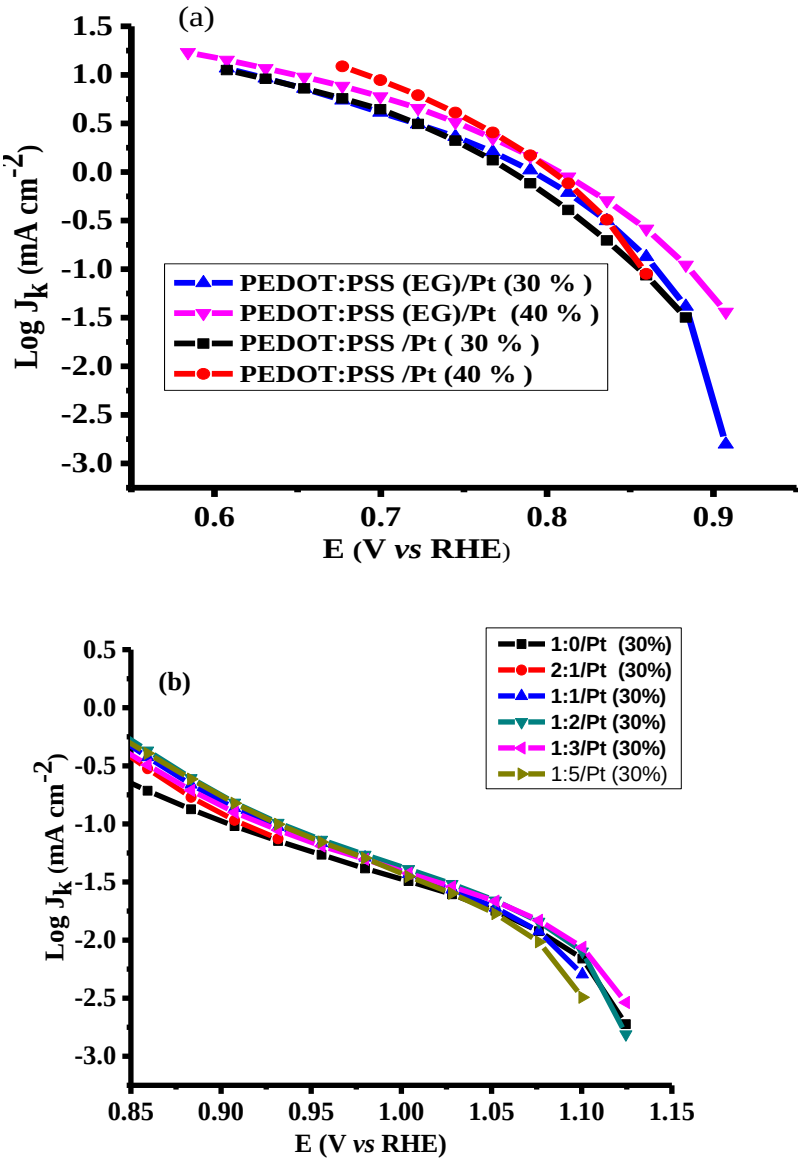

Figure 44. Mass transport corrected Tafel plots for (a) PEDOT:PSS/Pt, PEDOT:PSS(EG)/Pt and (b) rGO/PEDOT:PSS(EG)/Pt obtained from disk current in the cathodic sweep at 1600 rpm. Scan rate: 20 mV s^{-1}.

4.1.5.3 Linear sweep voltammetric studies at RRDE

RRDE measurements are used to assess the extent of peroxide formation, the number of electrons transferred per O_2 molecule (n), and the ORR pathway. The disk current represents the

oxygen reduction current referring to the ORR activity. The ring current indicates the oxidation current of intermediates on the Pt ring electrode, referring to the production of H_2O_2 during the ORR process. The most positive onset potential and largest limiting current density on the disk electrode as well as very low ring currents characterizes the perfect catalytic material for the 4-electron ORR.

Determination of collection efficiency (N)

The ring and the disk currents in the negative sweep direction (10 mV s^{-1}) at a constant ring potential of 1.3 V for the determination of collection efficiency Pt (30%) deposited on rGO (1:0) are shown in Figure 45.

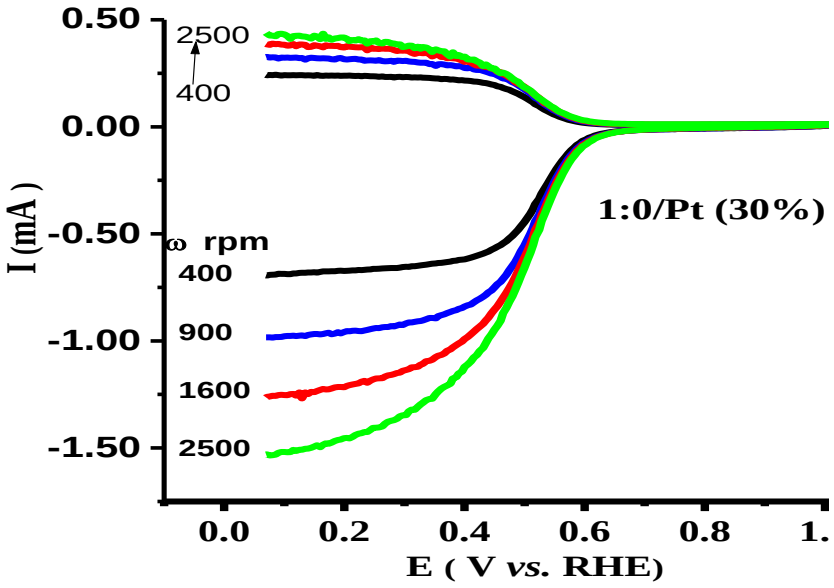

Figure 45. Ring ($Fe(CN)_6^{4-} \rightarrow Fe(CN)_6^{3-} + e^-$) and disk ($Fe(CN)_6^{3-} + e^- \rightarrow Fe(CN)_6^{4-}$) currents for the determination of the collection efficiency on 1:0 in 1 M KNO_3 supporting electrolyte with 10 mM $K_3Fe(CN)_6$. Negative sweeps at 20 mV s^{-1}; E_{Ring} = 1.3 V.

The N values of the RRDE loaded with catalysts (Figure 46) are lower than the bare RRDE (0.37) as supplied by the manufacturer. The N values of Pt (30%) on 2:1 (0.35), 1:1 (0.36) and 1:2 (0.36) are close to 0.37 but even lower values for 1:0 (0.31), 1:3 (0.30), and 1:5 (0.32) were recorded.

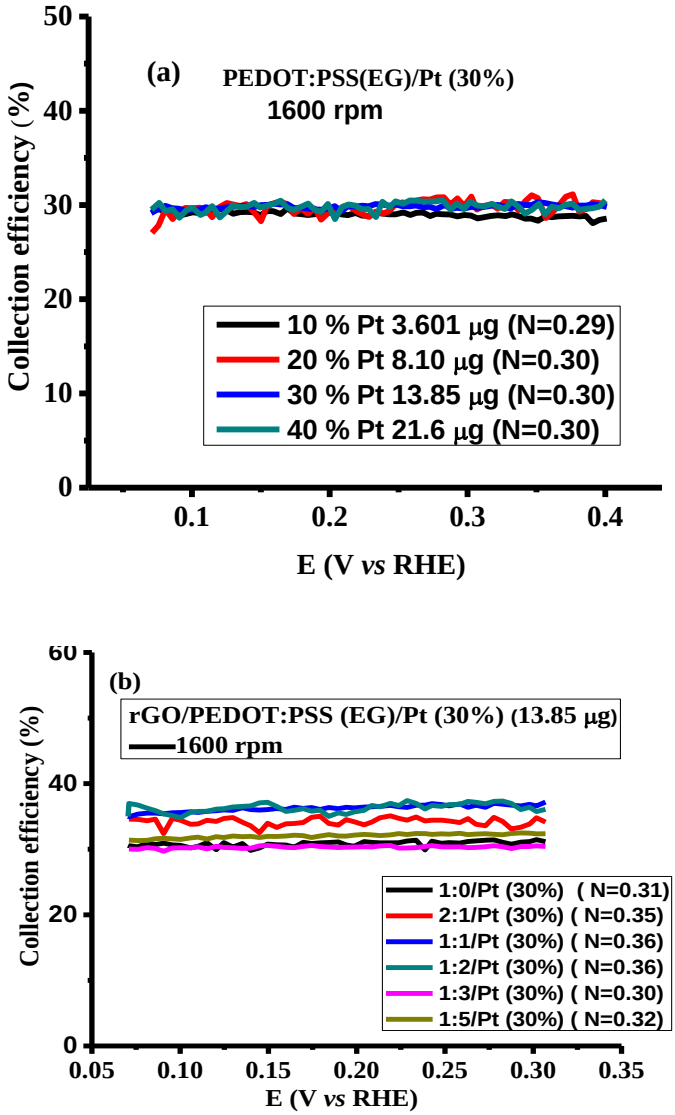

Figure 46. Variation of the collection efficiency with potential and catalyst loading for the different catalysts (a) PEDOT:PSS(EG)/Pt and (b) rGO/PEDOT:PSS(EG)/Pt (30%).

Figure 47 a, b shows typical RRDE voltammograms including the ring and the disk currents *versus* the disk potential for rGO/PEDOT:PSS/Pt at different rGO and PEDOT:PSS ratios. The number of electrons transferred (n) derived from RRDE result using Equation (17) over the potential range of 0.07 to 0.3 V was 3.86, 3.88, 3.92, 3.93, 3.91, and 3.85, respectively for Pt (30%) deposited on 1:0, 2:1, 1:1, 1:2, 1:3 and 1:5 as shown in Figure 47c which confirms the improvement of the electrocatalytic activity of rGO up on the addition of PEDOT:PSS(EG).

The percentage of H_2O_2 generated was quantified using Equation (18) and found to be 7.9% for Pt (30%) deposited on 1:0 composition and significantly reduced to 3.3% for 1:2 composition (Figure 47d). Hence, the 1:2 composition (rGO/PEDOT:PSS(EG)/Pt (30%)) exhibits the largest limiting current density (on the disk electrode), the most positive onset potential, and the lowest % H_2O_2 indicating an excellent ORR activity *via* the 4-electron pathway. The detection of hydrogen peroxide at potentials below 0.8 V in Figure 47b indicates that the two-electron pathway does in fact occur on the surface of rGO/PEDOT:PSS(EG)/Pt (30%). The yield of H_2O_2 increase with decreasing potential and a significant increase in H_2O_2 formation was observed at potentials < 0.1 V. This can partly be attributed to the blockage of surface active sites by adsorbed hydrogen atoms, preventing the dissociative adsorption of oxygen molecules[92]. The higher activity and number of electron transfer observed for rGO/PEDOT:PSS(EG)(1:2)/Pt (30%) could be related to the decreased H_2O_2 formation by further reduction of H_2O_2 to H_2O[25]. Therefore, the electrocatlytic ORR on rGO/PEDOT:PSS(EG)/Pt (30%) largely proceeds *via* a sequential pathway *via* H_2O_2 species, rather than via direct reduction of O_2.

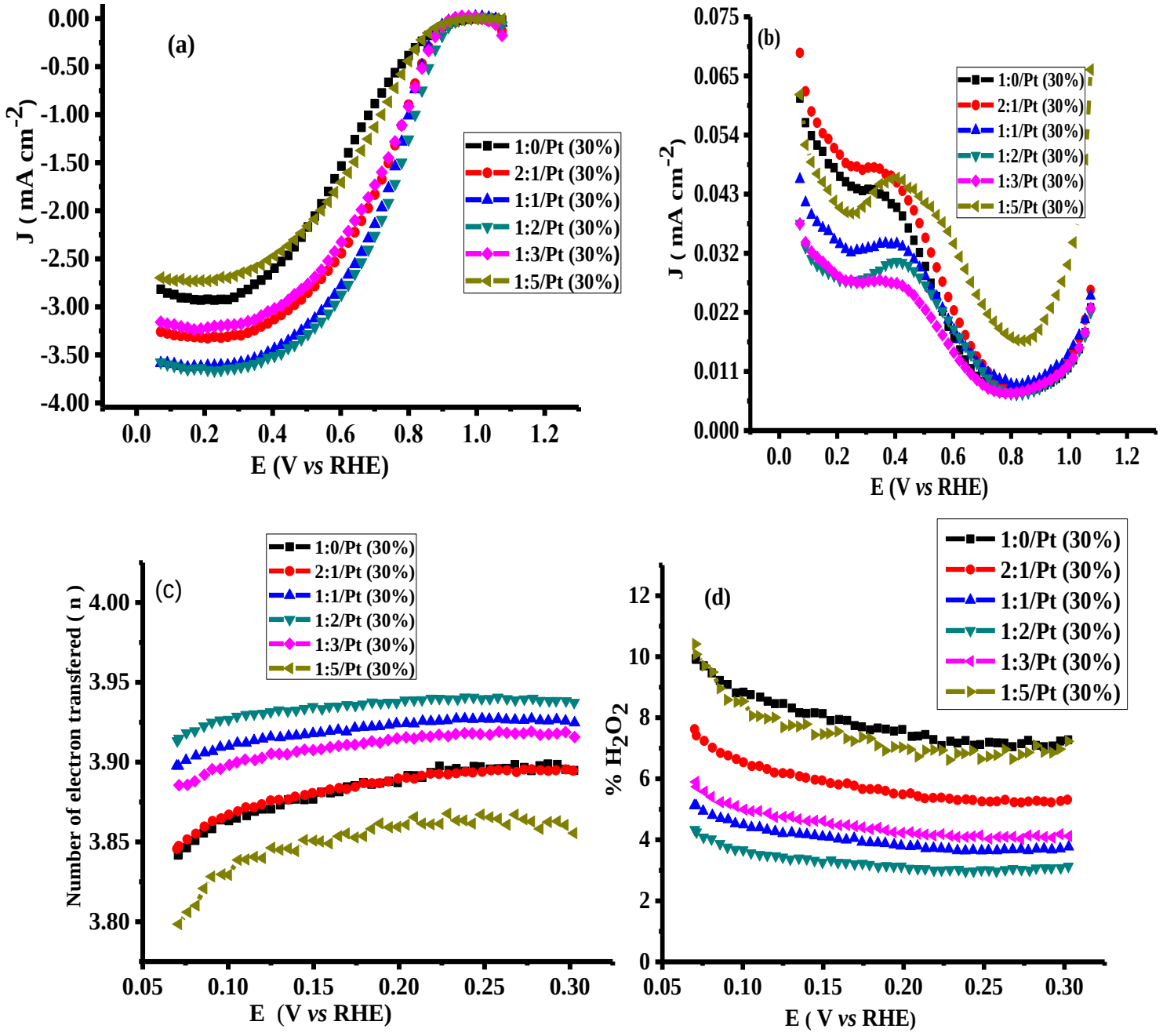

Figure 47. (a) RRDE voltammograms disk current density, (b) ring current density, (c) the number of electron transferred, and (d) % H_2O_2 formation as a function of the disk potential for various rGO/PEDOT:PSS composite at 1600 rpm in 0.1 M $HClO_4$ solution.

For comparison, the RRDE voltammograms, n, and % H_2O_2 formation as a function of the disk potential for various Pt loadings (10%, 20%, 30%, and 40%) on PEDOT:PSS(EG) were studied and are shown in Figure 48.

The % H_2O_2 yield determined for 10%, 20%, 30% and 40% Pt loading on PEDOT:PSS(EG) were found to be 52%, 24%, 12%, and 4.5%, respectively. The electron transfer numbers (n) over the potential range of 0.07 to 0.3 V were found to be 2.96, 3.52, 3.78, and 3.91, respectively, for 10, 20, 30, and 40% Pt loading on PEDOT:PSS(EG). PEDOT:PSS(EG)/Pt (10%) displays the largest % H_2O_2 indicating that electrochemistry is largely dominated by the PEDOT:PSS[132].

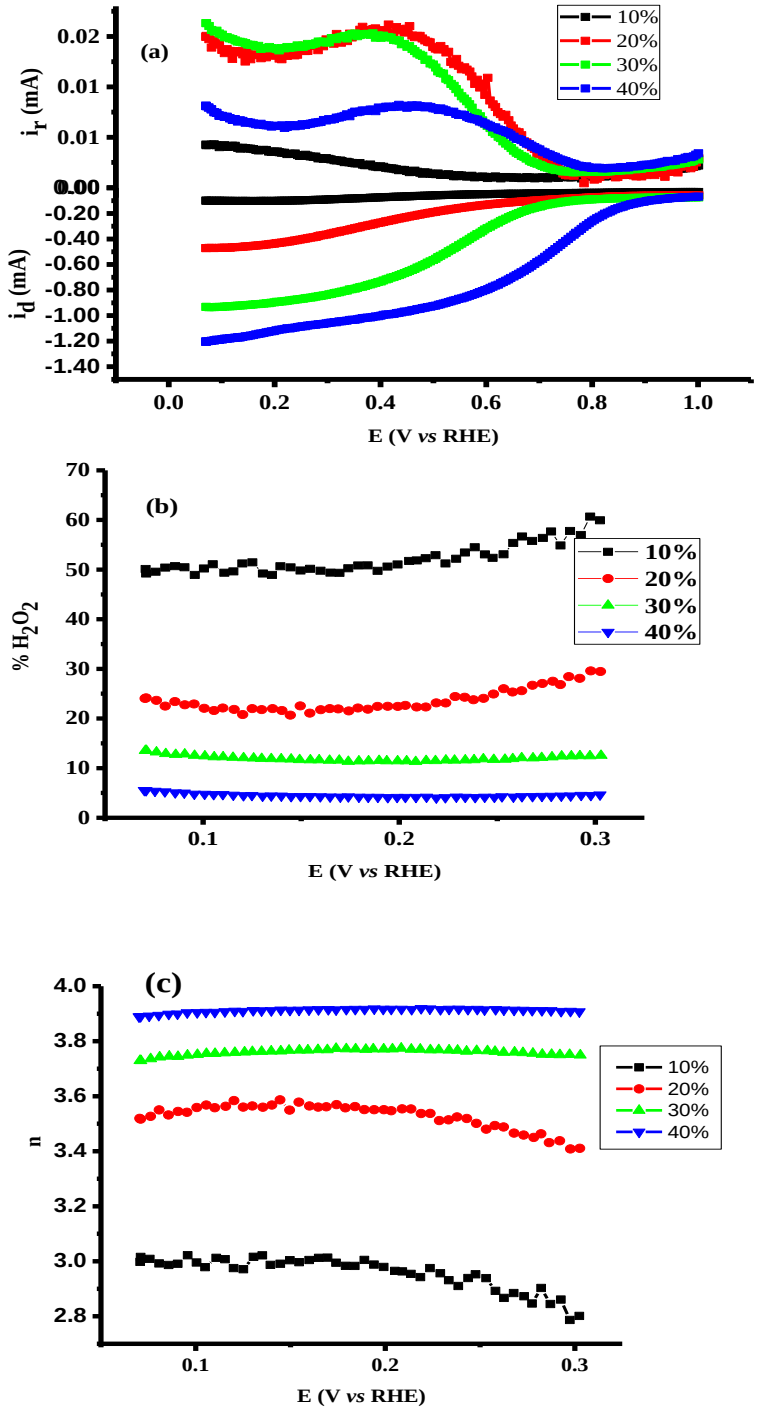

Figure 48. (a) RRDE volatmmograms, (b) % H_2O_2 formation and (c) electron transfer number (n) as a function of the disk potential for various platinum loadings on PEDOT:PSS(EG) at 1600 rpm in 0.1 M $HClO_4$ solution.

The % H_2O_2 yields and n for 30% Pt loading on PEDOT:PSS(EG), rGO and rGO/PEDOT:PSS(EG)(1:2) are shown in Figure 49. Lower % H_2O_2 and higher n were found for Pt particles deposited on rGO/PEDOT:PSS(EG) composite. The MA for ORR on Pt particles deposited on rGO, PEDOT:PSS(EG), and rGO/PEDOT:PSS(EG) were found to be 7.8, 8.7, and 22.3 A g^{-1}, respectively (Table 2). Hence, a 2.9 fold increase in mass activity was found in the optimized composite ratio.

The electrocatalytic performance of the optimized composite material was compared with previously reported values of Pt deposited on PEDOT:PSS and Vulcan carbon treated with EG (Table 3). The composite shows better electrocatalytic performance and the use of commercially available materials (PEDOT:PSS and rGO) and their synergistic effect further give promise for widespread application.

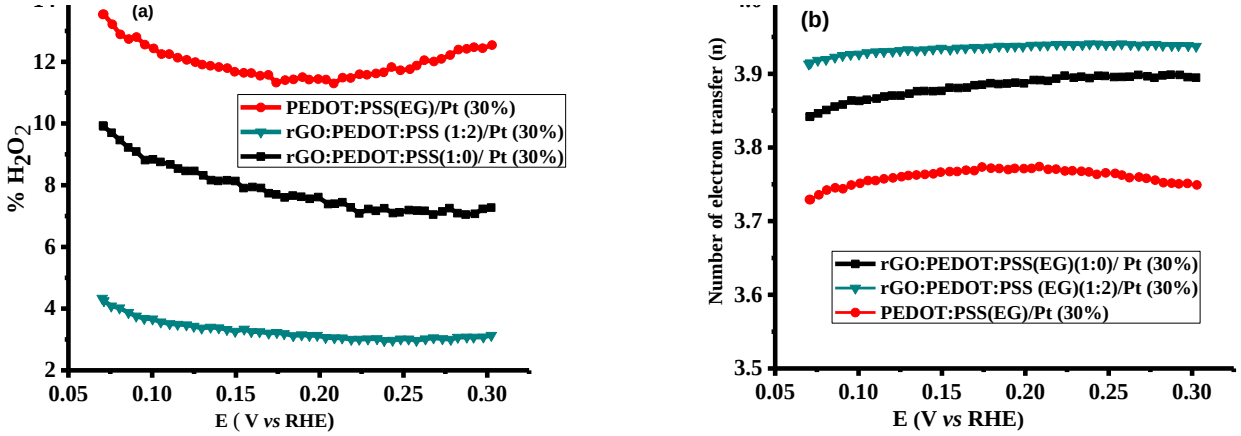

Figure 49. (a) % H_2O_2 and (b) n as a function of the disk potential for PEDOT:PSS(EG)/Pt (30%), rGO/PEDOT:PSS(EG)(1:0)/Pt (30%) and rGO/PEDOT:PSS(EG)(1:2)/Pt (30%) at 1600 rpm in 0.1 M $HClO_4$ solution.

Table 3. Comparison of the kinetic parameters of the electrocatalyst materials for ORR.

Samples	Pt loading (μg cm^{-2})	A_r (cm^2)	ECSA (m^2 g^{-1})	Tafel slope (mV dec^{-1}) lcd/hcd	n	SA (μA cm^{-2} Pt)	MA (mA mg_{Pt}^{-1})	References
Pt/C(Vulcan) (pulse current deposition), (EG)	55	1.83	16.9	-	-	33[b]	5.6 [b]	35
PEDOT:PSS/Pt (73 μg cm^{-2})	73	0.8	15.5	66/159	-	17[a]	-	132
PEDOT:PSS/Pt(138 μg cm^{-2})	138	1.5	15.37	90/200	3.7	87[a]	-	132
PEDOT:PSS/ Pt(30%)	71	0.41	2.93	68/154	3.46	132[c], 156[d]	4.62[d]	This work
PEDOT:PSS/ Pt(40%)	110	0.526	2.32	70/133	3.71	137[c], 291[d]	7.1[d]	This work
PEDOT:PSS(EG)/ Pt(30%)	71	0.526	3.8	61/146	3.75	144[c], 175[d]	6.65 [d]	This work
PEDOT:PSS(EG)/ Pt(40%)	110	0.61	2.68	62/120	3.91	262[c], 376[d]	10.61[d]	This work
rGO/PEDOT:PSS(EG)/ (1:2)/Pt (30%)	71	0.65	4.72	66/125	3.93	158[c], 188[d]	10.54[d]	This work

lcd/hcd -low current density/high current density
a - rotational rate = 750 rpm, E (V *vs* RHE) = 0.836
b - rotational rate = 1000 rpm, E (V *vs* RHE) = 0.800
c - rotational rate = 400 rpm, E (V *vs* RHE) = 0.836
d - rotational rate = 900 rpm, E (V *vs* RHE) = 0.836

Stability and electrochemical crossover effect are two important factors to evaluate the performance of an electrocatalyst in fuel cells. To further verify the electrocatlaytic performance of the catalyst, a small quantity of 3 M methanol was introduced at 500^{th} s in chronoamperometric (CA) measurement (Figure 50) for ORR at rGO/PEDOT:PSS(EG)(1:2)/Pt (30%) and commercial Pt/C (Etek, 20%). A sharp and immediate jumping in current on rGO/PEDOT:PSS(EG)(1:2)/Pt (30%) and commercial Pt/C catalyst upon the addition of methanol indicates the occurrence of methanol oxidation. The rGO/PEDOT:PSS(EG)(1:2)/Pt (30%) electrode exhibited better methanol tolerance with 15% current decay compared with a 22% current decay for commercial Pt/C electrode.

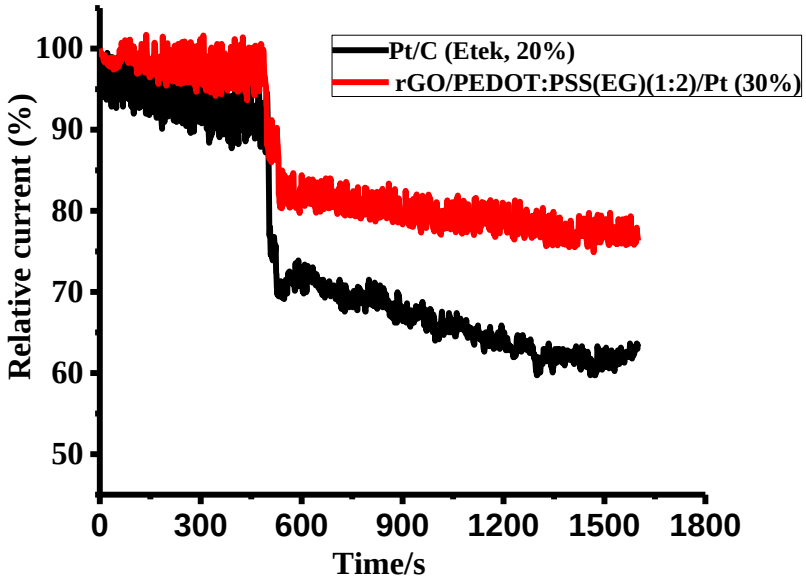

Figure 50. Comparative study of methanol tolerance ability of rGO/PEDOT:PSS(EG)(1:2)/Pt (30%) and Pt/C (Etek, 20%) by chronoamperometry at 0.8 V in O_2-saturated 0.1 M $HClO_4$ with a rotational speed of 1600 rpm.

The durability of rGO/PEDOT:PSS(EG)(1:2)/Pt (30%) and commercial Pt/C catalysts was also investigated by I-t measurement. As shown in Figure 51, rGO/PEDOT:PSS(EG)(1:2)/Pt (30%) exhibits a very slow attenuation with high current retention of 96.02% after 9000 s. By contrast, the Pt/C electrode exhibited a gradual decrease with 86.2% current retention after the same period indicating that rGO/PEDOT:PSS(EG)(1:2)/Pt (30%) electrocatalyst is much more stable than the commercial Pt/C catalyst.

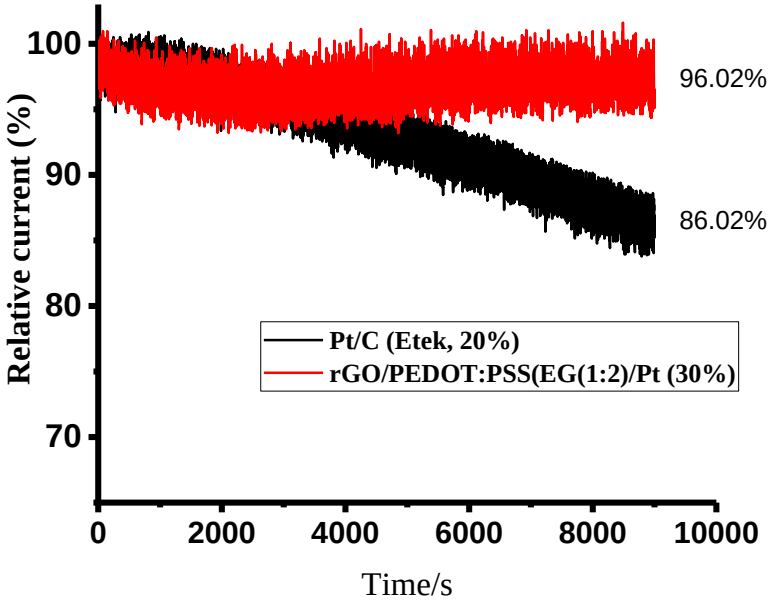

Figure 51. Chronoamperometric responses of rGO/PEDOT:PSS(EG)(1:2)/Pt (30%) and Pt/C (Etek, 20%) by chronoamperometry at 0.8 V in O_2-saturated 0.1 M $HClO_4$ with a rotational speed of 1600 rpm.

4.2 Amino-substituted naphthalene sulfonic acid/graphene composite as metal-free catalysts for oxygen reduction reactions

4.2.1 Background

Oxygen reduction reaction (ORR) is one of the most important reactions in a fuel cell, metal-air batteries, chloroalkali electrolyzer, metal corrosion, sensors, industrial electrolytic process, and electro-organic reactions[115, 214, 215]. However, ORR is kinetically sluggish, involves several steps and many intermediates which makes it challenging for researchers in the field. The most efficient catalyst generally considered so far for ORR are noble metals such as platinum (Pt) and its alloy. Nevertheless, these catalysts have a high price, scarcity, poor durability, poor tolerance for CO poisoning, and methanol crossover. In order to overcome these challenges researchers explore and develop non-precious metals or metal-free catalysts for ORR[82, 214, 216-218].

Graphene is becoming a promising candidate for ORR electrocatalysts due to its excellent conductivity, unique specific surface area, and customized surface chemistry[219, 220]. Graphene oxide has become the most common precursor for the cost-effective and mass production of graphene-based materials. Graphene oxide (GO) needs a reduction to restore the disrupted π system/sp^2 hybridized network using chemical or electrochemical reduction or thermal annealing. The electrochemical reduction method is advantageous over the others in that it is simple, fast, and doesn't require the use of any toxic reducing agents. Reduced graphene oxide (rGO) sheet shows low dispersibility in solvents and tends to restack as a graphite-like structure due to the removal of most of the oxygen functionalities. This aggregation of the rGO sheets reduces the available surface area, limits electron and ion transport which resulted in poor

electrochemical performance. One applied strategy to solve this problem is the composite formation of rGO with conducting polymers. The most commonly used conducting polymers are polypyrrole, polyaniline, polythiophene, and their derivatives[68, 74, 121, 221].

In recent years, graphene composited with poly(3,4-ethylenedioxythiophene):poly(styrenesulfonate) (PEDOT:PSS)[138], polypyrrole[222], polyaniline[149, 223] has been reported as an electrocatalyst for ORR. In this work, composite films of amino-substituted naphthalene sulfonic acid-based polymers and graphene layers were synthesized for metal-free electrocatalyst for oxygen reduction reaction in alkaline media. Enhanced durability for metal-free over metal catalysts is observed in alkaline media[14].

4.2.2 Surface characterization

The XRD pattern of graphite and GO were recorded in order to verify the structural changes occurring during the conversion of graphite to GO and are shown in Figure 52. The intense sharp peak ($2\theta = 26.6°$) for graphite powder (Figure 52a) corresponding to the (002)[76] reflection plane disappeared and shifted to a lower 2θ angle of 11.4° after being oxidized to GO (Figure 52b). The shift is attributed to the intercalation of oxygen-containing groups during oxidation with $KMnO_4$.[224]. An interlayer distance of ~0·78 nm was calculated using Bragg's equation for GO, which is larger than that of graphite powder (~0.34 nm). The small peak (Figure 52) at $2\theta = 42.6^0$ is corresponding to the (100) in-plane hexagonal atom arrangement[225].

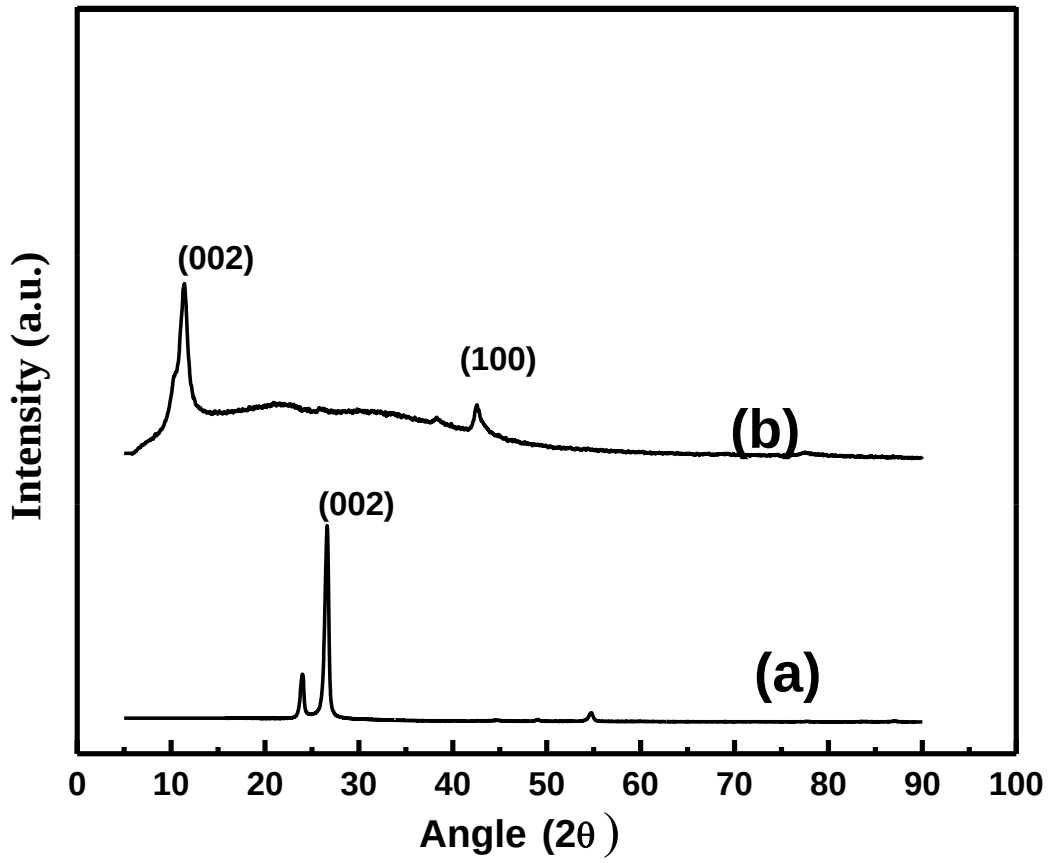

Figure 52. XRD patterns of (a) graphite and (b) GO.

The FTIR spectra of GO (Figure 53b) shows several characteristic peaks. A broad and intense peak at 3414 cm^{-1} attributed to O-H stretching of carboxyl groups, a weak peak at 1735 cm^{-1} assigned to C=O stretching of carbonyl groups, an intense peak at 1632 cm^{-1} corresponds to C=C stretching, a sharp peak at 1399 cm^{-1} and a broad peak at 1065 cm^{-1} are assigned to C-O stretching vibration of carboxyl and alkoxy group, respectively [56, 76, 225]. The relative intensity of these oxygen functionalities characteristic peaks in graphite (Figure 53a) are to a much lower value compared to GO. This is in agreement with the XRD results.

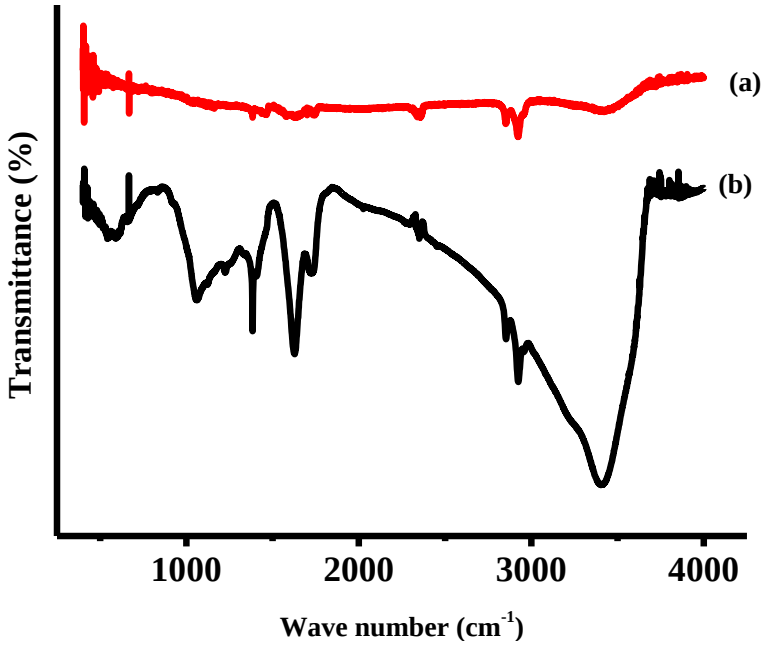

Figure 53. FT-IR spectra of (a) graphite and (b) GO.

4.2.3 Modification of glassy carbon electrode

Figure 54a shows typical cyclic voltammograms for the electropolymerization of 8-ANSA on a polished glassy carbon rotating disk electrode. During the first cycle, anodic and cathodic peaks at 0.78 V and -0.0811 V, respectively, were observed. In the successive scans, three new anodic peaks appeared at 0.251 V, 0.332 V, and 0.6139 V. Unlike the peak at 0.78 V which is due to the redox activity of the monomer[226], all the peaks increase with an increasing number of cycles which shows the formation of a polymer film on the surface of the glassy carbon electrode (GC) [36].

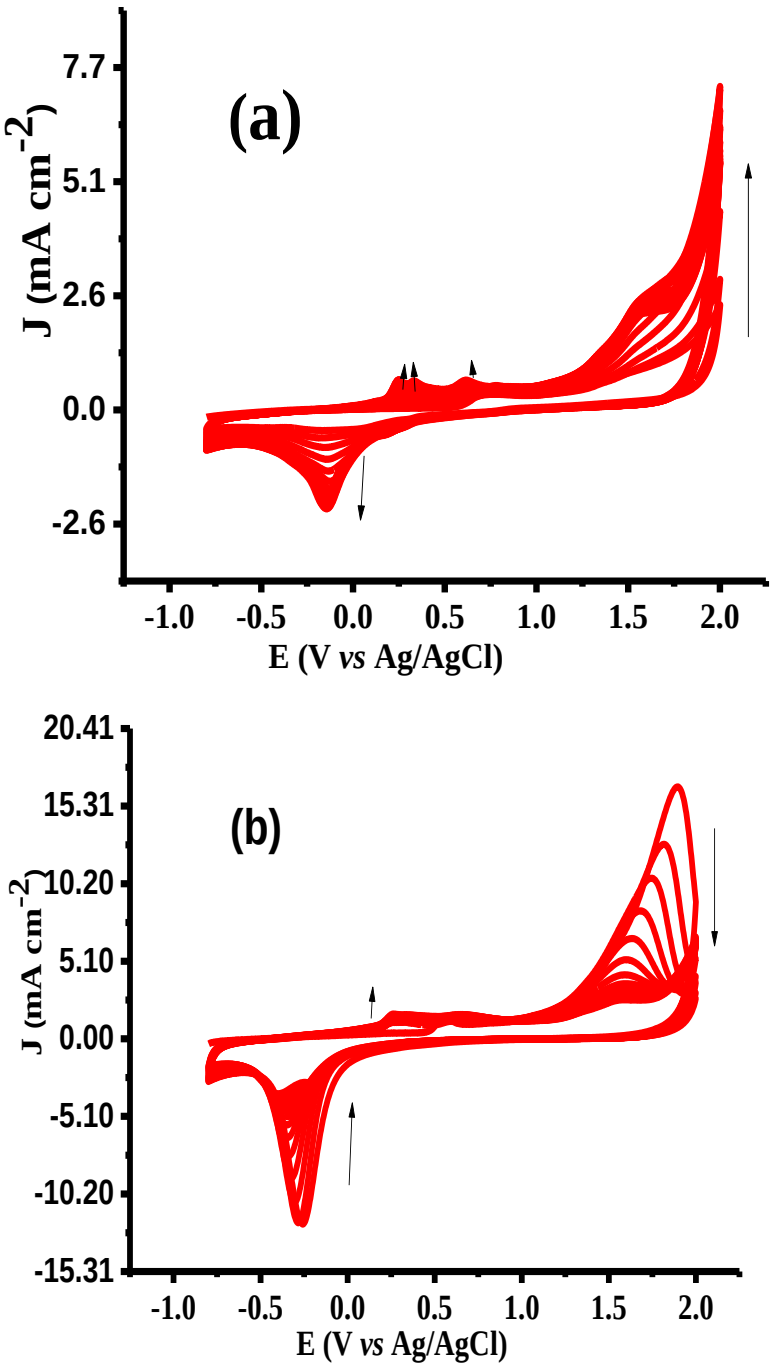

Figure 54. Cyclic voltammograms obtained for the electropolymerization of (a) 8-ANSA on GC and (b) 8-ANSA on GC/rGO from a solution containing 2 mM 8-ANSA monomer in 0.1 M HNO_3 at a scan rate of 100 mV s^{-1} for 16 scans between -0.8 V to 2.0 V *vs* Ag/AgCl.

During the first cycle of potentiodynamic polymerization of 8-ANSA onto rGO (Figure 54b) coated electrodes, two anodic peak and a cathodic peak at 0.55 V, 1.9 V and -0.25 V appeared. The peak current at 0.55 V diminished in the subsequent cycles. The peak currents at 1.9 V and -0.25 V decreases in each cycle which are due to monomer oxidation to the cation radical and monomer reduction. The anodic peak at 0.25 V increases in each cycle which is an indication of film growth on rGO/GC[226]. Peak currents for polymerization of 8-ANSA onto rGO (Figure 54b) coated electrode is higher than polymerization on the surface of the glassy carbon electrode (Figure 54a) since modification by rGO leads to a larger electroactive surface area.

Figure 55a shows the electrochemical reduction of graphene oxide (GO) on bare glassy carbon electrode. The observed reduction peak for GO in the first scan disappeared in subsequent scans confirming the electrochemical formation of rGO. A similar trend as a reduction of GO on GC was observed for the reduction of GO to rGO on 8-ANSA modified glassy carbon electrode (Figure 55b).

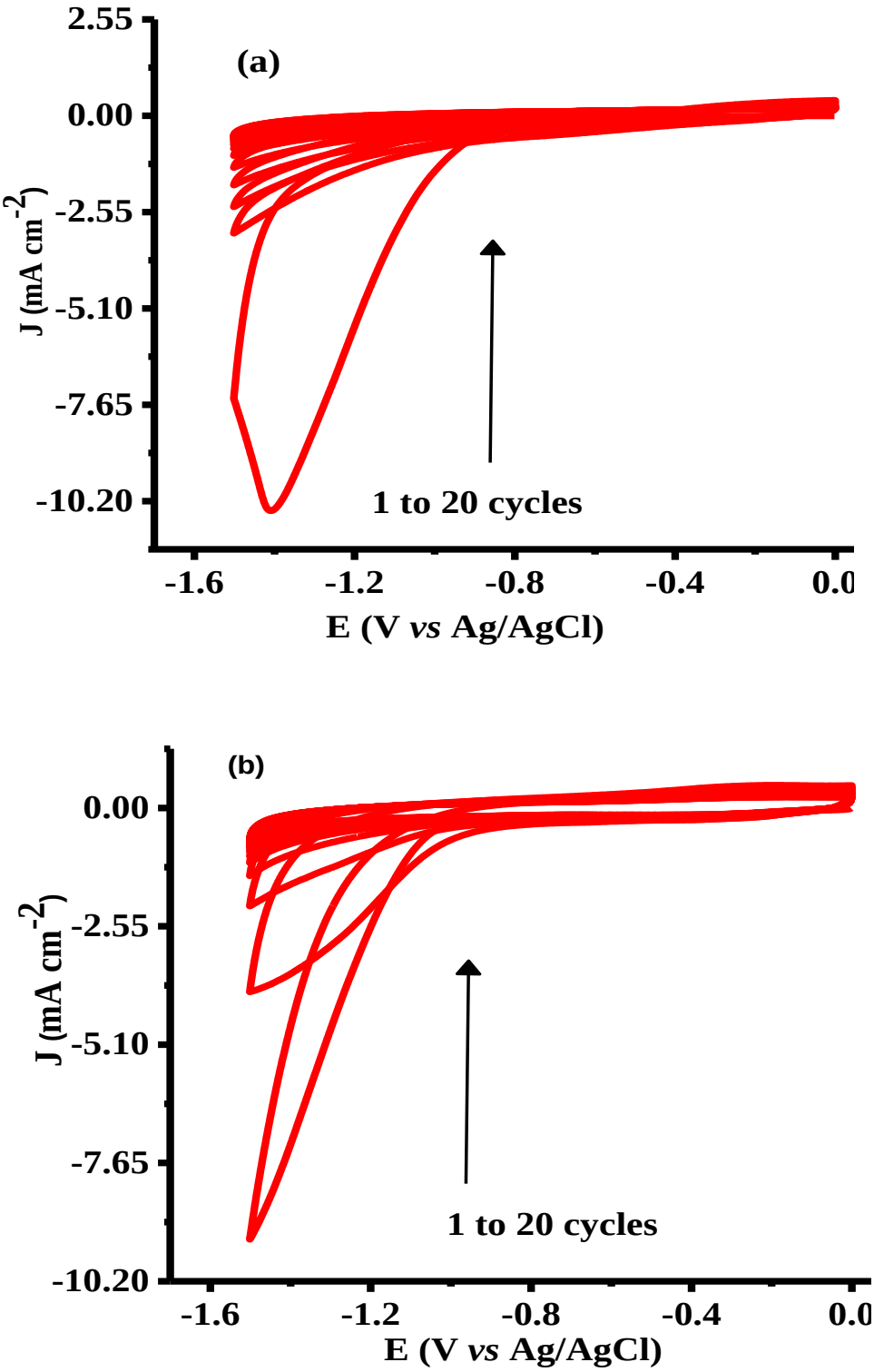

Figure 55. Electrochemical reduction of GO on (a) bare glassy carbon and (b) 8-ANSA in 0.1 M Na_2SO_4 solution for 20 cycles at a scan rate of 50 mV s^{-1}.

4.2.4 Computational study of ORR on poly(2-ANSA), poly(4-ANSA), poly(5-ANSA) and poly(8-ANSA)

The reaction mechanism of oxygen reduction involves diffusion in the bulk of the electrolyte and the conducting films, adsorption process, and electron transfer[110]. Any of these processes might be rate controlling and can be one of the criteria for the catalytic activity of materials. To explain the catalytic activity of poly(5-ANSA), poly(4-ANSA), poly(2-ANSA), and poly(8-ANSA), quantum-chemical calculations of the electronic structure for all the amino-substituted naphthalene sulfonic acid and their adsorption complexes with molecular oxygen were performed using density functional theory (DFT). The dimers (Figure 56) and their adsorption complexes with oxygen were used for all the calculations. To identify the adsorption sites, we used the natural charges from the Natural Bond Orbital (NBO) analysis. From the results in Table 4, the maximum negative change are concentrated on carbon atoms in positions C_3, C_4, C_8, C_9, C_{14}, C_{15}, C_{17}, and C_{18}. Each carbon atoms can in principle be an adsorption site for oxygen binding, however, the carbon atoms with larger negative charges are more preferable for the oxygen adsorption.

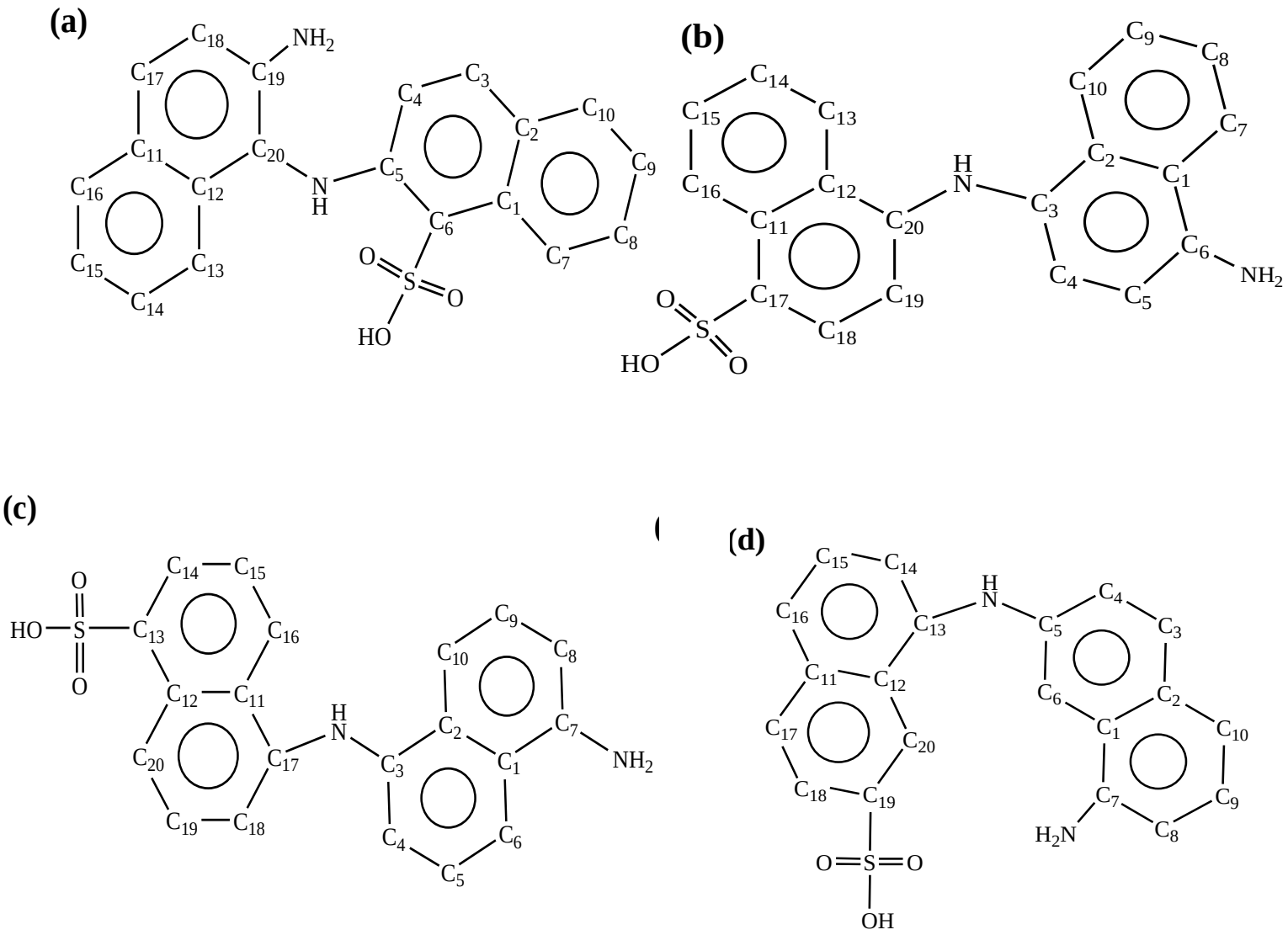

Figure 56. Dimers of (a) 2-ANSA, (b) 4-ANSA, (c) 5-ANSA, and (d) 8-ANSA molecular cluster. Hydrogen atoms were omitted for clarity.

Table 4. Natural charges obtained from the natural bond orbital (NBO) analysis in the dimers and dimer-O_2 complexes (where the binding site in all dimers is C_8-C_9), calculated using B3LYP/6-311++G(d,p)/PCM/water calculations. Other possible binding sites are also shown in *bold-italic* fonts.

Atom	2-ANSA	2-ANSA-O_2	4-ANSA	4-ANSA-O_2	5-ANSA	5-ANSA-O_2	8-ANSA	8ANSA-O_2
C_1	-0.047	-0.060	-0.065	-0.030	-0.081	-0.049	-0.084	-0.089
C_2	-0.097	-0.073	-0.085	-0.051	-0.060	-0.029	-0.066	-0.102
C_3	***-0.123***	-0.123	0.175	0.186	0.182	0.190	**-0.165**	-0.211
C_4	***-0.232***	-0.219	-0.301	-0.294	***-0.240***	-0.236	**-0.227**	-0.198
C_5	0.239	0.228	0.280	0.284	***-0.202***	-0.201	0.155	0.106
C_6	-0.370	-0.333	0.117	0.088	-0.202	-0.234	-0.217	-0.202
C_7	-0.152	-0.235	-0.187	-0.234	0.189	0.139	0.177	0.244
C_8	***-0.207***	***0.077***	***-0.219***	***0.071***	***-0.270***	***0.077***	***-0.252***	***0.098***
C_9	***-0.222***	***0.072***	***-0.201***	***0.096***	***-0.186***	***0.078***	***-0.207***	***0.081***
C_{10}	-0.168	-0.122	-0.202	-0.164	-0.248	-0.213	-0.226	-0.205
C_{11}	-0.079	-0.082	-0.072	-0.075	-0.071	-0.077	-0.070	-0.068
C_{12}	-0.050	-0.051	-0.051	-0.051	-0.043	-0.046	0.013	0.009
C_{13}	-0.208	-0.208	-0.201	-0.193	-0.265	-0.260	0.185	0.192
C_{14}	***-0.195***	-0.193	***-0.170***	-0.183	***-0.174***	-0.190	***-0.243***	-0.254
C_{15}	***-0.236***	-0.234	***-0.204***	-0.202	***-0.206***	-0.207	***-0.173***	-0.170
C_{16}	-0.162	-0.161	-0.191	-0.176	-0.149	-0.137	-0.217	-0.225
C_{17}	***-0.170***	-0.140	***-0.231***	-0.231	0.205	0.202	***-0.147***	-0.148
C_{18}	***-0.217***	-0.237	***-0.205***	-0.207	-0.250	-0.255	***-0.205***	-0.206
C_{19}	0.172	0.180	0.318	0.322	-0.169	-0.168	-0.302	-0.304
C_{20}	0.077	0.068	0.120	0.116	-0.224	-0.231	-0.175	-0.175
O_{43}	-	***-0.327***	-	***-0.336***	-	***-0.329***	-	***-0.345***
O_{44}	-	***-0.335***	-	***-0.331***	-	***-0.322***	-	***-0.367***

The results listed in Table 4 show a clear increase in the negative charge on O_2 (from 0.0 to −0.367; see the last two rows of Table 4), and a positive charge on the adsorption sites (C_8-C_9) in the complexes (2-ANSA–O_2, 4-ANSA–O_2, 5-ANSA–O_2, and 8-ANSA–O_2), indicating the adsorption of O_2 on the dimers.

The Gibbs free energy of formation (ΔG_f) (Table 5) between the oxygen atoms and the carbon atoms in positions 8 and 9 are lower for all ANSA-O_2 complexes than for other carbon atoms (e.g, C_{14} and C_{15}). This clearly shows that positions 8 and 9 are the most preferable O_2 adsorption sites.

The electron density transferred to O_2 and occupies the antibonding MO's of O_2 (adsorbed) is responsible for the destabilization of the O–O bond in O_2. This is evident from the O–O bond length which is elongated to 1.498, 1.5, 1.497, and 1.492 Å for 2-ANSA–O_2, 4-ANSA–O_2, 5-ANSA–O_2, and 8-ANSA–O_2, respectively, from that of 1.21 Å for the bare O_2 molecule. The O-C_x and O-C_y bond lengths also show the adsorption of the O_2 molecule. Thus, chemisorbed O_2 molecules have a fairly high degree of activation and can be easily reduced, which accounts for the catalytic activity of the ANSA polymers. Furthermore, 8-ANSA followed by 2-ANSA, with lowest ΔG_f and more possible adsorption sites, are the best electrocatalytic materials for oxygen reduction reaction.

Table 5. Change in Gibbs free energy of formation, ΔG_f (kcal mol^{-1}), equilibrium interatomic distances (Å) between the oxygen atoms, *r*(O=O), and the carbon atoms, *r*(O-C), in the dimers and dimer-O_2 complexes.

	Binding site (C_x-C_y)	**ΔG_f**	***r*(O=O)**	***r*(O-C_x)**	***r*(O-C_y)**
O_2	-	-	1.205	-	-
2ANSA-O_2	C_8-C_9	10.73	1.498	1.490	1.467
	C_{14}-C_{15}	10.89	1.499	1.495	1.467
4ANSA-O_2	C_8-C_9	12.99	1.500	1.489	1.467
	C_{14}-C_{15}	14.94	1.497	1.484	1.466
5ANSA-O_2	C_8-C_9	12.68	1.497	1.484	1.466
	C_{14}-C_{15}	14.90	1.497	1.484	1.466
8ANSA-O_2	C_8-C_9	10.71	1.492	1.545	1.455
	C_{14}-C_{15}	11.14	1.497	1.535	1.455

4.2.5 Oxygen reduction study using cyclic and linear sweep voltammetry

The oxygen reduction reaction for graphene oxide (GO) and reduced graphene oxide (rGO) modified glassy carbon electrodes are shown in Figure 57. The peak potential for oxygen reduction is shifted positively from -0.6 V in GC/GO to -0.36 V at GC/rGO electrode. This result shows electrochemically reduced GO has better ORR catalytic activity than that of GO.

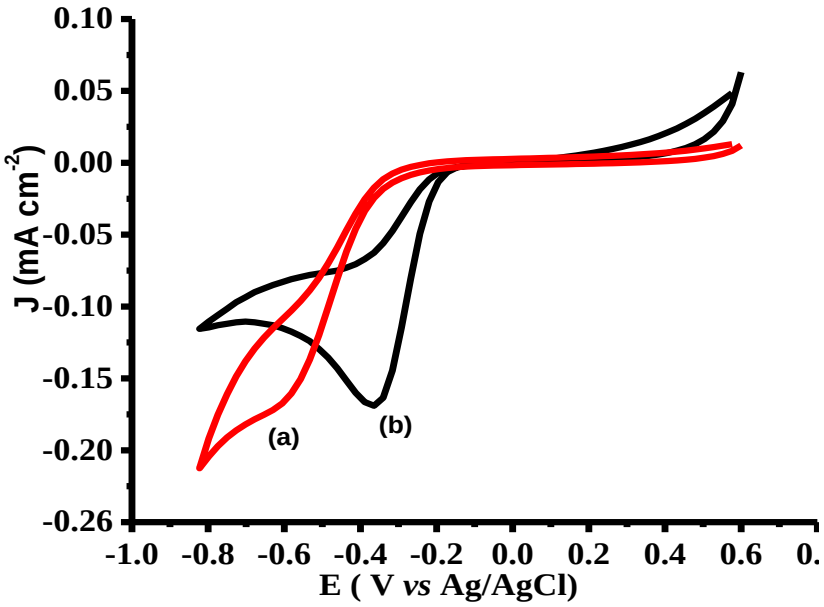

Figure 57. CVs of oxygen reduction at (a) GO and (b) rGO modified glassy carbon electrode in an O_2-saturated 0.1 M KOH solution at a scan rate of 20 mV s^{-1}.

After the electrosynthesis of all the monomers (8-ANSA, 2-ANSA, 4-ANSA, and 5-ANSA) on bare RDGC electrode under similar conditions, electrochemical reduction of GO on polymer-modified GC electrodes were performed.

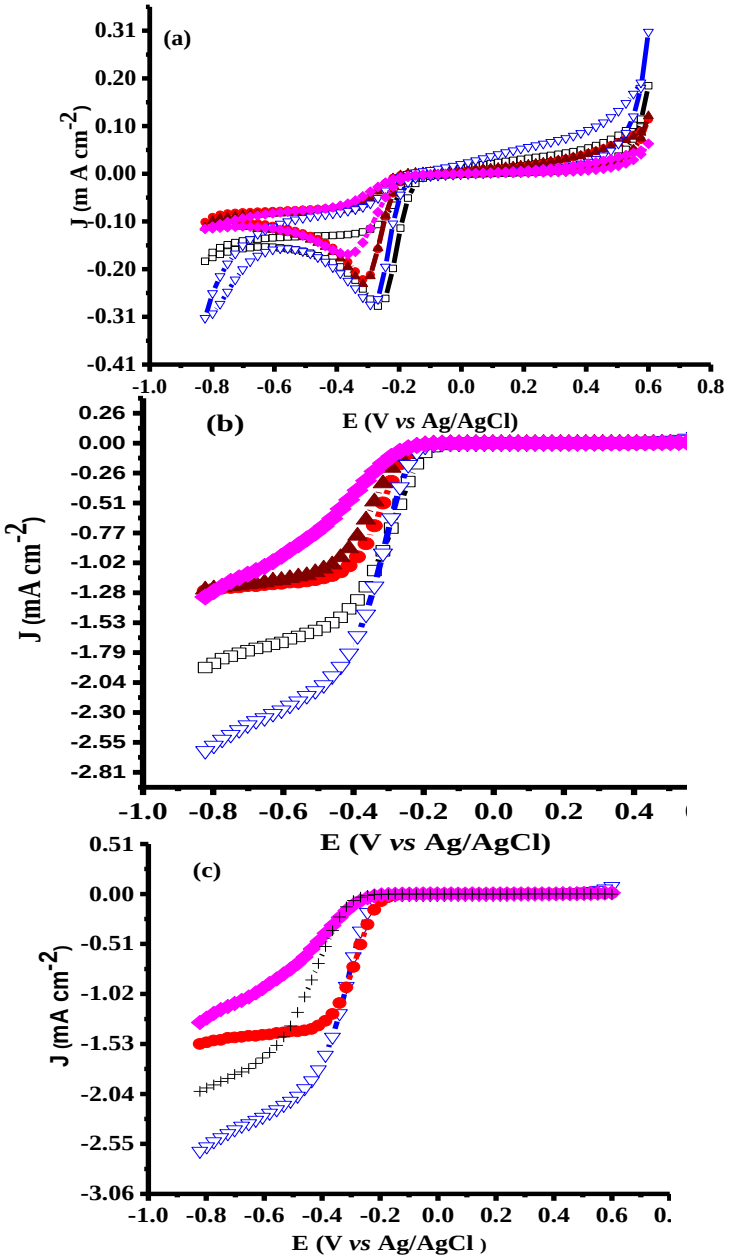

Figure 58. Comparison of the background corrected (a) cyclic voltammograms and (b) linear sweep voltammograms of (♦) GC/rGO, (▲) GC/poly(5-ANSA)/rGO, (●) GC/poly(4-ANSA)/rGO, (□) GC/poly(2-ANSA)/rGO, and (▽) GC/poly(8-ANSA)/rGO (c) linear sweep voltammograms of (♦) GC/rGO, (+) GC/poly(8-ANSA), (▽) GC/poly(8-ANSA)/rGO, and (●) GC/rGO/poly(8-ANSA) electrodes in 0.1 M KOH at a scan rate of 20 mV s^{-1} rotating at 1600 rpm.

Cyclic (CV) and linear sweep (LSV) voltammetry measurements were performed in O_2-saturated 0.1 M KOH to compare the electrocatalytic activity of the four different amino-substituted naphthalene sulfonic acid polymers composited with rGO. rGO modified GC electrode was also used in the comparison as a reference. The results are depicted in Figure 58a,b. The ORR activity for all the polymers-rGO modified GC electrode was found to be higher than that of GC/rGO. The onset potentials of GC/poly(2-ANSA)/rGO and GC/poly(8-ANSA)/rGO were more positive compared to that of GC/poly(4-ANSA)/rGO and GC/poly(5-ANSA)/rGO composite films. In terms of the current density, GC/poly(8-ANSA)/rGO has the highest value among all the polymers. This is in agreement with the computational prediction. Thus, GC/poly(8-ANSA)/rGO composite was chosen for further analysis.

The electrocatalytic activities for ORR of GC/rGO, GC/poly(8-ANSA), GC/poly(8-ANSA)/rGO and GC/rGO/poly(8-ANSA) were studied using linear sweep voltammetry in N_2 and O_2 saturated 0.1 M KOH solution and compared with each other in Figure 58c. Background corrected polarization curves (Figure 58c) at 1600 rpm shows GC/poly(8-ANSA)/rGO has the highest current density and more positive onset potential than GC/poly(8-ANSA) as well as GC/rGO, which indicates better electrocatalytic activity of GC/poly(8-ANSA)/rGO. GC/rGO/poly(8-ANSA) composite exhibits lower electrocatalytic activity towards ORR. At -0.6 V for instance, the current density recorded for ORR on the GC/ poly(8-ANSA)/rGO is 2.27 mA cm^{-2} which is much higher than GC/rGO/ poly(8-ANSA)(1.44 mA cm^{-2}). This is attributed to oxidation potential applied to electropolymerized 8-ANSA on GC/rGO to produce GC/rGO/ poly(8-ANSA) which could also possibly oxidize the previously synthesized rGO forming less conductive graphene oxide (GO).

The kinetics of the ORR activity of GC/poly(8-ANSA)/rGO were further investigated at different electrode rotational rates from 400 to 2500 rpm in 0.1 M KOH as shown in Figure 59. The onset of the O_2 reduction wave on GC/poly(8-ANSA)/rGO begins at a potential close to -0.21 V (*vs* Ag/AgCl). The current density increased when the rotational rates were increased from 400 rpm to 2500 rpm, indicating that the ORR is controlled by mass diffusion[138].

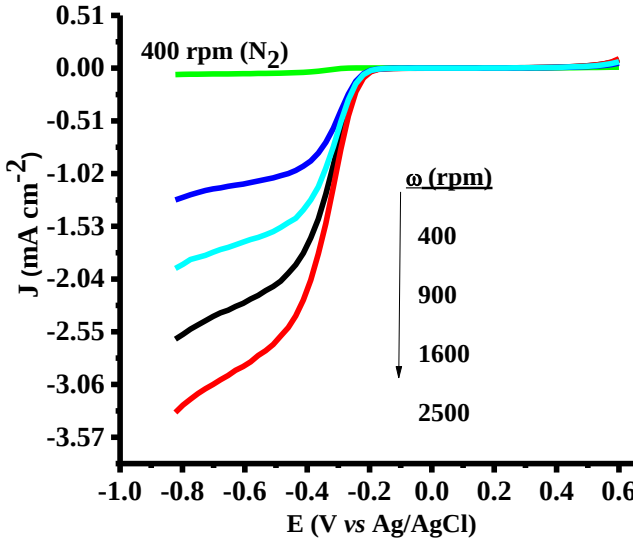

Figure 59. Linear sweep voltammograms of GC/poly(8-ANSA)/rGO at different rotation speeds (400, 900, 1600 and 2500 rpm) and a scan rate of 20 mV s^{-1}.

Koutecky-Levich (K-L) equation was applied in a mixed kinetic-diffusion controlled region in order to estimate the transferred electron number per oxygen molecule involved in the ORR. In 0.1 M KOH, the bulk concentration of O_2 (C_0) is 1.2×10^{-3} M, the diffusion coefficient of oxygen (D_0) is 1.9×10^{-5} cm^2 s^{-1}, the kinematic viscosity of the electrolyte (ν) is 0.01 cm^2 s^{-1}. The calculated values for the heterogeneous rate constant (k_f), and Γ (the surface coverage)of the catalyst on GC electrode as given in Table 6. The surface coverage Γ was evaluated using

Equation (7) by integrating the cathodic peak under the background correction at low scan rate from Figure 57a.

K-L plots (J^{-1} vs $\omega^{-1/2}$) for GC/poly(8-ANSA)/rGO (Figure 60) are parallel and linear, confirming that ORR follows first-order kinetics with respect to O_2 molecule. Furthermore, the plots do not pass through the origin indicating a mixed kinetic diffusion-controlled mechanism[149, 150]. The number of electrons transferred (n) and J_K can be obtained from the slope and intercept of the K-L plots[142].

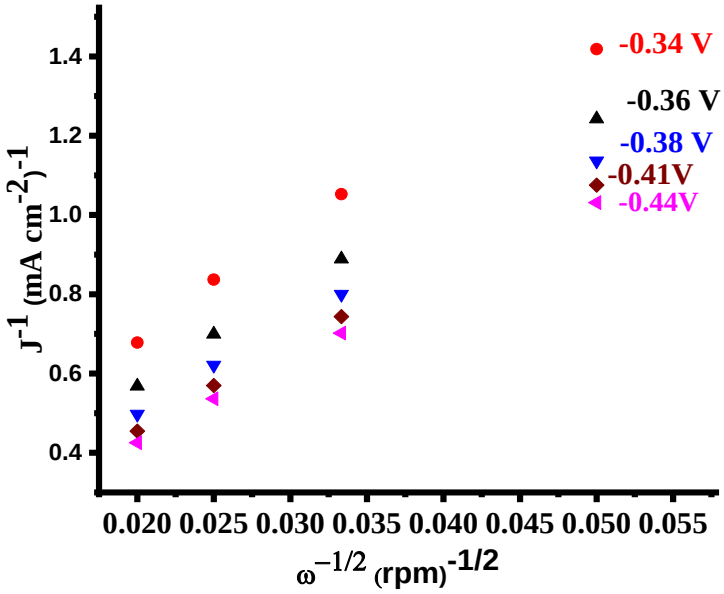

Figure 60. K-L plots (J^{-1} *vs* $\omega^{-1/2}$) at different electrode potentials in 0.1 M KOH.

The heterogeneous rate constants (k_f) for the reduction of oxygen were calculated from J_K and reported in Table 6. The ORR occurs either *via* direct four electrons pathway where O_2 is reduced to OH^-or 2-electron reduction pathway, where O_2 is reduced to HO_2^-[216]. The electron

transfer number (Figure 61) were calculated using K-L plots over the potential region of -0.36 to -0.43 V to be 2.5 - 2.8 for GC/poly(8-ANSA)/rGO, 2 - 2.13 for GC/rGO, and 1.8 - 2.5 for GC/poly(8-ANSA). These results demonstrated that the ORR process at the GC/poly(8-ANSA) and GC/rGO composite proceed with two electrons (2e−) pathway with the formation of HO_2^- but a mixture of HO_2^- and OH^- for GC/poly(8-ANSA)/rGO[216]. The direct, green and in situ electroreduction of O_2 dissolved in alkaline media to HO_2^- on GC/rGO and GC/poly(8-ANSA) electrodes is an attractive alternative to the current anthraquinone-based industrial production of H_2O_2, which produces a large number of chemical pollutants in a multistep energy-intensive process[227].

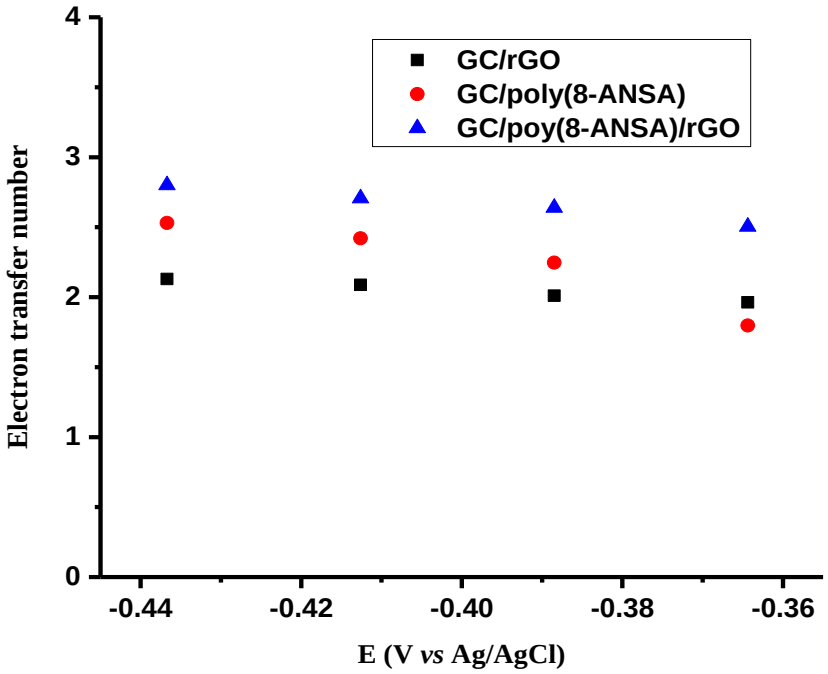

Figure 61. Electron transfer number as a function of potential of GC/rGO, GC/poly(8-ANSA), and GC/poly(8-ANSA)/rGO.

The RRDE was used further to evaluate the ORR pathway by monitoring the intermediate peroxide species of HO_2^- generated at the disk electrode in the alkaline medium during the ORR process at the GC/poly(8-ANSA)/rGO, GC/rGO, and GC/poly(8-ANSA) electrodes. As shown in Figure 62, all three catalysts generate ring currents over the potential range from −0.2 to −0.7 V for ORR. The electron transfer numbers (n) derived from RRDE result using Equation (17) over the potential range of -0.36 to -0.43 V to be 2.1 - 2.18 for GC/poly(8-ANSA), 2.14 - 2.15 for GC/rGO, and 2.76 - 2.82 for GC/poly(8-ANSA)/rGO, being consistent with the RDE results. Hence, the HO_2^- yields determined using Equation (18) for GC/poly(8-ANSA)/rGO (57%) significantly lower than GC/rGO (93%), and GC/poly(8-ANSA) (92%). All these values demonstrate the synergistically enhanced electrocatalytic efficiency of the composite (GC/poly(8-ANSA/rGO).

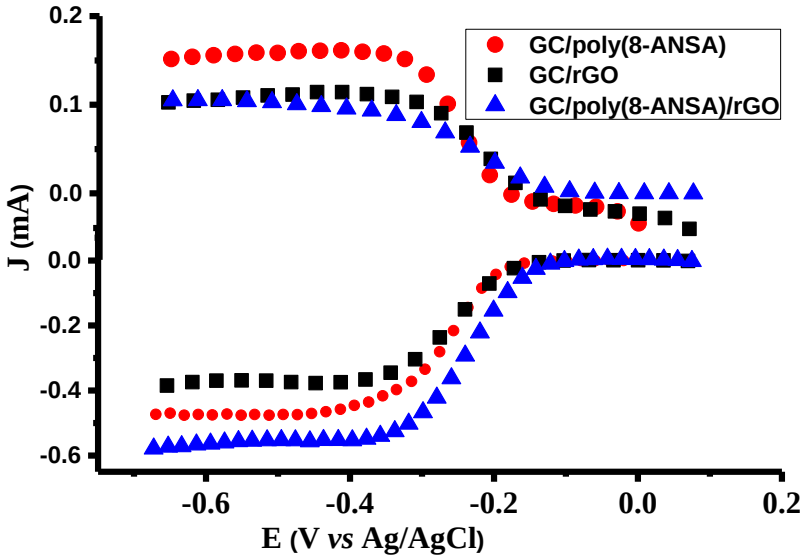

Figure 62. RRDE voltammograms of GC/rGO, GC/poly(8-ANSA), and GC/poly(8-ANSA)/rGO at 1600 rpm. The ring current was polarized at + 1.0 V.

The logarithm of J_k was plotted against the potential (Figure 63) to analyze the Tafel behavior for GC/poly(8-ANSA)/rGO, GC/poly(8-ANSA), and GC/rGO catalysts. The reaction kinetics can be evaluated using Tafel Equations (13) and (14). Using Equation (13), the high value of J_0 and low value of b will give high J_k value under the same overpotential ($E–E_0$). J_0 is a key parameter that reflects intrinsic rates of electron transfer between the solution and the electrode. It can be used to judge the catalytic efficiency of materials[116, 117].

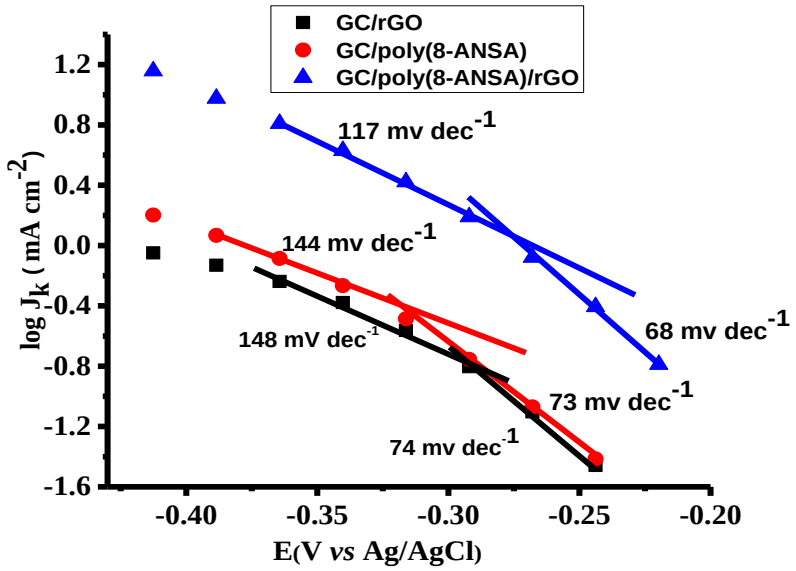

Figure 63. Tafel plots for the ORR at GC/poly(8 ANSA)/rGO (▲), GC/poly(8-ANSA) (●), and GC/rGO (■) at an electrode rotation rate of 1600 rpm.

The Tafel plots clearly show the electrocatalytic activity differences among the electrode materials. At -0.36 V, for instance, the kinetic current density of ORR on the GC/poly(8-ANSA)/rGO is 7.53 mA cm^{-2}, which is significantly higher than GC/rGO (0.58 mA cm^{-2}) and GC/poly(8-ANSA) (0.82 mA cm^{-2}). Tafel slopes and exchange current density were estimated from the linear portion of the Tafel plot at a low current density region (Figure 63) and presented

in Table 6. Therefore, incorporation of 8-ANSA between GC and rGO reduces the Tafel slope from 74 mV dec^{-1} to 68 mV dec^{-1} indicating more favorable kinetics for ORR[213]. The exchange current densities (J_o) were estimated from the intercept of a linear portion of the Tafel plots[117]. The J_o values for GC/8-ANSA/rGO is much higher than that of GC/rGO and GC/8-ANSA, showing an improved catalytic efficiency of the composite for ORR.

The reaction order (m) of ORR on GC/rGO, GC/poly(8-ANSA), and GC/poly(8-ANSA)/rGO catalysts was checked further by plotting log i *versus* log[(i-i/id)][228]. From Figure 64 and Table 6, the first-order dependence of the kinetics of the ORR was performed on GC/rGO, GC/poly(8-ANSA), and GC/poly(8-ANSA)/rGO.

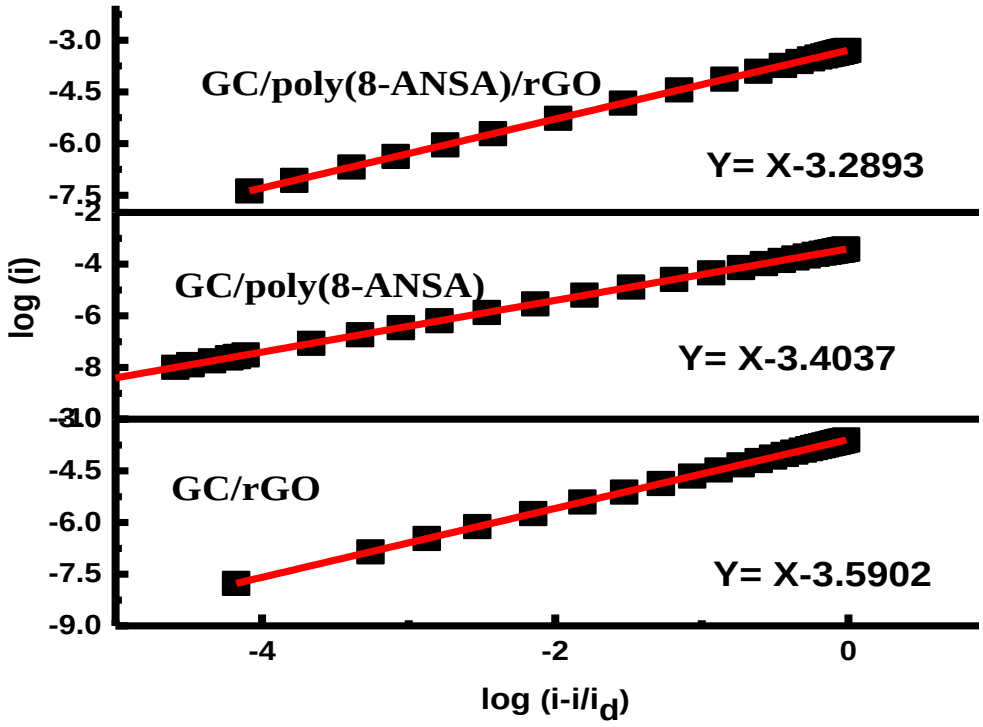

Figure 64. Reaction order plot for oxygen reduction reaction on GC/rGO, GC/poly(8-ANSA), and GC/poly(8-ANSA)/rGO (the slope stands for the reaction order number).

Table 6. Tafel slopes and exchange current densities for the ORR at GC/rGO, GC/8-ANSA, and GC/8-ANSA/rGO.

Catalyst	m	N		α	b	J_0	Γ	k_f
		K-L	RRDE		(mV dec^{-})	(mA cm^{-2})	(mol cm^{-2})	(cm s^{-1})
GC/rGO	1	2.04	2.01	0.8	74	1.76×10^{-5}	1.87×10^{-8}	2.7×10^{-3}
GC/8-ANSA	1	2.3	2.12	0.81	73	1.78×10^{-5}	2.01×10^{-8}	3.8×10^{-3}
GC/8-ANSA/rGO	1	2.7	2.8	0.87	68	9.58×10^{-5}	2.36×10^{-8}	3.5×10^{-2}

The value of k_f depends on the intrinsic activity of the catalyst sites and the surface concentration of catalyst sites[150]. In the present work, the surface coverage of all the catalyst films has the same order of magnitude (10^{-8} mol cm^{-2}) therefore, the surface concentration of the catalysts is assumed to be constant. GC/rGO, GC/poly(8-ANSA), and GC/poly(8-ANSA)/rGO yielded a slope of 74, 73, and 68 mV dec^{-1}, respectively at a low current density and the Tafel slopes increase at a higher current density. A Tafel slope of 60 mV dec^{-1} at 25°C would suggest a fast electron transfer reaction followed by a rate-determining chemical step. Furthermore, an increase in Tafel slope at the more negative potential in alkaline solution would also attribute to the chemical rate-determining step[150, 229]. A mechanistic scheme that is consistent with these results is as follows:

$$GC/Q + e^- \rightarrow GC/Q^- \quad \text{(a)}$$

$$GC/Q^- + O_2 \rightarrow GC/Q{-}O_2^- \quad \text{(b)}$$

$$GC/Q{-}O_2^- + H_2O + e^- \rightarrow GC/Q + HO_2^- + OH^- \quad \text{(c)}$$

$$HO_2^- + H_2O + 2e^- \rightarrow 3\,OH^- \quad \text{(d)}$$

Where, GC/Q is glassy carbon modified with rGO, poly(8-ANSA), or poly(8-ANSA)/rGO. Reaction (b) is the rate-determining slow chemical step that occurred after a fast electron transfer step (reaction (a)).

The specific performance of GC/poly(8-ANSA)/rGO is comparable or better with similar other values reported in the literature in Table 7.

Table 7. Comparison of materials and specific performance of the catalyst in 0.1 M KOH.

Catalyst	**Peak potential (*vs* Ag/AgCl)**	***b*(mv dec^{-1})**	***α***	***J^{o}* (mA cm^{-2})**	**Reference**
rGO-DAB	-0.28 V	62	-	-	82
PEDOT:PSS/rGO	-0.27 V	-	-	-	138
Py-EGO	-0.28 V	-	-	-	219
Fe-N/ rGOHN500	-	88	0.67	$2x10^{-5}$	224
Fe-N/rGO sonic	-	86	0.69	$2x10^{-5}$	224
(G-dye-FeP)n MOF	-0.23 V	-	-	-	230
CN*x*/graphene	-0.19 V	-	-	-	231
PPy/rGO	-0.30 V	-	-	-	231
N -doped graphene	-0.32 V	-	-	-	232
GC/poly(8ANSA)/rGO	-0.29 V	68	0.87	9.58×10^{-5}	This work

-DAB-1,4-diaminobutane

-Py-EGO-pyridine functionalized graphene nanosheets

-HN500- thermal annealed under H_2–N_2 atmosphere at 500°C

-Sonic- ultrasonication

-(G-dye-FeP)n MOF-dye functionalized rGO- iron−porphyrin metal-organic framework

-Carbon-nitrogen (x =0.15)

-PPy -polypyrrole

4.3 Roll-to-roll printed high voltage supercapattery in lead-contaminated aqueous electrolyte

4.3.1 Background

Portability in electronic devices is increasingly prevalent in the modern world which strongly demands the development of light-weighted, flexible, wearable, inexpensive, and environmental-friendly energy storage devices[233-236]. Electrochemical capacitors (supercapacitors), particularly flexible and wearable supercapacitors have great potential and suitable for portable electronic devices owing to high power-density, fast charging-discharging rate, and long operational life[74, 235, 237]. Supercapacitors are classified as the ideal electrical double-layer capacitors (EDLCs) and pseudocapacitors (SCs). The ideal EDLCs exhibit significantly low energy density (< 10 Wh kg-1) than batteries which limits their potential applications[238]. Hence, several investigations were carried out to improve the energy density by using materials that do have pseudocapacitance behaviors, like transition metal oxides and conducting polymers[79, 168, 176, 180, 239-243].

Conducting polymers (CPs) are a distinct group of pseudocapacitive materials that can accumulate energy *via* both redox and pseudo-capacitive properties. CP store and release energy based on the fast and reversible faradic reaction which combines the charge injected into the polymer backbone and ion exchange with the electrolyte to keep electrical neutrality in the film. This redox reaction requires that the CP has high electronic and ionic conductivity. The rate of the redox reaction is influenced by the mass transport of ions through the film and therefore it is highly dependent on electrode variable (material, surface area, geometry, surface condition),

solution variables (concentration, pH, solvent type), electrical variables (potential, current, quantity of electricity) and external variables (temperature, pressure, time)[74, 112, 176, 244].

Polypyrrole, poly(3,4-ethylenedioxythiophene), polyaniline and its derivatives, are the most common CPs used as pseudocapacitore electrode material[39, 79, 112, 176]. Among CPs, poly(3,4-ethylenedioxythiophene):(styrene sulfonate) (PEDOT:PSS), is a suitable material for solution-processable and roll-to-roll printable charge storage devices due to its excellent flexibility[40], high and tunable electrical conductivity[40, 245], chemical stability under ambient conditions[245], commercial availability[41, 50], dispersibility in water and some organic solvents[144]. Although CPs possess the capacity to accumulate energy, they have still low energy density when used alone. One of the strategies to improve their performance is by incorporating redox-active metals and metal oxides into the conducting polymer to form a composite material[237]. Some of these composite materials exhibit an intense peak on the cyclic voltammograms and a non-linear shape in the galvanostatic charge-discharge curves. This led to the third class of supercapacitors named supercapattery. Such composites combine high energy density battery-type materials with high power capability supercapacitor materials[8, 159, 161, 163, 164].

PEDOT:PSS can capture and used to remove toxic metals like lead by applying a potential and the adsorbed toxic metal can be further released by applying a reverse potential into another reservoir, which allows the regeneration of the adsorbent material without using additional chemicals and introducing additional costs and wastes[246]. However, one needs to find a way to use the highly concentrated toxic metal found in the second reservoir after cleaning the water. In the report on the potential application of PEDOT:PSS for electrosorption/desorption of Pb^{2+} ions,

a significant redox activity on the PEDOT:PSS was observed which can be harnessed for charge storage through faradic processes[246]. Hence, this work report a roll-to-roll printed PEDOT:PSS-based plastic electrode which has a potential application for a self-detoxifying printable plastic supercapattery electrode.

4.3.2 Electrochemical deposition of $PbCl_2$ on PEDOT:PSS/ITO/PET film

A representative cyclic voltammograms for ITO/PET, PEDOT:PSS/PET and PEDOT:PSS/ITO/PET electrode cycled 10 times in 1 mM Pb^{2+}/0.1 M NaCl in order to form reduciable/oxidizable $PbCl_2$ onto the working electrode are shown in Figure 65. To avoid over oxidation of PEDOT at higher potential, the negative scan of potential was beginning at 0.8 V[247] and extend to -1 V to include complete redox peaks. In the first negative scan of the preliminary 10 cycles (Figure 65), lead was electrodeposited on the working electrode from the solution containing Pb^{2+} in 0.1 M Cl^-. On the anodic scan, lead on the surface of the electrode oxidize and form $PbCl_2$ film ($Pb + 2Cl^- \rightarrow PbCl_2 + 2e^-$)[248-250]. On repeated cycling, the oxidation products ($PbCl_2$) formed during the positive half cycle are reduced to metallic lead in parallel with the electrodeposition of Pb^{2+} ions from the solution forming a thicker film of $PbCl_2$ up on reduction[249].

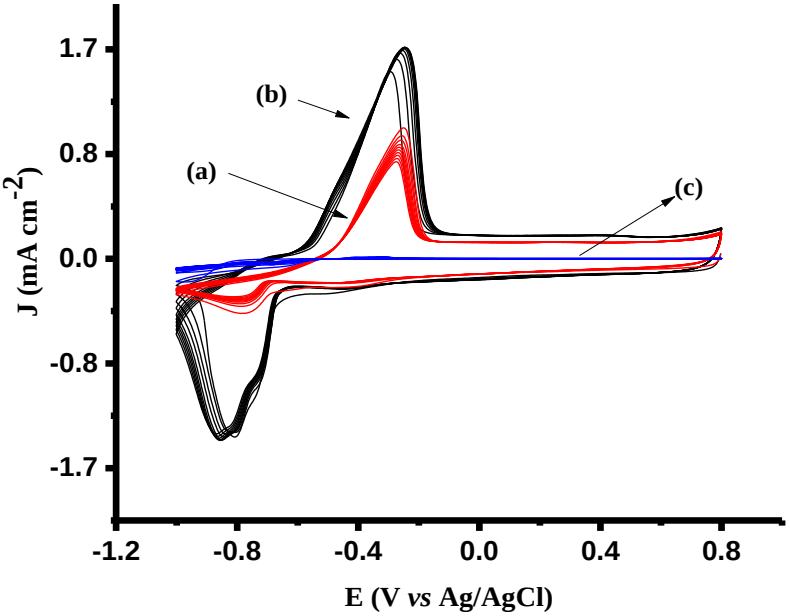

Figure 65. CV curves of 10 cycles for (a) PEDOT:PSS/PET, (b) PEDOT:PSS/ITO/PET (c) ITO/PET in 1 mM Pb^{2+}/0.1 M NaCl at a scan rate of 50 mV s^{-1}.

4.3.3 XPS study of PEDOT:PSS/ITO

X-ray photoelectron spectroscopy (XPS) was used to investigate the change in surface chemistry of the PEDOT:PSS/ITO/PET films in the presence and absence of Pb^{2+} in 0.1 M NaCl aqueous solution. Typical full-range XPS survey spectra before and after deposition of lead from 3 mM Pb^{2+}/0.1 M NaCl aqueous solution on PEDOT:PSS/ITO films are depicted in Figure 66a. The incorporation of lead and chlorine into the PEDOT:PSS/ITO/PET film can be seen from the appearance of the characteristics peaks of lead around 140 eV and chlorine at 198.1 eV (Figure 66a (b') which were not present in the pristine film before the deposition of lead (Figure 66a (a'). After electrochemical deposition of lead, the doublets characteristic peaks of lead were observed at a binding energy of 138.6 (Pb $4f_{7/2}$) and 143.4 eV (Pb $4f_{5/2}$) as shown in the resolved spectra (Figure 66b). The presence of a peak at 138.6 eV (Pb-Cl) in Figure 66b and peak at 198.1 eV

(Cl 2p) in Figure 66c showed that $PbCl_2$ adlayers were formed on the surface of PEDOT:PSS/ITO/PET[251-253].

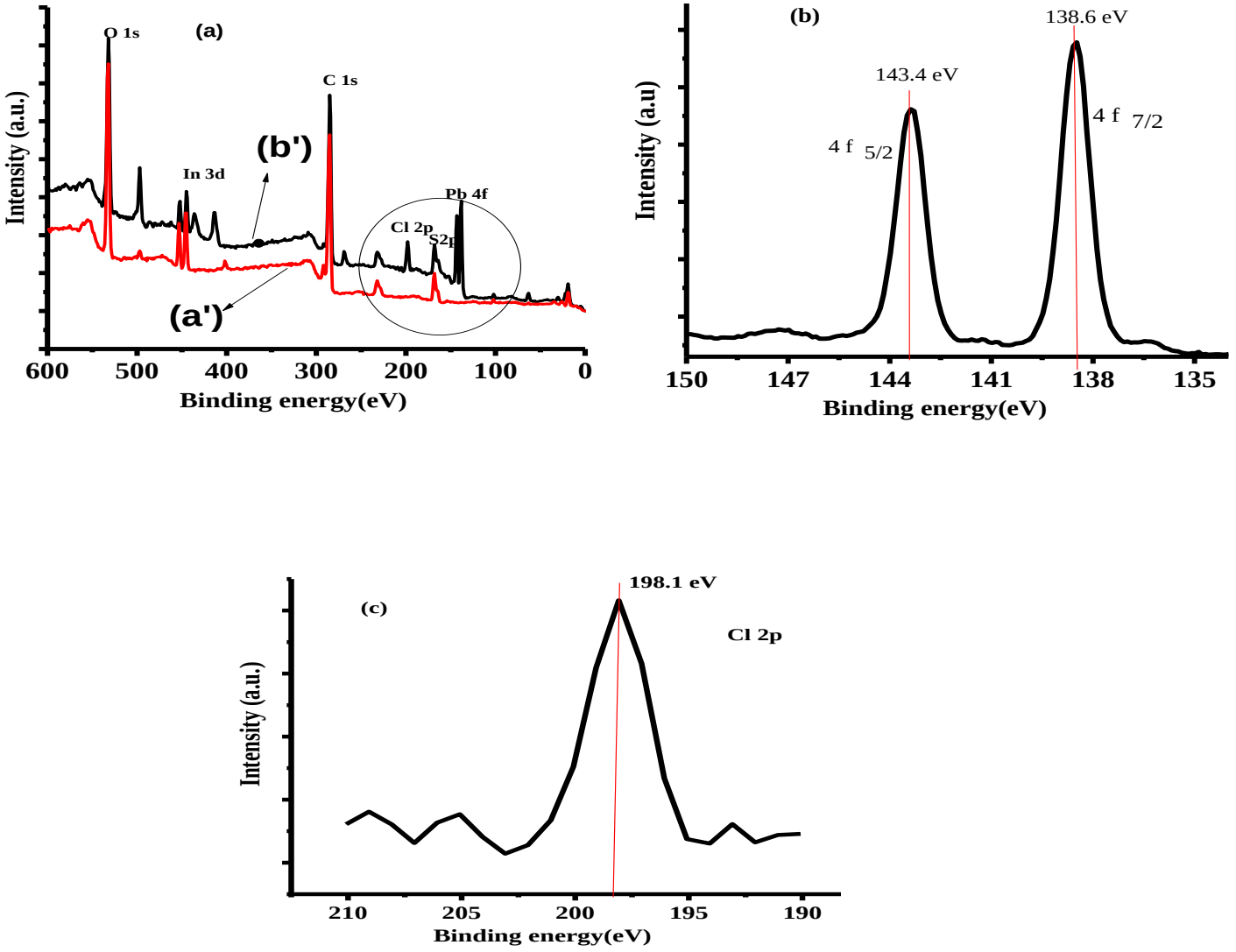

Figure 66. (a) Full range survey X-ray photoelectron spectra of the PEDOT:PSS/ITO/PET film (a') before and (b') after deposition of Pb (b) Pb 4f spectra for adsorbed lead ions on PEDOT:PSS/ITO/PET and (c) Cl 2p spectra on PEDOT: PSS/ITO/PET.

4.3.4 Cyclic voltammetry studies on PEDOT:PSS/ITO/PET films

Figure 67 shows the CV curves (1 cycle) after a steady state is obtained for 10 cycles. Comparing the CV curves of PEDOT:PSS/PET in 0.1 M NaCl and 1 mM Pb^{2+}/ 0.1 M NaCl electrolyte (Figure 67 a, b), a cathodic peak at -0.8 V and an anodic peak at -0.26 V (Figure 67b) were observed for Pb^{2+} containing 0.1 M NaCl solution. These redox peaks correspond to the oxidation and reduction of $Pb/PbCl_2$ onto the roll to roll printed PEDOT:PSS film similar to battery type of electrode process: $Pb + 2Cl^- \rightarrow PbCl_2 + 2e^-$. The lead-acid anode process, $Pb \rightarrow PbSO_4$, behaves similarly[159]. Both 0.1 M NaCl and 1 mM Pb^{2+}/0.1 M NaCl electrolyte on PEDOT:PSS/PET in the potential region 0 to 0.8 V shows an ideal rectangular curve characteristics of PEDOT:PSS[74, 176]. The CV curve obtained for PEDOT:PSS on ITO/PET (Figure 67c) showed a distinctly higher in redox peak current compared to PEDOT:PSS on PET (Figure 67b) and ITO/PET (Figure 67d).

The overall integral capacity of 0.5 mAh g^{-1}, 19 mAh g^{-1}, 31 mAh g^{-1} were calculated from Figure 67 b, c and d for ITO/PET, PEDOT:PSS/PET, and PEDOT:PSS/ITO/PET, respectively. Clearly, the capacity on ITO/PET is small but enhanced charge storage properties were observed for roll to roll printed PEDOT:PSS on ITO/PET. Therefore, PEDOT:PSS/ITO/PET was thus used for subsequent experiments. The separation of peak potential ($\Delta E_p = E_{anodic} - E_{cathodic}$) for PEDOT:PSS/ITO/PET in Pb^{2+}/0.1 M NaCl were 0.64 V. Based on ΔE_p as an indicative test for reversible processes which is always close to 59/n mV at 25^oC, the formation of $PbCl_2$ during oxidation and its reduction to metallic lead is an irreversible process[112]. However, the deviation is a direct result of an increase in the amount of $PbCl_2$ reduced from that originally formed product at the anode accompanied by an increase of ΔE_p. In spite of these deviations, the

chemical and stoichiometric changes of the electroactive species involved remain reversible[159, 249]. The Pourbaix diagram of Pb-H_2O-Cl in a neutral solution shows immunity at a potential below -0.47 V *vs* Ag/AgCl, the formation of tribasic $PbCl_2$ ($3PbO.PbCl_2$) between -0.47 V and 0.54 V and formation of PbO_2 at a higher potential[248, 254].

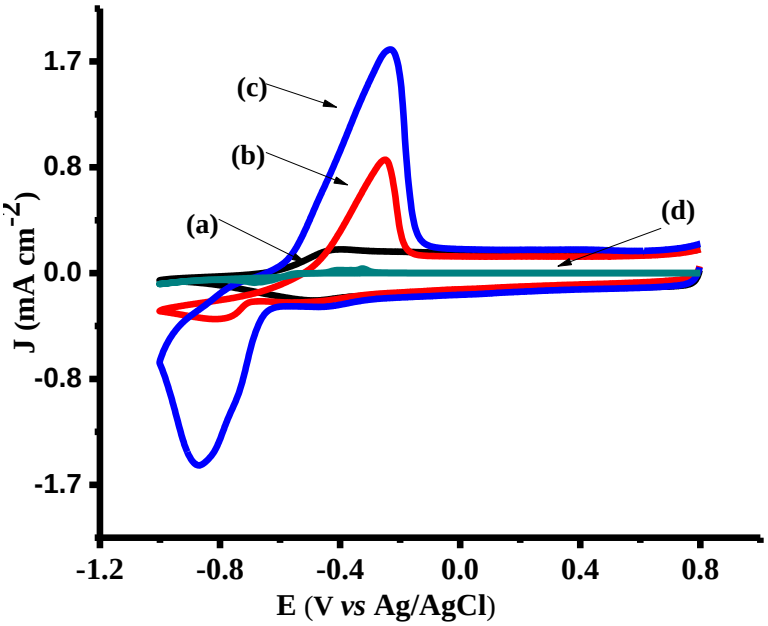

Figure 67. CV curves (a) PEDOT:PSS/PET film in 0.1 M NaCl, (b) PEDOT:PSS/PET in 1 mM Pb^{2+}/0.1 M NaCl, (c) PEDOT:PSS/ITO/PET in 1 mM Pb^{2+}/0.1 M NaCl and (d) ITO/PET in 1 mM Pb^{2+}/0.1 M NaCl at a scan rate of 50 mV s^{-1}.

CV was performed for PEDOT:PSS/ITO/PET electrode between -1.0 V and 0.8 V in 0.1 M NaCl at different concentration of Pb^{2+} (Figure 68). The current response increase with increasing the concentration of lead from 0.5 mM to 2 mM.

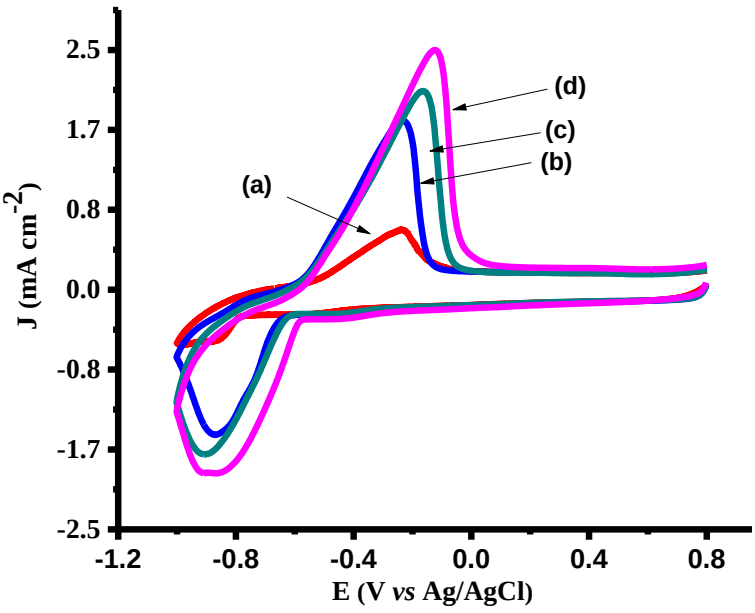

Figure 68. CV curves of PEDOT:PSS/ITO/PET (a) 0.5 mM Pb^{2+}/0.1 M NaCl, (b) 1 mM Pb^{2+}/0.1 M NaCl, (c) 1.5 mM Pb^{2+}/0.1 M NaCl, (d) 2 mM Pb^{2+}/ 0.1 M NaCl, at a scan rate of 50 mV s^{-1}.

4.3.5 Galvanostatic charge-discharge studies on PEDOT:PSS/ITO/PET films

Typical GCD curves for PEDOT:PSS/ITO/PET at different concentration of Pb^{2+} ions in 0.1 M NaCl and measured at 0.2 mA cm^{-2} under a potential window of -1.0 V to 0.8 V (*vs* Ag/AgCl) are depicted in Figure 69.

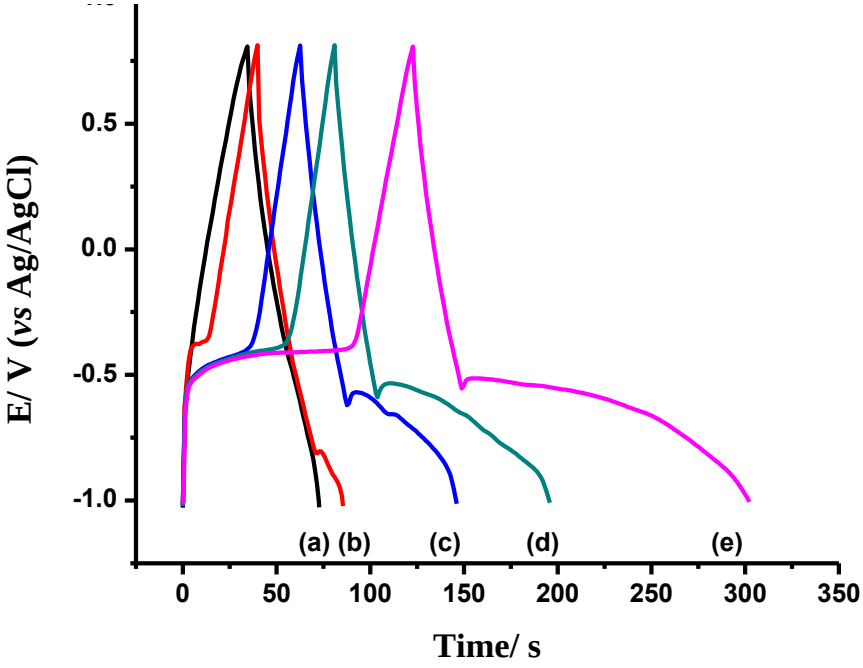

Figure 69. GCD curves of PEDOT:PSS/ITO/PET in (a) 0.1 M NaCl, (b) 0.5 mM Pb^{2+}/0.1 M NaCl, (c) 1 mM Pb^{2+}/0.1 M NaCl, (d) 1.5 mM Pb^{2+}/0.1 M NaCl, and (e) 2 mM Pb^{2+}/0.1 M NaCl at 0.2 mA cm^{-2}.

Non-ideal triangular shape with a voltage plateau region for Pb^{2+}/0.1 M NaCl solution is in agreement with the observations in the CV curves. These nonlinear GCD behaviors originated from the battery-type charge storage behavior as a result of the lead incorporated in PEDOT:PSS plastic film electrode. This mechanistic behavior in a single electrode is what is termed as supercapattery electrode[242].

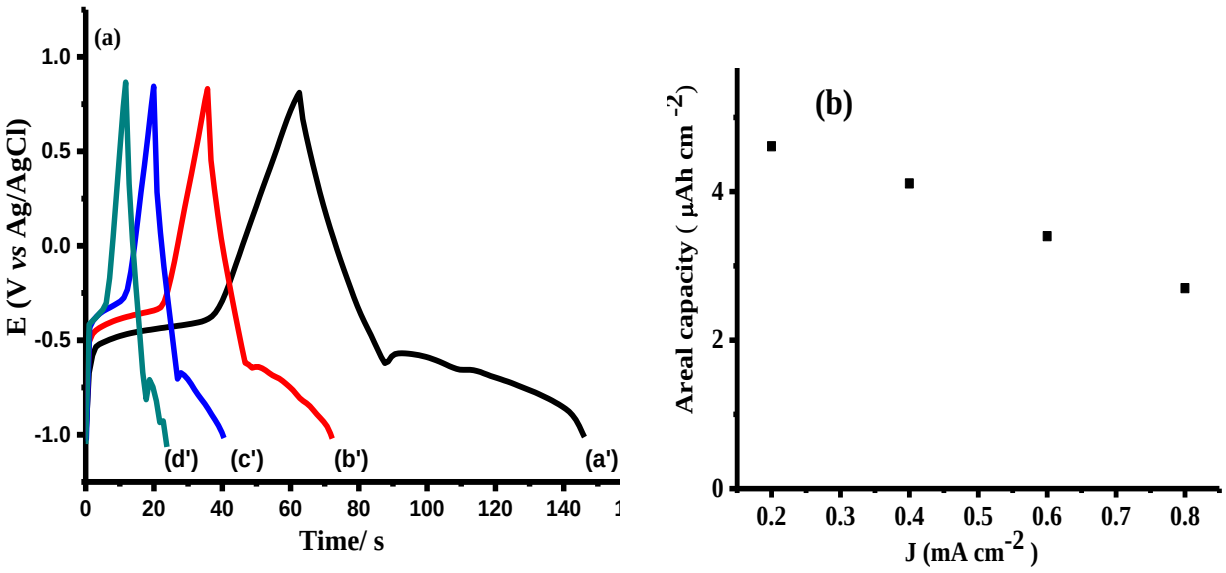

Figure 70. (a) GCD curves of PEDOT:PSS/ITO/PET in 1 mM Pb^{2+}/0.1 M NaCl at (a') 0.2 mA cm^{-2}, (b') 0.4 mA cm^{-2}, (c') 0.6 mA cm^{-2} and (d') 0.8 mA cm^{-2}. (b) Areal capacity of PEDOT:PSS/ITO/PET in 1 mM Pb^{2+}/0.1 M NaCl at different current density.

Figure 70a shows the GCD curves of PEDOT:PSS/ITO/PET in 1 mM Pb^{2+}/0.1 M NaCl at different current densities. About 84% of the specific capacity is retained (Figure 70b) on average for each 0.2 mA cm^{-2} increment in the current density, which suggests a good power capability of the PEDOT:PSS/ITO/PET. Generally, an increase in discharging current densities gradually decreases the capacity since insufficient active materials are involved in the redox reaction[255].

The areal capacitance and specific capacitance of PEDOT:PSS/ITO/PET in 0.1 M NaCl were calculated using Equations (24) and (26) due to linear behavior of the charge-discharge curves. The capacitances for an active material loading of 0.046 mg cm^{-2} calculated from the discharge curve (Figure 69, a) at 0.2 mA cm^{-2} are compared with similar other values reported in the

literature in Table 8. A better performance in a neutral aqueous solution was observed for PEDOT:PSS on ITO/PET substrate. The specific capacity of PEDOT:PSS/ITO/PET electrode in 0.5 mM Pb^{2+}/0.1 M NaCl was 2.54 μAh cm^{-2} (55.2 mAh g^{-1}). As the concentration of the Pb^{2+} ions in 0.1 M NaCl solution increased from 1 mM to 1.5 mM, and 2 mM Pb^{2+} the specific capacity increased from 4.64 μAh cm^{-2} (100.9 mAh g^{-1}) to 6.4 μAh cm^{-2} (138.8 mAh g^{-1}), and 10 μAh cm^{-2} (216.8 mAh g^{-1}) at 0.2 mA cm^{-2} (4.34 A g^{-1}), respectively.

Table 8. Comparison of our result with some reported values of PEDOT based electrodes.

Materials	**Electrolyte**	**Test condition**	**Areal capacitance (mF cm^{-2})**	**Specific Capacitance (F g^{-1})**	**References**
PEDOT/PET	$BMIMBF_4$	100 mV s^{-1}	11	-	74
PBOTT-BTD/ITO/PET	0.1M $TBAPF_6$/ACN	0.1 mA cm^{-2}	2.5	31	39
PEDOT/ITO/PET	0.1 M $TBAPF_6$/ACN	0.1 mA cm^{-2}	4.3	108	39
PEDOT:PSS/PET	PVA/H_3PO_4	0.025 mA cm^{-2}	1.64	28.76	40
PEDOT/ITO glass	1 M H_2SO_4(aq)	0.2 mA cm^{-2}	$\sim\frac{1}{3}$(43.75)	-	76
PEDOT:PSS-SWNT	1 M $NaNO_3$(aq)	5 mV s^{-1} (0.67 A g^{-1})	-	133	256
PEDOT:PSS/PET	0.5 M K_2SO_4(aq)	100 mV s^{-1}	1	-	257
Ru_2O/PEDOT/PET	1 M H_2SO_4	100 mV s^{-1}	1.2	-	178
PEDOT/PANI hydrogel	1 M H_2SO_4	5 mV s^{-1}	-	112.6	180
PEDOT:PSS/ITO/PET	0.1 M NaCl	0.2 mA cm^{-2} (4.4 A g^{-1})	4.3	93	This work

$BMIMBF_4$ - 1-butyl-3-methylimidazolium tetrafluoroborate

PBOTT-BTD - Poly[4,7-bis(3,6-dihexyloxy-thieno[3,2-b]thiophen-2-yl)]benzo[c][1,2,5]thiadiazole

$TBAPF_6$ - Tetra-n-butylammonium hexafluorophosphate

ACN - Acetonitrile

rGO - Reduced graphene oxide

PVA - Polyvinyl alcohol

SWNT - Single walled carbon nanotubes

PANI -. Polyaniline

4.3.6 Cyclic stability study of PEDOT:PSS/ITO/PET films

The cyclic stability of the electrode material, which is an important parameter for the energy storage material, was investigated by cycling PEDOT:PSS/ITO/PET electrode 1000 times in 1 mM $Pb^{2+/}$ 0.1 M NaCl solution at a higher current density of 0.4 mA cm^{-2}.

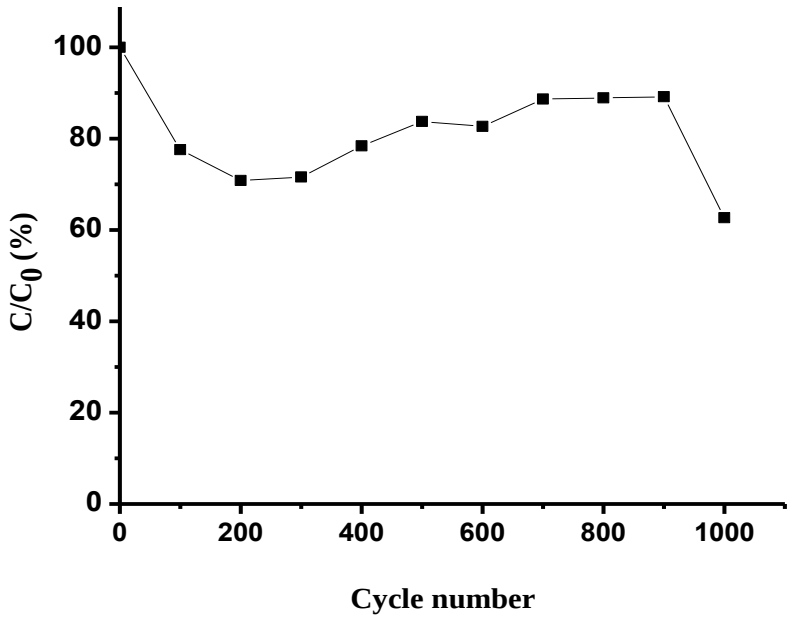

Figure 71. Normalized capacity against number of cycles for PEDOT:PSS/ITO/PET in 1 mM Pb^{2+}/0.1 M NaCl at a current density of 0.4 mA cm^{-2}.

Figure 71 shows the capacity retention, C/C_0 (expressed in %) as a function of cycle numbers where C is the specific capacity of each cycle, and C_0 is the specific capacity before the charge-discharge cycle. The capacity initially decreases by 30% until 200 cycles, but after 200 cycles the capacity increased and become 89% of the initial capacity after 900 cycles. After 1000 cycles, 63% of the initial capacity was recorded on PEDOT:PSS/ITO/PET. The increase in the

capacity after 200 cycles may most likely be due to an increase in the rate of the reaction on cycling for a fresh compact $PbCl_2$ film on PEDOT:PSS/ITO/PET which could be difficult to be fully utilized at the beginning of the electrochemical reaction. A similar increase in capacity with cycling was also reported and the observed result was due to a conditioning effect on the carbon/Pb-$PbSO_4$ interface or a Pb dissolution/precipitation reaction on the electrode surface[258].

4.3.7 Electrochemical studies of symmetric devices

To obtain a more realistic data for the application of PEDOT:PSS/ITO/PET electrode in real devices, two PEDOT:PSS/ITO/PET electrodes were assembled in symmetric structure with aqueous NaCl electrolyte with and without Pb^{2+}. An extended potential window up to 2.2 V could be obtained using a neutral medium[259]. CV and the GCD curves of symmetric PEDOT:PSS/ITO/PET supercapacitor and supercapattery with 0.1 M NaCl, 1 mM Pb^{2+}/0.1 M NaCl, 2 mM Pb^{2+}/0.1 M NaCl, and 3 mM Pb^{2+}/0.1 M NaCl are shown in Figure 72a, b. Rectangular CV curve and ideal triangular GCD curve are observed for supercapacitors with 0.1 M NaCl. This indicates that the material charges and discharges quickly and efficiently[74]. The peaks in the CV curve and non -ideal triangular shape of the GCD curve for lead (Pb^{2+}) containing 0.1 M NaCl are an indication for non-capacitive charge storage in the devices[165]. From the GCD measurement for the symmetric device in 0.1 M NaCl the specific capacitance was 15.7 F g^{-1} (7.9 mAh g^{-1}) whereas the specific capacity in 1.0 mM Pb^{2+}/0.1 M NaCl, 2 mM Pb^{2+}/ 0.1 M NaCl, and 3 mM Pb^{2+}/0.1 M NaCl were found to be, 8.8, 12.7 and 18.4 mAh g^{-1} for a current density of 0.1 mA cm^{-2} (1.1 A g^{-1}).

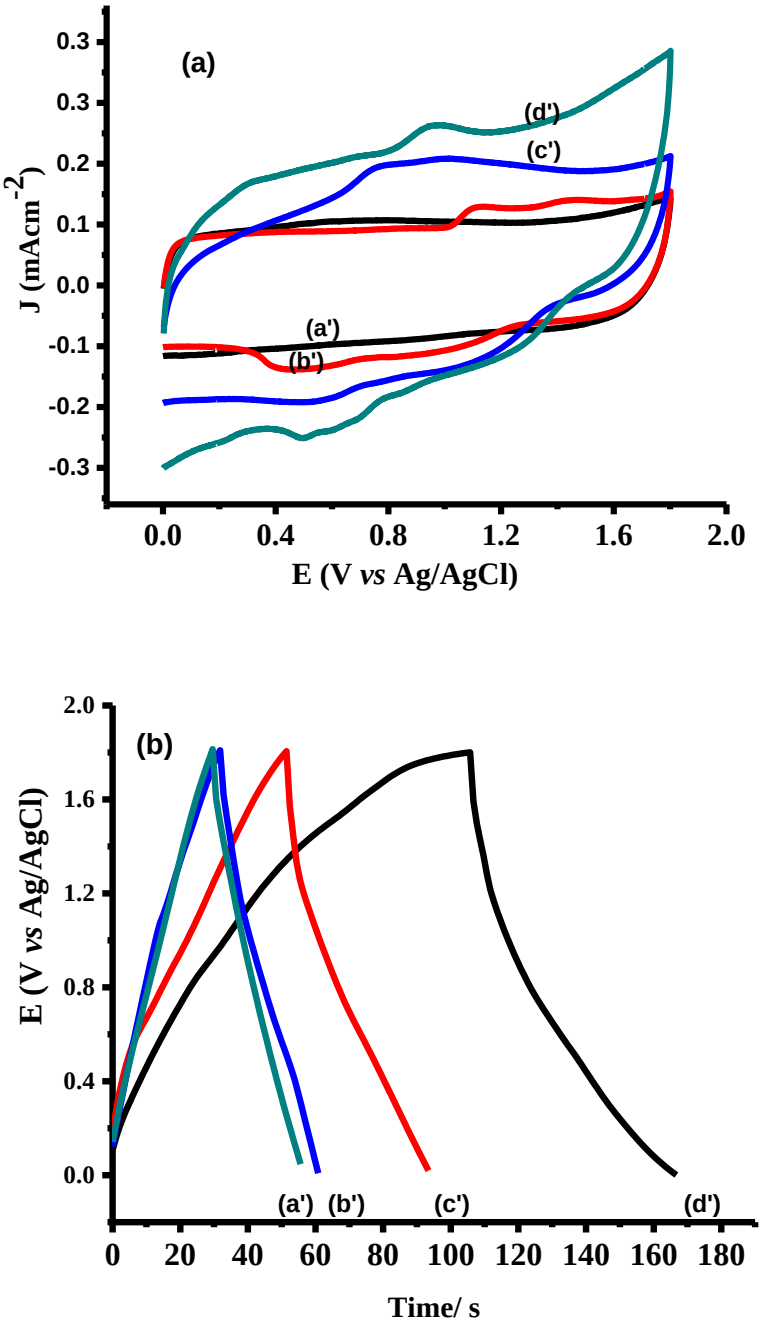

Figure 72. (a) CV curves and (b) GCD curves (0.1 mA cm^{-2} or 1 A g^{-1}) PEDOT:PSS/ITO/PET symmetric devices with (a') 0.1 M NaCl, (b') 1 mM Pb^{2+}/0.1 M NaCl, (c') 2 mM Pb^{2+}/0.1 M NaCl, and (d') 3 mM Pb^{2+}/0.1 M NaCl.

Ragone plot obtained from the devices operating at 1.8 V with 0.1 M NaCl, 1 mM Pb^{2+}/0.1 M NaCl, 2 mM Pb^{2+}/0.1 M NaCl, and 3 mM Pb^{2+}/0.1 M NaCl are shown in Figure 73. The energy densities of a supercapattery with Pb^{2+} are higher than that of a supercapacitor with 0.1 M NaCl. The energy density of the devices with 0.1 M NaCl was 6.2 Wh kg^{-1} and enhanced in 1 mM, 2 mM, and 3 mM Pb^{2+} to 6.8, 8.5, and 11 Wh kg^{-1} at nearly the same power density (0.7 kW kg^{-1}), respectively. Better or comparable energy and power density were recorded compared with other similar reported data as shown in Table 9.

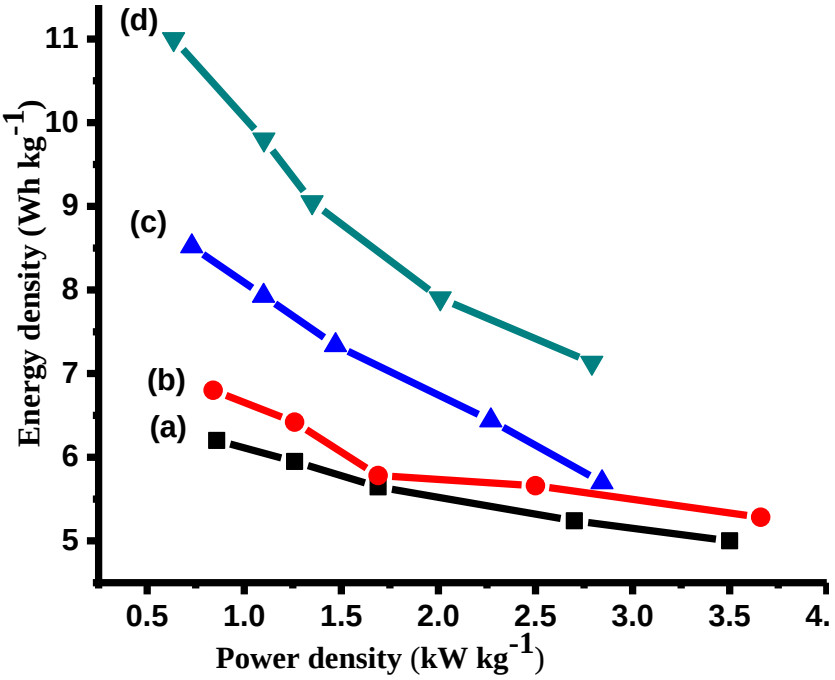

Figure 73. Ragone plots for PEDOT:PSS/ITO/PET symmetric devices with (a) 0.1 M NaCl, (b) 1 mM Pb^{2+}/0.1 M NaCl, (c) 2 mM Pb^{2+}/0.1 M NaCl, and (d) 3 mM Pb^{2+}/0.1 M NaCl.

Table 9. Comparison of values in our work with reported symmetric supercapacitor devices.

Materials	Electrolyte	Voltage	Energy density	Power density	References
PEDOT/GO/PET	1 M NaCl	0.9 V	1.65 μWh cm^{-2} at 0.06 mA cm^{-2}	2.5 mW cm^{-2}	74
PEDOT/rGO/PET	1 M NaCl	0.9 V	2.16 μWh cm^{-2} at 0.06 mA cm^{-2}	4.1 mW cm^{-2}	74
PBOTT-BTD/ITO/PET	0.2 M-$TBAPF_6$-PMMA-PC	0.6 V	0.3 Wh kg^{-1} at 0.2 mA cm^{-2}	0.2 kW kg^{-1}	39
PEDOT:PSS/PET	PVA/H_3PO_4	0.8 V	0.13 mwh cm^{-2} at 0.025 mA cm^{-2}	0.036 w cm^{-2}	40
PEDOT:PSS-SWNT/ITO/glass	1 M $NaNO_3$	1 V	7 Wh kg^{-1} at 1 A g^{-1}	0.825 kW kg^{-1}	256
PEDOT:PSS/CC	PVA/H_3PO_4	1 V	2.22 Wh kg^{-1} at 1 A g^{-1}	0.25 kW kg^{-1}	177
PEDOT:PSS/MoS_2/PEDOT	PVA/H_3PO_4	1 V	0.2 μ Wh cm^{-2} at 0.125 mA cm^{-2}	0.09 mW cm^{-2}	179
PEDOT:PSS/ITO/PET	0.1 M NaCl	1.8 V	6.2 Wh kg^{-1}/ 0.57 μ Wh cm^{-2} at 0.1 mA cm^{-2} (1 A g^{-1})	0.858 kW kg^{-1} (0.079 mW cm^{-2})	This work
PEDOT:PSS/ITO/PET	3 mM Pb^{2+}/0.1 M NaCl	1.8 V	11Wh kg^{-1} / 0.992 μ Wh cm^{-2} at 0.1 mA cm^{-2} (1 A g^{-1})	0.636 kW kg^{-1} (0.06 mW cm^{-2})	This work

PMMA- Polymethylmethacrylate, PC- propylene carbonate, GO-graphene oxide, CC- Carbon cloth

4.4 Roll-to-roll printed Phosphomolybdic acid/Lignin/PEDOT:PSS composite for supercapattery

4.4.1 Background

The rise of wearable and portable electronics including mobile phones, laptops, cameras, smartwatch, and many more stimulated to explore flexible, lightweight, and environmentally friendly energy storage devices[260, 261]. Supercapacitors (SCs) are energy storage devices that can be used to power such devices when fast charge/discharge rate, high power density, and long cycle life are required[177, 179, 262]. The existing commercial SCs are produced as a large and bulk shape which presents some major drawbacks for their use in practical wearable and portable applications. Recently, flexible supercapacitors (FSCs) have emerged as a new class of energy storage devices and have attracted considerable attention in such applications[38, 260, 263]. Similar to conventional supercapacitors, FSCs exhibit fast charge/discharge rate, high power density, and long cycle. Depending on the charge-storage mechanism, FSCs can be classified into electrical double-layer capacitors (EDLCs) and pseudocapacitors[38].

Carbonaceous materials, such as carbon nanotubes and graphene, which have high surface area can store and release energy based on the accumulation of charges at the interface between a porous electrode and the electrolyte are excellent electrode materials for EDLC whereas transition metal oxides/hydroxide and conducting polymers (CPs) which store charge on fast and reversible faradaic redox reactions at the surface and/or in the bulk are ideal electrode materials for pseudocapacitors[74, 172, 182, 264]. Among these materials, CPs have been considered as the most promising materials for FSCs due to their high redox active-specific capacitance, high

conductivity, ease of synthesis, and high intrinsic flexibility[37, 39, 51, 180]. CPs, such as polypyrrole and polyaniline, have shown very high specific capacitance 600 and 800 F g^{-1}, respectively but are unstable and quickly degrade due to large volume changes during the charging/discharging processes, leading to irreversible changes in 3-D structure[74, 79]. Although PEDOT does not possess the highest specific capacitance of CPs, it is widely studied for SCs application due to its high conductivity, high chemical and thermal stability, and electrochemical stability in a relatively wide potential window[74]. PEDOT, which is insoluble in most solvents, can be dispersed in water by using water-soluble insulating PSS and form PEDOT:PSS.

In this work, an attempt has made to permanently anchor redox-active organic molecule lignosulfonate (LS) and a multi-oxidation state heteropolyacid on PEDOT:PSS/ITO/PET during the roll-to-roll printing for use in flexible solid-state SCs. LS is a derivative of lignin, which is the second most abundant biopolymer which can store electrical energy in its phenolic groups by switching between the benzoquinone and hydroquinone states[79, 168] whereas the heteropolyacid contribute their faradaic charge-storage by switching among its multi oxidation states[168, 265]. The electrochemical profile of these redox materials deviated from regular rectangular cyclic voltammogram and linear shapes in charge/discharge curve that are observed in typical EDLC and pseudocapacitive electrode. This battery like material in combination with the capacitive behavior of PEDOT:PSS termed as supercapattery[266]. The redox reaction of the battery like material in supercapattery extended discharge time and improved energy density without altering the power density. Hence, in this section, a roll-to-roll printed ternary composite system consisting of PEDOT:PSS, LG, and phosphomolybdic acid were used in gel electrolytes for solid-state FSCs.

4.4.2 Structural and compositional studies

The survey spectra of PEDOT:PSS, Lg/PEDOT:PSS, Mo/PEDOT:PSS and Mo/Lg/PEDOT:PSS on ITO/PET films are shown in Figure 74. Signals from C1s, O1s, In3d, and S2p levels are common to the survey spectra of all films, but the Mo/PEDOT:PSS/ITO/PET and Mo/Lg/PEDOT:PSS/ITO/PET films show an additional signal from Mo3d.

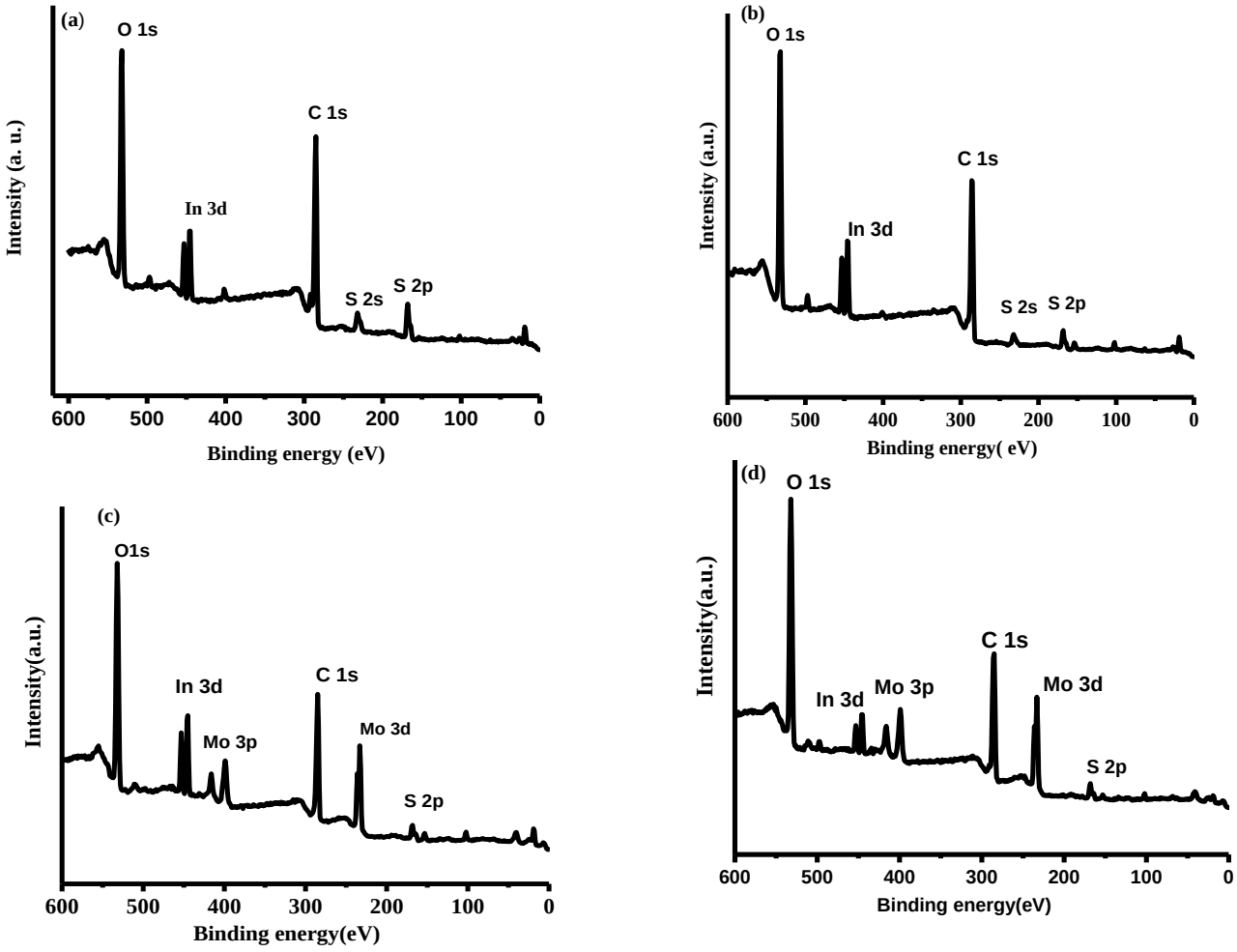

Figure 74. XPS survey spectra of (a) PEDOT:PSS/ITO/PET, (b) Lg/PEDOT:PSS/ITO/PET, (c) Mo/PEDOT:PSS/ITO/PET and (d) Mo/Lg/PEDOT:PSS/ITO/PET.

The deconvoluted C1s, core level spectrum (Figure 75a, b) consists of peaks at 284.8 eV, 286.5 eV, and 288.6 eV corresponds to C-C, C-O, and O-C=O bond, respectively[267, 268]. High-resolution XPS spectra for O1s (Figure 75c) show two components at 531 and 532.5 eV corresponding to C=O and C-O bonds of PEDOT and PSS moieties, respectively[268].

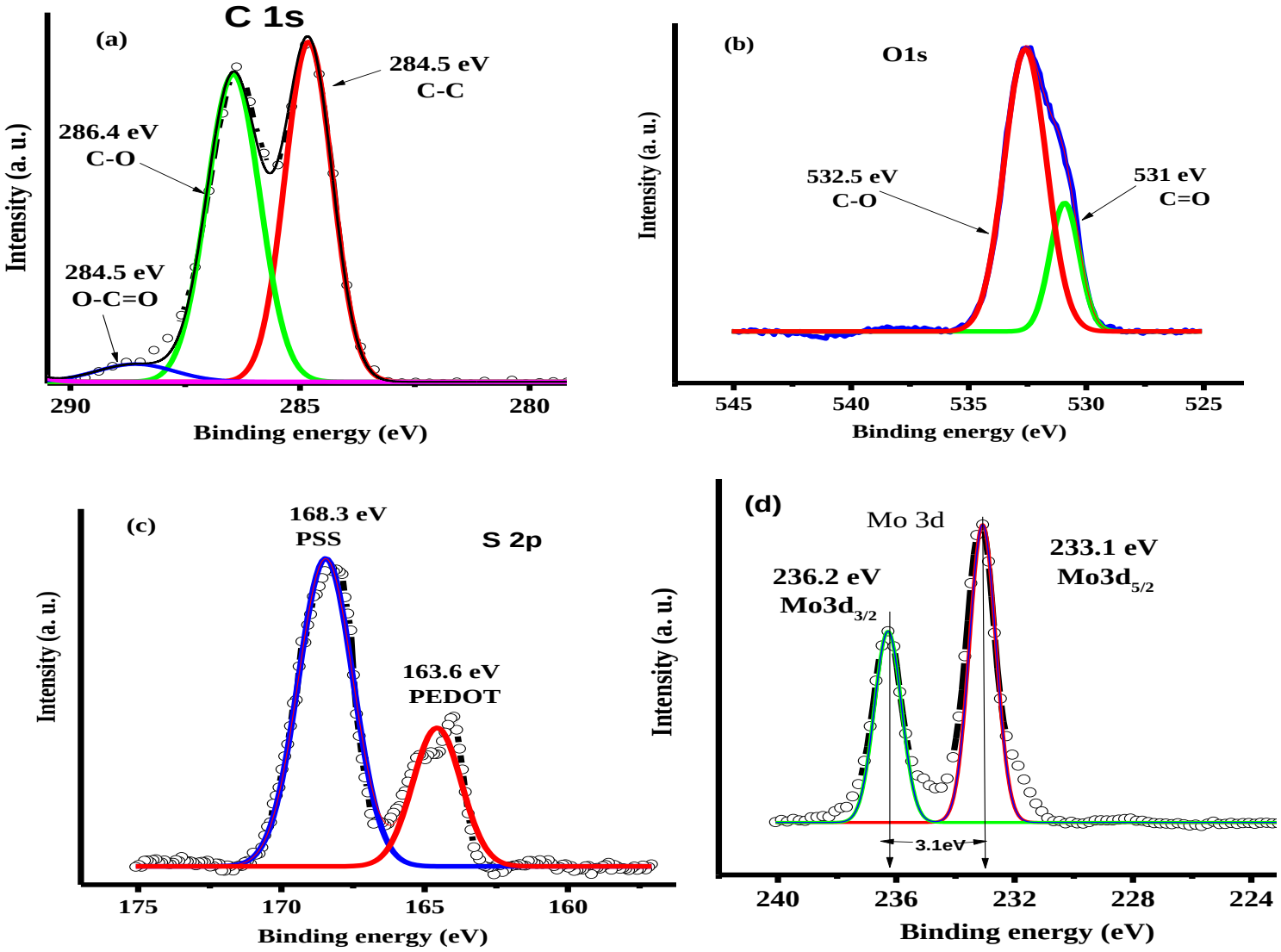

Figure 75. Deconvoluted core level spectra of (a) C1s, (b) O1s, (c) S2p and (d) Mo3d of a Mo/Lg/PEDOT:PSS/ITO/PET film.

Figure 75d shows high-resolution S2p spectra of PEDOT:PSS film with peaks at around 163.6 and 168.3 eV, assigned to the sulfur atoms in the thiophene ring of PEDOT and sulfur atoms in the sulfonic acid of PSS polymer[268]. Fitted spectra of Mo3d region in Figure 75d for Mo/Lg/PEDOT:PSS/ITO/PET with the binding energies at 233.1 and 236.2 eV corresponding to $Mo3d_{5/2}$ and $Mo3d_{3/2}$, respectively. The binding energy and calculated splitting width (3.1 eV) are in good agreement with Mo^{6+} oxidation state[269].

4.4.3 Cyclic voltammetric studies on PEDOT:PSS/ITO/PET films

The CV curves at various scan rates from 10 - 100 mV s^{-1} for PEDOT:PSS, Lg/PEDOT:PSS and Mo/PEDOT:PSS on ITO/PET are shown in Figure 76. The CV curves for PEDOT:PSS (Figure 76a) are rectangular and well maintained upon increasing the scan rate. This indicates that the material charges and discharges quickly and efficiently with high interfacial kinetics[74, 240]. A pair of strong reduction/oxidation curves is observed for Lg/PEDOT:PSS/ITO/PET (Figure 76b). These redox peaks are the redox activity of the quinone functional groups in lignin[239]. The cathodic and anodic peak current was found to vary linearly with the square root of the scan rate (Figure 77a) with R-value 0.999 and 0.997, respectively, and suggesting the diffusion-controlled characteristics of the redox reaction[242]. The CV curves (Figure 76c) of Mo/PEDOT:PSS/ITO/PET shows three distinct reversible redox peaks (i_a/i_c, ii_a/ii_c and iii_a/iii_c) at $E_{1/2}$ of about 0.3, 0.184 and 0.05 V. These redox peaks corresponded to a two-electron redox reversible reaction of the phosphomolybdate, which can be explained by the following reactions[270, 271]:

$$PMo_{12}O_{40}^{3-} + 2e^- + 2H^+ \leftrightarrow H_2\,PMo_2^{V}Mo_{10}^{VI}O_{40}^{3-} \quad \text{(a)}$$

$$H_2\,PMo_2^{V}Mo_{10}^{VI}O_{40}^{3-} + 2e^- + 2H^+ \leftrightarrow H_4\,PMo_4^{V}Mo_8^{VI}O_{40}^{3-} \quad \text{(b)}$$

$$H_4\,PMo_4^{V}Mo_8^{VI}O_{40}^{3-} + 2e^- + 2H^+ \leftrightarrow H_6\,PMo_6^{V}Mo_6^{VI}O_{40}^{3-} \quad \text{(c)}$$

The three distinct cathodic and anodic peak currents were found to vary linearly with the square root of the scan rate (Figure 77b) with R-value 0.999 for all cathodic and anodic peaks suggesting the diffusion-controlled characteristics of the redox reaction[242].

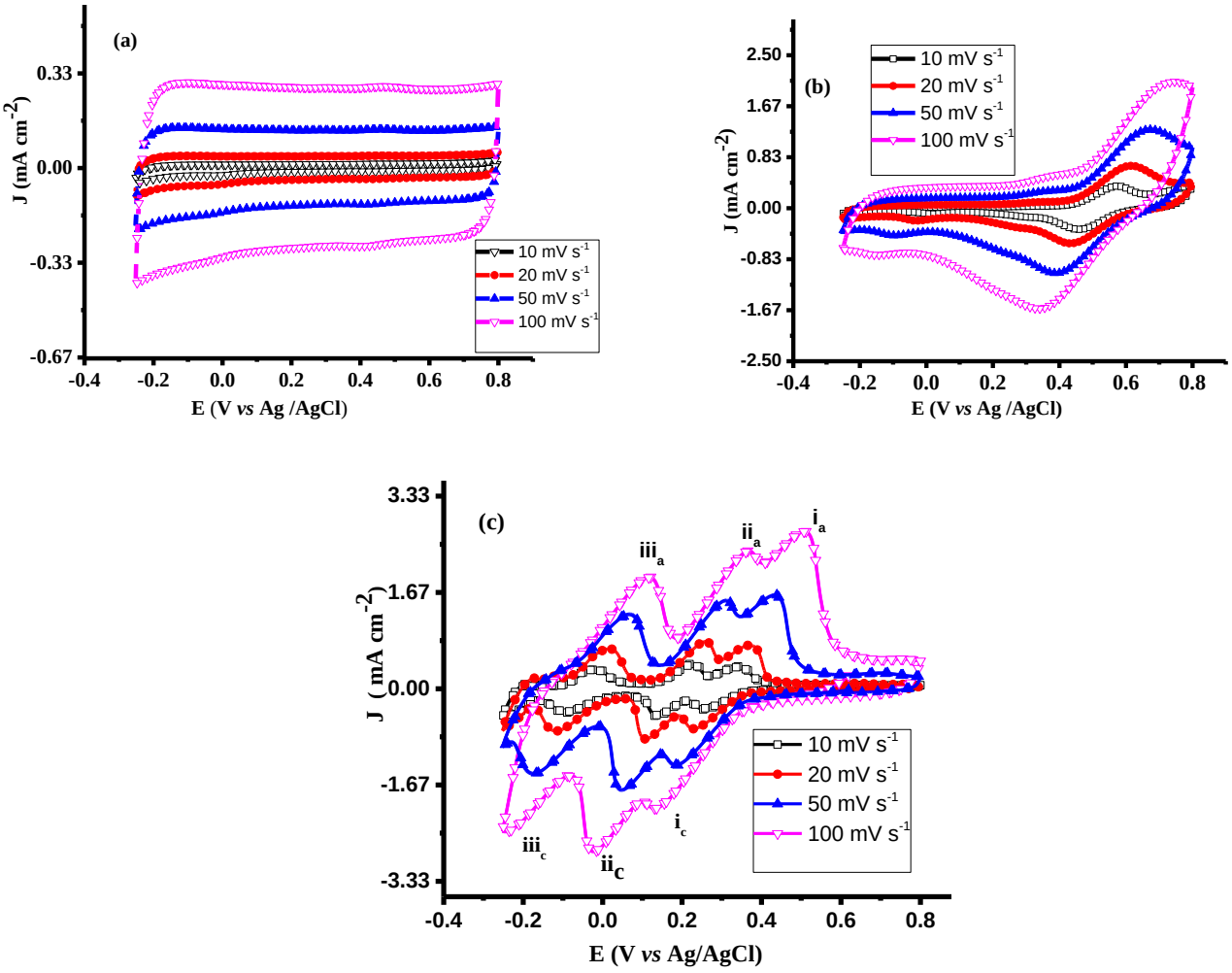

Figure 76. Cyclic voltammograms of (a) PEDOT:PSS/ITO/PET, (b) Lg/PEDOT:PSS/ITO/PET and (c) Mo/PEDOT:PSS/ITO/PET at different scan rate in 0.1 M $HClO_4$.

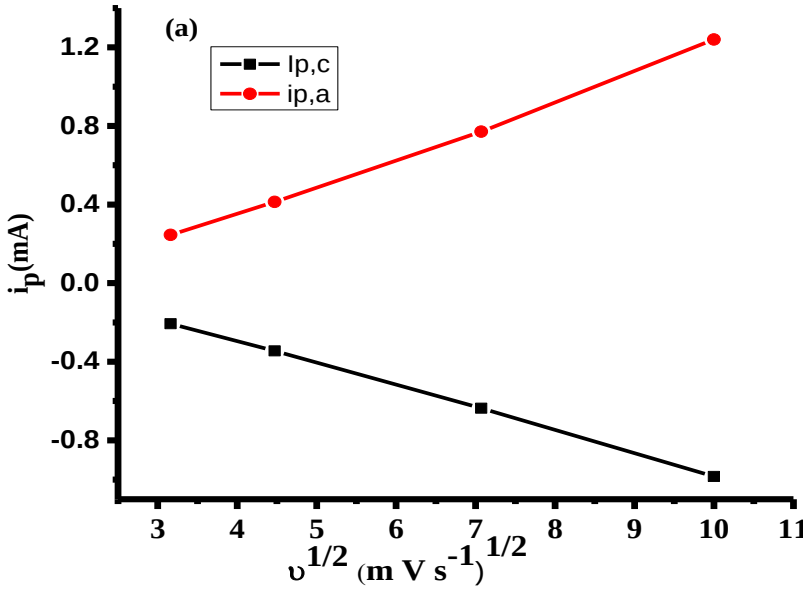

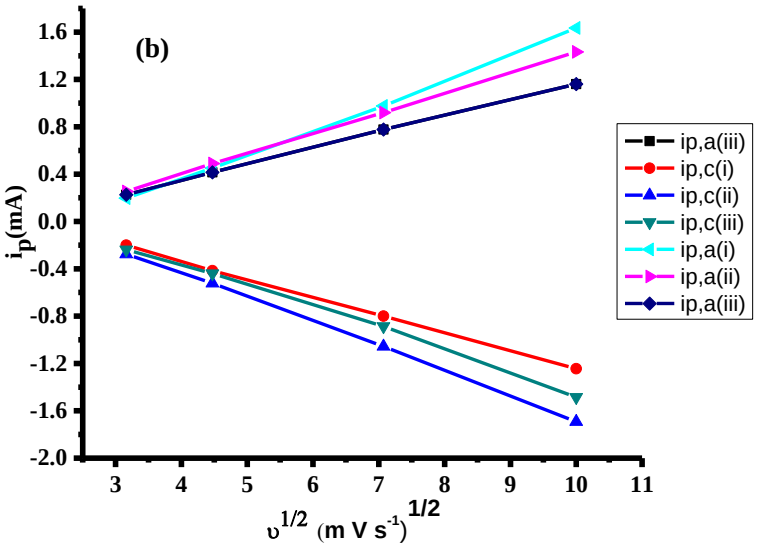

Figure 77. Plots of peak currents *versus* square root of scan rates (a) Lg/PEDOT:PSS/ITO/PET and (b) Mo/PEDOT:PSS/ITO/PET.

Typical cyclic voltammograms of the ternary composites (Mo/Lg/PEDOT:PSS) on ITO/PET obtained at different scan rates are depicted in Figure 78a. Four distinct reversible redox peaks were observed. The redox peaks from the quinone functional groups of lignin at more anodic potentials and three distinct peaks of phosphomolybdate anion were combined with the capacitance of PEDOT:PSS in a single electrode. This redox activity of the composite can be harnessed for charge storage in electrochemical supercapacitor[265]. Figure 78b shows the CV curves of PEDOT:PSS, Lg/PEDOT:PSS, Mo/PEDOT:PSS and Mo/Lg/PEDOT:PSS on ITO/PET in 0.1 M $HClO_4$ aqueous electrolyte at a scan rate of 20 mV s^{-1}. The current density of PEDOT:PSS is very low but a substantial increase in current density was observed for the ternary composite (Mo/Lg/PEDOT:PSS) electrode material. The result was an outcome of redox features from the biopolymer lignin and phosphomolybdate anion of the inorganic acid. This approach allows for a substantial boost of the energy density of a strategic material of the conducting polymer PEDOT:PSS. Peak current in the potential region of the inorganic acid and lignin biopolymer decrease in the ternary composites (Mo/Lg/PEDOT:PSS). This is due to the competition for the available positive sites in the polymer backbone[168].

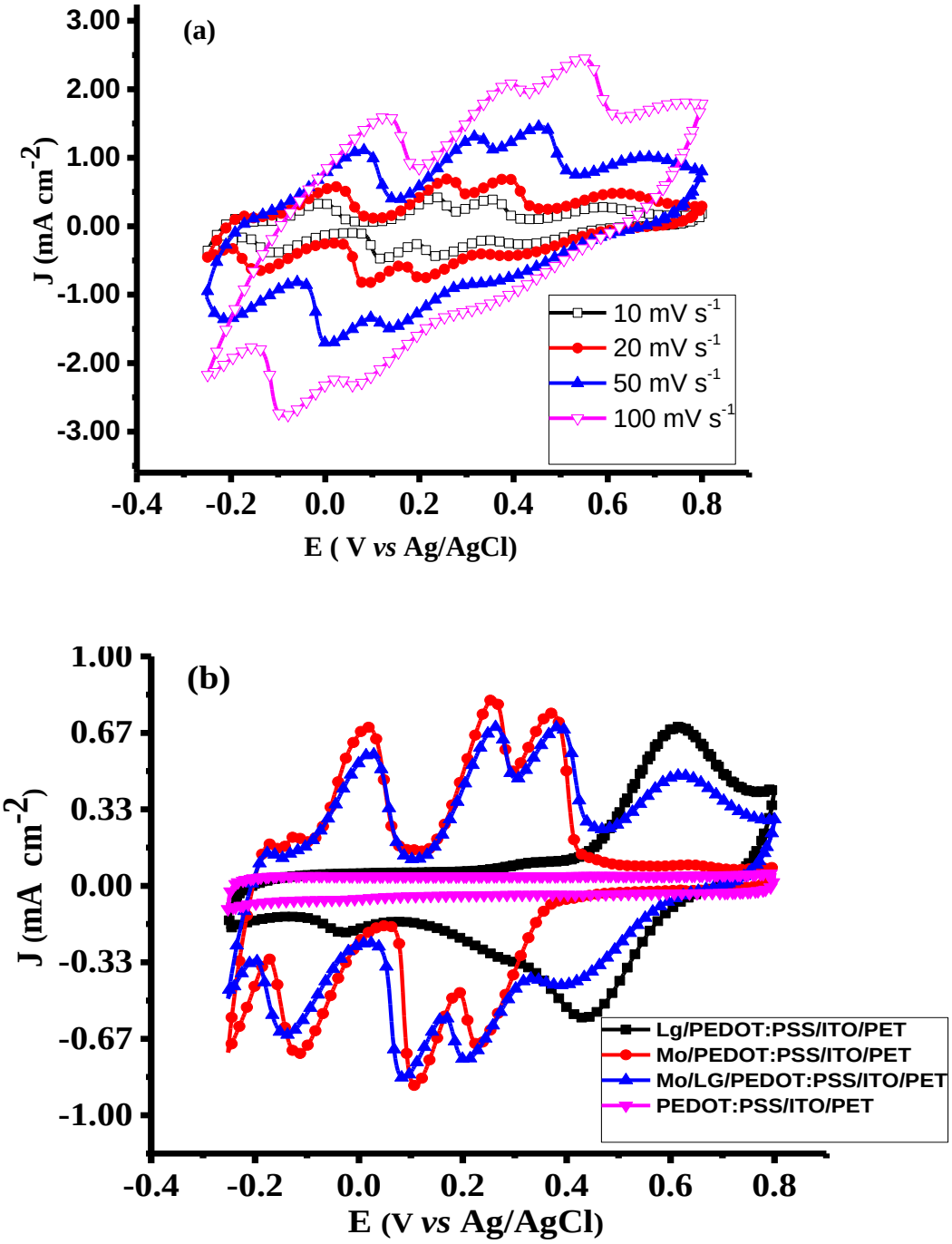

Figure 78. CV curves of (a) Mo/Lg/PEDOT:PSS/ITO/PET at different scan rate in 0.1 M $HClO_4$, (b) Lg, Mo, Lg/Mo composited with PEDOT:PSS on ITO/PET and pristine PEDOT:PSS/ITO/PET at 20 mV s^{-1} in 0.1 M $HClO_4$.

4.4.4 Galvanostatic charge-discharge studies on binary and ternary composites of PEDOT:PSS/ITO/PET films

Typical GCD curves for PEDOT:PSS, Lg/PEDOT:PSS, Mo/PEDOT:PSS and Mo/Lg/PEDOT:PSS at different current densities under a potential window of -0.2 V to 0.8 V (*vs* Ag/AgCl) are depicted in Figure 79. The GCD curves of PEDOT:PSS (Figure 79a) were close to a symmetrical triangle shape, illustrating that a good reversible charge/discharge process occurred in the electrochemical reaction of the electrode/electrolyte. However, the GCD curves Lg/PEDOT:PSS (Figure 79b), Mo/PEDOT:PSS (Figure 79c) and Mo/Lg/PEDOT:PSS (Figure 79d) shows non-ideal triangular shape with a voltage plateau region which is in agreement with the observations in the CV curves. Mo/Lg/PEDOT:PSS (Figure 79d) shows a voltage plateau of the contribution of a redox species arising from the quinones in the lignin biopolymer and phosphomolybdate anion of phosphomolybdic acid. The nonlinear GCD behaviors originated from the battery-type charge storage behavior as a result of the lignin and phosphomolybdate anion incorporated in PEDOT:PSS plastic film electrode. This mechanistic behavior in a single electrode is what is termed as supercapattery electrode [242].

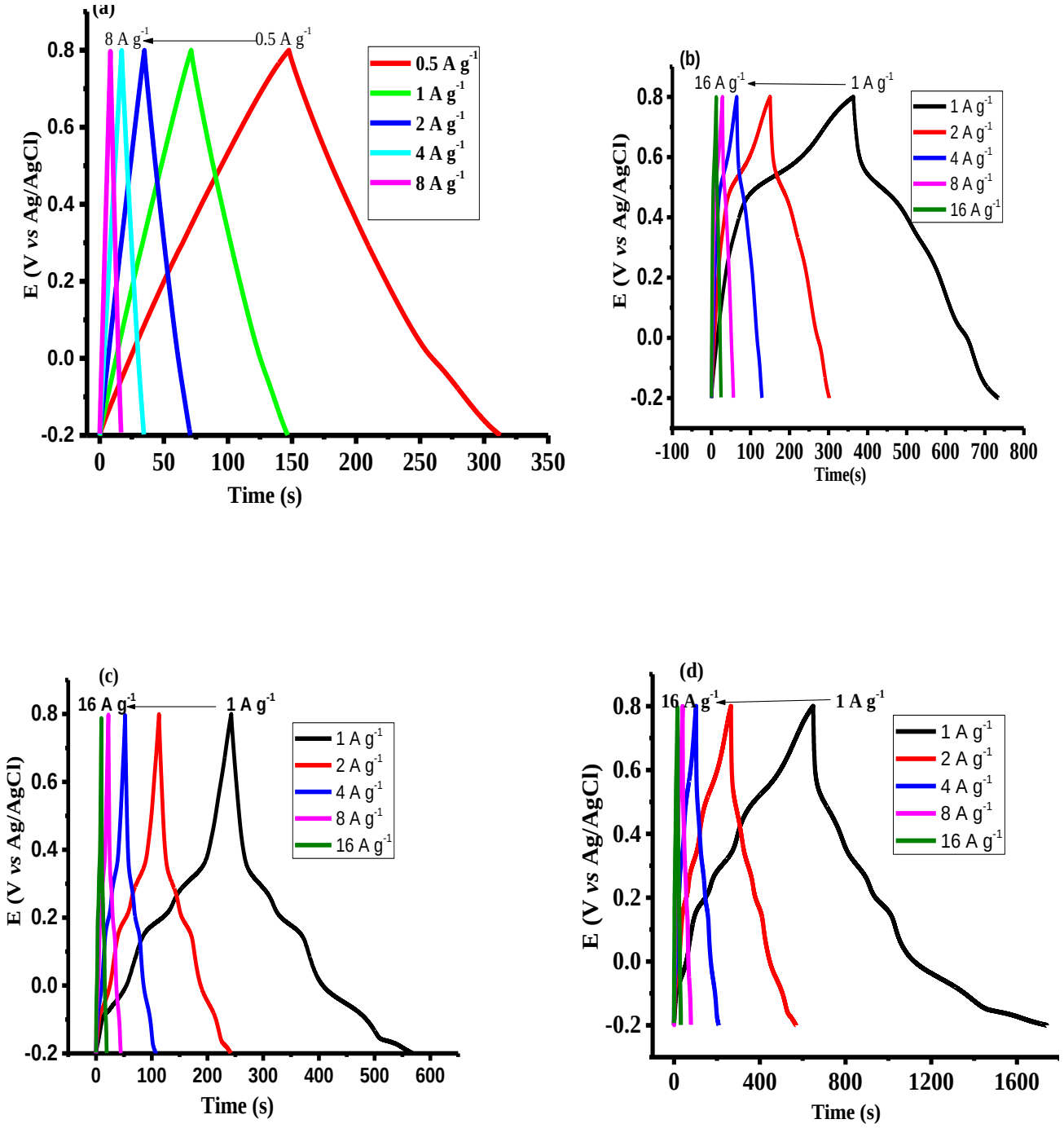

Figure 79. GCD curves (a) PEDOT:PSS/ITO/PET, (b) Lg/PEDOT:PSS/ITO/PET (c) Mo/PEDOT:PSS/ITO/PET and (d) Mo/Lg/PEDOT:PSS/ITO/PET at different current density in 0.1 M $HClO_4$.

The comparative galvanostatic charge/discharge (GCD) curves (Figure 80a) of PEDOT:PSS, Lg/PEDOT:PSS, Mo/PEDOT:PSS and Mo/Lg/PEDOT:PSS electrodes on ITO/PET at a constant charge/discharge specific current of 1 A g^{-1}. GCD of Mo/Lg/PEDOT:PSS/ITO/PET demonstrated a longer charge/discharge time indicating excellent electrochemical performance, which is well in agreement with the CV analysis. The specific capacity (Cs) of the supercapattery electrodes were calculated using Equation (25). For comparison purposes, Cs of PEDOT:PSS/ITO/PET is also calculated in mAh g^{-1}.

The specific capacity of PEDOT:PSS electrode was 20.88 mAh g^{-1} (75.2 C g^{-1}) but increased to 90.6 mAh g^{-1} (326.1 C g^{-1}), to 103.1 mAh g^{-1} (371 C g^{-1}), and 303.1 mAh g^{-1} (1091 C g^{-1}) at 1 A g^{-1} for Mo/PEDOT:PSS, Lg/PEDOT:PSS and Mo/Lg/PEDOT:PSS, respectively. Figure 80b shows the GCD curves of all electrodes at different current densities. The specific capacity of all electrodes steadily decreases with an increase in specific current. Generally, an increase in discharging current densities gradually decreases the capacity because the electrolyte ions have less probability to utilize the whole portion of the active material at a higher current density and the outer active surface of the electrode material can only be utilized as a result insufficient active materials are involved in the redox reaction[242, 255].

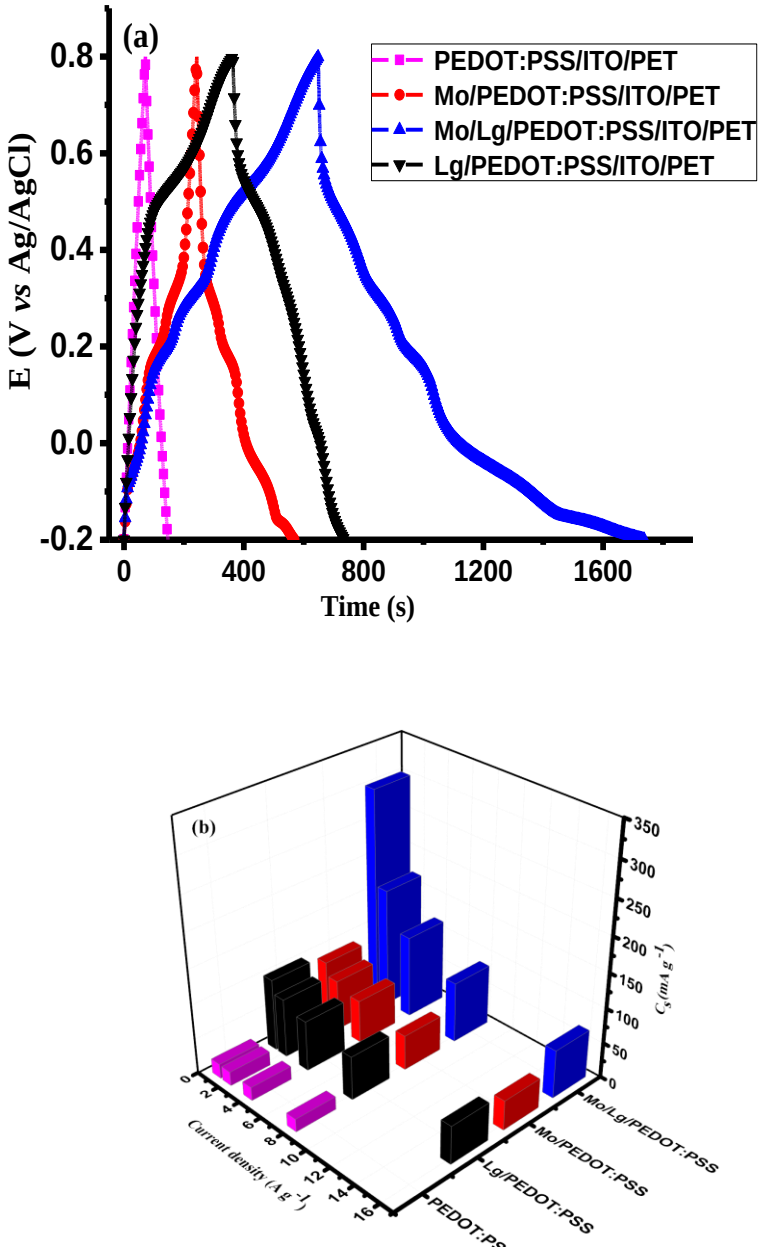

Figure 80. (a) A plot of potential *versus* time of Mo/PEDOT:PSS, Lg/PEDOT:PSS and Mo/Lg/PEDOT:PSS at 1.0 A g^{-1} (b) the specific capacity of electrodes at different current density.

4.4.5 Electrochemical studies of symmetric devices

To obtain a more realistic data for the application of the electrodes in real devices, a sandwich-type symmetric cell was fabricated using two pieces of PEDOT:PSS/ITO/PET, Lg/PEDOT:PSS/ITO/PET, Mo/PEDOT:PSS/ITO/PET and Mo/Lg/PEDOT:PSS/ITO/PET electrodes separated by PVA-H_2SO_4 gel electrolyte. Figure 81a, shows the CV curves of symmetric devices of PEDOT:PSS, Lg/PEDOT:PSS, Mo/PEDOT:PSS, and Mo/Lg/PEDOT:PSS on ITO/PET at a scan rate of 20 mV s^{-1}. Similar to the single cell, a rectangular CV curve with very low current density was observed for PEDOT:PSS devices but a slight increase in current density for the Lg/PEDOT:PSS electrode material were observed as a result of redox features of the biopolymer lignin. A pronounced battery like behavior with well-defined redox peaks was observed for Mo/PEDOT:PSS and Mo/Lg/PEDOT:PSS. Comparative GCD curves of a symmetric device of PEDOT:PSS/ITO/PET, Lg/PEDOT:PSS/ITO/PET, Mo/PEDOT:PSS/ITO/PET and Mo/Lg/PEDOT:PSS/ITO/PET at 0.5 A g^{-1} are shown in Figure 81b. All the GCD curves are well agreed with the CV curves and Mo/Lg/PEDOT:PSS/ITO/PET demonstrated a longer charge/discharge time indicating excellent electrochemical performance.

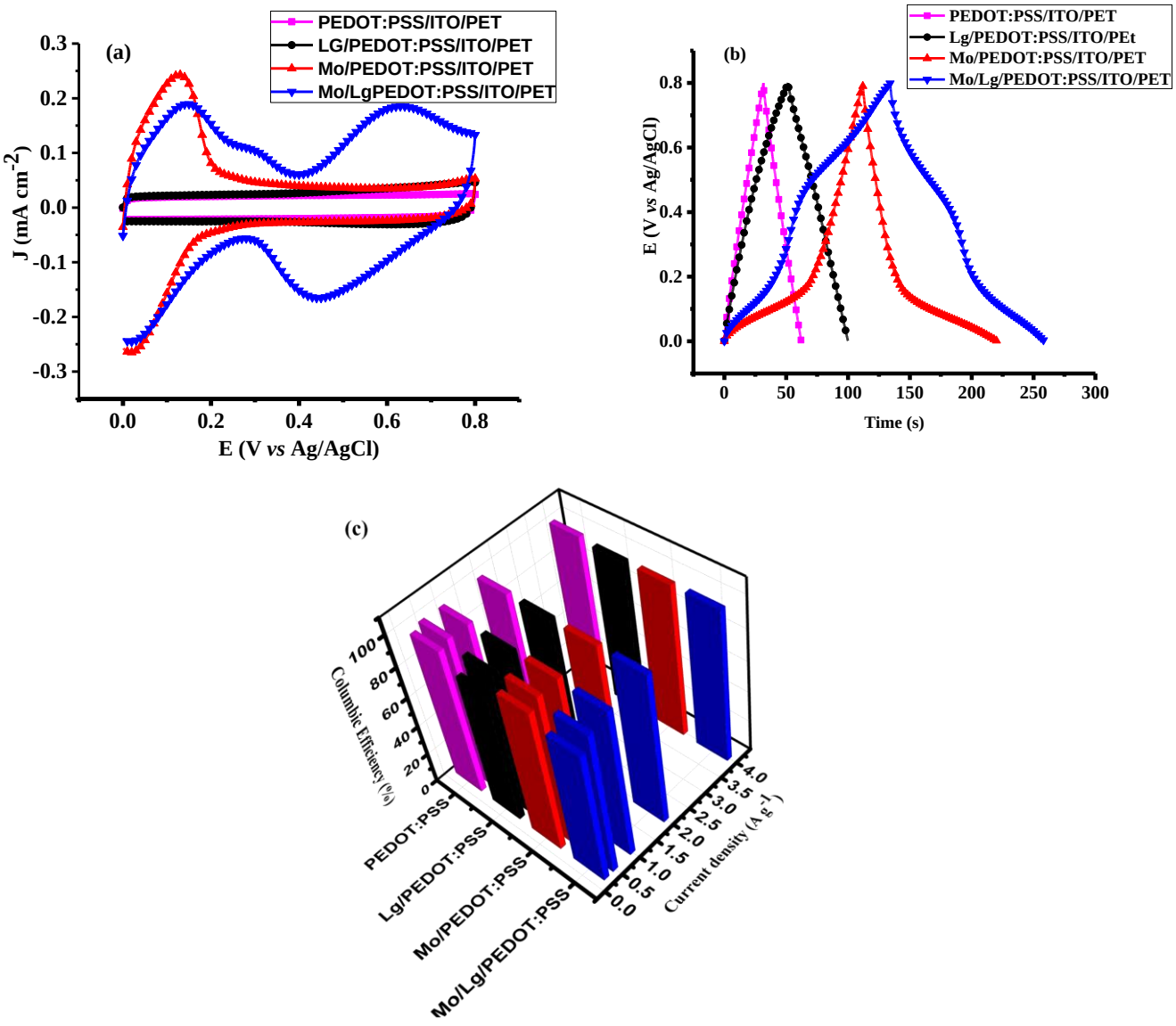

Figure 81. (a) CV curves at a scan rate of 20 mV s^{-1}, (b) GCD curves at a current density of 0.5 A g^{-1} and (c) columbic efficiency of PEDOT:PSS, Lg/PEDOT:PSS, Mo/PEDOT:PSS and Mo/Lg/PEDOT:PSS on ITO/PET.

The specific capacity of PEDOT:PSS devices was 4.32 mAh g^{-1} (15.6 C g^{-1}) but increased to 6.71 mAh g^{-1} (24.2 C g^{-1}), to 15.1 mAh g^{-1} (54.4 C g^{-1}), and 17.3 mAh g^{-1} (62.4 C g^{-1}) at 0.5 A g^{-1} for Mo/PEDOT:PSS, Lg/PEDOT:PSS and Mo/Lg/PEDOT:PSS, respectively. The columbic efficiency (η_C) calculated at various current density (0.25 – 4 A g^{-1}) using Equation (28) is shown in Figure 81c. The calculated columbic efficiency for devices made of Mo/Lg/PEDOT:PSS:ITO/PET are 85.5%, 92.9%, 96.3%, 97.8% and 98.3% at the current density of 0.25, 0.5, 1, 2 and 4 A g^{-1}, respectively. The same trend in efficiency was observed for PEDOT:PSS:ITO/PET, Lg/PEDOT:PSS:ITO/PET and Mo/PEDOT:PSS:ITO/PET at the measured current density as shown Figure 81c. The values of the columbic efficiency show an efficient electron transfer within a device which is one of the criteria for the characterization of energy storage devices[155].

The cyclic stability of PEDOT:PSS, Mo/PEDOT:PSS, Lg/PEDOT:PSS, Lg/Mo/PEDOT:PSS on ITO/PET electrodes are investigated. As shown in Figure 82, after 1000 cycles at 1 A g^{-1}, PEDOT:PSS, Mo/PEDOT:PSS, Lg/Mo/PEDOT:PSS 86.7% , 80.4% and 70%. The capacity of Lg/PEDOT:PSS electrode increases in the first 100 cycles due to the self-activation process[272] and does not display change for the next 700 cycles. It retains 102.3% of the first cycle after 1000 cycles. According to the GCD measurement of the first and last five cycles (inset Figure 82) for Lg/Mo/PEDOT:PSS, the charge-discharge curve can still maintain the original shape after testing.

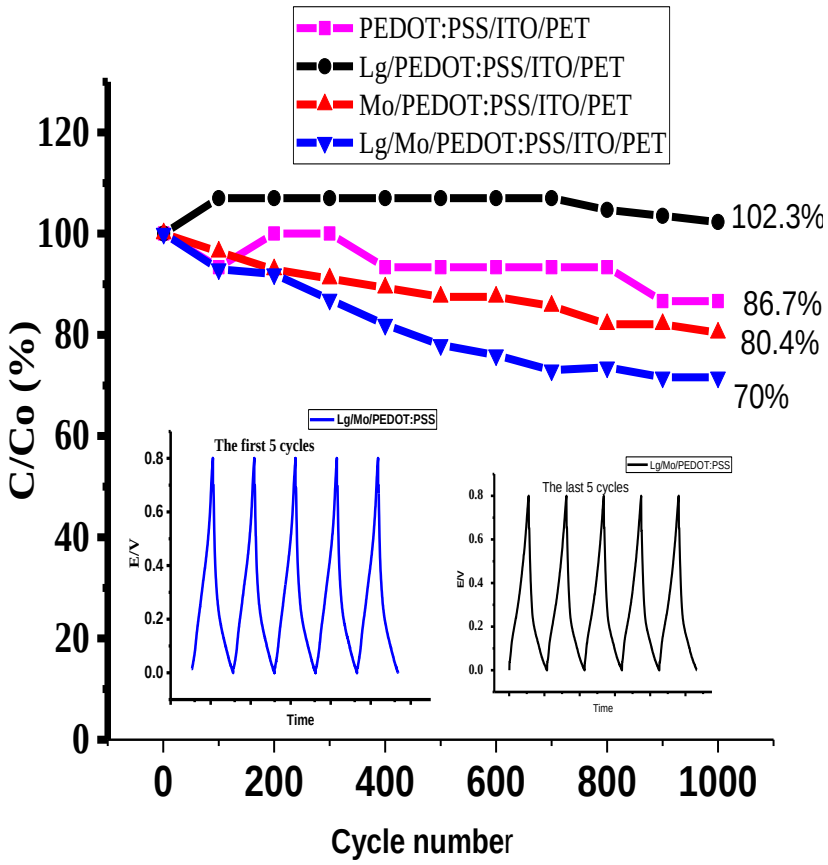

Figure 82. Cycle life of all devices and the inset is the GCD curves of the first five cycles and the last five cycles for Lg/Mo/PEDOT:PSS/ITO/PET.

The Ragone plot, an essential parameter of power density against energy density, obtained from the devices operating at 0.8 V are shown in Figure 83. The energy density of the devices with PEDOT:PSS/ITO:PET was 0.7 mWh cm^{-3} at a power density of 39 mW cm^{-3} and enhanced to 1.9 mWh cm^{-3} for Mo/Lg/PEDOT:PSS/ITO:PET at a power density of 22 mW cm^{-3}. Based on the Ragon plots, the performance of our device for energy storage is better than most of the reported PEDOT composites based supercapacitors (Figure 83)[179, 180, 273-278].

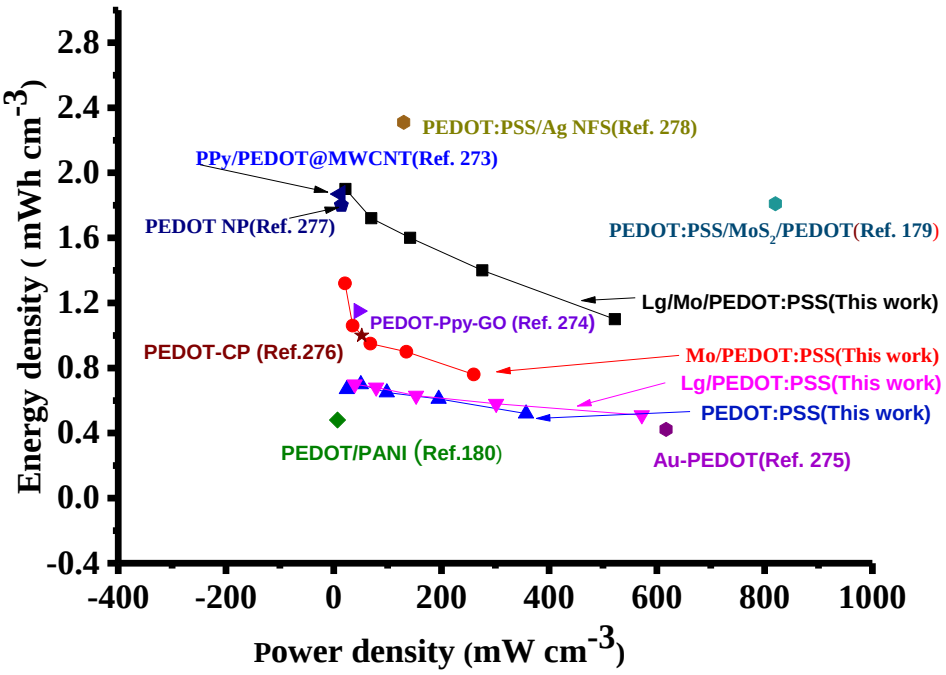

Figure 83. The Ragone plots of this work and values for previously reported supercapacitor devices.

5. Conclusions

Electroreduction of oxygen on platinum nanoparticles and metal-free catalyst was studied in acidic media and alkaline media employing the rotating disk and rotating ring-disk electrode techniques. The platinum nanoparticles was anchored on PEDOT:PSS, rGO, and their composite either galvanostatically or potentiostatically from the metal salt solution. The addition of ethylene glycol reduces the particle size and distributes platinum particle uniformly on PEDOT:PSS. Composite of rGO and PEDOT:PSS(EG) was investigated for different (w/w) ratio of PEDOT:PSS and rGO. rGO/PEDOT:PSS(EG)(1:2)/Pt (30%) electrodes exhibited higher electrocatalytic activity for the four-electron reduction of oxygen in acidic solution. rGO/PEDOT:PSS(EG)(1:2)/Pt (30%) exhibits better tolerance to methanol crossover effect and longer durability than that of the Pt/C catalyst. The composite of rGO and PEDOT:PSS(EG) is a promising support material for platinum in the oxygen reduction reaction in low-temperature polymer electrolyte fuel cells. The reduction of oxygen was also studied on metal-free catalysts made from amino-substituted naphthalene sulfonic acid and graphene composite in an alkaline solution. Quantum mechanical (QM) calculations have shown that the existence of electrocatalytic activity for oxygen reduction reaction on different amino-substituted naphthalene sulfonic acid. The calculations also predict a much better catalytic activity for poly(8-amino-2-naphthalene sulfonic acid) than 2-ANSA, 5-ANSA, and 4-ANSA. The preparation and characterization of 8-ANSA, 2-ANSA, 5-ANSA, and 4-ANSA with rGO as composite electrocatalytic material for oxygen reduction reaction were investigated electrochemically. Analysis of the electrochemical reduction of oxygen at GC/poly(8-ANSA)/rGO exhibits enhanced catalytic activity with high exchange current density and high kinetic current towards oxygen reduction reaction in alkaline solution compared to GC/rGO and GC/poly(8-ANSA).

The application of roll-to-roll printed PEDOT:PSS, PEDOT:PSS/Lignin, PEDOT:PSS/Molybdenum, and PEDOT:PSS/Lignin/Molybdenum on flexible ITO/PET were investigated for supercapattery in neutral aqueous and gel electrolyte. A symmetric device with a high operating voltage of 1.8 V has been built using PEDOT:PSS/ITO/PET electrode in neutral aqueous electrolyte. This device exhibits an energy density of 11 Wh kg^{-1} at a power density of 0.636 kW kg^{-1} in 3 mM Pb^{2+}/0.1 M NaCl. A ternary roll to roll printed film was also prepared from an aqueous suspensions of commercially available PEDOT:PSS blended with redox-active phosphomolybdic acid and lignosulfonate. The flexible symmetric SC from the ternary electrode with PVA-H_2SO_4 gel-electrolyte exhibits an energy density of 1.9 mWh cm^{-3} and a power density of 22 mW cm^{-3}. Considering the large-scale production and simplicity of electrode preparation of the PEDOT:PSS/ITO/PET electrode, this method has a potential application to be used in portable and wearable electronic devices.

6. References

1. J. R. Fanchi, *Energy in the 21st century*, World scientific publishing Co. Pte.Ltd. , 2005.

2. K. Jäger, O. Isabella, A.H.M. Smets, R. A.C.M.M. van Swaaij and M. Zeman, *Solar Energy: Fundamentals, Technology, and Systems*, Delft University of Technology, 2014.

3. E. Csefalvay and I. T. Horvath, *ACS Sustainable Chemistry & Engineering*, 2018, **6**, 8868-8874.

4. A. B. Stambouli, *Renewable and Sustainable Energy Reviews*, 2011, **15**, 4507-4520.

5. A. González, E. Goikolea, J. A. Barrena and R. Mysyk, *Renewable and Sustainable Energy Reviews*, 2016, **58**, 1189-1206.

6. Á. Cunha, J. Martins, N. Rodrigues and F. P. Brito, *International journal of energy research*, 2015, **39**, 889-918.

7. M. Winte and R. J. Brodd, *Chemical reviews*, 2004, **104**, 4245-4269.

8. L. Yu and G. Z. Chen, *Journal of Power Sources*, 2016, **326**, 604-612.

9. D. Higgins, P. Zamani, A. Yu and Z. Chen, *Energy & Environmental Science*, 2016, **9**, 357-390.

10. M. E. Scofield, H. Liu and S. S. Wong, *Chemical Society reviews*, 2015, **44**, 5836-5860.

11. N. Zhou, N. Wang, Z. Wu and L. Li, *Catalysts*, 2018, **8**, 1-16.

12. L. Feng, X. Sun, S. Yao, C. Liu, W. Xing and J. Zhang, in *Rotating Electrode Methods and Oxygen Reduction Electrocatalysts*, eds. W. Xing, G. Yin and J. Zhang, Elsevier B.V., 2014.

13. Y. Xua, L. Chena, X. Wanga, W. Yaob and Q. Zhanga, *Nanoscale*, 2015, **7**, 10559-10583.

14. X. Zhou, J. Qiao, L. Yang and J. Zhang, *Advanced Energy Materials*, 2014, **4**, 1-25.

15. S. Patra and N. Munichandraiah, *Langmuir*, 2009, **25**, 1732-1738.

16. E. Teran-Salgado, D. Bahena-Uribe, P. A. Márquez-Aguilar, J. L. Reyes-Rodriguez, R. Cruz-Silva and O. Solorza-Feria, *Electrochimica Acta*, 2019, **298**, 172-185.

17. E. Antolini and E. R. Gonzalez, *Applied Catalysis A: General*, 2009, **365**, 1-19.

18. Y. Nie, L. Li and Z. Wei, *Chemical Society reviews*, 2015, **44**, 2168-2201.

19. S. Domínguez-Domínguez, J. Arias-Pardilla, Á. Berenguer-Murcia, E. Morallón and D. Cazorla-Amorós, *Journal of Applied Electrochemistry*, 2007, **38**, 259-268.

20. M. Endo, Y. A. Kim, M. Ezaka, K. Osada, T. Yanagisawa, T. Hayashi, M. Terrones and M. S. Dresselhaus, *Nano Letters*, 2003, **3**, 723-726.

21. Y. Kim, D. Lee, Y. Kwon, T.-W. Kim, K. Kim and H. J. Kim, *Journal of Electroanalytical Chemistry*, 2019, **838**, 89-93.

22. E. Bertin, A. Münzer, S. Reichenberger, R. Streubel, T. Vinnay, H. Wiggers, C. Schulz, S. Barcikowski and G. Marzun, *Applied Surface Science*, 2019, **467-468**, 1181-1186.

23. Q. He and S. Mukerjee, *Electrochimica Acta*, 2010, **55**, 1709-1719.

24. W. J. Khudhayer, N. N. Kariuki, X. Wang, D. J. Myers, A. U. Shaikh and T. Karabacak, *Journal of the Electrochemical Society*, 2011, **158**, B1029-B1041.

25. E. Fabbri, S. Taylor, A. Rabis, P. Levecque, O. Conrad, R. Kötz and T. J. Schmidt, *ChemCatChem*, 2014, **6**, 1410-1418.

26. Z. Li, Z. Liu, B. Li, Z. Liu, D. Li, H. Wang and Q. Li, *Electrochimica Acta*, 2016, **221**, 31-40.

27. A. Marinoiu, M. Raceanu, E. Carcadea, M. Andrulevicius, A. Tamuleviciene, T. Tamulevicius, C. Capris and M. Varlam, *International Journal of Hydrogen Energy*, 2020, **45**, 26226-26237.

28. J. Zhu, G. He, Z. Tian, L. Liang and P. K. Shen, *Electrochimica Acta*, 2016, **194**, 276-282.

29. T. Lagarteira, S. Delgado, C. Fernandes, C. Azenha, C. Mateos-Pedrero and A. Mendes, *International Journal of Hydrogen Energy*, 2020, **45**, 20594-20604.

30. L. Pak Hoe, M. Boaventura, T. Lagarteira, L. Kee Shyuan and A. Mendes, *International Journal of Hydrogen Energy*, 2018, **43**, 16998-17011.

31. W. Yohannes, S. V. Belenov, V. E. Guterman, L. M. Skibina and N. V. Lyanguzov, *International Journal of Advanced and Nanomaterials*, 2015, **1.1**, 13-26.

32. M. K. L. Mendoza, B. J. V. Tongol, S. Shanmugam and H. Kim, *International Journal of Hydrogen Energy*, 2018, **43**, 19930-19938.

33. H. Tang, J. Chen, L. Nie, D. Liu, W. Deng, Y. Kuang and S. Yao, *Journal of Colloid and Interface Science*, 2004, **269**, 26-31.

34. F.Gloaguen, J.-M. Leger and C. Lamy, *Journal of Applied Electrochemistry*, 1997, **27**, 1052-1060.

35. W. Yohannes, S. V. Belenov, V. E. Guterman, L. M. Skibina, V. A. Volotchaev and N. V. Lyanguzov, *Journal of Applied Electrochemistry*, 2015, **45**, 623-633.

36. B. W. Zewde and S. Admassie, *Journal of Power Sources*, 2012, **216**, 502-507.

37. I. Shown, A. Ganguly, L.-C. Chen and K.-H. Chen, *Energy Science & Engineering*, 2015, **3**, 2-26.

38. Y. Han and L. Dai, *Macromolecular Chemistry and Physics*, 2019, **220**, 1-14

39. Y. Guo, W. Li, H. Yu, D. F. Perepichka and H. Meng, *Advanced Energy Materials*, 2016, **7**, 1-7.

40. T. Cheng, Y.-Z. Zhang, J.-D. Zhang, W.-Y. Lai and W. Huang, *Journal of Materials Chemistry A*, 2016, **4**, 10493-10499.

41. Y. H. Kim, C. Sachse, M. L. Machala, C. May, L. Müller-Meskamp and K. Leo, *Advanced Functional Materials*, 2011, **21**, 1076-1081.

42. G. Inzelt, *Conducting Polymers*, Springer-Verlag, Leipzig, Germany, 2008.

43. M. S. Freund and B. A. Deore, *Self-doped Conducting Polymers*, John Wiley & Sons, 2007.

44. H. Shirakawa, E. J. Louis, A. G. Macdiarmid and A. J. Heeger, *Journal of the Chemical Society, Chemical Communications*, 1977, 578-580.

45. T. H. Le, Y. Kim and H. Yoon, *Polymers*, 2017, **9**, 1-32.

46. M. H. Naveen, N. G. Gurudatt and Y.-B. Shim, *Applied Materials Today*, 2017, **9**, 419-433.

47. R. Balint, N. J. Cassidy and S. H. Cartmell, *Acta biomaterialia*, 2014, **10**, 2341-2353.

48. A. J. Heeger, *Reviews of Modern Physics*, 2001, **73**, 681-700.

49. H. Pang, L. Xu, Ding-Xiang and Y. Z.-M. Li, *Progress in Polymer Science*, 2014, **39**, 1908-1933.

50. K. Jüttner, K.-M. Mangold, M. Lange and K. Bouzek, *Russian Journal of Electrochemistry*, 2004, **40**, 359-368.

51. Y. Xuan, M. Sandberg, M. Berggren and X. Crispin, *Organic Electronics*, 2012, **13**, 632-637.

52. A. K. Geim and K. S. Novoselov, *Nature Materials*, 2007, **6**, 183-191.

53. P. R. Wallace, *Physical Review*, 1947, **71**, 622-634.

54. D. R. Dreyer, R. S. Ruoff and C. W. Bielawski, *Angewandte international edition Chemie*, 2010, **49**, 9336-9344.

55. T. Kuilla, S. Bhadra, D. Yao, N. H. Kim, S. Bose and J. H. Lee, *Progress in Polymer Science*, 2010, **35**, 1350-1375.

56. S. Y. Toh, K. S. Loh, S. K. Kamarudin and W. R. W. Daud, *Chemical Engineering Journal*, 2014, **251**, 422-434.

57. K. S. Novoselov, A. K. Geim, S. V. Morozov, D. Jiang, Y. Zhang, S. V. Dubonos, I. V. Grigorieva and A. A. Firsov, *Science*, 2004, **306**, 666-669.

58. K. S. Novoselov, D. Jiang, F. Schedin, T. J. Booth, V. V. Khotkevich, S. V. Morozov and A. K. Geim, *Proceedings of the National Academy of Sciences of the United States of America*, 2005, **102**, 10451-10453.

59. X. Li, W. Cai, J. An, S. Kim, J. Nah, D. Yang, R. Piner, A. Velamakanni, I. Jung, E. Tutuc, S. K. Banerjee, L. Colombo and R. S. Ruoff, *Science*, 2009, **324**, 1312-1314.

60. D. Wei, Y. Liu, Y. Wang, H. Zhang, L. Huang and G. Yu, *Nano Letters*, 2009, **9**, 1752-1758.

61. W. Zhang, J. Cui, C. A. Tao, Y. Wu, Z. Li, L. Ma, Y. Wen and G. Li, *Angewandte international edition Chemie*, 2009, **48**, 5864-5868.

62. X. Li, X. Wang, L. Zhang, S. Lee and H. Dai, *Science*, 2008, **319**, 1229-1232.

63. Z. Zhang, J. Sun, C. Lai, Q. Wang and C. Hu, *Carbon*, 2017, **120**, 411-418.

64. K. Parvez, Z.-S. Wu, R. Li, X. Liu, R. Graf, X. Feng and K. Müllen, *Journal of the American Chemical Society*, 2014, **136**, 6083-6091.

65. J. Lee, S. Noh, N. D. Pham and J. H. Shim, *Electrochimica Acta*, 2019, **313**, 1-9.

66. N. Komba, Q. Wei, G. Zhang, F. Rosei and S. Sun, *Applied Catalysis B: Environmental*, 2019, **243**, 373-380.

67. F. Liu, F. Niu, T. Chen, J. Han, Z. Liu, W. Yang, Y. Xu and J. Liu, *Carbon*, 2018, **134**, 316-325.

68. S. K. Bikkarolla, P. Cumpson, P. Joseph and P. Papakonstantinou, *Faraday discussions*, 2014, **173**, 415-428.

69. Y. Zhan, J. Huang, Z. Lin, X. Yu, D. Zeng, X. Zhang, F. Xie, W. Zhang, J. Chen and H. Meng, *Carbon*, 2015, **95**, 930-939.

70. J. Zhu, M. Xiao, X. Zhao, C. Liu, J. Ge and W. Xing, *Nano Energy*, 2015, **13**, 318-326.

71. T. Varga, Á. T. Varga, G. Ballai, H. Haspel, Á. Kukovecz and Z. Kónya, *Carbon*, 2018, **133**, 90-100.

72. I. Haxhiaj, S. Tigges, D. Firla, X. Zhang, U. Hagemann, T. Kondo, J. Nakamura, G. Marzun and S. Barcikowski, *Applied Surface Science*, 2019, **469**, 811-820.

73. A. T. N'Diaye, J. Coraux, T. N. Plasa, C. Busse and T. Michely, *New Journal of Physics*, 2008, **10**, 043033.

74. S. Lehtimaki, M. Suominen, P. Damlin, S. Tuukkanen, C. Kvarnstrom and D. Lupo, *ACS Applied materials & Interfaces*, 2015, **7**, 22137-22147.

75. Y. Gao, *Nanoscale research letters*, 2017, **12**, 1-17.

76. X. Mao, W. Yang, X. He, Y. Chen, Y. Zhao, Y. Zhou, Y. Yang and J. Xu, *Materials Science and Engineering: B*, 2016, **216**, 16-22.

77. S. Pei and H.-M. Cheng, *Carbon*, 2012, **50**, 3210-3228.

78. I. E. Raschip, G. E. Hitruc, C. Vasile and M.-C. Popescu, *International Journal of Biological Macromolecules*, 2013, **54**, 230-237.

79. J. Edberg, O. Inganas, I. Engquist and M. Berggren, *Journal of Materials Chemistry A*, 2018, **6**, 145-152.

80. C. Xiong, W. Zhong, Y. Zou, J. Luo and W. Yang, *Electrochimica Acta*, 2016, **211**, 941-949.

81. C. Hu and L. Dai, *Angewandte international edition Chemie*, 2016, **55**, 2–25.

82. M. S. Ahmed and Y.-B. Kim, *Carbon*, 2017, **111**, 577-586.

83. Z. Wu, M. Song, JieWang and X. Liu, *catalysts*, 2018, **8**, 196.

84. S. M. Haile, *Acta Materialia*, 2003, **51**, 5981-6000.

85. A. Singh, P. Baredar, H. Khare and A. Kumar, in *Low Carbon Energy Supply: Trends, Technology, Management*, eds. A. Sharma, A. Shukla and L. Aye, Springer, Singapore, 2018.

86. N. Chawla, *Materials Today Chemistry*, 2019, **12**, 324-331.

87. Y. Xue, H. Miao, S. Sun, Q. Wang, S. Li and Z. Liu, *Journal of Power Sources*, 2015, **297**, 202-207.

88. M. M. Dinesh, K. Saminathan, M. Selvam, S. R. Srither, V. Rajendran and K. V. I. S. Kaler, *Journal of Power Sources*, 2015, **276**, 32-38.

89. X. Feng, ed., *Nanocarbons for Advanced Energy Conversion*, Wiley-VCH, Weinheim, Germany, 2015.

90. N. A. Kumar and J.-B. Baek, in *Carbon-Based Metal-Free Catalysts: Design and Applications*, ed. L. Dai, Wiley-VCH, 2018.

91. E. Santos and W. Schmickler, eds., *Catalysis in electrochemistry*, JohnWiley & Sons, Inc., 2011.

92. S. Taylor, E. Fabbri, P. Levecque, T. J. Schmidt and O. Conrad, *Electrocatalysis*, 2016, **7**, 287-296.

93. X. Tian, X. F. Lu, B. Y. Xia and X. W. Lou, *Joule*, 2020, **4**, 45-68.

94. A. Kulkarni, S. Siahrostami, A. Patel and J. K. Norskov, *Chemical reviews*, 2018, **118**, 2302-2312.

95. I. E. L. Stephens, A. S. Bondarenko, U. Grønbjerg, J. Rossmeislc and I. Chorkendorff, *Energy & Environmental Science*, 2012, **5**, 6744-6762.

96. A. J. Medford, A. Vojvodic, J. S. Hummelshøj, J. Voss, F. Abild-Pedersen, F. Studt, T. Bligaard, A. Nilsson and J. K. Nørskov, *Journal of Catalysis*, 2015, **328**, 36-42.

97. J. Kari, J. P. Olsen, K. Jensen, S. F. Badino, K. B. R. M. Krogh, K. Borch and P. Westh, *ACS Catalysis*, 2018, **8**, 11966-11972.

98. H. A. G. Wolf Vielstich, Arnold Lamm and Harumi Yokokawa., *Handbook of Fuel Cells – Fundamentals, Technology and Applications*, John Wiley & Sons, Ltd., 2010.

99. M. Shao, *Electrocatalysis in Fuel Cells*, Springer-Verlag 2013.

100. L. Khotseng, in *Electrocatalysts for Fuel Cells and Hydrogen Evolution*, ed. A. Ray, IntechOpen, 2018, DOI: 10.5772/intechopen.79098, ch. 2, pp. 25-50.

101. A. B. Anderson, J. Roques, S. Mukerjee, V. S. Murthi, N. M. Markovic and V. Stamenkovic, *Journal of physical chemistry B*, 2005, **109**, 1198-1203.

102. Y. Sha, T. H. Yu, B. V. Merinov, P. Shirvanian and W. A. Goddard, *The Journal of Physical Chemistry Letters*, 2011, **2**, 572-576.

103. Y. Sha, T. H. Yu, B. V. Merinov, P. Shirvanian and W. A. Goddard, *The Journal of Physical Chemistry C*, 2012, **116**, 21334-21342.

104. J. K. Nørskov, J. Rossmeisl, A. Logadottir, L. Lindqvist, J. R. Kitchin, T. Bligaard and H. Jonsson, *Journal Physical Chemistry B*, 2004, **108**, 17886-17892.

105. M. Li, X. Bi, R. Wang, Y. Li, G. Jiang, L. Li, C. Zhong, Z. Chen and J. Lu, *Matter*, 2020, **2**, 32-49.

106. K. Kakaei, M. D. Esrafili and A. Ehsani, *Interface Science and Technology*, 2019, **27**, 203-252.

107. Y. Jiao, Y. Zheng, M. Jaroniec and S. Z. Qiao, *Journal of the American Chemical Society*, 2014, **136**, 4394-4403.

108. L. Zhang and Z. Xia, *The Journal of Physical Chemistry C*, 2011, **115**, 11170-11176.

109. Y. Zheng, Y. Jiao, L. Ge, M. Jaroniec and S. Z. Qiao, *Angewandte international edition Chemie*, 2013, **52**, 3110-3116.

110. V. G. Khomenko, V. Z. Barsukov and A. S. Katashinskii, *Electrochimica Acta*, 2005, **50**, 1675-1683.

111. J. Wang, *Analytical Electrochemistry*, Wiley-VCH, 2nd edn., 2000.

112. A. J. Bard and L. R. Faulkner, *Electrochemical methods. Fundamentals and Applications*, John Wiley & Sons Inc., 2nd edn., 2001.

113. Y. Saito and T. kikuchi, *Voltammetry Theory, Types And Applications*, Nova Science Publishers, Inc., 2014.

114. J. M. D. Rodríguez, J. A. H. Melián and J. P. Peña, *Journal of Chemical Education*, 2000, **77**, 1195-1197.

115. S. A. Kumar and S.-M. Chen, *Journal of Molecular Catalysis A: Chemical*, 2007, **278**, 244-250.

116. T.-H. Hu, Z.-S. Yin, J.-W. Guo and C. Wang, *Journal of Power Sources*, 2014, **272**, 661-671.

117. A. Muthukrishnan, Y. Nabae, T. Hayakawa, T. Okajima and T. Ohsaka, *Catalysis Science & Technology*, 2015, **5**, 475-483.

118. R. Zhou, Y. Zheng, M. Jaroniec and S.-Z. Qiao, *ACS Catalysis*, 2016, **6**, 4720-4728.

119. H. Wu, T. Peng, Z. Kou, J. Zhang, K. Cheng, D. He, M. Pan and S. Mu, *Chinese Journal of Catalysis*, 2015, **36**, 490-495.

120. H. Zhang, J. Zhang, K. Liu, Y. Zhu, X. Qiu, D. Sun and Y. Tang, *Green Energy & Environment*, 2019, **4**, 245-253.

121. G. Gnana kumar, C. J. Kirubaharan, S. Udhayakumar, C. Karthikeyan and K. S. Nahm, *Industrial & Engineering Chemistry Research*, 2014, **53**, 16883-16893.

122. C. Xu, X. Wang and J. Zhu, *Journal of physical chemistry C*, 2008, **112**, 19841-19845.

123. H.-W. Ha, I. Y. Kim, S.-J. Hwang and R. S. Ruoff, *Electrochemical and Solid-State Letters*, 2011, **14**, B70-B73.

124. Y. Li, Y. Li, E. Zhu, T. McLouth, C. Y. Chiu, X. Huang and Y. Huang, *Journal of the American Chemical Society*, 2012, **134**, 12326-12329.

125. S. Hussain, N. Kongi, L. Matisen, J. Kozlova, V. Sammelselg and K. Tammeveski, *Electrochemistry Communications*, 2017, **81**, 79-83.

126. M. A. Hoque, F. M. Hassan, M.-H. Seo, J.-Y. Choi, M. Pritzker, S. Knights, S. Ye and Z. Chen, *Nano Energy*, 2016, **19**, 27-38.

127. K. Parvez, S. Yang, Y. Hernandez, A. Winter, A. Turchanin, X. Feng and K. Mullen, *ACS Nano*, 2012, **6**, 9541-9550.

128. J. Bai, Q. Zhu, Z. Lv, H. Dong, J. Yu and L. Dong, *International Journal of Hydrogen Energy*, 2013, **38**, 1413-1418.

129. M. J. Croissant, T. Napporn, J.-M. Leger and C. Lamy, *Electrochimica Acta*, 1998, **43**, 2447-2457.

130. U. A. Paulus, T. J. Schmidt, H. A. Gasteiger and R. J. Behm, *Journal of Electroanalytical Chemistry*, 2001, **495**, 134-145.

131. C. Coutanceau, M. J. Croissant, T. Napporn and C. Lamy, *Electrochimica Acta*, 2000, **46**, 579-588.

132. J. Shan and P. G. Pickup, *Electrochimica Acta*, 2000, **46**, 119-125.

133. E. K. W. Lai, P. D. Beattie and S. Holdcroft, *Synthetic Metals*, 1997, **84**, 87-88.

134. V. Tsakova, *Journal of Solid State Electrochemistry*, 2008, **12**, 1421-1434.

135. K. M. Kost, D. E. Bartak, B. Kazee and T. Kuwana, *Analytical chemistry*, 1988, **60**, 2379-2384.

136. P. Gajendran, S. Vijayanand and R. Saraswathi, *Journal of Electroanalytical Chemistry*, 2007, **601**, 132-138.

137. H. Begum, M. S. Ahmed, S. Cho and S. Jeon, *Journal of Power Sources*, 2017, **372**, 116-124.

138. M. Zhang, W. Yuan, B. Yao, C. Li and G. Shi, *ACS applied materials & interfaces*, 2014, **6**, 3587-3593.

139. Q. Lv, W. Si, J. He, L. Sun, C. Zhang, N. Wang, Z. Yang, X. Li, X. Wang, W. Deng, Y. Long, C. Huang and Y. Li, *Nature communication*, 2018, **9**, 3376-3387.

140. M. A. Molina-García and N. V. Rees, *Applied Catalysis A: General*, 2018, **553**, 107-116.

141. B. Winther-Jensen, O. Winther-Jensen, M. Forsyth and D. R. Macfarlane, *Science*, 2008, **321**, 671-674.

142. B. Wondimu and S. Admassie, *Bulletin of the Chemical Society of Ethiopia*, 2012, **26**, 449-454.

143. Q. Zhou and G. Shi, *Journal of the American Chemical Society*, 2016, **138**, 2868-2876.

144. Y. Xia, K. Sun and J. Ouyang, *Advanced materials*, 2012, **24**, 2436-2440.

145. H. Shi, C. Liu, Q. Jiang and J. Xu, *Advanced Electronic Materials*, 2015, **1**, 1-16.

146. C. Deetuam, D. Weise, C. Samthong, P. Praserthdam, R. R. Baumann and A. Somwangthanaroj, *Journal of Applied Polymer Science*, 2015, **132**, 1-9.

147. Y. Xiao, J.-Y. Lin, S.-Y. Tai, S.-W. Chou, G. Yue and J. Wu, *Journal of Materials Chemistry*, 2012, **22**, 19919-19925.

148. F. Yusoff and N. A. B. Muhamad, *Materials Today: Proceedings*, 2019, **16**, 2023-2029.

149. S. Mutyala and J. Mathiyaras, *ECS Transactions*, 2015, **64**, 33-42.

150. G. Zhang and F. Yang, *Electrochimica Acta*, 2007, **52**, 6595-6603.

151. H. Deng, Q. Li, J. Liu and F. Wang, *Carbon*, 2017, **112**, 219-229.

152. B.E. Conway, *Electrochemical Supercapacitors: Scientific Fundamentals and Technological Applications*, Kluwer Acadamic, New york, 1999.

153. F. Beguin and E. Frackowiak, *Supercapacitors Materials, Systems, and Applications*, Wiley-VCH, Germany, 2013.

154. M. Jayalakshmi and K. Balasubramanian, *International Journal of Electrochemical Science*, 2008, **3**, 1196-1217.

155. A. Noori, M. F. El-Kady, M. S. Rahmanifar, R. B. Kaner and M. F. Mousavi, *Chemical Society reviews*, 2019, **48**, 1272-1341.

156. A. Burke, *Journal of Power Sources*, 2000, **91**, 37-50.

157. L. L. Zhang and X. S. Zhao, *Chemical Society reviews*, 2009, **38**, 2520-2531.

158. T. Brousse, D. Bélanger and J. W. Long, *Journal of The Electrochemical Society*, 2015, **162**, A5185-A5189.

159. B. E. Conway and W. G. Pell, *Journal of Solid State Electrochemistry*, 2003, **7**, 637-644.

160. C. Zhong, Y. Deng, W. Hu, J. Qiao, L. Zhang and J. Zhang, *Chemical Society reviews*, 2015, **44**, 7484-7539.

161. D. P. Dubal, O. Ayyad, V. Ruiz and P. Gomez-Romero, *Chemical Society reviews*, 2015, **44**, 1777-1790.

162. J. Lee, P. Srimuk, S. Fleischmann, X. Su, T. A. Hatton and V. Presser, *Progress in Materials Science*, 2019, **101**, 46-89.

163. K. Kopczyński, Ł. Kolanowski, M. Baraniak, K. Lota, A. Sierczyńska and G. Lota, *Current Applied Physics*, 2017, **17**, 66-71.

164. N. S. Punde, A. S. Rajpurohit and A. K. Srivastava, *Energy Technology*, 2019, **7**, 1-12.

165. L. Guan, L. Yu and G. Z. Chen, *Electrochimica Acta*, 2016, **206**, 464-478.

166. Y. Wang, Y. Song and Y. Xia, *Chemical Society reviews*, 2016, **45**, 5925-5950.

167. S. Zhang and N. Pan, *Advanced Energy Materials*, 2015, **5**, 1-19.

168. S. Admassie, A. Elfwing, E. W. H. Jager, Q. Bao and O. Inganäs, *Journal of Materials Chemistry A*, 2014, **2**, 1974-1979.

169. K. V. Sankar and R. Kalai Selvan, *Carbon*, 2015, **90**, 260-273.

170. F. Wang, X. Wu, X. Yuan, Z. Liu, Y. Zhang, L. Fu, Y. Zhu, Q. Zhou, Y. Wu and W. Huang, *Chemical Society reviews*, 2017, **46**, 6816-6854.

171. A. Laheäär, P. Przygocki, Q. Abbas and F. Béguin, *Electrochemistry Communications*, 2015, **60**, 21-25.

172. G. A. Snook, P. Kao and A. S. Best, *Journal of Power Sources*, 2011, **196**, 1-12.

173. B. N. Grgur, M. Janačković, B. Z. Jugović and M. M. Gvozdenović, *Materials Science and Engineering: B*, 2019, **243**, 175-182.

174. A. A. Alguail, A. H. Al-Eggiely and B. N. Grgur, *Journal of Saudi Chemical Society*, 2017, **21**, 575-582.

175. A. V. Volkov, K. Wijeratne, E. Mitraka, U. Ail, D. Zhao, K. Tybrandt, J. W. Andreasen, M. Berggren, X. Crispin and I. V. Zozoulenko, *Advanced Functional Materials*, 2017, **27**, 1-10.

176. A. M. Osterholm, D. E. Shen, A. L. Dyer and J. R. Reynolds, *ACS Applied Materials & Interfaces*, 2013, **5**, 13432-13440.

177. N. Kumar, R. T. Ginting and J.-W. Kang, *Electrochimica Acta*, 2018, **270**, 37-47.

178. C. Zhang, T. M. Higgins, S.-H. Park, S. E. O'Brien, D. Long, J. N. Coleman and V. Ncolosi, *Nano Energy*, 2016, **28**, 495-505.

179. Y. Chen, X. Zhu, D. Yang, P. Wangyang, B. Zeng and H. Sun, *Electrochimica Acta*, 2019, **298**, 297-304.

180. Z. Yang, J. Ma, B. Bai, A. Qiu, D. Losic, D. Shi and M. Chen, *Electrochimica Acta*, 2019, **322**, 1-9.

181. Y. Zhu, N. Li, T. Lv, Y. Yao, H. Peng, J. Shi, S. Cao and T. Chen, *Journal of Materials Chemistry A*, 2018, **6**, 941-947.

182. B. Pal, S. Yang, S. Ramesh, V. Thangadurai and R. Jose, *Nanoscale Advances*, 2019, **1**, 3807-3835.

183. E. Kovalska and C. Kocabas, *Materials Today Communications*, 2016, **7**, 155-160.

184. N. Blomquist, T. Wells, B. Andres, J. Backstrom, S. Forsberg and H. Olin, *Scientific reports*, 2017, **7**, 1-7.

185. F. Chekol, S. Mehretie, F. A. Hailu, T. Tolcha, N. Megersa and S. Admassie, *Electroanalysis*, 2019, **31**, 1104-1111.

186. J. Schmidt, H. A. Gasteiger, G. D. Stab, P. M. Urban, D. M. KoIb and R. J. Behm, *Journal of Electrochemical society*, 1998, **145**, 2354-2358.

187. Y. Garsany, O. A. Baturina, K. E. S-Lyons and S. S. Kocha, *Analytical Chemistry*, 2010, **82**, 6321-6328.

188. X. Min, Y. Chen and M. W. Kanan, *Physical chemistry chemical physics : PCCP*, 2014, **16**, 13601-13604.

189. G. Zhang, Q. Wei, X. Yang, A. C. Tavares and S. Sun, *Applied Catalysis B: Environmental*, 2017, **206**, 115-126.

190. W.S.Hummers and R. E. Offeman, *Journal of American Chemical Society*, 1958, **80**, 1339.

191. Y. Shao, J. Wang, M. Engelhard, C. Wang and Y. Lin, *Journal of Materials Chemistry*, 2010, **20**, 743-748.

192. N. Kurra, M. K. Hota and H. N. Alshareef, *Nano Energy*, 2015, **13**, 500-508.

193. M. J. Frisch, G. W. Trucks, H. B. Schlegel, G. E. Scuseria, M. A. Robb, J. R. Cheeseman, G. Scalmani, V. Barone, G. A. Petersson, H. Nakatsuji, X. Li, M. Caricato, A. Marenich, J. Bloino, B. G. Janesko, R. Gomperts, B. Mennucci, H. P. Hratchian, J. V. Ortiz, A. F. Izmaylov, J. L. Sonnenberg, D. Williams-Young, F. Ding, F. Lipparini, F. Egidi, J. Goings, B. Peng, A. Petrone, T. Henderson, D. Ranasinghe, V. G. Zakrzewski, J. Gao, N. Rega, G. Zheng, W. Liang, M. Hada, M. Ehara, K. Toyota, R. Fukuda, J. Hasegawa, M. Ishida, T. Nakajima, Y. Honda, O. Kitao, H. Nakai, T. Vreven, K. Throssell, J. J. A.

Montgomery, J. E. Peralta, F. Ogliaro, M. Bearpark, J. J. Heyd, E. Brothers, K. N. Kudin, V. N. Staroverov, T. Keith, R. Kobayashi, J. Normand, K. Raghavachari, A. Rendell, J. C. Burant, S. S. Iyengar, J. Tomasi, M. Cossi, J. M. Millam, M. Klene, C. Adamo, R. Cammi, J. W. Ochterski, R. L. Martin, K. Morokuma, O. Farkas, J. B. Foresman and D. J. Fox, *Gaussian Inc. Wallingford CT*, 2009.

194. A. D. Becke, *Journal of Chemical Physics*, 1993, **98**, 5648-5652.

195. C. Lee, W. Yang and R. G. Parr, *Physical review. B, Condensed matter*, 1988, **37**, 785-789.

196. P. J. Stephens, F. J. Devlin, C. F. Chabalowski and M. J. Frisch, *The Journal of Physical Chemistry*, **98**, 11623-11627.

197. R. Krishnan, J. S. Binkley, R. Seeger and J. A. Pople, *The Journal of Chemical Physics*, 1980, **72**, 650-654.

198. J.Tomasi, B. Mennucci and R. Cammi, *Chemical reviews*, 2005, **105**, 2999-3093.

199. F. Weinhold and C. R. Landis, *Chemistry Education: Research and Practice In Europe*, 2001, **2**, 91-104.

200. F. Weinhold and C. R. Landis, *Discovering Chemistry with Natural Bond Orbitals*, John Wiley and Sons, 2012.

201. K. Jukk, N. Kongi, A. Tarre, A. Rosental, A. B. Treshchalov, J. Kozlova, P. Ritslaid, L. Matisen, V. Sammelselg and K. Tammeveski, *Journal of Electroanalytical Chemistry*, 2014, **735**, 68-76.

202. N. Zhang, L. Li, Y. Chu, L. Zheng, S. Sun, G. Zhang, H. He and J. Zhao, *Catalysis Today*, 2019, **332**, 101-108.

203. X. Song, N. Li, H. Zhang, H. Wang, L. Wang and Z. Bian, *Journal of Power Sources*, 2019, **435**, 1-9.

204. Q. Liu, S. Cao and Y. Qiu, *International Journal of Hydrogen Energy*, 2017, **42**, 29274-29282.

205. A. Jindal, D. K. Gautam and S. Basu, *Journal of Electroanalytical Chemistry*, 2016, **775**, 198-204.

206. F. Jiang, Z. Yao, R. Yue, J. Xu, Y. Du, P. Yang and C. Wang, *Journal of Solid State Electrochemistry*, 2012, **17**, 1039-1047.

207. H. Feng, Y. Liu and J. Li, *Chemical communications*, 2015, **51**, 2418-2420.

208. M. Beltrán-Gastélum, M. I. Salazar-Gastélum, J. R. Flores-Hernández, G. G. Botte, S. Pérez-Sicairos, T. Romero-Castañon, E. Reynoso-Soto and R. M. Félix-Navarro, *Energy*, 2019, **181**, 1225-1234.

209. T. Getachew, F. Addis, T. Beyene, S. Mehretie and S. Admassie, *Bulletin of the Chemical Society of Ethiopia*, 2019, **33**, 359-372.

210. K. Sun, S. Zhang, P. Li, Y. Xia, X. Zhang, D. Du, F. H. Isikgor and J. Ouyang, *Journal of Materials Science: Materials in Electronics*, 2015, **26**, 4438-4462.

211. C. Che, M. Vagin, K. Wijeratne, D. Zhao, M. Warczak, M. P. Jonsson and X. Crispin, *Advanced Sustainable Systems*, 2018, **2**, 1-7.

212. Y.-J. Wang, N. Zhao, B. Fang, H. Li, X. T. Bi and H. Wang, *RSC Advances*, 2015, **5**, 56570-56577.

213. S. Chen, J. Duan, J. Ran, M. Jaroniec and S. Z. Qiao, *Energy & Environmental Science*, 2013, **6**, 3693-3699.

214. J. Yang, H. Sun, H. Liang, H. Ji, L. Song, C. Gao and H. Xu, *Advanced materials*, 2016, **28**, 4606-4613.

215. Z. Gong, G. Zhang and S. Wang, *Journal of Chemistry*, 2013, **2013**, 1-9.

216. J. Tang, Z. Ou, R. Guo, Y. Fang, D. Huang, J. Zhang, J. Zhang, S. Guo, F. M. McFarland and K. M. Kadish, *Inorganic chemistry*, 2017, **56**, 8954-8963.

217. Q. Li, R. Cao, J. Cho and G. Wu, *Advanced Energy Materials*, 2014, **4**, 1-19.

218. Y. A. Pimonova, A. P. Budnyk, W. Yohannes, A. L. Bugaev and T. A. Lastovina, *ACS Omega*, 2019, **4**, 19548-19555.

219. A. A. Ensafi, M. Jafari-Asl and B. Rezaei, *Electrochimica Acta*, 2016, **194**, 95-103.

220. X. Tong, Q. Wei, X. Zhan, G. Zhang and S. Sun, *Catalysts*, 2016, **7**, 1-26.

221. A. Geto and C. M. A. Brett, *Journal of Solid State Electrochemistry*, 2016, **20**, 2969-2979.

222. S. M. Unni, S. Devulapally, N. Karjule and S. Kurungot, *Journal of Materials Chemistry*, 2012, **22**, 23506-23513.

223. X. Huang, X. Yin, X. Yu, J. Tian and W. Wu, *Colloids and Surfaces A: Physicochemical and Engineering Aspects*, 2018, **539**, 163-170.

224. L. Osmieri, A. H. A. Monteverde Videla and S. Specchia, *Journal of Solid State Electrochemistry*, 2016, **20**, 3507-3523.

225. S. G. Patnaik, R. Vedarajan and N. Matsumi, *ACS Applied Energy Materials*, 2018, **1**, 1183-1190.

226. S. Kakhki, M. M. Barsan, E. Shams and C. M. A. Brett, *Synthetic Metals*, 2012, **161**, 2718-2726.

227. Y. Wang, M. Yi, K. Wang and S. Song, *Chinese Journal of Catalysis*, 2019, **40**, 523-533.

228. V. Stamenković, T. J. Schmidt, P. N. Ross and N. M. Marković, *Journal of Electroanalytical Chemistry*, 2003, **554-555**, 191-199.

229. M. S. Hossain, D. Tryk and E. Yeager, *Electrochimica Acta*, 1989, **34**, 1733-1737.

230. M. Jahan, Q. Bao and K. P. Loh, *Journal of American Chemical Society*, 2012, **134**, 6707-6713.

231. Y. Ma, L. Zhang, J. Li, H. Ni, M. Li, J. Zhang, X. Feng, Q. Fan, Z. Hu and W. Huang, *Chinese Science Bulletin*, 2011, **56**, 3583-3589.

232. S. Yang, L. Zhi, K. Tang, X. Feng, J. Maier and K. Müllen, *Advanced Functional Materials*, 2012, **22**, 3634-3640.

233. D. P. Dubal, J. G. Kim, Y. Kim, R. Holze, C. D. Lokhande and W. B. Kim, *Energy Technology*, 2014, **2**, 325-341.

234. Z. Liu, Z.-S. Wu, S. Yang, R. Dong, X. Feng and K. Müllen, *Advanced materials*, 2016, **28**, 2217-2222.

235. Z. Li, J. Cai, P. Cizek, H. Niu, Y. Dua and T. Lin, *Journal of Materials Chemistry A*, 2015, **3**, 16162-16167.

236. S. Admassie, T. Y. Nilsson and O. Inganas, *Physical Chemistry Chemical Physics*, 2014, **16**, 24681-24684.

237. M. N. Rantho, M. J. Madito and N. Manyala, *Electrochimica Acta*, 2018, **262**, 82-96.

238. I. Heng, F. W. Low, C. W. Lai, J. C. Juan, N. Amin and S. K. Tiong, *Journal of Alloys and Compounds*, 2019, **796**, 13-24.

239. S. Admassie, *Bulletin of the Chemical Society of Ethiopia*, 2016, **30**, 153-160.

240. H. Chen, J. Zhou, Q. Li, K. Tao, X. Yu, S. Zhao, Y. Hu, W. Zhao and L. Han, *Inorganic Chemistry Frontiers*, 2019, **6**, 2481-2487.

241. J.-H. Jeong, J. W. Park, D. W. Lee, R. H. Baughman and S. J. Kim, *Scientific reports*, 2019, **9**, 1-8.

242. B. C. Kim, R. Manikandan, K. H. Yu, M.-S. Park, D.-W. Kim, S. Y. Park and C. J. Raj, *Journal of Alloys and Compounds*, 2019, **789**, 256-265.

243. K. O. Oyedotun, M. J. Madito, D. Y. Momodu, A. A. Mirghni, T. M. Masikhwa and N. Manyala, *Chemical Engineering Journal*, 2018, **335**, 416-433.

244. S. Admassie, A. Elfwing and O. Inganäs, *Advanced Materials Interfaces*, 2016, **3**, 1-6.

245. P.-O. Schwartz, M. Pejic, M. Wachtler and P. Bäuerle, *Synthetic Metals*, 2018, **243**, 51-57.

246. F. Checkol, A. Elfwing, G. Greczynski, S. Mehretie, O. Inganäs and S. Admassie, *Advanced Sustainable Systems*, 2018, **2**, 1-7.

247. M. Marzocchi, I. Gualandi, M. Calienni, I. Zironi, E. Scavetta, G. Castellani and B. Fraboni, *ACS Applied Materials & Interfaces*, 2015, **7**, 17993-18003.

248. K. Appett, *Electrochimica Acta*, 1968, **13**, 1521-1532.

249. A. M. A. El-Halim, M. H. Fawzy and A. Saty, *Journal of Electroanalytical Chemistry*, 1991, **316**, 275-292.

250. M. O. Salles, V. L. Martins, R. M. Torresi and M. Bertotti, *Electrochimica Acta*, 2012, **78**, 347-352.

251. Z. Zhang, C. Liu and X. Zhao, *The Journal of Physical Chemistry C*, 2015, **119**, 5626-5632.

252. L. R. Pederson, *Journal of Electron Spectroscopy and Related Phenomena*, 1982, **28**, 203-209.

253. J. Y. Woo, J. H. Ko, J. H. Song, K. Kim, H. Choi, Y. H. Kim, D. C. Lee and S. Jeong, *Journal of American Chemical Society*, 2014, **136**, 8883-8886.

254. R. J. Thibeau and C. W. Brown, *Journal of the Electrochemical Society*, 1980, **127**, 1702-1706.

255. N. Padmanathan, H. Shao, D. McNulty, C. O'Dwyer and K. M. Razeeb, *Journal of Materials Chemistry A*, 2016, **4**, 4820-4830.

256. D. Antiohos, G. Folkes, P. Sherrell, S. Ashraf, G. G. Wallace, P. Aitchison, A. T. Harris, J. Chen and A. I. Minett, *Journal of Materials Chemistry*, 2011 **21**, 15987-15994.

257. T. M. Higgins and J. N. Coleman, *ACS Applied Materials Interfaces*, 2015, **7**, 16495-16506.

258. A. Jaiswal and S. C. Chalasani, *Journal of Energy Storage*, 2015, **1**, 15-21.

259. K. Fic, G. Lota, M. Meller and E. Frackowiak, *Energy and Environmental Science*, 2012, **5**, 5842-5850.

260. D. P. Dubal, N. R. Chodankar, D. H. Kim and P. Gomez-Romero, *Chemical Society reviews*, 2018, **47**, 2065-2129.

261. X. Lu, M. Yu, G. Wang, Y. Tong and Y. Li, *Energy & Environmental Science*, 2014, **7**, 2160-2181.

262. S. A. Pawar, D. S. Patil and J. C. Shin, *Electrochimica Acta*, 2018, **259**, 664-675.

263. Y. Z. Zhang, Y. Wang, T. Cheng, L. Q. Yao, X. Li, W. Y. Lai and W. Huang, *Chemical Society reviews*, 2019, **48**, 3229-3264.

264. A. Muzaffar, M. B. Ahamed, K. Deshmukh and J. Thirumalai, *Renewable and Sustainable Energy Reviews*, 2019, **101**, 123-145.

265. J. Suarez-Guevara, V. Ruiz and P. Gomez-Romero, *Physical chemistry chemical physics : PCCP*, 2014, **16**, 20411-20414.

266. T. Getachew, S. Mehretie, H. L. Yip, R. Xia and S. Admassie, *Physical chemistry chemical physics : PCCP*, 2020, **22**, 5597-5603.

267. Z. Wang, J. Cheng, Q. Guan, H. Huang, Y. Li, J. Zhou, W. Ni, B. Wang, S. He and H. Peng, *Nano Energy*, 2018, **45**, 210-219.

268. H. Alhummiany, S. Rafique and K. Sulaiman, *The Journal of Physical Chemistry C*, 2017, **121**, 7649-7658.

269. X. Xia, W. Lei, Q. Hao, W. Wang and X. Wang, *Electrochimica Acta*, 2013, **99**, 253-261.

270. L. Lu and Y. Xie, *New Journal of Chemistry*, 2017, **41**, 335-346.

271. S. Khadempir, A. Ahmadpour, M. T. Hamed Mosavian, N. Ashraf, F. F. Bamoharram, R. Fernández-Pacheco, J. M. de la Fuente and S. G. Mitchell, *RSC Advances*, 2016, **6**, 5359-5366.

272. Y. Li, G. Ren, Z. Zhang, C. Teng, Y. Wu, X. Lu, Y. Zhu and L. Jiangac, *Journal of Materials Chemistry A*, 2016, **4**, 17324-17332.

273. C. Sun, X. Li, J. Zhao, Z. Cai and F. Ge, *Electrochimica Acta*, 2019, **317**, 42-51.

274. N. Wang, X. Wang, Y. Zhang, W. Hou, Y. Chang, H. Song, Y. Zhao and G. Han, *Journal of Alloys and Compounds*, 2020, **835**, 1-9.

275. N. Wanga, G. Hana, H. Song, Y. Xiaoa, Y. Lia, Y. Zhanga and H. Wanga, *Journal of Power Sources*, 2018, **395**, 228-236.

276. B. Anothumakkool, R. Soni, S. N. Bhange and S. Kurungot, *Energy & Environmental Science*, 2015, **8**, 1339-1347.

277. Z. Wang, P. Tammel, J. Huo, P. Zhang, M. Strømme and L. Nyholm, *Journal of Materials Chemistry A*, 2016, **4**, 1714-1722.

278. S. B. Singh, T. Kshetri, T. I. Singh, N. H. Kim and J. H. Lee, *Chemical Engineering Journal*, 2019, **359**, 197-207.